Downloaded from orbit.dtu.dk on: May 06, 2023

DTU Library

Development and Utilization of Bio-based Platform Chemicals for Renewable Materials

Larsen, Daniel Bo

Publication date:
2018

Document Version
Publisher's PDF, also known as Version of record

Link back to DTU Orbit

Citation (APA):
Larsen, D. B. (2018). *Development and Utilization of Bio-based Platform Chemicals for Renewable Materials*. Technical University of Denmark.

General rights
Copyright and moral rights for the publications made accessible in the public portal are retained by the authors and/or other copyright owners and it is a condition of accessing publications that users recognise and abide by the legal requirements associated with these rights.

- Users may download and print one copy of any publication from the public portal for the purpose of private study or research.
- You may not further distribute the material or use it for any profit-making activity or commercial gain
- You may freely distribute the URL identifying the publication in the public portal

If you believe that this document breaches copyright please contact us providing details, and we will remove access to the work immediately and investigate your claim.

Development and Utilization of Bio-based Platform Chemicals for Renewable Materials

Ph.D. Thesis

Daniel Bo Larsen

Department of Chemistry

Technical University of Denmark

April 2018

Preface

This thesis is the product of three years of work at the Technical University of Denmark (DTU). The work was carried out under initial supervision of Dr. Peter Fristrup and Associate Professor Anders E. Daugaard, and later under Professor Jens. Ø. Duus due to Dr. Peter Fristrup pursuing a new career. The work was carried out at the Department of Chemistry and the Danish Polymer Center (DPC), both at DTU. Furthermore, a three month external stay at Kungliga Tekniska Högskolan (KTH) was carried out in the fall of 2017, in collaboration of Professor Mats Johansson and Ph.D. student Samer Nameer.

The thesis is divided into two major chapters; the first concerning theoretical calculations through Density Functional Theory, and the second investigates procedures for synthesizing new types of bio-based materials. The projects has been supported financially by DTU, and the external stay was funded by Augustinus Fonden and Otto Mønsteds Fond.

Daniel Bo Larsen

Kongens Lyngby, 2018

Abstract

In the progression of modern society, the inevitable exhaustion of fossil resources becomes an increasingly concerning matter. These resources are not only the cornerstone of the energy production of the world, but also the precursor for many important platform chemicals used in the plastics industry. With a disappearance of fossil resources on the horizon, alternatives have to be developed, for example, tackling the energy crisis through revolutions in the field of renewable energy. However, regarding platform chemicals, a new and sustainable source has to be used, such as biomass. One of the larger challenges when employing biomass as a renewable resource, is the natural high abundance of oxygen compared to the petrol-based precursors, which calls for the development of catalytic reactions capable of oxygen removal, in order to obtain useful platform chemicals mimicking those used today.

The first part of this thesis concerns development of two of these reactions; the deoxydehydration and the hydrodeoxygenation reactions. The deoxydehydration reaction is studied both using vanadium and rhenium catalysts, whereas the hydrodeoxygenation reaction is preformed using a molybdenum catalyst. The studies revolve around examination of the reactions by applying the computational method Density Functional Theory, which allows for elucidation of the intrinsic mechanism of the reactions. This leads to discoveries of new types of mechanisms for both reactions, explaining differences in reactivity compared to what has previously been observed in literature for similar catalytic systems. An example of utilization of these reactions is the production of allyl alcohol, which can be obtained from deoxydehydration of glycerol – a compound yielded as a side-product from the bio-diesel industry.

The second part of the thesis focuses on the utilization of bio-based platform chemicals for synthesis of novel thermoset polymer materials. Common ground for all of these studies is the diallyl furan-2,5-dicarboxylate monomer, which is tested through a plethora of different crosslinking techniques. This monomer is of high interest due to being derived from allyl alcohol and the bio-based building block 2,5-furandicarboxylic acid, the latter showing application as a replacement for phthalates. In the studies, this new monomer is tested in various ways; firstly through UV-initiated crosslinking to thiol-ene networks, then synthesis of larger prepolymeric structures for crosslinking, and finally expansion into epoxy networks through copolymerization with epoxidized fatty acid esters. These studies lead to various new materials, along with new methods for determinations of molecular weights of branched polymer systems, by examining the intrinsic growth patterns of hyperbranched polyester systems.

With this thesis, foundation for further development of methods for production of bio-based platform chemicals have been developed along with new methods for the utilization of these chemicals for renewable materials. These materials represents a plausible replacement of their petrol-based analogues, hereby laying parts of the groundwork for a more sustainable and renewable future.

Resumé

Med et konstant udviklende samfund leder den uundgåelige udtømning af de fossile ressourcer til en stigende bekymring. Disse ressourcer er ikke kun grundstenen i vores energiproduktion, men er også udgangsstoffer til en lang række kemikalier som bliver brugt i plastikindustrien. Med evigt svindende fossile ressourcer i horisonten, bliver vi nødsaget til at udvikle bæredygtige alternativer, for eksempel ved at udnytte anderledes ressourcer som biomasse. En af de større udfordringer ved brug af biomasse til udvikling af platformkemikalier er det naturligt høje indhold af oxygen sammenlignet med deres oliebaserede ækvivalenter. Dette leder til søgen efter reaktioner, som er i stand til at reducere dette oxygen-indhold, så man kan producere brugbare kemikalier som kan efterligne dem man bruger i dag.

Den første del af denne afhandling omhandler udviklingen af to af disse typer reaktioner: deoxydehydrering og hydrodeoxygenering. Deoxydehydreringen er blevet undersøgt med brug af både vanadium og rhenium baserede katalysatorer, mens hydrodeoxygeneringen er blevet studeret ved brug af molybdæn. Disse studier fokuserer på undersøgelser foretaget med den computerkemiske metode, Density Functional Theory, hvorved reaktionernes specifikke mekanismer kan bestemmes. Dette har vist nye typer af mekanismer for de to undersøgte reaktioner, som yderlige kan hjælpe til at forklare forskelle i reaktivitet, sammenlignet med det som tidligere har været observeret. Et eksempel på brugen af disse reaktioner er deoxydehydreringen som kan bruges til fremstilling af allylalkohol fra glycerol – et kemikalie som produceres som et sideprodukt fra biodiesel industrien.

Den anden del af afhandlingen fokuserer på brugen af nogle af disse biobaserede kemikalier til syntese af nye thermosætmaterialer. Fælles for alle studier i denne del er brugen af diallyl furan-2,5-dicarboxylat, som bliver testet gennem et udvalg af forskellige krydsbindingsmetoder. Denne monomer er yderst interessant da den kan fremstilles fra allylalkohol og den biobaserede byggeblok 2,5-furandicarboxylsyre, den sidstnævnte værende en byggeblok som kan anvendes som erstatning for phthalater. I disse studier bliver monomeren testet gennem en række metoder; først UV-initieret krydsbinding til thiol-ene netværk, herefter gennem syntese af større prepolymersystemer til efterfølgende krydsbinding og til sidst videreudvikling til epoxy-kemi, hvor thermosæt epoxy resiner bliver undersøgt gennem copolymerisering med epoxiderede fedtsyreestre. Udover en række nye materialer, førte disse studier også til udviklingen af en ny metode for bestemmelse af molekylevægt for forgrenede polyestere ved nærundersøgelse af vækstmønstre for systemerne.

Med denne afhandling er der blevet grundlagt en række principper for videreudvikling og brug af biobaserede platformkemikalier til syntese af miljørigtige materialer. Disse materialer kan repræsentere en mulighed for erstatning af deres oliebaserede ækvivalenter, og herved lægge et fundament for en mere bæredygtig fremtid.

Acknowledgements

First and foremost I would like to extend my sincere appreciation to my supervisors Anders E. Daugaard, Jens Ø. Duus and Peter Fristrup. Their continuous guidance and support throughout the passing three years has allowed me to work on interesting projects, with a large degree of freedom, giving me the opportunity to put my own mark on the research. Also thank you to my colleagues in building 206 and 207, with special mention of Christian, Rita, Samuel, Gauthier, Nacho and Ronja, for the numerous scientific discussion and coffee breaks and to Christian and Rita for proof-reading parts of my thesis.

I would like to thank Mats Johansson and Samer Nameer for an excellent collaboration in the fall of 2017 at KTH. Also, thank you to the entirety of the Division of Coating Technology for welcoming me with open arms. A special acknowledgement goes to Samer, not only for our collaboration, but also for his friendship and helping me finding my feet when moving to a new country.

Thank you to my collaborators Allan Petersen, Lasse Olsen and Johannes Dethlefsen from the former Fristrup group, and thank you to my students Mathias, Kristoffer, René and Alexandros for their scientific contributions.

I owe a large thanks to my family for their support, and especially Poul for his efforts in proof-reading my thesis, even if the subject matter was outside his field of expertise.

Thank you to Casper and Victor for our travels which helped me stay sane throughout the more stressful parts of the studies. And last, but not least, I would like to thank my friends (in random order), Rasmus, Rikke, Cecilia, Martin, Ali, Stefania, Toft, Glantz, Annette, Bjarne, Christoffer, Tina, Julie, Dagmar, Christian, Anders, Christoffer, Geanna, Carlos, Daniel, Niels, Mads, Niklas, Tenna, Claus, Maya, Kevin, Michael, Mathias, Lasse, Arne and Charlotte who have supported me and have attempted to appear interested in my scientific ramblings throughout the last three years. Also a sincere apology to anyone I may have forgotten in this section.

List of Abbreviations

AE	Atom Economy
AHM	Ammoniumheptamolybdate
B3LYP	Becke, 3-parameter, Lee-Yang-Parr
CalB	Candida Antarctica lipase B
COSY	Correlation Spectroscopy
DAFDC	Diallyl furan-2,5-dicarboxylate
DCP	Dicumyl peroxide
DFT	Density Functional Theory
DGFDC	Diglycidyl furan-2,5-dicarboxylate
DMTA	Dynamic Mechanical Thermal Analysis
DODH	Deoxydehydration
DSC	Differential Scanning Calorimetry
DPM	*trans*-2,5-dihydroxy-3-pentenoic acid methyl ester
EMLEN	Epoxidized Methyl Ester of Linolenic Acid
EMLO	Epoxidized Methyl Ester of Linoleic Acid
EMO	Epoxidized Methyl Ester of Oleic Acid
EMX	Joint description for EMO, EMLO and EMLEN
ETTMP	Ethoxilated-trimethylolpropan tri(3-mercaptopropionate)
FDCA	2,5-Furandicarboxylic acid
FTIR	Fourier Transform Infrared
GGA	General Gradient Approximation
HDO	Hydrodeoxygenation
HMF	Hydroxymethylfurfural
HPC	High Performance Computing
HSQC	Heteronuclear single quantum coherence
KTH	Kungliga Tekniska Högskolan
LACVP	Los Alamos Effective Core Valence Potential
LDA	Local Density Approximation

LO	Linseed Oil
m-CPBA	*m*-Chloroperoxybenzoic acid
$\overline{M_n}$	Average Number Molecular Weight
MSPV	Meerwein-Schmidt-Ponndorf-Verley
MVG	Methyl vinyl glycolate
NMR	Nuclear Magnetic Resonance
PCL4MP	Polycaprolactone tetra(3-mercaptopropionate)
PBF	Poisson Boltzmann Finite element method
PE	Polyethylene
PEF	Polyethylene furanoate
PET	Polyethylene terephthalate
PETMP	Pentaerythritol tetrakis(3-mercaptopropionate)
PLA	Polylactic acid
PP	Polypropylene
PS	Polystyrene
PVC	Polyvinyl chloride
QST	Quadratic Synchronous Transit
SCF	Self-Consistent Field
SEC	Size Exclusion Chromatography
TA	Terephthalic acid
TATATO	Triallyl-1,3,5-triazine-2,4,6-trione
TEMPIC	Tris[2-(3-mercaptopropionyloxy)ethyl]isocyanurate
T_g	Glass Transition Temperature
TGA	Thermal Gravimetric Analysis
T_m	Melting Temperature
TMPMP	Trimethylolpropane tri(3-mercaptopropionate)
TOF	Turn-Over Frequency
UV	Ultra-Violet

Publications

Nielsen, L. B. †; **Larsen, D. B.** †; Dethlefsen, J. R.; Fristrup, P. "Vanadium-Catalyzed Deoxydehydration of Vicinal Diols using Isopropyl Alcohol as the Reductant". (Submitted to ChemCatChem)

Larsen, D. B.†; Petersen, A. R. †; Dethlefsen, J. R.; Teshome, A.; Fristrup, P. "Mechanistic Investigation of Molybdate-Catalyzed Transfer Hydrodeoxygenation", *Chem. Eur. J.* **2016**, *22*, 16621-16631.

Larsen, D. B.; Sønderbæk-Jørgensen, R.; Duus, J. Ø.; Daugaard A. E. "Investigation of curing rates of bio-based thiol-ene films from diallyl 2,5-furandicarboxylate"*, Eur. Polym. J.* **2018,** *102*, 1-8.

Larsen, D. B. †; Rønsbro, K.; Duus, J. Ø.; Daugaard, A. E. " Synthesis of Functionalized Hyperbranched FDCA Polyesters and Characterization of Molecular Weight and Branching by NMR". (Submitted to Macromolecules)

Nameer, S. †; **Larsen, D. B.** †; Johansson, M. K. G. "Bio-based cationically polymerizable epoxy thermosets from furan and fatty acid derivatives". (Submitted to ACS Sustainable Chemistry and Engineering)

†*Shared first authorship.*

Furthermore, contributions to three publications have not been included in this thesis:

Andersen, J. E. T.; Glasdam, S.-M.; **Larsen, D. B.**; Molenaar, N. "New Concepts of Quality Assurance in Analytical Chemistry: Will They Influence the Way We Conduct Science in General?", *Chem. Eng. Commun.* **2016,** *203***,** 1582-1590**.**

Parto, S. G.; Christensen, J. M.; Pedersen, L. S.; Tjosås, F.; Hansen, A. B.; Damsgaard, C. D.; Spiga, C.; **Larsen, D. B.**; Duus, J. Ø.; Jensen A. D. " Liquefaction of lignosulfonate in supercritical ethanol using alumina supported NiMo catalyst: Analysis of the products and parameter study" (Manuscript in preparation)

Parto, S. G.; Jørgensen, E. K.; Christensen, J. M.; Pedersen, L. S.; **Larsen D. B.**; Duus, J. Ø.; Jensen, A. D. " One-pot catalytic conversion of beech wood and Organosolv lignin over NiMo/Al2O3" (Manuscript in preparation)

Table of Contents

1 Background and Objective

1.1 Consumption of Fossil Resources and Future Outlook

The expansive growth of modern societies leads to increased energy demands. A fundamental pillar of basic societal function is the fossil resource reserves, serving not only as fuel but also for numerous chemical applications, either directly or as precursors for platform chemicals. With consumption of fossil resources and production rising steadily throughout the past 25 years,[1] and with the knowledge that this is an exhaustible resource, the prospect of dwindling reserves will have an enormous impact on modern industry. Through the last decade, consumption of fossil resources has increased significantly (Figure 1). Although a significant rise is also observed for production of biofuels and renewable energy, these sources of energy are still produced on a minor scale compared to the fossil resource equivalents. The constant rise in consumption is made possible by a constant discovery of new oil and gas reserves around the globe, causing an increase in the total known reserves of the world.[1]

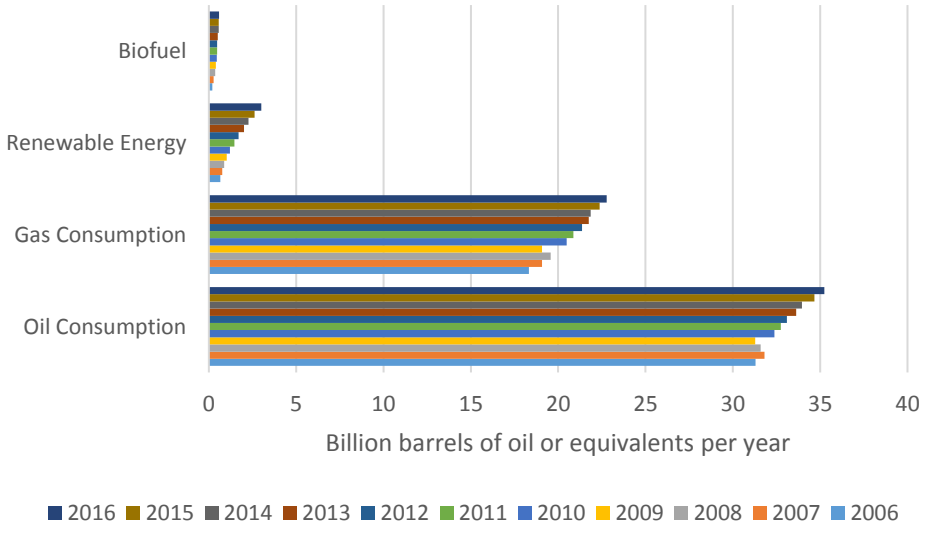

Figure 1: Consumption of energy through the last decade. All data are pulled from the BP Annual Review 2017.[1]

Though acknowledged that the reserves will exhaust in the future, predictions of the exact time frame are hampered by the continuous discovery of new reserves. Predictions estimate a peak of the oil production approximately in 2025 (Figure 2)[2] which leads to the necessity of developing alternative strategies for counteracting the impact caused by the gradual depletion of these fossil resources. The tackling of this problem has been dubbed *The Terawatt Challenge* due to the massive amounts of renewable energy required in an oil-deficient future.[3]

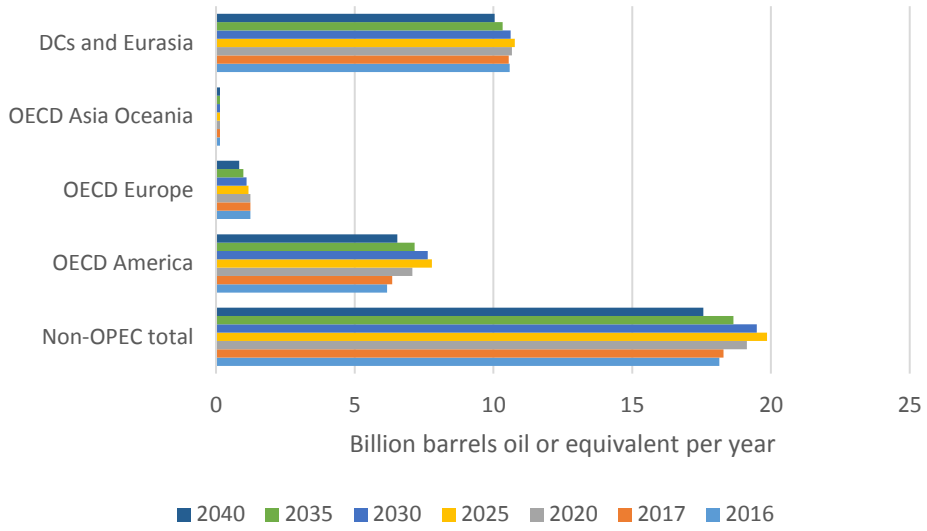

Figure 2: Prediction of oil production through the coming 25 years. All data are pulled from the World Oil Outlook 2040 report.[2]

The fossil resources are primarily used for either electricity production or in the transportation sector,[1] a field already being revolutionized by increasing implementation of renewable energy over the latest years (Figure 1).

However, though prospects of solving an energy crisis are attractive, but hopefully achievable, chemical industries which relies on oil based chemicals also needs alternative feedstocks, which leads to the necessity of development of green and sustainable chemistry, for the production of platform chemicals. A prominent method for achieving this is the utilization of biomass.

1.2 Green Chemistry and Biomass Utilization

1.2.1 Defining a Green Process

Green chemistry as a field is relatively new and has been defined as efficient use of (preferably renewable) raw materials, which eliminates waste, avoids the use of toxic and/or hazardous reagents and eliminates solvents in the manufacture and application of chemical products.[4]

Though most researchers have a general idea of how to develop environmentally friendly and sustainable manufacturing processes, the field is still vaguely defined not only due to a scarcity of chemical empirical evidence, but also due to vaguely defined environmental and socioeconomic factors. This leads to a challenge when attempting to develop an overall set of rules for when a process can be considered "green". A guideline to consider when evaluating a process is the twelve principles of green chemistry proposed in 2005 by Poliakoff and coworkers,[5] which can be condensed to the mnemonic device PRODUCTIVELY shown below.

Prevent wastes
Renewable materials
Omit derivatization steps
Degradable chemical products
Use safe synthetic methods
Catalytic reagents
Temperature, pressure ambient
In-Process monitoring
Very few auxiliary substances
E-factor, maximize feed in product
Low toxicity of chemical products
Yes, it is safe

Several suggestions for determinable properties for quantification of the green aspect of a process have been suggested. One of the earliest is determination of Atom Economy (AE), proposed by Trost in 1991 as a method of evaluating the efficiency of organic syntheses.[6] The AE is described as the sum of molecular weights of the obtained products, divided by the sum of molecular weights of applied reactants (Equation 1).

$$AE = \frac{\sum M_{product}}{\sum M_{reactants}} * 100\% \qquad (1)$$

As mentioned, the AE only evaluates efficiency of a given synthesis with no regard to environmental impact of the employed substrates. In order to accommodate this, a guideline known as the E-factor has been proposed by Sheldon in 1992, which evaluates the amount of waste produced from a given reaction.[4,7] This is achieved by dividing the sum of mass of all chemicals used in the process (water excluded) by the mass of the obtained product (Equation 2). In a hypothetical perfect process the E-factor would equal zero.[7]

$$E_{factor} = \frac{m_{waste}}{m_{product}} \quad (2)$$

Though Equations 1 and 2 give an overall idea of the renewability of a given process, this method shows a large shortcoming from all types of chemicals being weighed equally. This is where the challenge of defining a green process reveals itself. In order to establish a general method for evaluating the environmental hazard of a process, Sheldon proposed the Environmental Quotient (EQ) as a solution, which extends the description of the E-factor by multiplying it with an arbitrary *unfriendliness quotient* (Q) based on an assessment of a given chemical.[8] The assessment of the unfriendliness of chemicals is however highly debatable since quantification of environmental hazard is not a straight-forward process and technically every single chemical ever created would have to be classified.

1.2.2 Utilization of Biomass

In order to adhere to the definition of green chemistry, preferably renewable raw materials should be employed for the synthesis of platform chemicals. From a chemical point of view the most important renewable resource is biomass which can be divided firstly into edible and inedible sources. Edible biomass sources consist mainly of carbohydrates in form of either mono- or disaccharides, proteins, oils and fats, whereas the inedible biomass is divided into three major sub-groups; cellulose, hemicellulose and lignin.[9] A vast amount of reactions have been developed for the production of platform chemicals based on these sub-groups, leading to both renewable synthetic pathways to known chemical compounds as well as novel bio-based building blocks.[10,11]

Fatty acids are currently being used for the production of biodiesel. This energy substrate is produced mostly from transesterification of triglycerides, yielding methylated fatty esters and glycerol as a byproduct. This has led to a large increase in the production of glycerol, making it an interesting precursor for other chemicals.[11]

A major challenge when developing chemicals from carbohydrates is the high content of oxygen in their chemical structure. This leads to the necessity of reactions capable of reducing the amount of oxygen. Though this method yields unfavorable AE, it is of high importance in order to create bio-based substrates which mimics the platform chemicals currently used.[12] In order to maintain efficient and renewable reactions, catalysis is the most commonly used type of reaction and have been described as one of the foundational pillars of green chemistry.[13] When optimizing a given type of catalytic reaction, it is a large advantage to know the intricate mechanism of the system. The mechanism of the reaction can be determined through experimental studies, such as Hammett studies or by utilization of labeled compounds. However, by applying advanced computational quantum chemical methods, the catalytic mechanisms can be elucidated without the necessity of laboratory experiments, and allows for the possibility of *in silico* screening various catalytic systems and substrates.

The production of bio-based platform chemicals is especially important for the development of a renewable plastic industry. Here the alkene precursors for the four major commodity plastics, polyethylene (PE), polypropylene (PP), polyvinyl chloride (PVC) and polystyrene (PS), are all mainly produced from fossil resources.[14–18] Recent research has however begun discovering bio-based alternatives to some of these alkenes, for example the production of bio-ethylene from ethanol.[19] Also replacement of PS through the bio-based polylactic acid (PLA) has received interest through the latest years.[20] The fifth most produced commodity plastic is polyethylene terephthalate (PET), which is used mainly for the production of plastic bottles and containers. As for the other commodity plastics, traditionally both building blocks, ethylene glycol and terephthalic acid (TA), have been produced from fossil resources.[21,22] However, recent research shows the possibility of producing bio-based ethylene glycol from for example cellulose,[23] whereas a renewable solution for production of TA has not been discovered. Hence, for a fully bio-based PET system, an analogue chemical to TA had to be employed. 2,5-Furandicarboxylic acid (FDCA) is one such analogue which interestingly can be produced from carbohydrates and have been used to synthesize polyethylene furanoate (PEF), which show comparable properties with PET.[24]

1.3 Thesis Outline

This thesis consist of two large chapters with seven subchapters in total. Chapter 2 revolves around elucidation of mechanisms for oxygen-reducing reactions. Here two reactions are investigated; the deoxydehydration (DODH) and hydrodeoxygenation (HDO) reactions. Chapter 2.1 gives a short introduction to the field of computational quantum chemistry, and an

overview of the applied computational method utilized in Chapters 2.2-4. Chapter 2.2 provides a full mechanistic study of the vanadium catalyzed DODH reaction in combination with experimental work whereas Chapter 2.3 is an exclusively theoretical study of the oxidations states in the rhenium catalyzed DODH reaction. Lastly, Chapter 2.4 provides an elucidation of the mechanism of the molybdenum catalyzed HDO reaction through both experiments and theory.

The second part of this thesis focuses on expanding the scope of the FDCA building block beyond PEF plastics, through synthesis, characterization and testing of novel types of thermoset plastics from FDCA and other bio-based chemicals such as glycerol. Chapter 3.1 presents a synthesis a new bio-based building block, diallyl furan-2,5-dicarboxylate (DAFDC), and its application in thiol-ene chemistry. The use of the DAFDC monomer is expanded in Chapter 3.2, where it is used for synthesis of hyperbranched polyesters with high degree of allyl functionality which can undergo further crosslinking. This chapter also presents a new method for determining sizes and degrees of branching for these types of systems exclusively through Nuclear Magnetic Resonance (NMR) spectroscopy. Finally, Chapter 3.3 presents a project carried out at Kungliga Tekniska Högskolan (KTH) in Stockholm, where a collaboration with Professor Mats Johansson and Ph.D. Student Samer Nameer led to extension of the DAFDC monomer into bio-based epoxy resins with epoxidized fatty acid esters. The overall intend of these polymer studies are to create novel types of bio-based thermoset systems which can possibly rival some of the petrol-based compound used in industry, such as diallyl phthalate (DAP).

The work presented in this thesis has amounted to the five publications listed below.

Chapter 2.2: Nielsen, L. B.; **Larsen, D. B.**; Dethlefsen, J. R.; Fristrup, P. "Vanadium-Catalyzed Deoxydehydration of Vicinal Diols using Isopropyl Alcohol as the Reductant". (Submitted to ChemCatChem)

Chapter 2.4: **Larsen, D. B.**; Petersen, A. R.; Dethlefsen, J. R.; Teshome, A.; Fristrup, P. "Mechanistic Investigation of Molybdate-Catalyzed Transfer Hydrodeoxygenation", *Chem. Eur. J.* **2016**, *22*, 16621-16631.

Chapter 3.1: **Larsen, D. B.**; Sønderbæk-Jørgensen, R.; Duus, J. Ø.; Daugaard A. E. "Investigation of curing rates of bio-based thiol-ene films from diallyl 2,5-furandicarboxylate", *Eur. Polym. J.* **2018,** *102*, 1-8.

Chapter 3.2: **Larsen, D. B.**; Rønsbro, K.; Duus, J. Ø.; Daugaard, A. E. " Synthesis of Functionalized Hyperbranched FDCA Polyesters and Characterization of Molecular Weight and Branching by NMR". (Submitted to Macromolecules)

Chapter 3.3: Nameer, S.; **Larsen, D. B.**; Johansson, M. K. G. "Bio-based cationically polymerizable epoxy thermosets from furan and fatty acid derivatives". (Submitted to ACS Sustainable Chemistry and Engineering)

2 Theoretical Studies of Oxygen-reducing Reactions

As mentioned in the previous chapter, the generally high level of oxygen in biomass leads to a necessity for development of oxygen-reducing reactions. One type of reaction capable of reducing the oxygen contents of biomass is the deoxydehydration (DODH) reaction, which by use of a suitable catalyst and a sacrificial reductant can convert vicinal diols to alkenes (Scheme 1).

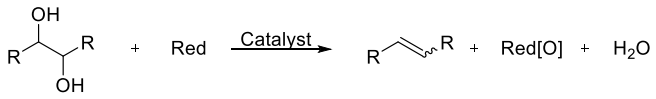

Scheme 1: General scheme for the catalytic deoxydehydration (DODH) reaction.

This reaction was discovered in 1963 by Corey and Winter,[25] however at the time it was not a catalytic reaction, using a cyclic thionocarbonate intermediate which could be reduced with $(MeO)_3P$, yielding the alkene. It was not until 1996 the first catalytic varieties of the DODH reaction emerged, with the discovery of the rhenium catalyzed reaction by Cook and Andrews,[26] utilizing the Cp^*ReO_3 catalyst with triphenylphosphine as the reductant. From 2009 and onward the reaction became subject to extensive research, a noteworthy example being the reaction with the methyltrioxorhenium(VII) (MTO) catalyst which could utilize hydrogen gas as a reductant.[27] The rhenium catalyzed reaction has later been performed using a variety of different rhenium complexes and reductants,[28–31] making it one of the most efficient and thoroughly researched DODH reactions. The overall mechanistic pathway for the DODH reaction, is described as a complexation and reduction (can occur in reverse order as well), to a diolate complex which can undergo an oxidative extrusion, regenerating the original catalyst (Figure 3).

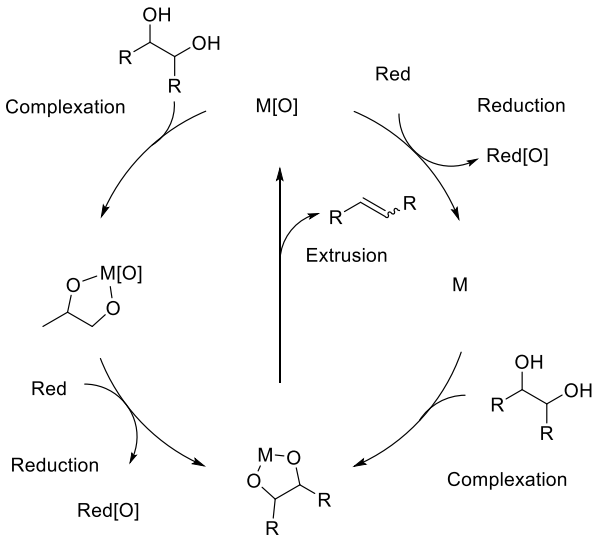

Figure 3: Generally accepted mechanism for the catalytic DODH reaction.

The main drawback of the rhenium catalyzed DODH reaction is however the price of rhenium. The price for pure rhenium was in 2017 1530 USD/kg[32], making it a rather expensive reaction. Therefore research has been dedicated to finding substitute metal complexes capable of reacting in the same fashion, but at a reduced cost. One of these cheaper substitutes have proven to be vanadium,[33,34] with a price at just 5.20 USD/(lbs. V_2O_5)[35] for the pure element making this reaction far more economically attractive. However, an odd type of selectivity is observed when applying vanadium as a catalyst, where only substrates with a primary and secondary vicinal diol can be converted to an alkene (Scheme 2). Chapter 2.2 focuses on theoretical studies of this reaction with the aim of elucidating the origin of this selectivity.

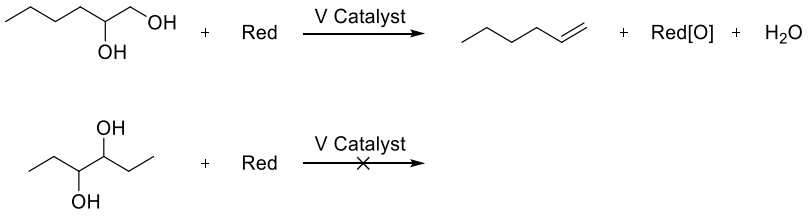

Scheme 2: Observed selectivity for the vanadium catalyzed DODH reaction.

As mentioned, the rhenium catalyzed DODH reaction has been studied through the last two decades. However, some conflicting experimental studies on the mechanism still exist. This conflict revolves around the oxidation state of rhenium during the catalytic cycle. Some studies claim that a catalyst such as MTO can act directly in the catalytic cycle, making the main oxidation states of rhenium +VII and +V throughout the mechanism.[36,37] However, other

studies show the possibility of rhenium initially undergoing a reduction before starting the catalytic cycle, achieving the oxidation states +V and +III instead.[38] Chapter 2.3 present a comparative theoretical study of these two mechanism in an attempt to provide evidence of the true mechanistic pathway.

Another type of DODH reaction which has been studied through the last years, is the molybdenum catalyzed DODH reaction.[39–41] Again, molybdenum represents a much cheaper alternative to rhenium with a price in 2017 at 18.00 USD/kg.[42] Interestingly, through the studies on this reaction, it was discovered that one of the applied catalysts, ammonium hexamolybdate (AHM), was capable of removal of benzylic alcohols through a hydrodeoxygenation (HDO) reaction (Scheme 3). Chapter 2.4 is a combined experimental and theoretical study of this reaction with the goal of determining its mechanism, since the reaction shows different properties than other previously observed HDO reactions which applies different metal catalysts.

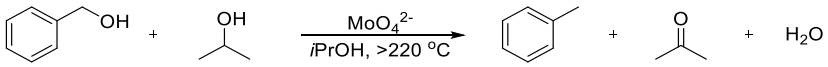

Scheme 3: Molybdenum catalyzed hydrodeoxygenation (HDO) reaction.

2.1 Computational Methods

2.1.1 Overview of Quantum Mechanics and Density Functional Theory

This section is meant to give an overview of the basic methodology of computational chemistry and DFT. Generally, for this thesis, DFT has been used as a tool and therefore the deeper mathematical proof and evaluation of various methods have been relatively subsided. Due to the field of quantum chemistry being affected by contributions from many different authors, a review from the Nobel Prize Lecture by Walter Kohn[43] has been used with support from relevant book chapters[44,45], unless otherwise noted.

For evaluation of mechanisms for these types of reactions, a quantum mechanical approach is usually used. These types of calculations are all rooted in the famous Schrödinger equation (Equation 3), relying on the construction of a wave function, Ψ, and the Hamiltonian operator, $\hat{H}$.[46]

$$\hat{H}\Psi = E\Psi \tag{3}$$

The Hamiltonian operator was originally a function developed in 19th century by William Hamilton, at the time being a function of position and momentum for determination of total energy of a given system,[47] and at the time, this was intended as an extension of Newtonian mechanics. However, from the Heisenberg uncertainty principle, it is stated that momentum and position cannot be determined simultaneously for quantum elements,[48] but the Hamiltonian could however be modified to be used in quantum mechanics. From the Schrödinger equation, theoretically any chemical problem can be solved, but unfortunately, due to its complexity, this equation is practically unsolvable for any system containing more than one electron, meaning that an exact solution can only be obtained for the hydrogen atom. In order to accommodate this limitation, several approximations and assumptions have to be applied. Perhaps one of the most fundamental approximations is the Born-Oppenheimer approximation, stating that due to the relative size and speed of the nuclei compared to the electrons, the nuclei can be considered fixed in space, which lowers the degrees of freedom for the system extensively.[49] This leads to a reduction of the Hamiltonian, giving the so-called electronic Schrödinger equation.

Even with the Born-Oppenheimer approximation, the Schrödinger equation remains unsolvable for multielectron systems. One of the more fundamental *ab-initio* methods for approximating a solution is Hartree-Fock method, utilizing the construction of the wave function from a Slater determinant and from N single electron wave functions (spin orbitals)

instead of the N-electron wave function.[50] With the idea of the construction of the wave function from the Slater determinant, the so-called Hartree-Fock energy can be determined by minimization through a Self-Consistent Field (SCF) method. An advantage compared to many later developed methods is the way the Hartree-Fock method is constructed, since when minimizing the energy, the results will always be higher than the actual energy obtained if the solution to the Schrödinger equation could be obtained. The drawback of this method is however a relatively low accuracy compared of some of the so-called post-Hartree-Fock methods which has been developed since.

One of the most widely used post-Hartree-Fock methods for calculations on small to medium size systems is Density Functional Theory (DFT), which instead of determining the energy of a system from the wave function, instead utilized the electronic density of the system. The earliest type of this method was the Thomas-Fermi model in 1927 using calculations on the fictitious system of a uniform electron gas.[51] However, this type of calculation could not be expanded to molecular systems, and the field of DFT did not emerge until almost 40 years later.

The breakthrough for DFT came in 1964 when Pierre Hohenberg and Walter Kohn proposed the Hohenberg-Kohn theorems.[52] The first theorem states that for any system of electrons moving under an external potential, this potential will be a functional of the electron density. The second theorem states that a functional working on the electron density only delivers the ground state energy if the input density is the true ground state density. These two theorems created the fundament of the DFT known today, albeit not by themselves yielding a method of determining the ground state density.

A method for determining the ground state density was proposed in 1965 by Kohn and Sham – the Kohn-Sham approach.[53] This discovery along with the Hohenberg-Kohn theorems, earned Kohn a shared Nobel's Price in 1998. The Kohn-Sham approach avoids examining the actual external potential on a system with interacting electrons, and instead replaces the external potential with the Kohn-Sham potential which acts on a non-interacting system. The Kohn-Sham potential is given in a way which leads to the potential on the non-interacting system being equal to the actual external potentials effect on the interacting system, without the exchange-correlation energy. Through this method a ground state density can be obtained, from an SCF method similar to that of the Hartree-Fock method. However, where the Hartree-Fock method uses a minimization of the energy to determine the wave function, the Kohn-Sham approach relies on convergence of the energy for determination of the density.

Even with the Kohn-Sham approach, a major obstacle of DFT calculation (or any quantum mechanical calculation) is the exchange-correlation energy, which corresponds to the non-classical electron-electron and self-interaction not covered by the non-interactive system. One of the earliest methods which is still used is the Local Density Approximation (LDA) which assumes that the electron density can be described as a uniform electron gas. This has been further expanded upon with the generalized gradient approximation (GGA) which takes the gradient change in electron density into account, allowing for more precise estimations for systems where the electron density undergoes rapid changes. The methods for approximating the exchange-correlation energies are known as exchange-correlation functionals. A widely applied method today is the use of hybrid functionals,[54,55] which estimates the exchange-correlation energy through a combination of the various exchange-correlation functionals. One of the most widely applied hybrid functionals is the Becke, 3-parameter, Lee-Yang-Parr (B3LYP) which uses exchange-correlation energies from LDA, GGA and Hartree-Fock methods.

All these types of calculations, relies on the construction of molecular orbitals. This is generally achieved by linear combinations of atomic orbitals, defined from a given basis set, with the most widely used type in DFT being the Pople basis sets.[56] The basis set is set of parameters used for the construction of the atomic orbitals, allowing for an initial estimation of the wave function or electronic density, which can henceforth be optimized through the SCF methods mentioned earlier.

With many options available for the computational quantum mechanical calculation, a challenge quickly becomes to select a suitable method, which yields reliable results, without increasing the computational cost of the experiments extensively.

2.1.1.1 Applied methodology for DFT calculations and software usage

For all DFT calculations performed in Chapters 2.2, 2.3 and 2.4, the B3LYP functional[54,55] with added D3 corrections[37] has been used. The LACVP** basis set was chosen, which applies the Hay–Wadt Effective-Core-Potential for all non-valence electrons of atoms larger than argon, and the 6-31G** basis set for everything else,[57] allowing quick calculations for some of the larger metal centers. This method is one of the more basic methods, and the basis set is almost minimal. This was chosen both for the increased calculation speed, allowing many different geometries to be examined, and due to previous work in the research group[39,40] and others[37,58] using this method, allowing for easier comparison of results. The addition of the D3 correction to the B3LYP functional increases the accuracy for especially Wan Deer Waals interactions, which might be an important factor when examining larger substrates with aliphatic chains.

All calculations were performed in Jaguar[59,60] using the graphical user interface Maestro[61] – both programs being part of the Schrödinger Suite (releases used: 2015-2 (Chapter 2.4), 2015-4 (Chapter 2.2) and 2016-1 (Chapter 2.3)). Transition states were found by either a quadratic synchronous transit (QST) search[62] or the standard transition state search incorporated in the Jaguar suite. Intermediates were found by minimizing the transition states toward both the expected starting material and the expected final product, confirming the correct transition state. All intermediates and transition states were characterized by a full, analytic frequency calculation at 293.15 K that resulted in only positive frequencies for intermediates and exactly one imaginary frequency for transition states. All transition states involving a proton transfer were modelled both as a direct transfer and as a transfer mediated through a water molecule. Approximate Gibbs free energies in the solution phase (G_{solv}) were obtained through addition of total Gibbs free energy and the solvation energy ($E_{\mathrm{SCF,solv}} - E_{\mathrm{SCF,gas}}$) obtained through a single point energy calculation with the Poisson–Boltzmann solver (PBF)[63,64] using standard parameters for methanol. The structural figures in the thesis were created using CYLview applying the POV raytracer for rendering.[65]

Calculations were run on the High Performance Computing (HPC) cluster at DTU or on a homemade cluster constructed from several computers. Appendix A contains a useful script for handling data extraction from the files produced with the Schrödinger Suite.

2.2 Theoretical Study of the Vanadium Catalyzed Deoxydehydration reaction

2.2.1 Introduction

The vanadium catalyzed DODH reaction is, as mentioned, a far cheaper alternative to its rhenium catalyzed analogue. Vanadium is showing promise in the valorization of glycerol, with the ability to convert it into allyl alcohol under neat reaction conditions.[66] Though only giving yields of ~22 %, this reaction shows comparable results with rhenium.[67,68] However, though several studies have been conducted on this reaction,[33,34] it is still showing lower efficiency for systems besides glycerol. One of the major obstacles for the reaction, is the limited substrate scope, where only diols consisting of a primary and secondary alcohol can be converted to an alkene (Scheme 4).

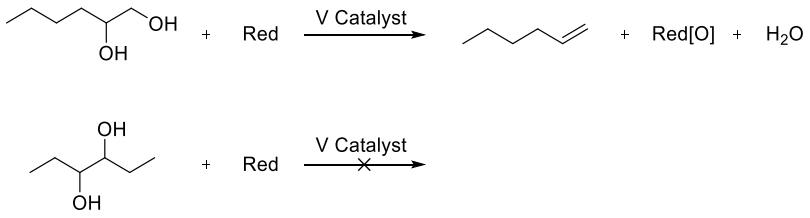

Scheme 4: Selectivity towards primary/secondary diols for the vanadium catalyzed DODH reaction.

The work presented in this chapter has been submitted to ChemCatChem and is currently in review. The manuscript is included in Appendix C.

2.2.2 Experimental Studies

For this project, experimental studies were carried out by Ph.D. student Lasse Bo Nielsen and Post.Doc. Johannes Dethlefsen. Only experimental results relating to the computational study are mentioned here, with all other experimental results being stated in the attached manuscript "Vanadium-Catalyzed Deoxydehydration of Vicinal Diols using Isopropyl Alcohol as the Reductant" (Appendix C).

The vanadium catalyzed DODH reaction using an alcohol as sacrificial reductant was tested extensively. Initially, tests on the substrate scope was performed showing, as mentioned, an inability to convert diols without a primary/secondary alcohol setup. A variety of diols were tested (Figure 4), however in this case only 1,2-hexanediol and 1,2-decanediol showed prominent conversion.

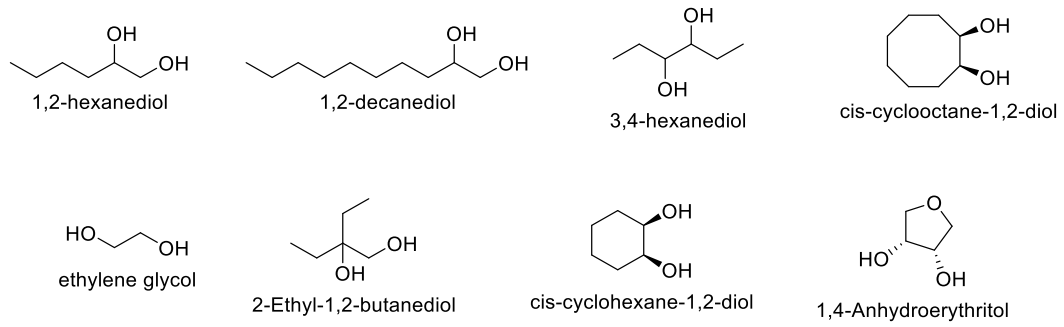

Figure 4: Experimentally examined substrates for the vanadium catalyzed DODH reaction.

Screening of various vanadium-based catalyst for the DODH of 1,2-decanediol proved high efficiency of the cheap ammonium metavanadate, NH_4VO_3, which was used throughout most experiments. Screening of solvents, showed the superior results when using isopropanol as solvent/reductant, as had been observed for molybdenum.[39,41] With no explanation available for the limited substrate scope, an in-depth computational study was required.

2.2.3 Computational Studies

2.2.3.1 Initial considerations

As with previous work,[39,40] the catalyst is treated as a neutral oxo-ligand in order to simplify the model. In this case the ammonium metavanadate is treated as the vanadium-oxo species VO_2OH. For general mechanistic calculations 1,2-propandiol is used as a substrate, being a close analogue to both 1,2-hexanediol and 1,2-decanediol, without having to account for the long aliphatic chain. Also, this diol gives the opportunity to examine differences in reactivity between primary and secondary alcohols.

It was anticipated that the mechanism would follow a similar trend as had been suggested for rhenium[36–38] and molybdenum.[39,40] This would be formation of a reduced diolate from the initial vanadium(V) species through a condensation and a reduction (Figure 5) to a vanadium(III) species. These two steps can proceed with either the condensation preceding the reduction (Pathway A) or vice versa (Pathway B).

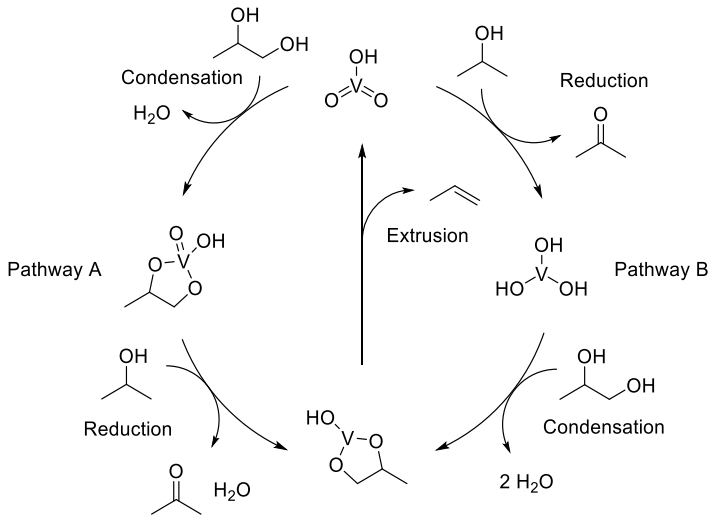

Figure 5: Proposed catalytic cycle for the vanadium catalyzed DODH reaction.

A previous study has shown favorable energies for a mechanism resembling Pathway B when using the vanadium complex with the dipicolinate (dipic) ligand and PPh_3 as reductant,[69] a method applied by Nicholas and coworkers.[33] For this study we were however interested in a reaction based on isopropanol, a much cheaper and easily recyclable reductant. Comparing to the suggested pathways for rhenium, and molybdenum, calculations have shown that initial reduction is more favored for rhenium[37] whereas initial condensation is favored for molybdenum.[40] For both catalyst types the reduction is in both cases the rate-determining step in regards to formation of the reduced diolate.

2.2.3.2 Formation of the reduced diolate

The condensation and reduction steps for Pathways A and B were calculated, accounting for all possible pathways (only intermediates of lowest energies are presented, for the rest consult the supporting information for the published article). The lowest energy mechanisms to the V(III) diolate **[5]** are shown in Figure 6 (the change in energy from **[A5]** and **[B5]** to **[5]/[5]*** is due to loss of micro solvation effect).

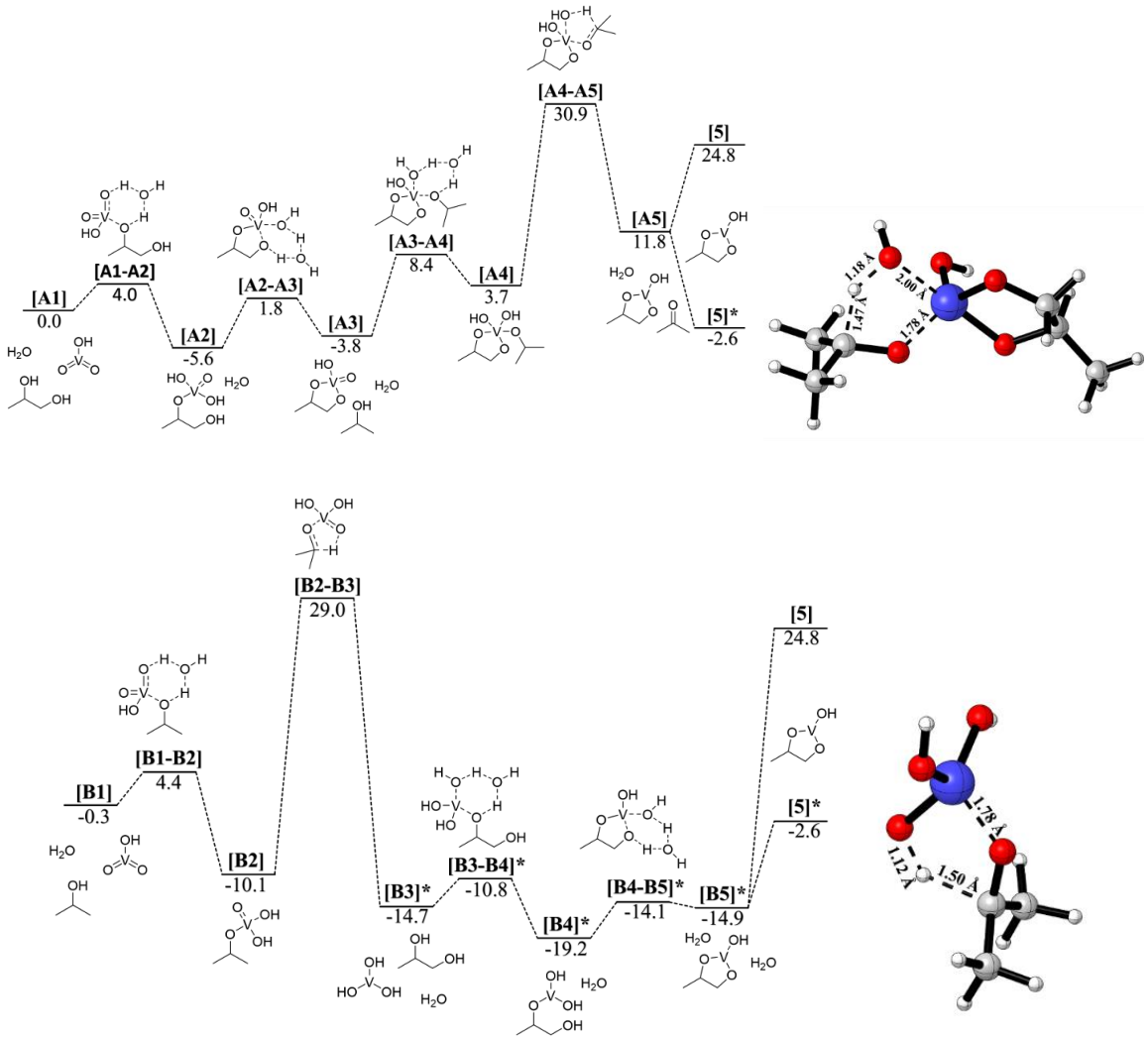

Figure 6: Gibbs free energy diagram of the modelled lowest energy mechanisms for Pathways A (upper) and B (lower), and their respective reduction transition states.

All vanadium(III) complexes proved to be more stable in the triplet state (noted with an asterisk). This stands to reason due to vanadium(III) having a d^2-configuration, and following Hund's rule and the Aufbau principle, these two electrons will always occupy two different orbitals (with the exception of a low-spin square antiprismatic complex). Though high stability of the triplet state is observed, the singlet state, **[5]**, is also shown due to the importance of its geometry for later calculations. Vanadium(V) intermediates and transition states are not considered due to the d^0-configuration, making complexes of higher spin multiplicity redundant. As seen for calculations for rhenium and molybdenum, calculations showed low energy barriers for the condensation steps as expected, with favorable energies for initial condensation to the secondary alcohol of the diol in both pathways (**[A1-A2]** and **[B3-B4]***).

Calculations proved the two mechanisms to have very similar energies with a slight selectivity towards Pathway B with **[B2-B3]** being 1.9 kcal/mol lower in energy than **[A4-A5]**.

2.2.3.3 Extrusion mechanism for various substrates

Initially a [2+3] extrusion mechanism in line with the molybdenum and rhenium mechanism was considered. It was observed that this type of extrusion could not proceed from the triplet state vanadium (III) complex **[5]***. Transition state energies could however be obtained from the singlet state. These energies were calculated for all the substrates which had been examined in the experimental studies, in hopes that this would show clues towards the substrate selectivity. Transition state **[A4-A5]** was also modelled in case the substrate would have an effect on the reduction step (the **[B2-B3]** reduction is not considered since this transition state is independent of substrate). All energies for the reduction and extrusions relative to the vanadium starting point are presented in Table 1, which show no significant correlation between substrate selectivity and activation energy, with all energies within relative sizes of each other. Furthermore, the energies obtained for the extrusion step was in all cases relatively high to what had been observed for molybdenum and rhenium, leading to the belief that this might not be the true extrusion mechanism.

Table 1: Gibbs free energy for the reduction and extrusion transitions for the experimentally examined substrates

Substrate	Reduction ΔG‡ (*kcal/mol*)	Extrusion ΔG‡ (*kcal/mol*)
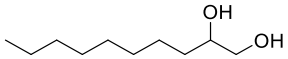 1,2-decanediol	11.7	30
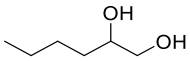 1,2-hexanediol	11.5	32.1
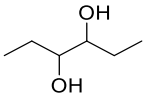 3,4-hexanediol	9.8	30.0
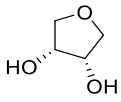 1,4-Anhydroerythritol	8.7	27.7

Substrate	Reduction ΔG‡ (*kcal/mol*)	Extrusion ΔG‡ (*kcal/mol*)
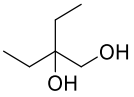 2-Ethyl-1,2-butanediol	9.4	28.4
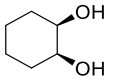 cis-cyclohexane-1,2-diol	12.8	33.5
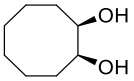 cis-cyclooctane-1,2-diol	13.5	29.9

2.2.3.4 Alternate extrusion mechanism

As mentioned, the [2+3] extrusion showed a high energy barrier of 48.6 kcal/mol compared to the vanadate starting point when using 1,2-propanediol. Another type of mechanism that has

been considered for the DODH extrusion as a rearrangement to a 4-membered oxetane followed by a [2+2] extrusion (Scheme 5).[40]

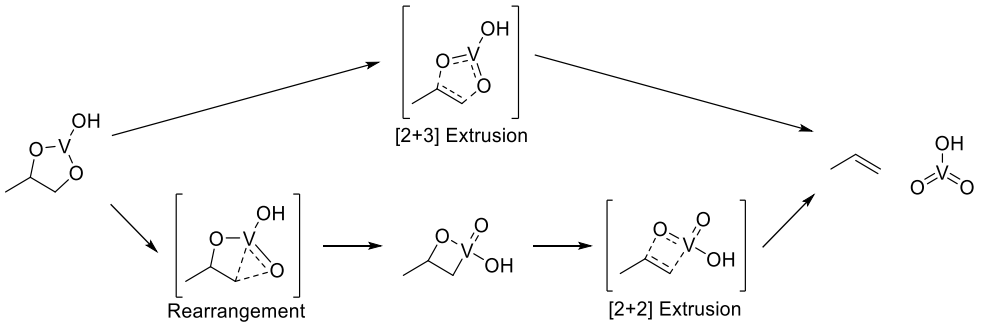

Scheme 5: Proposed alternate pathway for the extrusion mechanism for the vanadium catalyzed DODH reaction.

This other type of extrusion mechanism was modelled as shown in Figure 7. These two pathways proved nearly identical in energy barriers, with the [2+3] extrusion, **[5-1]**, having a barrier just 0.5 kcal/mol lower than the rearrangement, **[5-6]**. For the rearrangement **[5-6]** a small energy advantage of 1.5 kcal/mol was observed for cleavage of the primary C–O bond compared to the secondary. This energy difference along with the maintained high rearrangement energy was still not evidence for the selectivity. It was also noted that the oxetane was very stable with a very low energy barrier to the [2+2] extrusion **[6-1]** of just 2.2 kcal/mol.

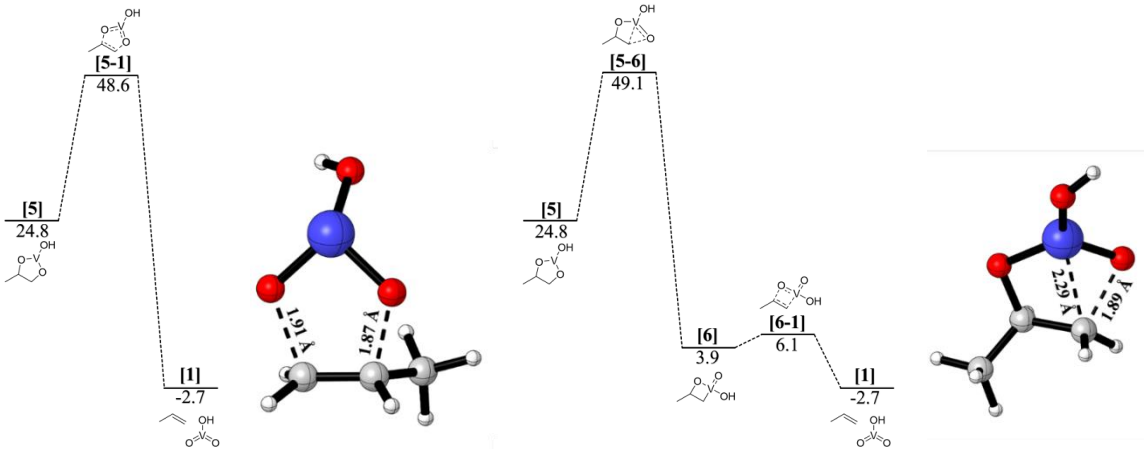

Figure 7: Gibbs free energy diagram for the classic [2+3] extrusion (left) and the proposed rearrangement and [2+2] extrusion.

As mentioned this type of extrusion was not possible from the singlet states of the vanadium(III) complexes, and this applied to the rearrangement mechanism as well. Further

calculations proved this to be stemming from an extrusion occurring in a step-wise manner in the triplet state, which causes the C–O bonds to break sequentially.[a] The absence of a [2+3] extrusion transition state was identified by the presence of two negative frequencies in the vibrational frequency calculations, for geometries resembling that of the [2+3] extrusion (C–O bond distances at 1.8, 1.9 and 2.0 Å). Further calculations showed that the cleavage of one C–O bond leads to the formation of the radical intermediate **[7]***, which following a spin cross-over to the single state could form a 4-membered oxetane,**[6']**, similar to the one discussed earlier. The breakage of the secondary C–O bond was favored over the primary bond with a difference of 0.4 kcal/mol. This mechanism has a much lower energy barrier than the classic [2+3] extrusion as shown in Figure 8. With this mechanism being favored by 17.7 kcal/mol compared to the previously examined extrusion mechanism, this led to the conclusion of the true pathway. This type of mechanism was further confirmed from experiments with hydrobenzoin. Hydrobenzoin was one of the few diols not containing a primary alcohol capable of forming alkenes (stilbene) to some degree. However, in all cases the *trans*-stilbene product was obtained from both types of hydrobenzoin diastereomers, which is only a possibility if free rotation around the C-C bond is available in the reaction mechanism. This means the concerted [2+3] extrusion would never yield this product from the *meso*-hydrobenzoin (R/S configuration), whereas intermediate **[7]*** would allow rotation before rearrangement to the oxetane **[6']**.

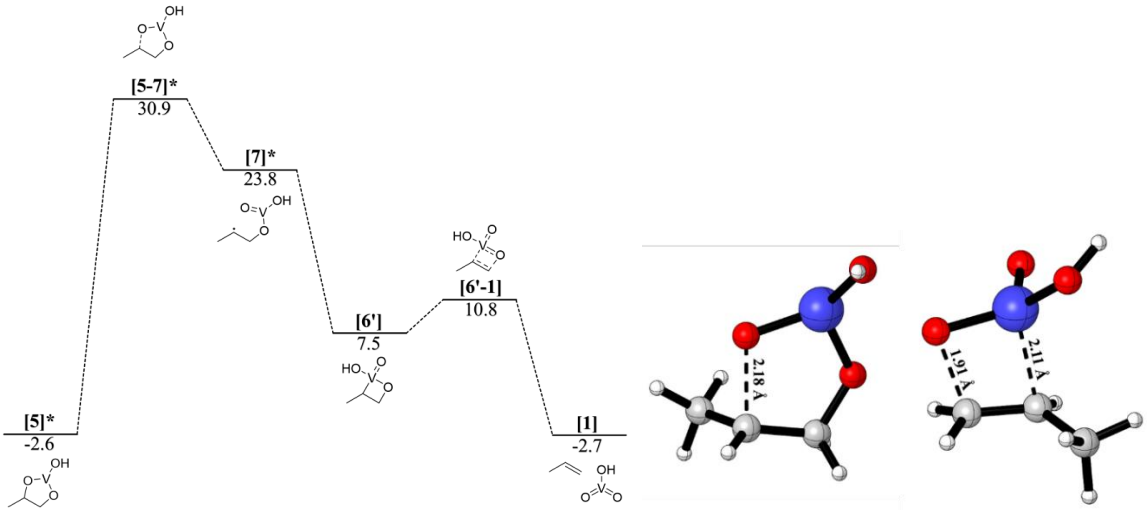

Figure 8: Gibbs free energy diagram for the new triplet-state mechanism and geometries of the involved transition states.

[a] During publication of this work, two other articles were published stating the same type of mechanism.[158,159]

2.2.3.5 Explaining the selectivity

As shown by the experiments, the vanadium-catalyzed DODH reaction only functions for a primary/secondary diol. Two of the most tested substrates were 1,2-hexanediol and 3,4-hexanediol, as these would be expected to show very similar reactivities. As seen from the energies presented in Table 2, neither the newly suggested high-spin mechanism, the classic [2+3] extrusion, nor the reduction can explain this selectivity. Only minor differences are observed in the energy barriers for the various transition states relative to the vanadate starting point, with the 3,4-hexanediol transition states generally being slightly favored.

Table 2: Gibbs free energy comparison of 1,2-hexanediol and 3,4-hexanediol.

Transition State	1,2-Hexanediol	3,4-Hexanediol
	ΔG‡ (kcal/mol)	
[A4-A5]	11.6	9.8
[5-1]	32.1	30.0
[5-7]*	13.1	12.2
[6'-1]	-11.6	-10.5

With even the new mechanism being incapable of explaining the selectivity of the reaction, the binding affinity of the different substrates with vanadium was examined. As seen from Figure 6, coordination of diols to the vanadium center proceed with small energy barriers compared to the other steps of the mechanism. This means that a possible irreversible binding of the substrate could lead to a potential "energy sink" which would inhibit the catalyst by increasing the energetic span of the mechanism. To confirm this possibility, all possible complexes with one or two diols bonded to the vanadium center were optimized (additional diols beyond two per vanadium center proved unfavored). An overview of these types of complexes is shown in Figure 9. All possible complexes were optimized and those of lowest energy are presented in Figure 9 (other complexes can be found in the supporting information of the published article).

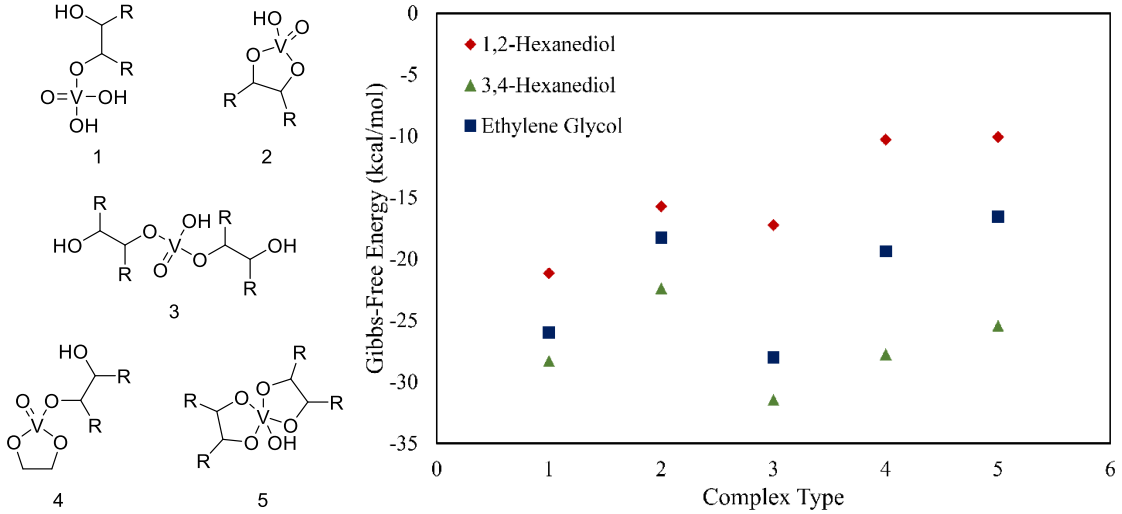

Figure 9: Examined complexes (left) and their respective Gibbs free energies (right).

These calculations showed that all 3,4-hexanediol complexes exhibit much lower energies than their 1,2-hexanediol analogues. Complex type 3 of 3,4-hexanediol is 10.3 kcal/mol lower in energy than the lowest energy complex of 1,2-hexandiol (complex type 1), which leads to the energetic span of the reaction being increased by this amount when the more substituted diol is used. We attribute this large difference energetic span as being responsible for the markedly different reactivity of vanadium towards diols that have two secondary hydroxyl groups. This behavior can be speculated to derive from the bulkier nature of the unreactive substrates. As an example, with an aliphatic side chain adjacent to the vanadium center, this could shield the center, lowering the reactivity. A similar energy sink for ethylene glycol was also found which provides an explanation for the lack of reactivity as well as an explanation for the inhibitory effect of ethylene glycol observed in the experimental studies.

This also explains why this phenomenon is only experienced with the vanadium-catalyzed DODH reactions, compared to the molybdenum and rhenium analogues. For rhenium[36,38] and molybdenum,[39,40] complexes 2, 4 and 5 would be favorable intermediates due to the ability to regenerate an active catalyst through oxidative cleavage of one of the coordinated diols whereas for vanadium this type of reactivity is not observed.

2.2.4 Concluding remarks

With the mindset of explaining the selectivity of the vanadium catalyzed DODH reaction, the research has led to the discovery of a new type of mechanism for the extrusion step of the catalytic cycle. This new mechanism showed the higher spin state for vanadium(III) being capable of sequential cleavage of C-O bonds which could be followed by a rearrangement to a 4-membered oxetane. This subsequently undergoes a [2+2] extrusion, giving a mechanism with a much lower energy barrier compared to the initially anticipated [2+3] mechanism. The odd selectivity for vanadium was however proved unrelated to this mechanism, but instead stemming from formation of stable vanadium-diol complexes, which increased the energetic span of the reaction.

2.3 Comparative Study of the Oxidation State of Rhenium in the DODH Reaction

2.3.1 Introduction

As mentioned, the rhenium catalyzed DODH reaction is one of the most documented cases of this type of reaction. Many different rhenium based catalysts has been used through the years with various sacrificial reductants such as sulfites,[28] phosphines,[26] hydrogen,[27] hydroaromatics[70] or cheap alcohols.[30,58,71] The mechanism for the DODH reaction has also been studied, both experimentally[36,38,72] and theoretically,[37,58] with general agreement of formation of a diolate from the diol and the reduced catalyst, however if other metals are used as catalyst, the order of the diolate condensation and reduction may vary.[39,40] One of the most applied catalysts is the methylrhenium trioxide (MTO) which with its simple structure has shown high efficiency. Studies on this catalyst have shown that the reaction proceeds through an initial reduction of MTO to methylrhenium dioxide (MDO) followed by the condensation to the diolate.[36–38] It was also calculated that MDO exists mainly in its hydrated form $ReO(OH)_2$.[37] Though the mechanism has been well researched, the nature of the oxidation state of rhenium in this reaction is still being discussed. Initially the mechanism was expected to go through a cycle between Re (VII) and Re (V),[26,36,37] however experimental data form *Abu-Omar et al.* has pointed towards two subsequent reductions leading to a catalytic cycle consisting of Re (V) and Re (III).[38] These catalytic cycles are outlined in Figure 10 (Pathway A and B).

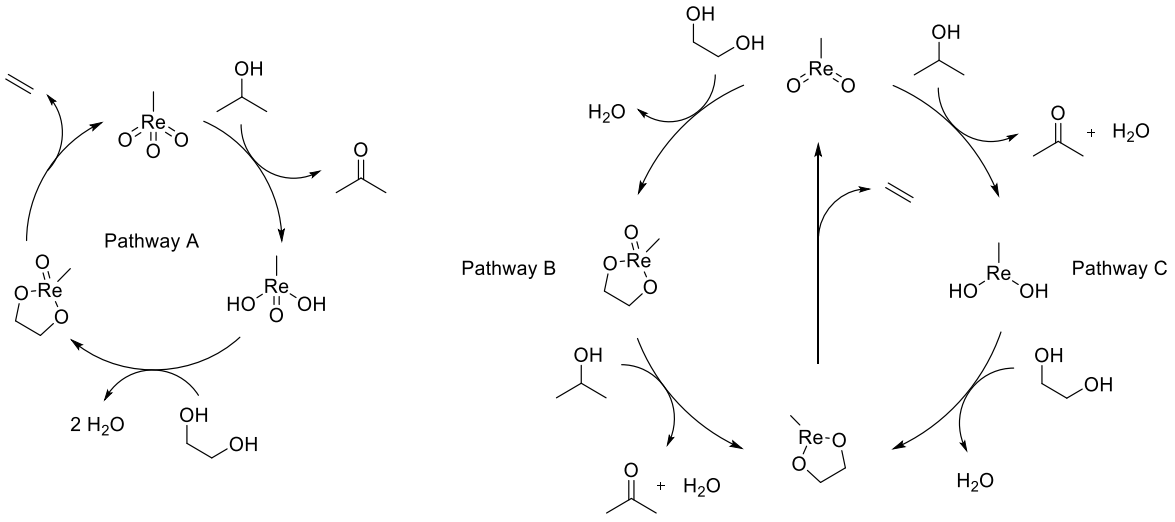

Figure 10: Proposed catalytic cycles for the rhenium catalyzed DODH reaction.

2.3.2 Computational Studies

2.3.2.1 Initial Considerations

The aim of this study is to provide a theoretical account of the two catalytic cycles through the use of DFT, in an attempt to elucidate the true nature of the rhenium catalyzed DODH reaction. It is the intention to examine not only the sole catalytic cycles, but also the influence from factors such as solvation, spin states and nature of the catalyst. In order to exhaust all possible pathways, a catalytic cycle, in which MTO is reduced twice to a free rhenium(III) species, methylrhenium monoxide (MMO), is examined as well (Pathway C). For construction of initial catalytic cycles, ethylene glycol was chosen as an initial model compound for the diol and isopropanol was used as the reductant, being the smallest possible diol. Since ethylene glycol is not an optimal substrate for the reaction, the obtained activation energies are expected to be higher than those of the actual applied substrates.

2.3.2.2 Catalytic Cycles and Rate-limiting Steps

Initially all pathways (A, B and C) were modeled from the MTO starting point, considering all viable pathways to the different intermediates, though only the pathways of lowest energies are presented here. Intermediates were obtained by optimizing transition states towards both reactant and product, yielding two intermediates between each transition state, with slightly different energies due to microsolvation effects.

Pathway A (Figure 11) was as mentioned presumed to go through a $ReMeO(OH)_2$ moiety, and the lowest energy pathway to this species was calculated from MTO. As seen in Figure 11, calculations showed a favorable energy for the reduction to MDO through first coordination with isopropanol, **[1-2]**, followed by the reduction **[2-3]** which was a barrier of 39.0 kcal/mol compared to the reference MTO, yielding MDO and acetone. Through two condensation steps, **[3-4]** and **[4-5]**, the Re(V) diolate **[5]** is formed which can undergo the extrusion **[5-1]** yielding MTO and the alkene, with a barrier of 28.9 kcal/mol compared to the reference point.

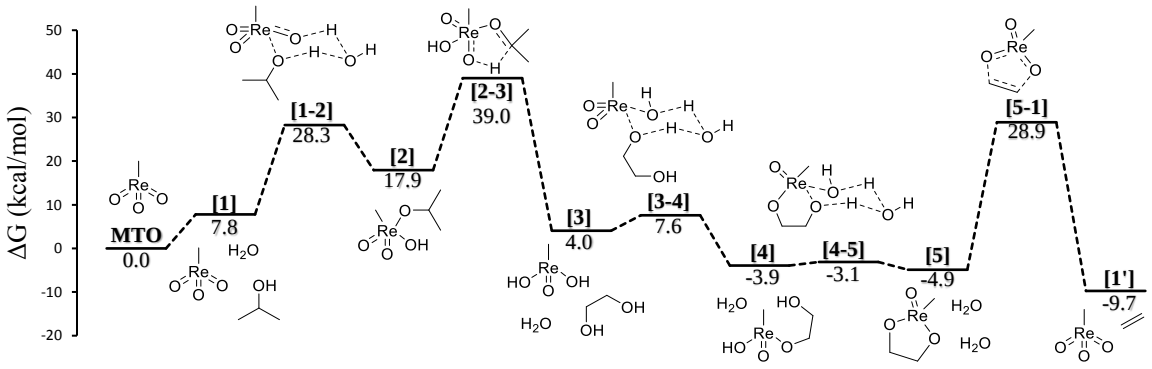

Figure 11: Calculated free energy diagram for Pathway A of the rhenium-catalyzed DODH reaction.

The suggested pathway B (Figure 12) had the lowest reaction barriers with the condensation, **[5-6]**, followed by the reduction **[6-7]** which led to the Re(III) diolate **[7]** with a barrier of 65.3 kcal/mol. This is followed by an extrusion, **[7-3']**, yielding the alkene and MDO in its dehydrated form **[3']**.

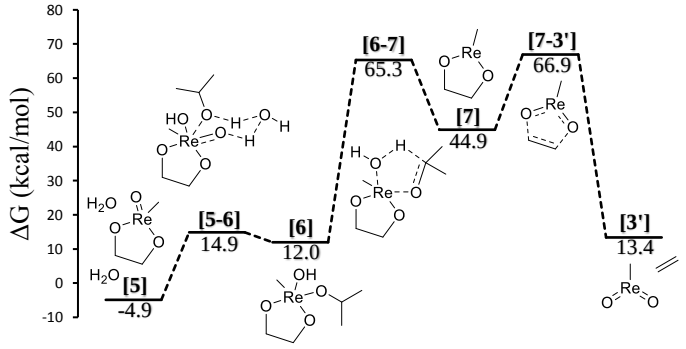

Figure 12: Calculated free energy diagram for Pathway B of the rhenium-catalyzed DODH reaction.

The lowest energy mechanism of Pathway C (Figure 13), proved to proceed through reduction of **[3']** (the mark is due to different microsolvation compared to **[3]**) with isopropanol, to the MMO species $MeRe(OH)_2$ through the transition state **[8-9]** with a barrier of 59.7 kcal/mol. This was followed by the condensation to the Re(III) diolate **[7']** which naturally showed the same barrier of 66.9 kcal/mol as seen for Pathway B.

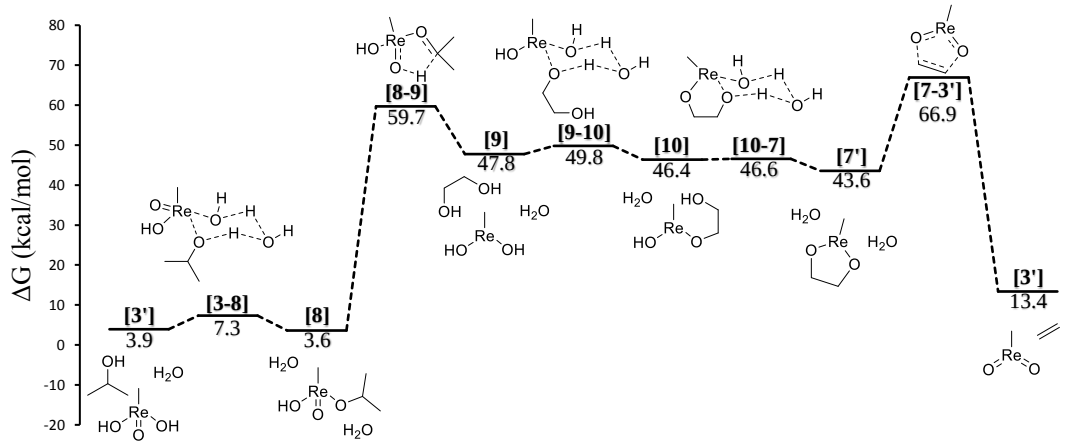

Figure 13: Calculated free energy diagram for Pathway C of the rhenium-catalyzed DODH reaction.

Though initially these calculation points towards the Re(VII)-Re(V) cycle (Pathway A) being clearly favored, there are multiple aspects of this reaction not taken into account yet, which will be discussed in the coming sections. These initial calculations, however show the transition states of interest being the reduction steps **[2-3]**, **[6-7]** and **[8-9]** along with the extrusion steps **[5-1]** and **[7-3']**.

2.3.2.3 Nature of the Catalyst

Research data have shown the possibility of MTO discarding the methyl group during the reaction yielding perrhenate ions (ReO4-).[36] In order to investigate the effect of this change, the transition states of interest were constructed using perrhenate instead of MTO. The results of these calculations are shown in Figure 14 in which they are stated relatively to the perrhenate equivalent of **[5-1]**. This circumvent the possible difficulties of determining the energy of the free charged perrhenate species.

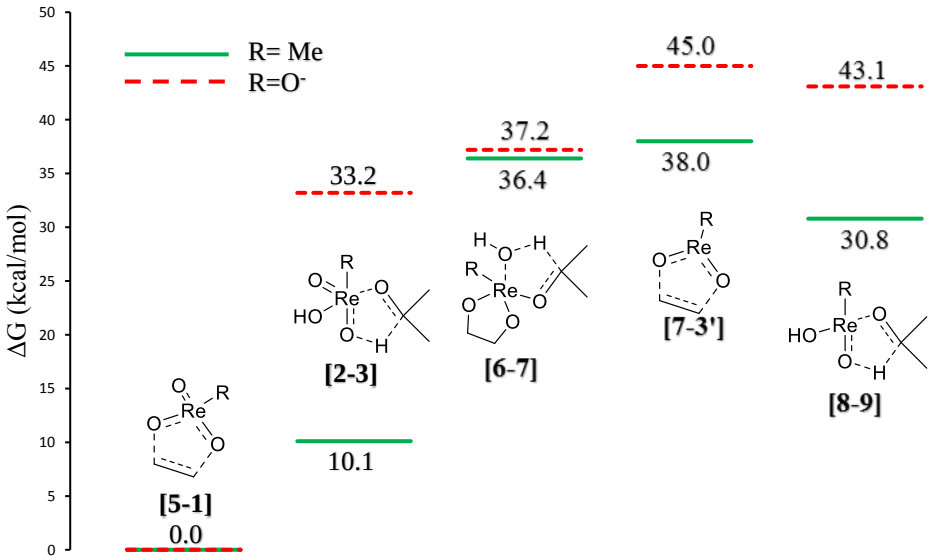

Figure 14: Energies for perrhenate equivalents of the discussed transition state (red, dashed lines), compared to the energies of the MTO catalyzed mechanism (green, solid lines).

As seen from the results sketched in Figure 14, the change from MTO to perrhenate ions causes a very significant increase in the relative transition state energy for **[2-3]** of 23.1 kcal/mol, whereas the three transition states, **[6-7]**, **[7-3']** and **[8-9]**, shows slight increases for 0.8, 7.0 and 12.3 kcal/mol respectively. From the general increase of energy barriers, it can be concluded that the mechanism proceeding through perrhenate ions instead of MTO is unfavorable for all of the proposed pathways.

2.3.2.4 Alternative Extrusion Mechanisms

As for the vanadium catalyzed DODH reaction discussed in the previous chapter, another suggested extrusion mechanism is a rearrangement to a 4-membered oxetane followed by a [2+2] extrusion. This leads to a worthwhile investigation for the Re(III) diolate **[7]**. The transition states were constructed for both **[7]**, **[5]** and the hydrated analogue of **[5]** (henceforth referred to as **[5b]**), however in all cases the rearrangement proved far higher in energy than their [2+3] extrusion equivalents, discarding this type of reaction mechanism as shown in Figure 15. However, a noteworthy observation was the very low energies observed for the 4-membered oxetane complexes formed from both **[5]** and **[7]**. However, only for the Rhenium (III) oxetane, a low energy barrier for the [2+2] extrusion was observed.

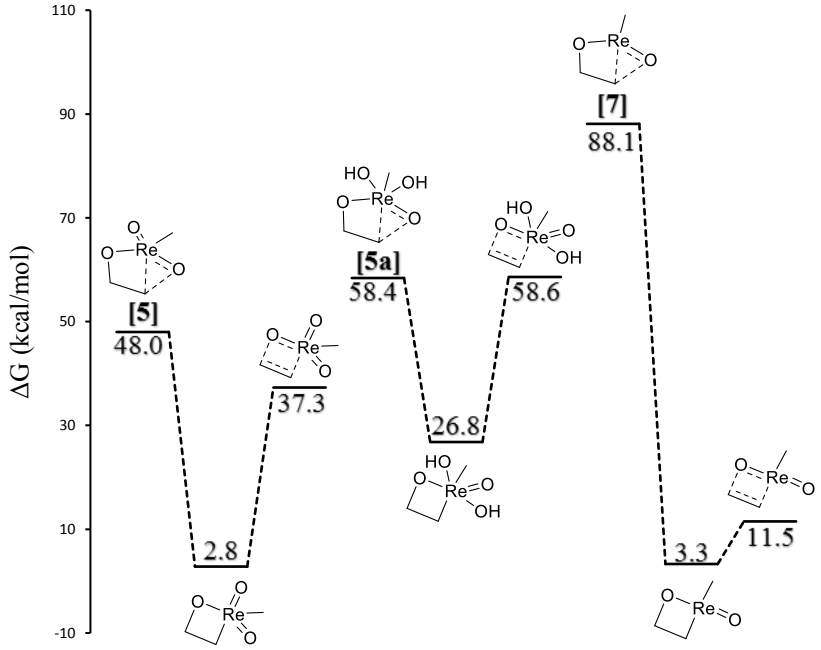

Figure 15: Calculated free energy diagrams for a diolate rearrangement followed by a [2+2] extrusion mechanism.

Furthermore, due to the electronic configuration of rhenium in oxidation state +3 and +5, there are possibilities of different spin multiplicities. For Re(V) there is possibility of multiplicity 1 and 3 whereas Re(III) complexes can theoretically exists with multiplicity 1, 3 and 5. As seen from the study on the vanadium catalyzed DODH reaction, spin state can have a significant effect on the reaction mechanism. Firstly the energies of the diolate complexes in the various possible multiplicities were examined. Almost all complexes with the exception of the free rhenium (III) species **[9]** exhibited lower energies with higher multiplicities (Table 3).

Table 3: Gibbs-Free energies for various multiplicities of complexes [5], [7] and [9] relative to their respective singlet state.

	[5a]	**[5b]**	**[7]**	**[9]**
Multiplicity	ΔG_{rel} *(kcal/mol)*			
1	0	0	0	0
3	-6.1	-7.5	-7.58	-0.1
5	N/A	N/A	-18.3	8.4

The diolate complexes mentioned in Table 3 exhibited the same nature as seen for the vanadium DODH, wherein the C-O bonds are broken sequentially at higher multiplicities instead of following the concerted [2+3] extrusion mechanism. However, examining the mechanistic pathways (Figure 16) it is observed that these transition states, unlike those for the vanadium catalyzed DODH reaction, are higher in energy than those for the concerted mechanism, these will not be discussed further for the rhenium catalyzed DODH reaction.

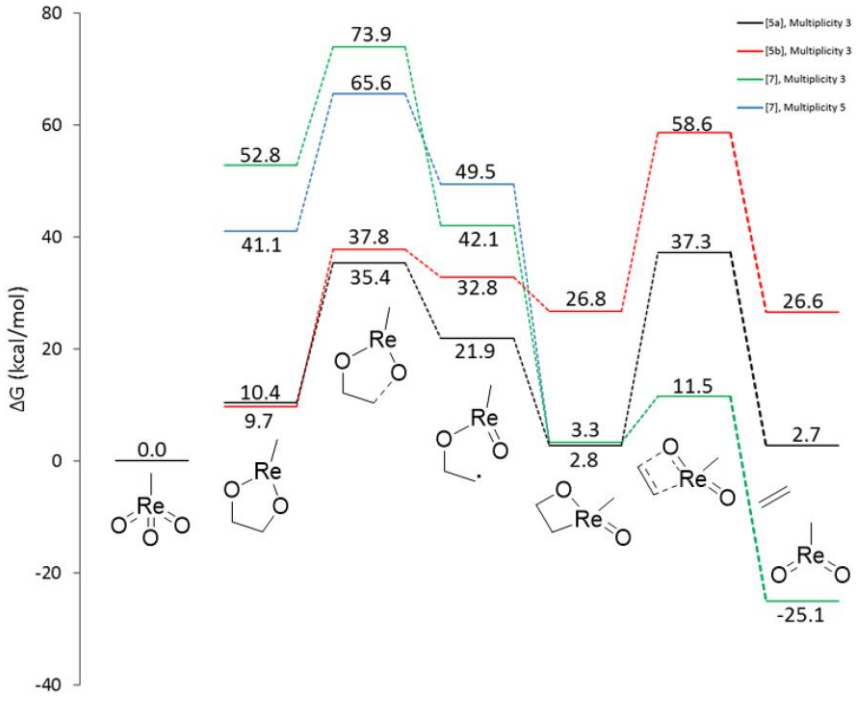

Figure 16: Gibbs free energy diagram of alternative extrusion mechanism (note that an oxygen atom has been omitted from [5a] and [5b] in the drawn structures).

2.3.2.5 Solvation

Since Re(III) complexes has a less shielded metal center, solvation of the species can have a large effect on the energy. It can be expected that the PBF solvent model applied is incapable of accounting for this effect. Therefore, the transition states involving Re(III) intermediates (**[6-7]**, **[7-3']** and **[8-9])** were inspected, using one or two solvent molecules for stabilization of the transition states. The change in energy for these microsolvated transition states are shown in Table 4 relative to the MTO starting point.

Table 4: Energies of microsolvated transition state, relative to their respective unsolvated transition state (left column) and to the MTO reference point (right column).

	$\Delta G_{rel\text{-}TS}$	$\Delta G_{rel\text{-}MTO}$
	kcal/mol	
[6-7]	0	65.3
1 *i*PrOH	1.7	67.0
2 *i*PrOH	6.4	71.7
[7-3']	0	66.9
1 *i*ProH	-7.9	59.0
2 *i*PrOH	-8.5	58.4
[8-9]	0	59.7
1 *i*ProH	-0.8	58.9
2 *i*PrOH	-10.8	48.9

The results from these transition states show that microsolvation with isopropanol greatly stabilizes transition states **[7-3']** and **[8-9]** by lowering the energetic barrier by 8.5 and 10.8 kcal/mol respectively. However, for transition state **[6-7]** a destabilization is observed, making the non-microsolvated transition state the favorable intermediate. This is most likely due to the bulkier nature of **[6-7]** compared to the other two transition states.

2.3.2.6 Effect from substrate

To this point, only the model compound ethylene glycol has been examined. However, through the years many different substrates have been employed. For the study stating the mechanism to go through a Re(III)-Re(V) catalytic cycle hydrobenzoin has been used[38] whereas other mechanistic investigation has employed aliphatic diols such as 1,2-tetradecanediol.[36] To examine this the transition states of interest were constructed with these two substrates, and their energetic barriers are compared in Table 5.

Table 5: Energies of the transition states of interest with various substrates relative to the MTO reference point

Substrate	Ethylene Glycol	(R,R)-Hydrobenzoin	1,2-tetra-dodecanediol
	ΔG *(kcal/mol)*		
MTO	0	0	0
[5-1]	28.9	19.1	27.2
[6-7]	65.3	62.5	63.3
[7-3']	66.9	58.0	65.5

From these data it is observed that the reduction step **[6-7]** is relatively unaffected by the substrate chosen. For the extrusions, **[5-1]** and **[7-3']**, the two aliphatic diols yield similar energies, whereas the transition state barriers for hydrobenzoin are lowered by 9.8 and 8.9

kcal/mol respectively. This stabilization is most likely due to the highly conjugated system obtained (stilbene).

2.3.2.7 Reductive Cleavage

Studies have suggested the rhenium[36,38,73] and molybdenum[39,40] catalyzed DODH reactions can contain a reduction step through oxidative cleavage of the diol substrate. Other studies point to the formation of Re(VII) diolates hinder the reaction with the Re(VII) diolate serving as a stable resting state for the catalyst, incapable of oxidative cleavage. The oxidative cleavage step may be affected by the different substrates discussed in the previous sections, mainly due to the conjugated benzaldehyde being formed from hydrobenzoin. To examine the effect of oxidative cleavage, equivalents to the reduction transition states **[2-3]**, **[6-7]** and **[8-9]** were attempted located.

Locating these types of transition states however proved difficult. For the **[2-3]** reduction, suitable transition states could be located, along with a hydrobenzoin transition state for **[6-7]**. A coordinate scan across the C-C bond cleavage revealed a possible reason. The **[6-7]** and **[8-9]** showed a constant increase in energy with the aliphatic diols upon increasing the C-C distance. As seen from the energies in Table 6, the energies for the transition states which could be located showed a rather interesting feature. Though transition states of the type **[2-3]** all showed a barrier above 50 kcal/mol for the oxidative cleavage, the energy of the **[6-7]** oxidative cleavage was at 29.0 kcal/mol – a much more plausible barrier compared to the alcohol-driven reduction at 59.7 kcal/mol. Though the high energies for [2-3] oxidative cleavages show the Re(VII) diolate hindering the reaction, the lower oxidation barrier shows a possibility of obtaining Re(III) moieties when using hydrobenzoin as a substrate.

Table 6: Gibbs free energies for various reductions of rhenium by oxidative cleavage.

	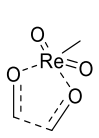	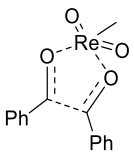	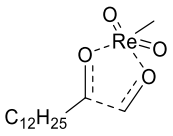	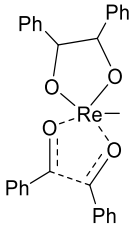
$\Delta G^{\ddagger}$ (kcal/mol)	56.9	55.1	52. 5	29.0

2.3.3 Concluding Remarks

We have presented a thorough DFT study of the rhenium catalyzed DODH reaction in regards to the oxidative state of Rhenium. The classically Re (VII)/(V) cycle along with the newly suggested Re(V)/(III) cycle has been examined, taking into account microsolvated states, temperature, spin states and alternative reduction mechanism. The presented calculations show no evidence for a viable Re(V)/(III) cycle with Gibbs-free energies for the rate limiting steps in general being more than 20 kcal/mol higher than their equivalents from the Re(VII)/(V) cycle. However, calculations show favorable energies for the reduction to the Re(III) moiety through an oxidative cleavage with hydrobenzoin as sacrificial reductant. This could lead to the observation of this type of catalytic cycle when employing this type of compound as substrate.

2.4 Mechanistic Study of the Molybdenum-catalyzed Transfer Hydrodeoxygenation

2.4.1 Introduction

An example of an oxygen-reducing reaction is the transfer hydrodeoxygenation (HDO) reaction, which removes a hydroxy-group by the addition of hydrogen. During earlier studies on the molybdenum catalyzed DODH reaction, it was discovered that the AHM catalyst was capable of this type of reaction when using benzylic alcohols as substrates (Scheme 6), using isopropanol as a sacrificial reductant in line with previous work on the DODH reaction.[39–41] This constitutes an interesting reaction considering the high amounts of benzylic alcohols present in a biomass source such as lignin. The HDO reaction is by no means new. Experiments employing various catalysts have been performed, with metal centers such as Ruthenium[74], Rhenium[75], Platinum[76] and Paladium[77]. However, a common attribute of all these examples is the use of hydrogen as a reductant, whereas the molybdenum catalyzed HDO reaction uses a sacrificial alcohol. This lead to the belief that a different mechanism was occurring which in turn sparked the necessity of an in-depth computational study. The reaction was carried out using the molybdenum complex ammonium heptamolybdate (AHM, $(NH_4)_6Mo_7O_{24}$), which, at high temperatures, is assumed to take the form of mononuclear molybdenum-oxo complexes.

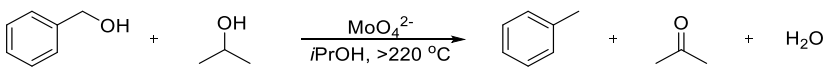

Scheme 6: Conversion of benzylic alcohol to toluene via the molybdenum catalyzed transfer HDO reaction.

The work presented in this chapter has been published in Chemistry, a European Journal and is included in Appendix D.

2.4.2 Experimental Studies

Experimental studies were carried out by Dr. Allan R. Petersen, Dr. Johannes R. Dethlefsen and Dr. Ayele Teshome, and will only be described briefly for highlights of data relevant to the computational studies. For a full description of the experimental findings, please consult the published paper (Appendix D).[78]

The reaction showed high yields of toluene when using benzyl alcohol as a substrate. Noteworthy was an appearance of some benzaldehyde when studying the reaction by gas chromatography. The presence was however only temporary and disappeared towards the end of the reaction. Hammett studies were performed for the reaction using benzylic alcohols, *p*-

substituted with CF_3, F, CH_3, Cl and SCH_3. All Hamett experiments proved highly irregular with no direct linear correlation with any type of the σ-values values (Figure 17).

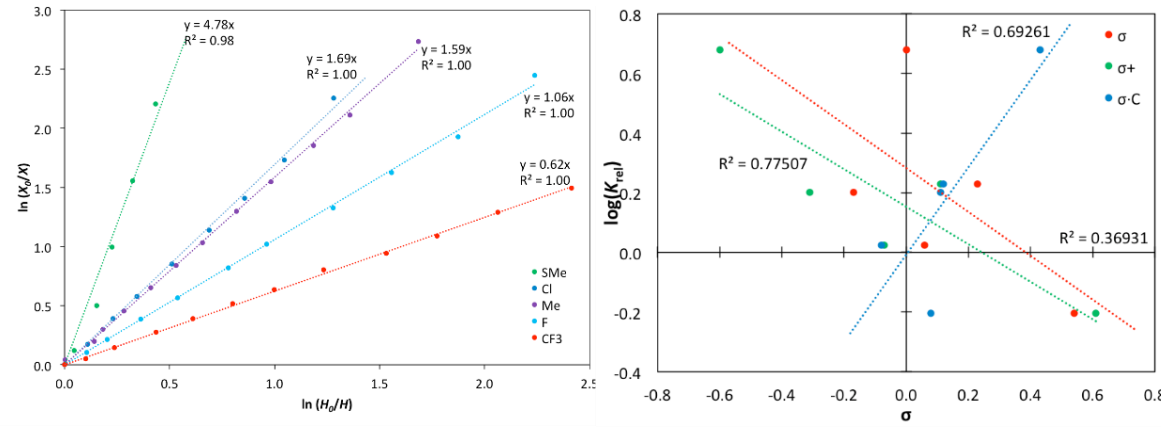

Figure 17: Rate studies (left) for various substrates and Hammett plot (left) the molybdenum catalyzed HDO reaction.

Two disproportionation reactions were performed with deuterated benzylic alcohol, one were the hydrogen of the hydroxyl-group was deuterated and an equivalent reaction with the deuteration on the benzylic carbon. This revealed that the hydrogen replacing the hydroxyl-group was originating from the benzylic carbon (Scheme 7). With the lack of a sacrificial alcohol as reductant, the disproportionation reaction also showed significant amounts of bibenzyl being formed.

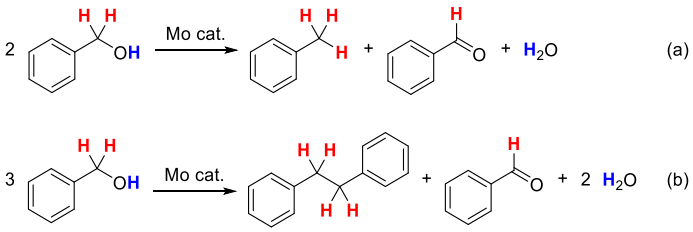

Scheme 7: Results from deuterated studies of the disproportionation of benzyl alcohol.

The highly irregular Hammett study led to the anticipation of a new mechanism, which in turn called for an in depth computational study of the molybdenum catalyzed transfer HDO reaction.

2.4.3 Computational Studies

2.4.3.1 Initial considerations

With the case of the non-linear Hammett plots, these types of experiments can often be assisted by computational chemistry.[79] In particular, determination of the rate-determining transition state (TS) can yield an understanding of the mechanistic properties of the reaction.

To elucidate the mechanism of this reaction, a DFT study using molybdenum oxo-complexes in oxidation state +VI as a starting point, the starting moiety being either molybdenum trioxide as used in previous molybdenum computational studies[39,40] or the hydrated form MoO_2OH_2. During the initial calculations, we attempted a direct hydride transfer from isopropanol, however no viable transition state could be located. Interestingly, we observed a tendency during optimization calculation that the molybdenum center would migrate to a position where it coordinated to the π-system of the benzene ring, leading to lowering of the energy of the complex. Since molybdenum is known to form π-allyl complexes[80–82] we assumed a π−benzyl complex to be a feasible intermediate. This type of complex was first characterized for the η^3-benzyl-metal complex, $[(C_5H_5)(\eta^3\text{-}C_6H_5CH_2)Mo(CO)_2]$, which was reported by King and Fronzaglia in 1966[83] and further supported by Cotton and LaPrade with the reported X-ray crystal structure of $[(C_5H_5)(\eta^3\text{-}p\text{-}MeC_6H_5CH_2)Mo(CO)_2]$.[84] The results from Cotton and LaPrade showed some tendency for a 4-carbon segment of the benzyl ring to take bond lengths similar to buta-1,3-diene in an *s-cis* conformation, leading to some localization of the π−system, and loss of aromaticity.[84]

We discovered two pathways to such an intermediate, both originating from a Mo(IV) moiety. This lead to three phases of this reaction: a reduction of Mo(VI) to Mo(IV), formation of π−benzyl complex and a hydride transfer from isopropanol.

2.4.3.2 Initial reduction

The initial step of the transfer hydrodeoxygenation was believed to be the reduction of Mo (VI) to Mo (IV) in order to allow the subsequent π-benzyl complex formation. Following the same type of alcohol-mediated reduction as seen before,[39,40] three different pathways were possible from the two chosen starting molybdenum moieties (MoO_3 or MoO_2OH_2). The reduction was expected to proceed through coordination of *i*PrOH to the Mo(VI) center, with *i*PrOH coordinating as $iPrO^-$, while the proton is transferred to an oxo-ligand. The coordination is followed by a reduction, yielding Mo(IV), acetone and water. The possible pathways were modeled including their water mediated equivalents (Figure 18). Molybdenum-hydride

complexes were briefly considered as intermediates, however these proved of low stability compared to the oxo-complexes in line with previous work.[39]

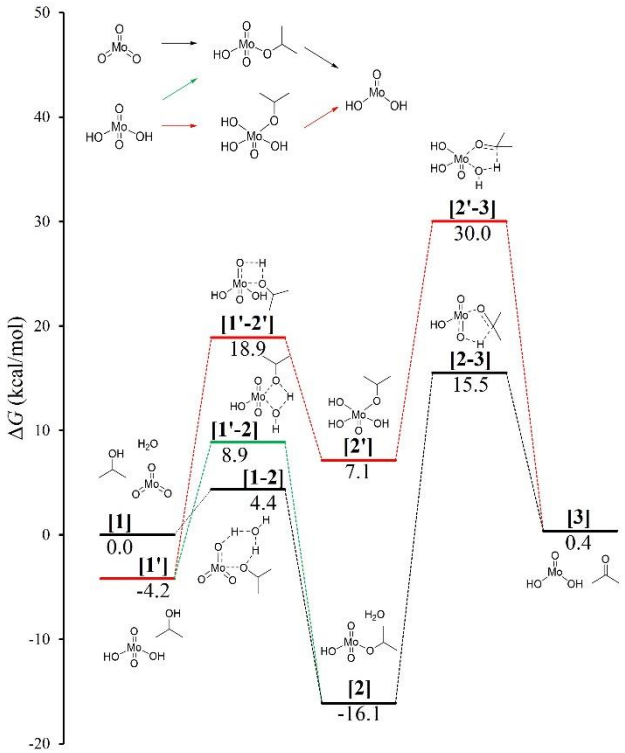

Figure 18: Gibbs free energy diagram of the initial reduction step from Mo(VI) to Mo(IV).

For the two initial molybdenum starting moieties, $MoO_2(OH)_2$ proved more stable, in line with what has been observed for the rhenium(V) complexes, CH_3ReO_2 versus $CH_3ReO(OH)_2$.[58] Figure 18 shows a favored pathway with complexation of *i*PrOH with MoO_3 through **[1-2]** compared to complexation with $MoO_2(OH)_2$ by 4.5 kcal/mol through **[1'-2]** and 14.5 kcal/mol through **[1'-2']**. In addition, this also led to the favored pathway for the reduction step since **[2-3]** is favored by 14.5 kcal/mol compared to **[2'-3]**.

2.4.3.3 Formation of π-benzyl complex

Following the reduction to $MoO(OH)_2$ we examined the possibility for formation of the π-benzyl complex. Initially a direct pathway in which the hydroxyl group acts as a leaving group was considered. However, the energy of this transition was rather high at 36.8 kcal/mol compared to the initial Mo (IV) moiety. This correlated well with the hydroxyl group being a poor choice of leaving group in reactions that require a π-system, for example the Tsuji-Trost reaction.[85] We later discovered that following a coordination of the molybdenum center to the benzylic alcohol, the molybdenum center could "fold" across the benzene ring allowing a transition state

similar to a [2,3]-sigmatropic rearrangement[86], cleaving the C-O bond while forming the π−system (Scheme 8).

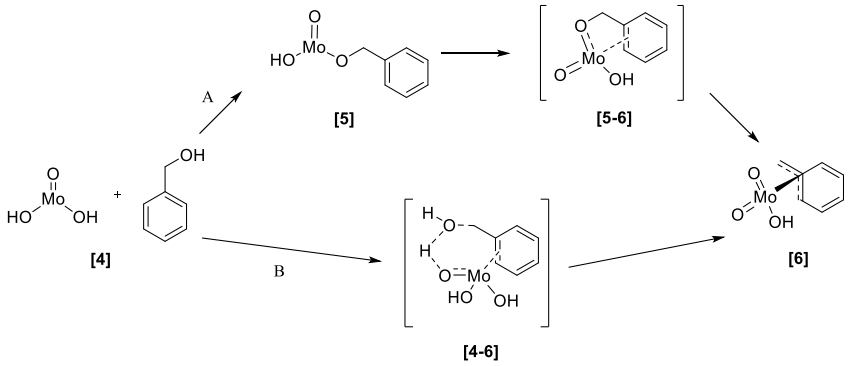

Scheme 8: Possible pathways for formation of a molybdenum π-benzyl complex from benzyl alcohol.

This type of transition was also examined using the Mo (VI) starting moieties, however no transition states could be located, most likely due to the additional substituents shielding the molybdenum center, making coordination to the π-system unfavorable. The [2,3]-sigmatropic rearrangement proved to be very low in energy compared to the direct approach attempted earlier, with a barrier for **[5-6]** being 26.2 kcal/mol lower when compared to the direct **[4-6]**. The Gibbs free energy diagram is shown in Figure 19 with the transition state geometries for **[4-6]** and **[5-6]** shown in Figure 20.

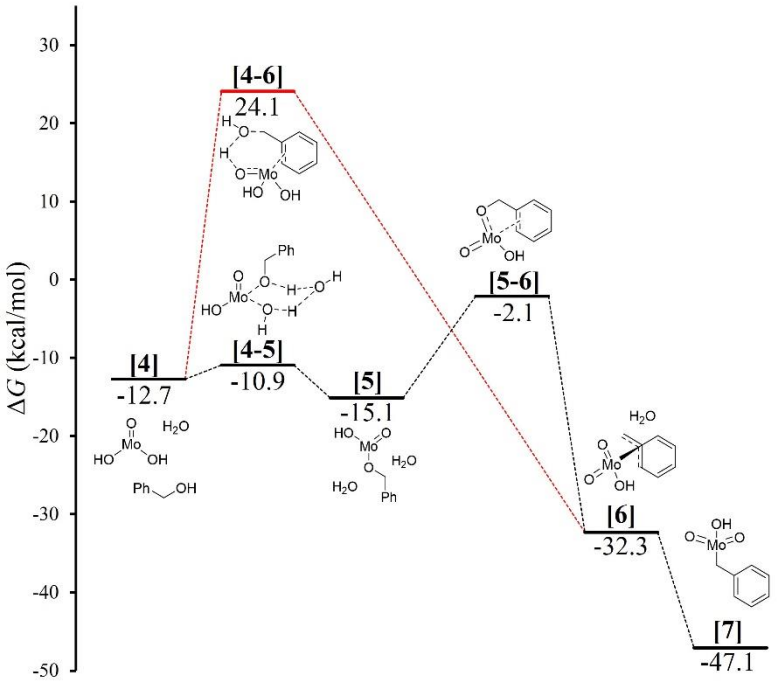

Figure 19: Gibbs free energy diagrams of possible pathways to the molybdenum π-benzyl complex.

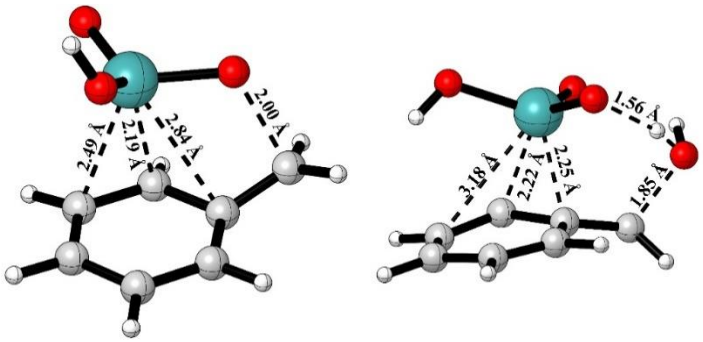

*Figure 20: π–allyl complex formation transition state geometries for **[5-6]** (left) and **[4-6]** (right).*

An alternative mechanism was considered for coordination of $PhCH_2OH$ to the molybdenum center prior to the oxidation of *i*PrOH. This would require an intermediate having both $PhCH_2OH$ and *i*PrOH coordinated to Mo(VI). However, for rhenium it has already been shown that in this type of reduction, the benzyl alcohol can also act as the sacrificial reductant, yielding benzaldehyde.[71] To evaluate the differences in oxidation of *i*PrOH and $PhCH_2OH$, calculations were carried out using a transition state similar to that of **[2-3]** (Scheme 9)

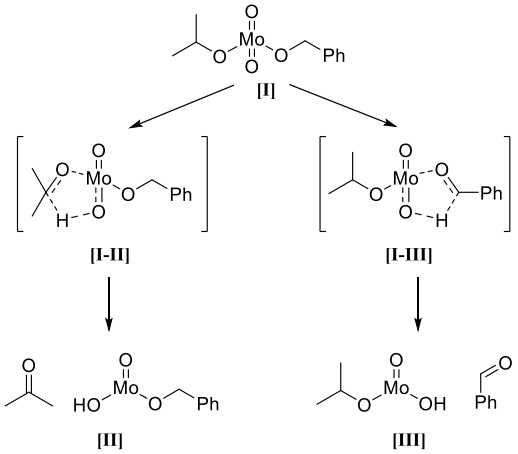

Scheme 9: Two possible oxidation pathways from a Mo(IV) complex coordinated to both benzyl alcohol and iPrOH.

Examining the reduction transition states **[I-II]** and **[I-III]**, only a small difference of 0.3 kcal/mol was observed, with the benzyl alcohol being slightly favored, showing possibility of both pathways. Furthermore, this result explains the presence of small amounts of benzaldehyde during the transfer HDO reaction of $PhCH_2OH$ in *i*PrOH. Since the presence of benzaldehyde is only temporary, it can speculated that it is subsequently reduced through a Meerwein–Schmidt–Ponndorf–Verley (MSPV) mechanism with a direct hydrogen transfer through a six-membered transition state.[87] Since no change in oxidation state of the catalyst is involved in the MSPV mechanism, the oxidation state of molybdenum can therefore be either +IV or +VI. Both pathways were calculated and showed similar energy barriers, namely 20.9 and 21.1 kcal/mol compared to the initial molybdenum-oxo complex **[1]**. The transition state geometries of these two reductions are shown in Figure 21. These energies correlate well with previously calculated results for the aluminum catalyzed MSPV reductions, which were found to have transition state energies of roughly 15–20 kcal/mol.[87]

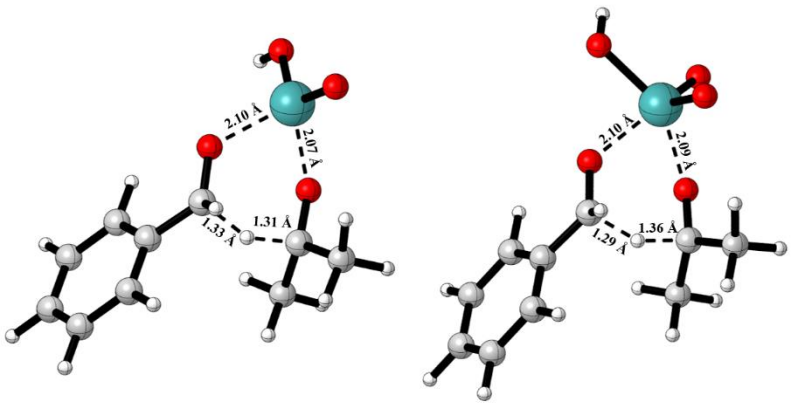

Figure 21: Transition state geometries for molybdenum +IV (left) and +VI (right) catalyzed MPSV reductions

2.4.3.4 Hydrogen transfer

As revealed by the deuterium studies, it was known that the hydrogen had to originate from the carbon of the isopropanol, making the hydrogen transfer a reductive process. A feasible transition state was found when isopropanol was coordinated to the molybdenum center followed by the transfer of the hydride, yielding the initial Mo (IV) moiety, acetone and toluene. However, a lower energy transition state was observed when the molybdenum center was pushed across the π-system (Figure 22). We observed that this type of transition state along with transition state **[4-6]** causes a break in aromaticity seen from unequal C-C bond lengths in the benzene ring (Figure 22). This leads to an explanation of the non-linear Hammett-studies since the σ–values will only correlate for aromatic systems.

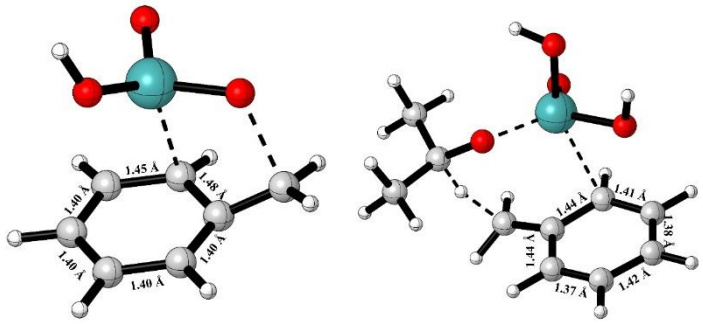

Figure 22: Transition state geometries for [4-6] (left) and [8-9] (right) showing disruption of the aromaticity of the benzene ring.

This yielded the final catalytic process in which the reduction to molybdenum (IV) serves as initiation (Figure 23).

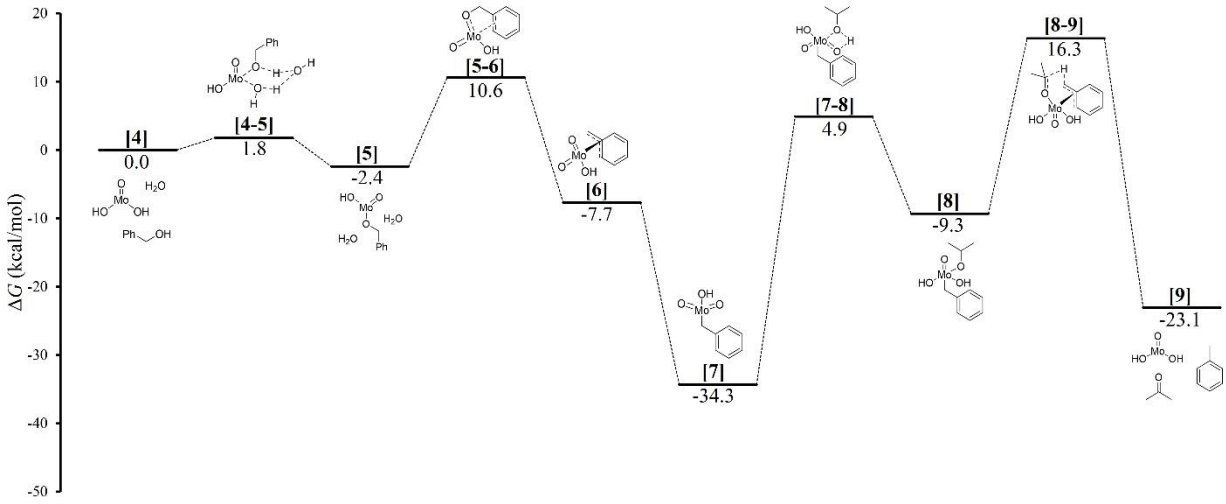

Figure 23: Gibbs free energy diagram of the full catalytic mechanism for the transfer HDO reaction.

2.4.3.5 Correlation to the Hammett Study

Albeit the Hammett study gave irregular results due to the break in aromaticity, the obtained relative rate constant still presents an opportunity to correlate the experiments to the theoretical model. In order to obtain relative rate constants, we aimed to be certain that the rate-determining step was the same for all of the involved substrates. Though **[8-9]** is shown as the rate-determining step, **[5-6]** and **[7-8]** show energy barriers in the same area. To accommodate eventual changes in the rate-determining step for various substrates or if several transition states would contribute to the reaction rate, we decided to model transition states **[5-6]**, **[7-8]** and **[8-9]** for all of the substrates used in the Hammett study, and calculate the relative Turn Over Frequencies (TOF) with the AUTOF program, through the energetic span method.[88] The advantage of this method is that for only one rate-determining step, Equation 4 applies.

$$TOF_{rel} \rightarrow k_{rel} \quad for \quad \Delta G \rightarrow \infty \tag{4}$$

Where TOF_{rel} is the relative TOF value for multiple transition states, k_{rel} is the relative rate constant calculated from only energetic span of the reaction and ΔG is the difference between highest and second highest transition state. For full outputs of the AUTOF program and transition state energies correlating to the Hammett studies, see the Supporting Information of the published article. Correlating the relative TOF values to the experimentally obtained rate constants yielded an almost linear trend (Figure 24).

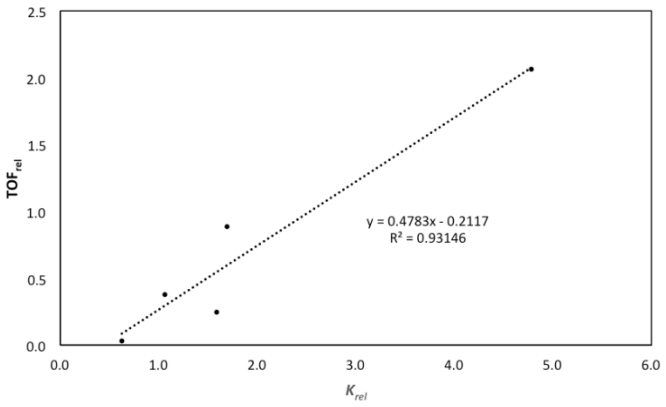

Figure 24: Correlation between relative reaction constants from Hammett studies and calculated relative TOF values.

Though the slope of the trend line ideally should equal one, this behavior is often observed when correlating experimental rate constants with DFT calculated rate constants[89] Although the linear correlation is not perfect, only the fluoride substitute benzyl alcohol represents an outlier, leading to the conclusion of a correctly suggested mechanism.

2.4.4 Concluding remarks

This study was aimed at elucidation of the mechanism of the molybdenum transfer hydrogenation reaction of benzyl alcohol. Due to Hammett-studies of the reaction yielding inconclusive results with none of the relative reaction constant correlating with any given σ-values, an in-depth computational study was necessary. Calculations showed that the formed molybdenum moieties were capable of undergoing rearrangement to π-benzyl complexes. These formed complexes could then in turn facilitate a hydrogen transfer from isopropanol yielding toluene. Calculations on relative turnover frequencies corresponded well to the relative reaction constants obtained from the Hammett-study, where the irregular experimental results obtained could be explained from a disruption of aromaticity during the hydrogen transfer stage of the reaction.

3 Synthesis and Characterization of Renewable Furan-based Thermosets

As described in Chapter 1, the polymer industry relies heavily on fossil resources. The necessity for renewable alternatives to counteract this can be tackled in one of two ways. Firstly by synthesis of renewable building blocks already being used, such as bio-ethylene, which can then be used directly as drop-in chemicals, without changing the overall layout of the production line. The second method is the use of chemical analogues to produce either similar or brand new types of plastic, such as methyl vinyl glycolate (MVG)[90] or *trans*-2,5-dihydroxy-3-pentenoic acid methyl ester (DPM)[91] can be envisioned. Due to its biodegradability polylactic acid (PLA) is currently used in the packaging industry[92] as well as in nanocomposites with improved gas permeability.[93,94] Another monomer receiving increased interest is glycerol, which, as mentioned in Chapter 1, is obtained from hydrolysis or transesterification of triglycerides[95] and can be used for block co-polymers or as branching points in polyesters.[96] Though glycerol can be directly incorporated into polymer chemistry as a suitable branching point in e.g. alkyds,[96–99] it also provides a platform for a vast amount of different chemical building blocks.[95] As mentioned in Chapter 2, the DODH reaction paves the way for allyl alcohol to be used as one of these building blocks.

Yet another chemical receiving much attention today is 5-Hydroxymethylfurfural (HMF) which has previously been identified as a green monomer of interest due to its multiple applications as bio-based platform molecule.[100] HMF is obtained by dehydration of simple sugars without the use of metal catalysts,[101–103] or from cellulose through dissolution in ionic liquids,[104] and its applications include production of bulk chemicals and bio-fuels, for example through oxidation to 2,5-furandicarboxylic acid (FDCA), a monomer proven suitable for synthesis of polyesters. FDCA can be obtained for example through oxidation of HMF by ruthenium hydroxide[105] or from cupper catalyzed oxidation.[106] The reason for the high attention given to FDCA as a bio-based building block is the high resemblance to terephthalic acid (TA).[107] TA is traditionally

made from xylene,[108] which, when polymerized with ethylene glycol, is used for the production of polyethylene terephthalate (PET) for synthetic fibers and plastic bottles. The emersion of FDCA as a building-block has led to the bio-based PET analogue polyethylene furanoate (PEF) which, in many ways, resembles PET.[107] The potential of using PEF as replacement has prompted several companies such as BASF, Avantium and Corbion to initiate large scale productions of FDCA, making this building-block a possible sustainable chemical for synthesis of commodity plastics. With this in mind, other types of FDCA based polymer systems are of high interest.

Considering on the one hand FDCA as a sustainable building-block and, on the other, the availability of allyl alcohol from renewable resources, polymer systems produced with the diallyl ester of FDCA, diallyl-2,5-furan dicarboxylate (DAFDC - Scheme 10), could be of high interest. This type of monomer would bear chemical resemblance to diallyl phthalate (DAP - Scheme 10), which has been used as a popular thermoset material, due to its high heat and solvent resistance.[109] Alternatives to DAP are also of high interest due to the suspected carcinogenicity of phthalates.[110] Though widely used, a drawback of polymerization of these types of chemicals is the poor reactivity of allyl esters in free radical polymerization makes direct crosslinking rather unfavorable. The aim of the following chapters is to examine different routes to FDCA based thermosets.

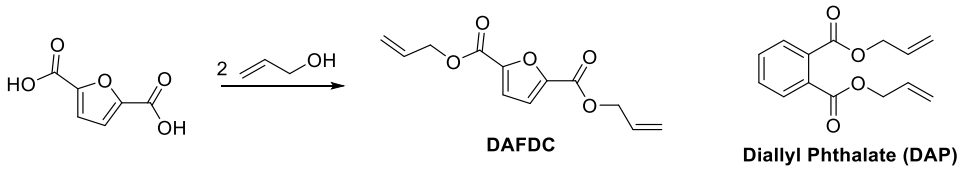

Scheme 10: Outline for synthesis of DAFDC from FDCA as an analogue to DAP.

3.1 Investigations of Furan-based Thiol-ene Networks

3.1.1 Introduction

With a direct crosslinking through a free radical polymerization pathway being disfavored for the allyl esters, other methods for synthesis of bio-based networks were sought. One type of network receiving a lot of attention through the last years is the crosslinking of alkenes with multifunctional thiols – a reaction which can proceed at room temperature and is initiated by UV radiation.[111,112] This type of reaction is based on the addition of thiols to alkenes discovered by Posner in 1905,[113] but was not employed in polymer chemistry until the 1970s when *Morgan et al.* proved how to use the reaction for UV-initiated polymerization, using benzophenone as an initiator.[114] This mechanism for the thiol-ene reaction is shown in Scheme 11, where initiation leads to a thiol radical which propagates with the alkene, forming a new radical. This radical can then undergo the same type of propagation with another thiol, restoring the original radical. Termination of this type of reaction can occur in three ways by combination of the two types of radical species.[111]

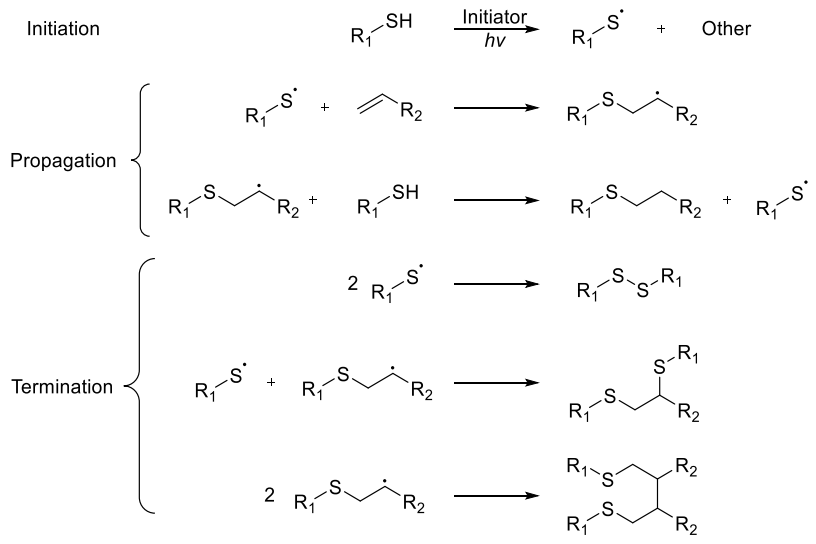

Scheme 11: General mechanism for the thiol-ene polymerization.

Thiol-ene networks have been widely used due to highly desirable mechanical properties with narrow glass transition temperatures,[115] uniformity of crosslinking, low stress in films and high adhesion to surfaces.[111] With the reacting species having widely different chemistry, these types of systems have been exploited in off-stoichiometric reaction,[116] giving functional surfaces which can be used for immobilization of enzymes[117,118] and particles.[119,120] Another

application of these types of polymers is a possible replacement for acrylic resins in restorative dental fillings due to the quick curing rates and low shrinkage of the final material.[121]

The target of this study was to synthesize both stoichiometric and off-stoichiometric thiol-ene (STE and OSTE) systems with various multifunctional thiols and the DAFDC monomer (Scheme 12). This way control of a functional surface of the final film should be achieved along with the possibility of targeting various mechanical features through the different chemistry of the applied thiols.

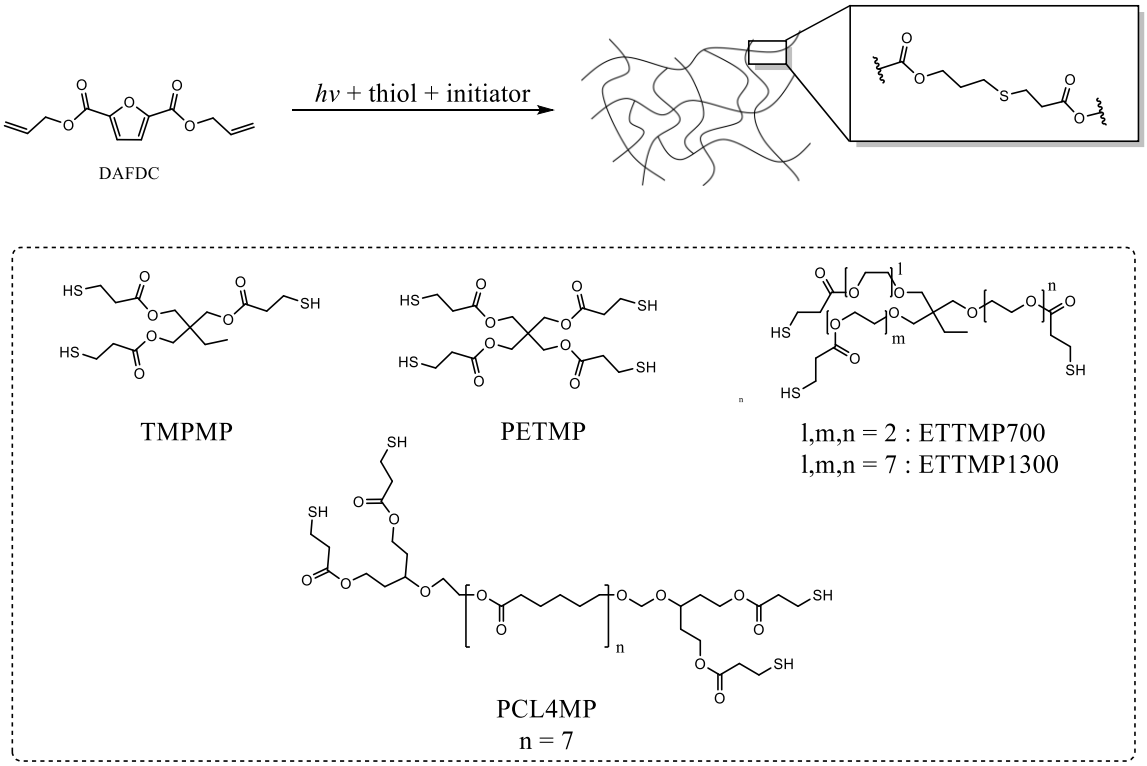

Scheme 12: Thermoset crosslinking of the DAFDC monomer with various thiols.

The work presented in this chapter has been published in European Polymer Journal and is included in Appendix E.

3.1.2 Results and Discussion

3.1.2.1 Synthesis of Diallyl Furan-2,5-dicarboxylate (DAFDC)

The DAFDC monomer was first synthesized in 1951 by R. Andrisano,[122] where the compound was reported as a yellow oil. However, no experiments on the polymerization had been reported, with the DAFDC solely being used as an intermediate for the synthesis of an epoxy-resin. We synthesized DAFDC in line with the procedure proposed by Andrisano,[122] using

FDCA, allyl alcohol and a catalytic amount of sulfuric acid (Scheme 13) and initial studies quickly proved why no polymerization reactions had been reported. The synthesized DAFDC was unstable at temperatures above 130 °C, yielding a black smudge for all types of thermal polymerizations (Figure 25).

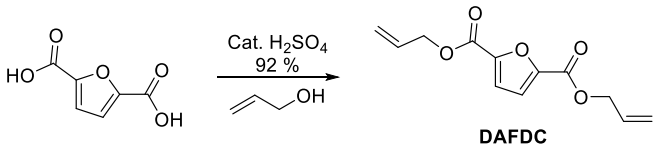

Scheme 13: Synthesis of the DAFDC monomer.

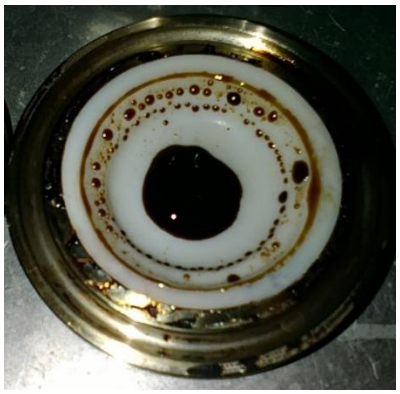

Figure 25: Black residue obtained from high temperature reaction of unpurified DAFDC monomer with dicumyl peroxide.

Though NMR results showed high purity of the material, a yellow crystalline product instead of an oil could be obtained from a basic workup, either through wash or by running it through a column with basic alumina. This led us to believe that some uncharacterized acidic residue was present in the product. Furthermore, a distillation after thorough basic workup could be completed yielding a pure white crystalline solid which was stable at higher temperatures.

Distillation of the yellow oil without basic workup caused efficient degradation of the compound and NMR analysis proved an increase in aromatic protons (Figure 26), which led to the belief that an inverse-electron-demand Diels-Alder reaction was occurring. The mechanism of this type of reaction would form an oxygen-bridged six-membered ring, with can undergo condensation to yield benzene rings (Scheme 14). Though the electron configuration of the DAFDC makes it an unsuitable diene of both normal and inverse-demand Diels-Alders reaction, studies have proven that Lewis acids can catalyze the reaction, and with the high temperatures applied this becomes feasible.[123] This type of reaction has been performed with the furan-2,5-

diylmethanol (a diol achieved by reducing HMF instead of oxidizing to FDCA), due to the more favorable electron configuration, allowing it to act as a suitable diene in the normal Diels-Alders reaction. This type of reaction has been used in crosslinking[124] and in synthesis of bio-based terephthalic acid.[125]

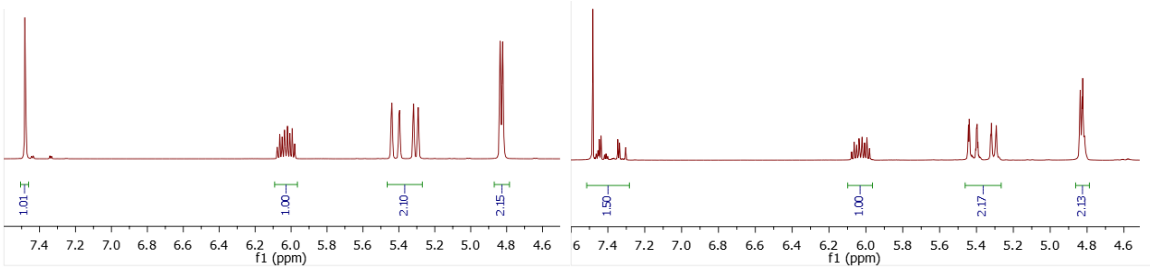

Figure 26: H-NMR spectra of the monomer before (left) and after (right) distillation of the monomer without basic work-up.

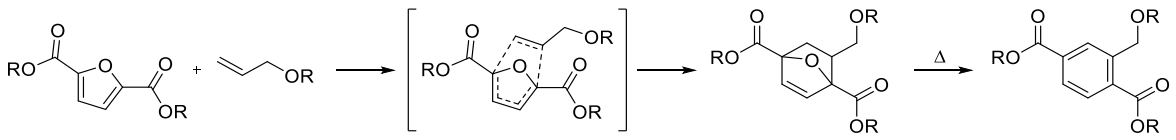

Scheme 14: Proposed mechanism for degradation of the monomer by inverse electron-demand Diels-Alder reaction.

The yield of the monomer synthesis could be improved by optimization of reaction time and controlled removal of excess allyl alcohol, never allowing the reaction solution to become completely dry. These two optimizations aided suppression of the Diels-Alders reaction which made it possible to obtain yields up to 92 %. Also, the controlled removal of excess allyl alcohol makes it easily recyclable since the only impurity is residual water which can be removed by drying, and an estimated minimum of 90 % of the allyl alcohol can possibly be recycled. Considering the E-factor for this monomer synthesis, the AE is 87 %, due to the removal of water in the esterification. Regarding the E-factor, a large amount of allyl alcohol and ethyl acetate are used, making the E-factor 12.4. However, if both ethyl acetate and allyl alcohol are recycled (10 % loss of allyl alcohol) the E-factor can be reduced to 0.39, making this a very renewable process.

3.1.2.2 Evaluation of Initiating Systems

To evaluate the efficiency of various initiating systems, three available candidates where tested on a known thiol-ene system consisting of tris(2-(3-mercaptopropionyloxy)ethyl)isocyanurate

(TEMPIC) and triallyl-1,3,5-triazine-2,4,6-trione (TATATO). The three systems tested were Lucerin (P1), Omnirad 1000 (P2) and Omnirad 4265 (P3), running stoichiometric reaction with 0.25 wt%, 0.05 wt% and 0.025 wt%, respectively, for each system. All system were cured during monitoring with Real-Time Fourier Transform Infrared Spectroscopy (RT-FTIR), where the allylic C-H out-of-plane bend at 930-940 cm^{-1} could be monitored (Figure 27) and the overall conversion could be calculated using Equation 5**,** where A(T) is the absorption at time T and A(0) is the initial absorption**.**

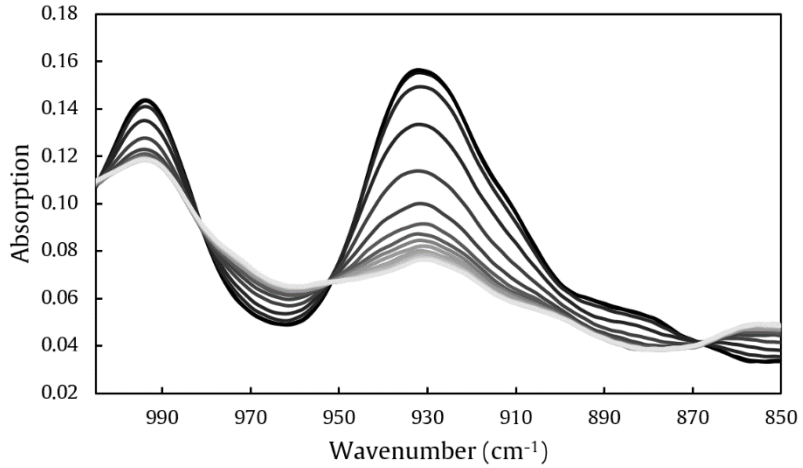

Figure 27: Allyl C-H out-of-plane bend monitoring by RT-FTIR.

$$x(t) = \frac{A(0) - A(t)}{A(0)} * 100\ \% \qquad (5)$$

The conversion was calculated using Equation 5 for all three initiators in all three concentration (Figure 28). To evaluate the kinetic parameters of the curing reactions, the maximum reaction rates were determined at the point with highest conversion rate (%/s) and the inhibition phase as the intercept of the tangent to this point with the *t*-axis. The maximum conversion was determined as the overall highest conversion observed. For estimation of total reaction time, the reaction was defined as complete when the reaction rate was less than 0.05 %/s. These kinetic parameters are presented in Table 7.

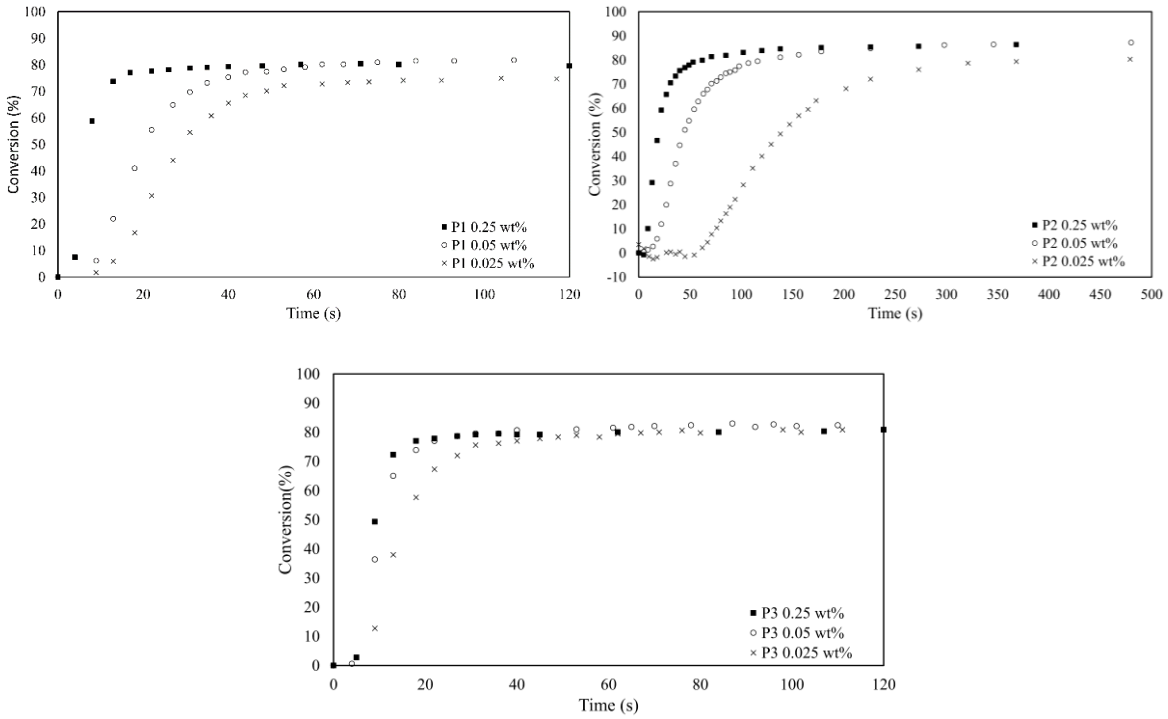

Figure 28: Conversions of the TEMPIC-TATATO test system with the three photoinitiators, P1 (upper left), P2 (upper right) and P3 (lower center).

Table 7: Kinetic parameters obtained for the TEMPIC-TATATO test system.

Sample	Max. Rate (%/S)	Rel. Rate	Inh. Phase (s)	Max. Conv. (%)	Conv. Time (s)
P1 0.25 wt%	12.85	1	3.4	82.04	48
P1 0.05 wt%	3.95	0.31	7.4	85.79	107
P1 0.025 wt%	3.48	0.27	13.2	76.99	117
P2 0.25 wt%	4.79	0.37	6.9	87.66	85
P2 0.05 wt%	2.19	0.17	17.9	88.56	226
P2 0.025 wt%	0.83	0.06	65.8	78.22	368
P3 0.25 wt%	11.63	0.91	4.8	82.83	40
P3 0.05 wt%	7.17	0.56	3.9	84.38	136
P3 0.025 wt%	6.30	0.49	7.0	82.55	151

A general trend that was expected was that higher concentration of the initiator leads to more rapid reaction rates. Almost all curings exhibited short inhibition phases, with the exception of P2, which shows significant inhibition times when reducing the concentration of the initiator

below 0.25 %. Additionally, P2 results in much lower reaction rates compared to P1 and P3. These initial experiments on the TEMPIC-TATATO system also show how the overall conversion can be affected by the choice of initiator. Interestingly, the highest conversion was obtained with a 0.05 wt% loading. For P1 and P2 it is observed that using only 0.025 wt% initiator limits the maximum conversion by 5-10%, whereas the overall conversion when employing P3 remains predominantly constant. P3 has thereby shown to have superior kinetic properties under the given conditions in the test system. This led to the initiating system P3 being the chosen initiator for further testing. A factor contributing to the higher performance of the P1 and P3 systems compared to P2, is most likely the choice of the UV source with a 365 nm wavelength, since P1 and P3 have absorption wavelengths at 370 and 379 nm respectively, whereas the highest absorption wavelength of P2 is 340 nm.

3.1.2.3 Kinetic Studies

With the optimal initiating system determined, similar UV-monitored reactions for all types of thiols (Scheme 12) were performed. Initial results showed that due to slower propagation of the allyl groups of DAFDC compared to the allyls of TATATO, the amount of initiator had to be increased to 2.5 wt% in order to obtain reaction rates equivalent to those observed for the test system. As with the test system the conversions were calculated from the RT-FTIR experiments yielding the conversion curves seen in Figure 29**.** In order to examine not only the effect of the various functionalities of the applied thiols, curing reactions were run with two off-stoichiometric feeds as well, using 1:1.3 surplus of allyls and thiols.

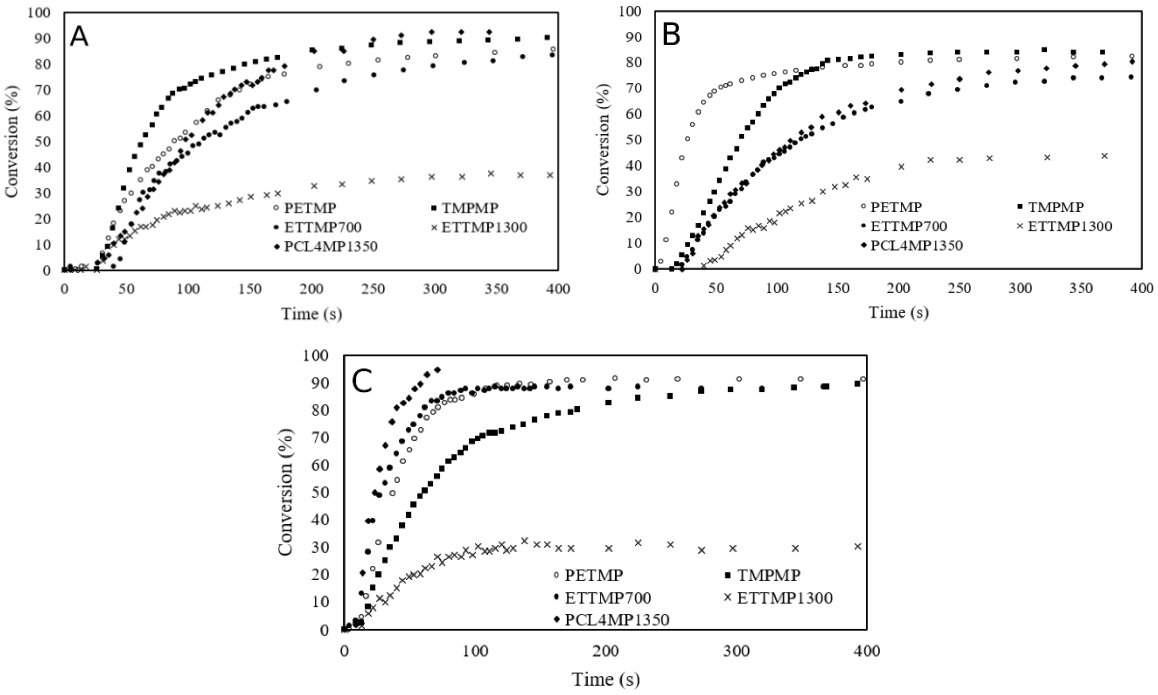

Figure 29: Conversions of the DAFDC-thiol networks. Allyl:thiol ratios: A. 1:1, B. 1.3:1, C. 1:1.3.

Overall conversion and conversion rates were monitored and estimated as for the test system, with all kinetic parameters stated in Table 8. All systems crosslinked to relative flexible products, with overall high conversions. The only exception being the ETTMP1300 which showed conversions at only 30-45 % for all stoichiometries. Also, after leaving the samples with ETTMP1300 for an extended period of time (>6 months) they reverted to a viscous state. IR analysis of this viscous state showed a broad peak at ~3400 cm^{-1} indicating presence of hydroxyl groups – most likely due to hydrolysis of the ester bonds in the crosslinked networks.

Table 8: Kinetic parameters for the crosslinking of DAFDC-thiol networks.

Thiol	[SH]:[C=C]	Max. Rate (%/s)	Rel. Rate	Inh. Phase (s)	Max. Conv. (%)	Conv. Time (s)
TMPMP	1.0:1.0	2.0	1.00	32.0	92.9	225
TMPMP	1.3:1.0	1.8	0.89	13.4	92.6	296
TMPMP	1.0:1.3	1.2	0.61	22.3	84.8	178
PETMP	1.0:1.0	1.5	0.75	27.8	91.6	278
PETMP	1.3:1.0	2.4	1.20	12.8	91.5	207
PETMP	1.0:1.3	2.7	1.38	6.0	84.5	202
ETTMP700	1.0:1.0	1.6	0.82	42.3	89.2	513
ETTMP700	1.3:1.0	3.1	1.54	8.8	88.6	202
ETTMP700	1.0:1.3	1.1	0.54	20.5	77.0	298
ETTMP1300	1.0:1.0	1.4	0.69	28.3	39.4	369
ETTMP1300	1.3:1.0	0.9	0.47	11.6	32.5	249
ETTMP1300	1.0:1.3	0.9	0.45	78.0	45.2	250
PCL4MP1350	1.0:1.0	1.1	0.57	24.3	92.5	321
PCL4MP1350	1.3:1.0	4.7	2.39	9.6	94.8	71
PCL4MP1350	1.0:1.3	1.7	0.86	27.5	83.8	298

The results obtained from kinetic analysis of the curings showed great impact from the choice of thiol monomer. While surplus of PCL4MP1350 proved the fastest curing, the systems with ETTMP1300 generally showed poor performance with lower reaction rates and overall conversions. This feature most like stems from the aforementioned instability of the ETTMP1300 monomer. The long ethoxylated chains of ETTMP1300 seem to have a major impact on the curing process, since increases in the amount of thiol for these systems all result in lowering of the overall conversion.

Beyond the ETTMP1300 systems, both STE and OSTE systems were able to achieve high conversions, generally in the area of 80-90 %. With the measurement originating from the RT-FTIR monitoring of the allyl peaks, calculated conversions of excess allyl OSTE systems should not be capable of exceeding 77 %. However, though lower conversions for these systems are observed, the value exceeds this limit. This leads to the hypothesis that besides the thiol-ene reaction, some allyl-allyl propagation is occurring. The similar overall conversions (except for the ETTMP1300 systems) can most likely be contributed to gelation of the systems, leading to dynamic restrictions in the networks preventing further reaction. Comparing the DAFDC

systems to the test system with TEMPIC and TATATO, generally higher conversions are observed, however this might be due to the increase in initiator loading.

3.1.2.4 Thermal Properties

DSC and TGA analyses were run for all types of systems, affording the thermal properties seen in Table 9. The obtained thermal properties show large dependencies on both the stoichiometry and choice of thiol, with glass transition temperatures ranging from -61.4 °C to 9.3 °C. This generally seem to be influenced by the choice of thiol and its size, flexibility and overall rotational freedom. For example, the PETMP systems exhibited the highest glass transitions with its small size and high functionality, and the ETTMP1300 and PCL4MP1350 systems gave very low glass transitions due to their long linear chains. TGA analyses showed a small initial weight loss most likely stemming from residual acetone in the curing. The actual degradations of the systems were initiated at temperatures in the range of 270 °C to 300 °C, with complete degradation occurring in the range of 400 °C to 500 °C, with an approximate mass loss of 90 %. The overall order of performance of the thiol monomers based on the end of degradation are rated as PETMP > TMPMP > PCL4MP1350 > ETTMP700 > ETTMP1300. The PETMP shows significantly higher thermal stability and a higher residual mass after degradation – most likely contributed to the higher abundance of DAFDC in this system. As with its analogue diallyl phthalate, DAFDC can be expected to help thermal stabilization and the higher residual mass can be due to general high stability of the aromatic functional groups. The stability order also reflects the aforementioned instability of the ETTMP based systems. The degradation starting points also reflect changes in the system, however to a much smaller degree. Examining the onset of degradation, ETTMP1300 performs surprisingly well along with PCL4MP1350 yielding the highest onset temperatures, followed by PETMP, ETTMP700 and TMPMP respectively decreasing in stability. A general trend that is observed, is that the stoichiometric systems tend to initiate degradation later than the off-stoichiometric systems, indicating an excess of functional groups contributing to the degradation process.

Table 9: Thermal properties for the DAFDC-thiol networks.

Thiol	[SH]:[C=C]	T_g (°C)	T_{start} degradation (°C)	T_{end} degradation (°C)	Mass loss (%)
TMPMP	1.0:1.0	-8.5	267.8	521.5	89.9
TMPMP	1.3:1.0	-54.8	268.4	521.4	83.0
TMPMP	1.0:1.3	-24.5	271.6	521.4	87.3
PETMP	1.0:1.0	9.3	280.7	539.7	77.5
PETMP	1.3:1.0	9.19	278.3	547.0	73.4
PETMP	1.0:1.3	0.0	277.3	543.1	76.3
ETTMP700	1.0:1.0	-55.5	280.2	485.3	88.9
ETTMP700	1.3:1.0	-35.0	267.6	489.3	94.4
ETTMP700	1.0:1.3	-55.5	279.7	483.6	88.3
ETTMP1300	1.0:1.0	-57.0	301.4	464.3	93.0
ETTMP1300	1.3:1.0	-53.4	283.9	457.4	93.3
ETTMP1300	1.0:1.3	-49.5	281.0	466.4	91.0
PCL4MP1350	1.0:1.0	-36.0	299.3	508.0	90.8
PCL4MP1350	1.3:1.0	-61.4	286.4	518.8	91.6
PCL4MP1350	1.0:1.3	-55.0	291.6	511.1	88.7

3.1.2.5 Tensile Testing

In order to evaluate the mechanical properties of the synthesized bio-based films, samples in dog-bone shapes were produced for tensile testing. These samples were made from a custom-cut steel plate with the dimensions 25x5x0.5 mm (of the elongated part of the dog-bone). Initially the samples were attempted pressed in a closed mold-like setup, where the cut steel plate would be pressed between two layers of a polymer film by two glass plates (Figure 30– a). However, after attempting this method with various polymer films and all types of systems, one of two results were obtained: either the material would stick too well to the film making removal of the final dog-bone impossible (observed with Teflon and PET films) or the film would cause large air bubbles to form when closed making the sample void (seen with polypropylene and polystyrene films). Therefore, a similar open setup with polypropylene and polystyrene films were attempted (Figure 30– b), where the mold would be left open and excess material would be removed by scraping with an industrial-grade razor blade. Though curing and removal of the sample worked well, the final product resulted in a dog-bone with a rifled surface making the samples void. This was expected to stem from polarity differences between the feed mixture and applied polymer films. Lastly, a mold setup without a polymer

film, directly on glass was attempted (Figure 30– c). Again, the excess material was removed by scraping with a razor, which in this case yielded smooth samples suitable for tensile testing. The drawback of this method however, was the poor contact between the steel and glass plates, causing a small amount of excess material to surge under the plate, making the thickness of the samples vary between 550 µm and 650 µm instead of the targeted 500 µm (all tensile tests have been corrected for sample thickness.

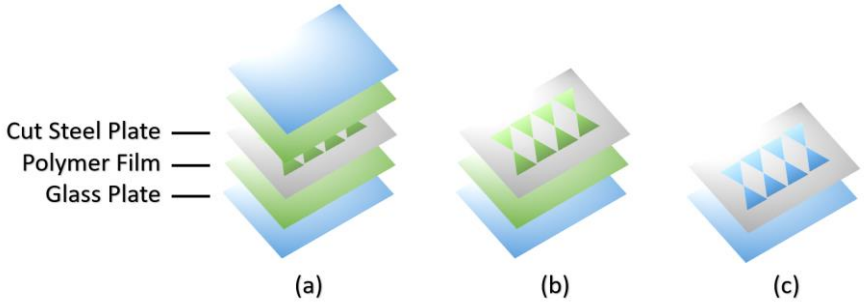

Figure 30: Schematic representation of three types of molding setups.

With the intent of evaluating both the effect of the feed stoichiometry as well as the choice of thiol, seven different sample sets were prepared. For testing the effect of the thiol, all five stoichiometric systems were prepared and tested, and for evaluation of the feed stoichiometry effect, the two OSTE systems with PETMP were tested as well. All systems were subjected to quintuple tests and the strain/stress curves are shown in Figure 31 for all systems.

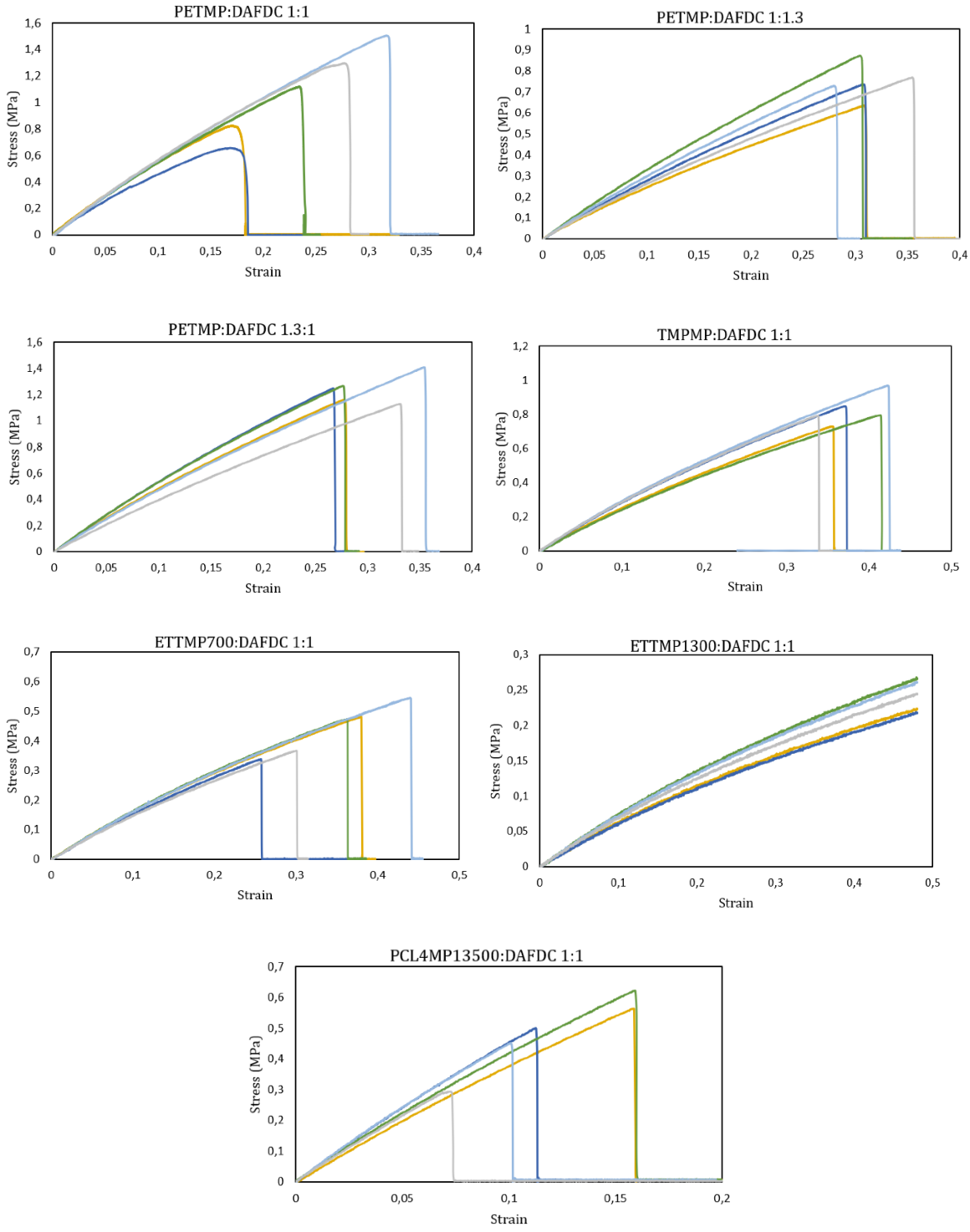

Figure 31: Strain/stress curves from tensile testing of the DAFDC-thiol networks.

From the strain/stress curves the modulus could be determined from the initial slope, and the Tensile strength and maximum stress could be determined from the fracture point (Table 10). When examining the point of fracture, a significant variation can be observed within the

experiments, most likely stemming from inconsistencies in the production of the small dog-bone samples, causing even the slightest deviations to have a large impact on the obtained data. However, much smaller variations for the moduli are observed. From the obtained parameters it was observed that the OSTE systems were more flexible than the STE system; a reasonable result due to the lower crosslinking density of the OSTE systems. It was observed that higher tensile strength was obtained for the system with excess thiol along with slightly lower modules. On the contrary, the tensile strength was reduced with excess DAFDC along with a lowering of approximately 50 % of the modulus. These results indicate that excess aliphatic thiols lead to a stronger network when compared to the furans and allyls of DAFDC.

The various thiols also resulted in great differences in the mechanical behavior of the systems. PETMP, TMPMP and PCL4MP1350 yielded relatively brittle materials whereas the two ETTMP systems yielded materials with a much more elastic nature, with the ETTMP1300 system being unable to fracture within the ~0.5 maximum strain limit of the apparatus used.

Table 10: Mechanical properties from tensile testing of the DAFDC-thiol networks.

Thiol	[SH]:[C=C]	Young's Modulus (MPa)	Tensile Strength (MPa)	Maximum Strain
PETMP	1.0:1.0	6.1±0.4	1.1±0.3	0.23±0.06
PETMP	1.3:1.0	5.4±0.7	1.2±0.1	0.30±0.04
PETMP	1.0:1.3	3.1±0.3	0.75±0.09	0.35±0.01
TMPMP	1.0:1.0	3.0±0.3	0.83±0.09	0.38±0.04
ETTMP700	1.0:1.0	1.69±0.03	0.44±0.09	0.35±0.07
ETTMP1300	1.0:1.0	0.67±0.03	N/A	N/A
PCL4MP1350	1.0:1.0	4.8±0.5	0.5±0.1	0.12±0.04

3.1.3 Concluding Remarks

With this study it has been shown how the DAFDC monomer can be used for synthesis of thiol-ene thermosets. Through UV-initiated thiol-ene crosslinking reaction, evaluation of three different photoinitiators have been studied in a model TEMPIC/TATATO system with the objective of determining the most suitable initiator. The results revealed Omnirad 4265 to be superior to both Lucerin and Omnirad 1000 under the tested conditions. With the Omnirad 4265 initiator, the thiol-ene crosslinking with DAFDC and a selection of different multifunctional thiols was studied through RT-FTIR experiments. For all systems, crosslinked systems could be obtained with high overall conversion for all systems with the exception of ETTMP1300-based networks. The experiments yielded materials with desirable thermal qualities, showing glass transition temperatures ranging between -61.4 °C and up to 9.3 °C. The systems were further studied through tensile testing showing drastic changes in the mechanical properties of the thermosets dependent on the choice of thiol, showing how different types of materials could be obtained by incorporation of FDCA into sulfide crosslinking chemistry. Considering Atom Economy (AE) and E-Factors, the crosslinking themselves are extremely efficient due to no material being lost, making the AE 100 % and the E-factor 0. Considering the synthesis of the monomer, the AE of 87 % and a possible E-factor of 0.39 makes this a very renewable process.

3.1.4 Experimental

3.1.4.1 Chemicals

The chemicals used were all purchased with the exception of DAFDC. Acetone (HPLC grade, 99.8 %), 1,3,5-triallyl-1,3,5-triazine-2,4,6-(1H,3H,5H)-trione (98 %), trimethylolpropan tri(3-mercaptopropionate) and pentaerythriol tetrakis(3-mercaptopropionate) (>95 %) were acquired from Sigma Aldrich® and used as received. Tris[2-(3-mercaptopropionyloxy)ethyl]isocyanurate, ethoxilated-trimethylolpropan tri(3-mercaptopropionate) (THIOCURE® ETTMP 700), ethoxilated-trimethylolpropan tri(3-mercaptopropionate) (THIOCURE® ETTMP 1300) and polycaprolactone tetra(3-mercaptopropionate) (THIOCURE® PCL4MP 1350) were obtained from Bruno Bock Thiocure® and used as received. The photo initiators Ommirad 1000 and Omnirad 4265 came from IGM Resins® while Lucirin is a product of BASF, all used as received. The three commercially available photo initiators used are Lucirin (P1) a yellow initiator consisting only of ethyl(2,4,6-trimethylbenzoyl)-phenyl phosphinate, Ommirad 1000 (P2) a clear initiator consisting of 80% Omnirad 73 (2-hydroxy-2-methyl-1-phenylpropanone) and 20% Omnirad 481 (1-hydroxycyclohexyl-phenyl ketone) and Omnirad 4265 (P3) a slightly yellow initiator consisting of 50% Lucirin and 50% Omnirad 481.

3.1.4.2 Analytical Methods

Fourier-Transformed Infrared Spectroscopy (FTIR)

Identification of thiol-ene compounds and determination of reaction kinetics were performed on Nicolet iS50 FT-IR equipped with an iS50 ATR crystal from Thermo Scientific. The software used for the analysis was Omnic 9.7.46 firmware version 1.14 along with the macro software Macro Basic version 10.0.

Differential Scanning Calorimetry (DSC)

Glass transition temperatures (T_g) and melting temperatures (T_m) were recorded using a TA instruments Discovery DSC. The thermal analysis was performed with a heating/cooling cycle of 10 K/min ranging from -90 °C to 210 °C. T_g was measured at the inflection point and T_m at the peak temperature. The thermogravimetric analysis (TGA) data supplied was obtained using TA instruments Discovery TGA. The measurement was performed from room temperature to 700 °C at a heating rate of 20 K/min.

Nuclear Magnetic Resonance Spectroscopy (NMR)

Nuclear Magnetic Resonance (NMR) spectra were obtained on a 400MHz Bruker Ascend magnet with an Avance II console and equipped with a Prodigy cryoprobe, at 400.13MHz for ^{1}H and 100.61 for ^{13}C. Samples were dissolved in DMSO and the chemical shift reference set at 2.54 PPM. Data were processed and plotted using Mnova software.

Tensile Testing

Tensile tests were performed on a TA Electroforce equipped with a 45 N load cell. Tests were carried out on dog-bones, molded with a cut-out steel plate on a glass surface with the length, width and thickness of the dog-bone being 25.0 mm, 5.0 mm and 0.5 mm respectively. The dog-bones were pulled at a rate of 0.1 mm/s for a total of 12 mm (the maximum of the instrument) or until rupture occurred. Young's moduli of the samples were determined from the slope of the initial 0.3 mm of the test, and ultimate strength and maximum strain were determined from the rupture point. All systems were tested with quintuplicate measurements.

3.1.4.3 Synthesis of Diallyl Furan-2,5-dicarboxylate (DAFDC)

Furan-2,5-dicarboxylic acid (100.0 g, 0.64 mol) was suspended in allyl alcohol (1000 mL) and concentrated sulfuric acid (4 mL) was added. The suspension was heated to reflux for 48 hours at approximately 115 ^{o}C, yielding a clear yellow solution. Excess allyl alcohol (approximately 950 mL) was removed by distillation and the remaining residue was dissolved in ethyl acetate (1000 mL). The organic solution was washed twice with saturated $NaHCO_3$ solution (2x1000mL), followed by concentration of the organic phase by rotary evaporation. The obtained black residue was distilled at reduced pressure (b. p. 112 ^{o}C at 4 mbar, correct b. p. 274 ^{o}C) yielding the desired diallyl furan-2,5-dicarboxylate as a white crystalline solid upon cooling (139.1 g, 92 %).

3.1.4.4 General procedure: Synthesis of thiol-ene TEMPIC/TATATO thin film

The general procedure applies to all the experiments performed for this paper exemplified with this synthesis. The thiol component Tris[2-(3-mercaptopropionyloxy)ethyl]isocyanurate (TEMPIC) (1.393 g, 2.65 mmol) was added to the allylic component 1,3,5-triallyl-1,3,5-triazine-2,4,6-(1H,3H,5H)-trione (TATATO) (0.672 g, 2.69 mmol) and the initiator Lucirin (5.04 mg, 0.016 mmol). The mixture was dissolved in acetone (1 ml) and stirred on a vortex mixer at 2500 rpm for approximately one minute or until fully dissolved. While being kept in darkness two drops of the solution were added to the ATR crystal with a pipette yielding a film of approximately 1 mm in thickness. Ambient light was blocked so that only the light from the UV-lamp initiated the reaction.

3.1.4.5 General procedure: Synthesis of films for tensile testing

DAFDC (2.20 g, 9.29 mmol), PETMP (2.40 g, 4.66 mmol) and OMNIRAD 4265 (109 mg) were weighed in a cup and mixed on a speed mixer for 10 minutes at 3500 RPM or until homogenous. The mixture was poured into a cut-out steel plate with dog-bone-shapes mounted on a glass plate and any excess was removed with an industrial razorblade. The plate was placed in an UV-chamber (365 nm) for 10 minutes yielding the cured dog-bones for tensile testing.

PETMP-DAFDC, 1:1 stoichiometry

DAFDC (2.20 g, 9.29 mmol), PETMP (2.40 g, 4.66 mmol) and OMNIRAD 4265 (109 mg) were mixed at 3500 rpm for 10 minutes and cured into dog-bones following the general procedure.

PETMP-DAFDC, 1:1.3 stoichiometry

DAFDC (3.08 g, 13.04 mmol), PETMP (2.59 g, 5.03 mmol) and OMNIRAD 4265 (146 mg) were mixed at 3500 rpm for 10 minutes and cured into dog-bones following the general procedure.

PETMP-DAFDC, 1.3:1 stoichiometry

DAFDC (2.35 g, 9.95 mmol), PETMP (3.34 g, 6.84 mmol) and OMNIRAD 4265 (131 mg) were mixed at 3500 rpm for 10 minutes and cured into dog-bones following the general procedure.

TMPMP-DAFDC, 1:1 stoichiometry

DAFDC (3.02 g, 12.78 mmol), TMPMP (3.47 g, 8.53 mmol) and OMNIRAD 4265 (159 mg) were mixed at 3500 rpm for 8 minutes and cured into dog-bones following the general procedure.

ETTMP700-DAFDC, 1:1 stoichiometry

DAFDC (3.23 g, 13.67 mmol), ETTMP700 (4.79 g, 6.84 mmol) and OMNIRAD 4265 (205 mg) were mixed at 3500 rpm for 4 minutes and cured into dog-bones following the general procedure.

ETTMP1300-DAFDC, 1:1 stoichiometry

DAFDC (2.19 g, 9.27 mmol), ETTMP1300 (5.99 g, 4.61 mmol) and OMNIRAD 4265 (199 mg) were mixed at 3500 rpm for 6 minutes and cured into dog-bones following the general procedure.

PCL4MP1350-DAFDC, 1:1 stoichiometry

DAFDC (2.15 g, 9.10 mmol), ETTMP1300 (6.19 g, 4.59 mmol) and OMNIRAD 4265 (209 mg mg) were mixed at 3500 rpm for 10 minutes and cured into dog-bones following the general procedure.

3.2 Synthesis and Characterization of Renewable Furan-based Hyperbranched Polyesters

3.2.1 Introduction

A way to circumvent the poor reactivity of allyl esters is by synthesis of larger prepolymeric systems, which can subsequently crosslink through for example free radical polymerization. This method is classically used for the polymerization of diallyl phthalate (DAP), where the system is prepolymerized with benzoyl peroxide and purified, yielding a resin capable of crosslinking.[109,126] However, early studies proved that this method was unfeasible for the DAFDC monomer, due to early crosslinking of the systems, making purification and post-polymerization impossible. Because of this, an alternative method for synthesis of prepolymeric systems was required. To achieve this, the intend was to synthesize linear and hyperbranched polyester systems with a high degree of allyl termination which could undergo crosslinking through either free radical polymerization or through thiol-ene crosslinking as described in Chapter 3.1. This can be achieved by employing a surplus of the DAFDC monomer in polyesterifications with polyols, in this case ethylene glycol for linear segments and glycerol for branching units (Scheme 15). The polyesterification can be performed using similar methods to those used for alkyd polyesters,[97–99,127] in this case using antimony(III)oxide as a mild Lewis acid to catalyze the reaction.[24] In order to estimate optimal curing conditions for post-polymerizations of these types of systems, extensive characterization would have to be performed.

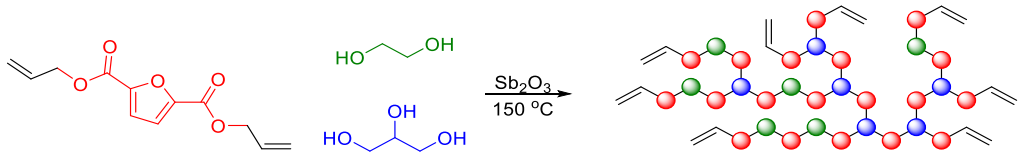

Scheme 15: Schematic representation of the synthesis of allyl functionalized hyperbranched polyesters.

Following the synthesis, the aim is to examine the ability and kinetics of possible crosslinking methods, using thermally activated curative DSC scans with dicumyl peroxide (DCP) as an initiator. The advantage of this method is the ability of DCP to initiate both free radical polymerization and thiol-ene crosslinking, and due to the chemical structure, no gasses are released in the curing process allowing for homogenous final materials.

The work presented in this chapter has been submitted to Macromolecules and is currently in review. The manuscript is included in Appendix F.

3.2.2 Results and Discussion

3.2.2.1 Synthesis of prepolymers systems

In order to examine the possibility of prepolymeric hyperbranched systems, both linear and branched polyesters were synthesized from the DAFDC monomer, ethylene glycol and glycerol (the latter only used in the branched systems), using a method which has been applied for production of PEF.[24] Eight systems in total was synthesized, three linear and five branched, and in order to obtain systems with varying sizes and degrees of branching (DB), different feed stoichiometries were used (Table 11). For different DBs in the branched polyesters, a percentage of ethylene glycol was replaced by glycerol (based on functional groups) in such a fashion that full conversion would never achieve critical crosslinking. The amounts of glycerol were determined through both Carother's and statistical methods,[128] keeping the amount of glycerol below both obtained values. The early experiments quickly showed a limitation of temperature, due to temperatures above 150 °C facilitating the Diels-Alders reaction described in Chapter 3.1 even at low concentrations of Lewis acid, making 150 °C the applied reaction temperature. Synthesis was performed by initially reacting the feed mixture under inert atmosphere for 20 hours before evacuating all condensate with vacuum for 8 hours. All systems remained liquid at this temperature and pressure, with the exception of BPE5 which vitrified, halting the reaction prematurely. All systems were synthesized and purified using precipitation, and their glass transitions and melting points were recorded using DSC, which showed LPE1-3 and BPE4 to be crystalline (Table 11). E-factors for all systems have also been calculated. Interestingly, for some reactions exhibiting relatively low yields, a decent E-factor is still obtained due to running the reactions in bulk.

Table 11: Overview of synthesized prepolymer systems (L/BPE: Linear/Branched Polyester, n.c.: non-crystalline).

Entry	Functionality of feed COOAll:OH	Glycerol Content % of EG	T_m °C	T_g °C	Yield %	E-factor
LPE1	2:1	0	151.6	-22.1	41	2.14
LPE2	1.5:1	0	173.4	-19.8	48	1.87
LPE3	1:1	0	186.1	15.6	78	1.10
BPE1	2:1	100	*n.c.*	8.7	56	1.26
BPE2	1.75:1	60	*n.c.*	15.1	63	1.10
BPE3	1.5:1	40	*n.c.*	9.5	63	1.19
BPE4	1.25:1	10	180.8	22.2	94	0.56
BPE5	1.1:1	5	*n.c.*	28.6	59	1.64

3.2.2.2 Determination of allyl functionalization

In order to estimate the optimal conditions for post-curing of the prepolymers systems, the amount of allyl termination had to be determined. To achieve this, thorough NMR analysis was performed on all systems, using deuterated trifluoroacetic acid (TFA) as a solvent, due to all systems showing good solubility and *d*-TFA have a reference peak at 11.50 ppm, yielding no overlap with other signals. The linear systems LPE1-3 showed no overlap of H-NMR peaks, making assignment straight-forward, and proving full allyl termination for LPE1 and LPE2. System LPE3 exhibited peaks corresponding to hydroxyl-chain ends of the ethylene glycol, corresponding to 23 % of all chains being terminated with ethylene glycol. However, examining the H-NMR spectra for the branched systems proved glycerol to cause overlap between the −C**H**OH- of the glycerol and the CH_2=C**H**-CH_2- of the allyl, as well as the C**H_2**OH-CHOH- of the glycerol overlapping with both the ethylene glycol hydrogens and the CH_2=CH-C**H_2**- of the allyls due to their diastereotopic nature. The overlap of these peaks could be determined through a combination of COSY and HSQC spectra and a schematic representation of this analysis is shown in Figure 32.

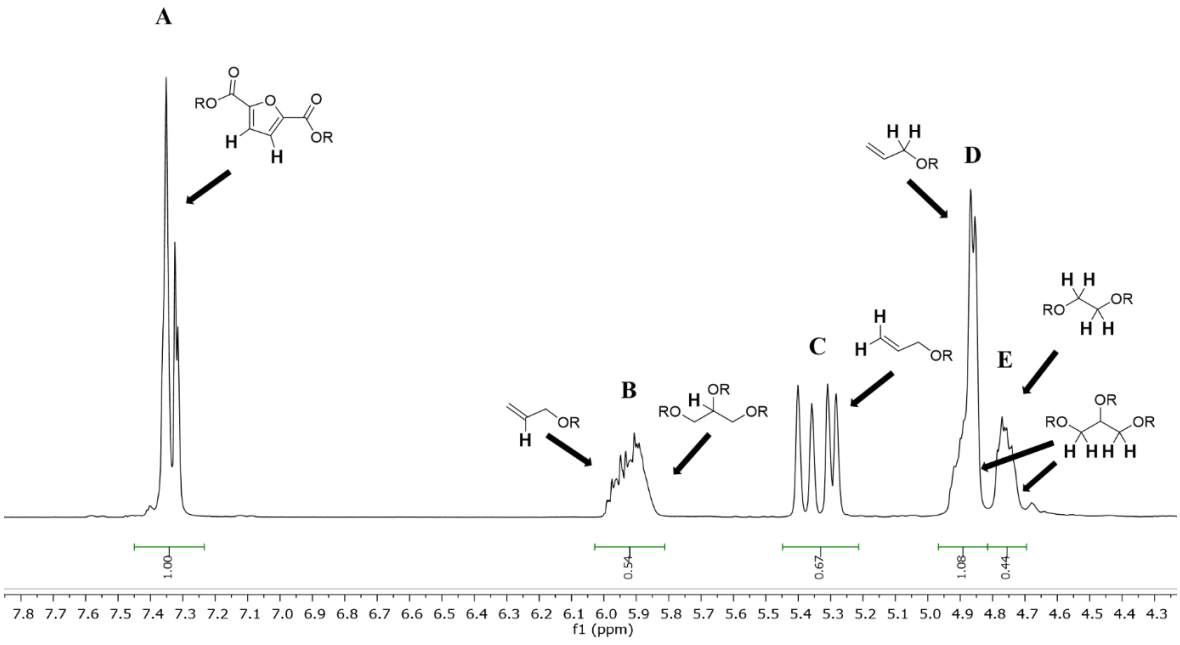

Figure 32: Schematic analysis of the H-NMR overlap of system BPE1 (note that this system has no ethylene glycol, making peak E only stem from glycerol).

Though large overlap with glycerol was observed, the signal from the terminal =CH2 group of the allyl (Figure 32 – Peak C) remained secluded, allowing for estimation of the relative stoichiometries of the different units through Equations 6-9 (the amount of allyls are

determined as an average of the signal from Peaks C and D, and the initial integral of Peak A is set to 1.00). Also, confirmation of correct assignment could be obtained by examining the balance of functional groups (Equation 10).

$$n_{Furane} = \frac{Int_A}{2} \tag{6}$$

$$n_{Glycerol} = Int_B - \frac{Int_C}{2} \tag{7}$$

$$n_{Ethylene\ glycol} = \frac{Int_E - 2 \cdot n_{Glycerol}}{4} \tag{8}$$

$$n_{Allyl} = \frac{\frac{Int_C}{2} + \frac{Int_D - 2 \cdot n_{Glycerol}}{2}}{2} \tag{9}$$

$$2 \cdot n_{Furane} = n_{allyl} + 3 \cdot n_{Glycerol} + 2 \cdot n_{Ethylene\ Glycol} \tag{10}$$

This allowed for final analysis of the relative stoichiometries presented in Table 12 and the abundances of the different units in $mmol/g_{polymer}$ and weight percentages (calculated from the individual molecular weights of each unit) presented in Table 13.

.

Table 12: NMR analysis and overlap correction for all synthesized polyesters.

	Integrals								
	Peak A	Peak B	Peak C	Peak D	Peak E				
	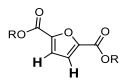	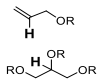		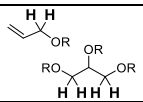	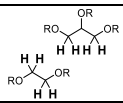				
LPE1	1.00	0.25	0.52	0.51	1.45	1.00	1.94	0	1.41
LPE2	1.00	0.20	0.42	0.43	1.53	1.00	2.35	0	1.8
LPE3	1.00	0.11	0.22	0.22	1.71	1.00	4.55	0	4.18
BPE1	1.00	0.54	0.67	1.08	0.44	1.00	1.49	0.61	0
BPE2	1.00	0.48	0.65	0.97	0.69	1.00	1.53	0.47	0.29
BPE3	1.00	0.38	0.53	0.78	0.95	1.00	1.85	0.43	0.67
BPE4	1.00	0.15	0.28	0.33	1.62	1.00	3.39	0.07	2.71
BPE5	1.00	0.20	0.34	0.42	1.47	1.00	2.86	0.17	2.01

Table 13: Abundances of the various units in the synthesized polyesters (for weight percentages the oxygens of the esters have been included with the furan).

	Abundances							
	mmol/g				*wt%*			
	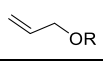	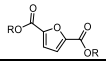	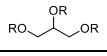	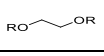	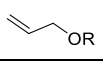	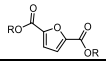	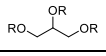	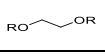
LPE1	2.66	5.11	0	3.71	10.82	78.79	0	10.4
LPE2	2.18	5.18	0	3.96	9.04	79.84	0	11.12
LPE3	1.16	5.26	0	4.84	4.75	81.08	0	14.16
BPE1	3.38	5.04	2.07	0	13.87	77.65	8.49	0
BPE2	3.27	5.02	1.56	0.95	13.52	77.41	6.4	2.68
BPE3	2.71	5.11	1.17	1.84	11.33	78.69	4.82	5.16
BPE4	1.48	5.28	0.11	4.22	6.39	81.33	0.43	11.84
BPE5	1.78	5.24	0.31	3.7	7.54	80.8	1.29	10.37

A general trend of decreasing concentrations of allyls with decreasing amounts of glycerol could be observed as expected. System BPE5 exhibited a deviation from this trend, with higher glycerol and allyl content compared to BPE4. This was most likely due to the prematurely halted reaction mentioned earlier. Regarding the amount of branching of the glycerol units, HSQC spectra of BPE1-5 all showed only a single correlation of the secondary position of the glycerol which corresponded to an ester, leading to the conclusion that all glycerol units were fully branched (Figure 33).

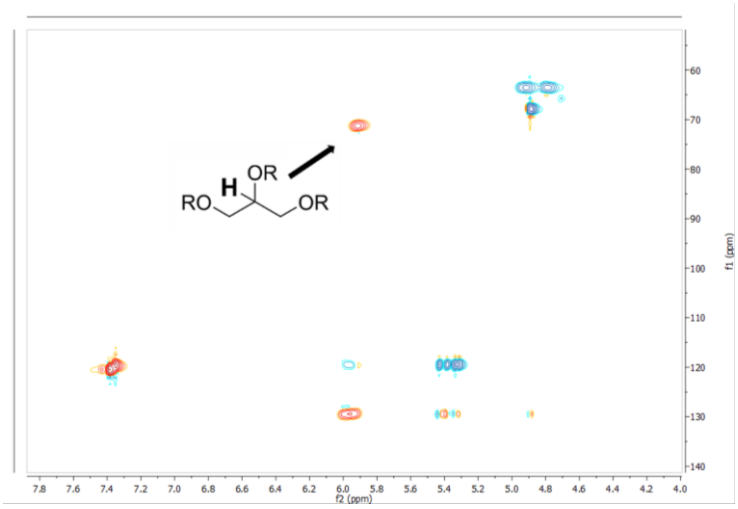

Figure 33: HSQC spectrum of BPE1 showing only one correlation of the secondary position of glycerol.

3.2.2.3 Determination of molecular weights and degree of branching

Due to no overlap within the H-NMR spectra of LPE1-3, molecular weights could easily be determined. However, for the branched systems, other methods had to be applied. Initially, Size Exclusion Chromatography (SEC) was attempted, but unfortunately all systems showed

poor solubility and high affinity for the column, causing the obtained molecular weights to be highly unprecise, calling for other methods to be considered. When analyzing the DB of a given system, the absolute amounts of the various units in the polymer are applied in either Equation 11[129] or the slightly simplified Equation 12[130] (D: dendritic segments, L: Linear segments, T: Terminal segments).

$$DB = \frac{D + T}{D + L + T} \tag{11}$$

$$DB = \frac{2D}{2D + L} \tag{12}$$

However, to determine the absolute amount of units, usually the relative amounts are obtained from NMR (as in Table 12) and corrected from a molecular weight obtained from SEC for example. In cases where the relative amounts of units cannot be determined exclusively from H-NMR, more advanced C-NMR[131] or 2D NMR[132] methods may be applied. With SEC excluded as an option for determination of molecular weights, a set of equations only reliant on the relative stoichiometries had to be derived. This would allow for determination of DB as well as the average number molecular weight of the polymer, $\overline{M_n}$. In this calculation the relative stoichiometries are denoted as n_x where the absolute amount of a given unit in the average polymer is denoted N_x. In order to distinguish between various types of segments, an AB_x nomenclature is introduced where, glycerol for example, is an A_3 dendritic segment (if fully branched), the FDCA unit is a B_2 linear segment, ethylene glycol is an A_2 linear segment and the allyl groups are an A_1 terminal unit. (A: alcohol, B: carboxylic acid). Considering the BPE1-5 systems, the relative amounts of units in the molecule follows an intrinsic growth pattern with increasing the amounts of branching units (in this case A_3) or linear units (A_2) as shown in Figure 34.

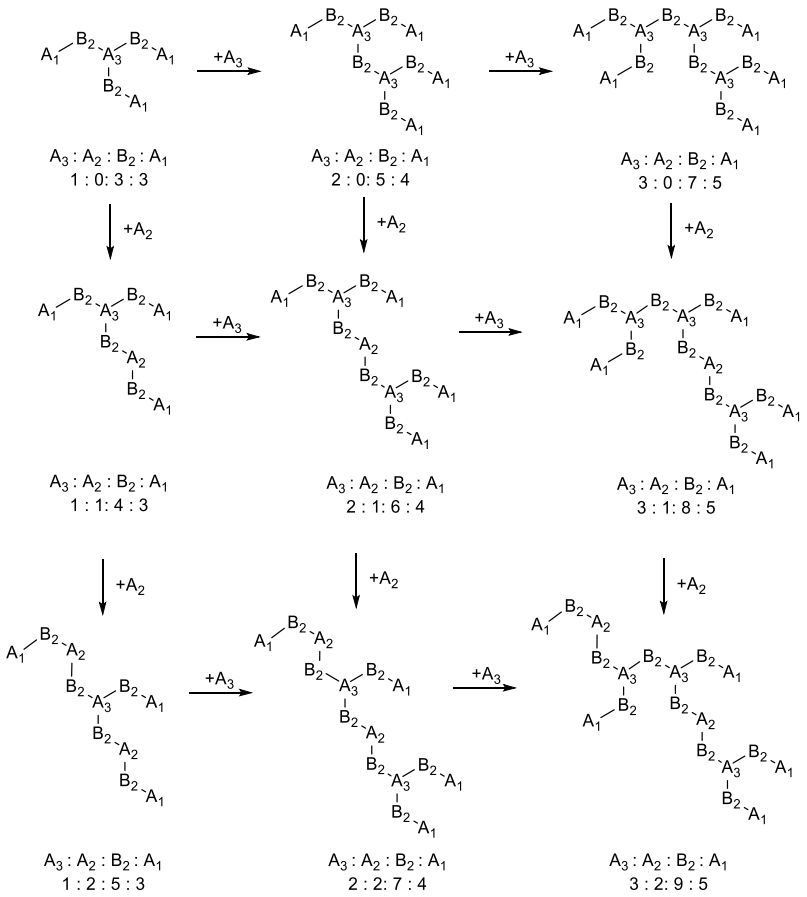

Figure 34: Growth patterns of BPE type systems with relative ratios of the various units.

For the sake of simplicity, system BPE1 is first considered due to no ethylene glycol being present, hence limiting the system to the first line of horizontal progression in Figure 34. Here it can be observed that every added A_3 dendritic unit increases the amount of A_1 terminal units by one and the amount of B_2 linear units by two. Considering the case where no A_3 dendritic units are present, the molecule will have two A_1 units and one B_2 unit (this would be the monomer). Combining this with the growth pattern leads to Equations 13 and 14, describing functions for A_1 and B_2 units respectively, solely dependent on the amount of A_3 units.

$$N_{A_1} = N_{A_3} + 2 \tag{13}$$

$$N_{B_2} = 2 * N_{A_3} + 1 \tag{14}$$

These equation can be applied in order to determine a constant, *k,* which satisfies the equation $k * n_x = N_x$ for all units, making it possible to convert relative stoichiometries into absolute amounts of units in the average molecule. Substituting this constant into Equation 13 and 14,

yields Equations 15 and 16, which can be used to isolate two expressions for *k* in Equations 17 and 18.

$$k * n_{A_1} = k * n_{A_3} + 2 \tag{15}$$

$$k * n_{B_2} = 2 * k * n_{A_3} + 1 \tag{16}$$

$$k = \frac{2}{n_{A_1} - n_{A_3}} \tag{17}$$

$$k = \frac{1}{n_{B_2} - 2 * n_{A_3}} \tag{18}$$

Due to some uncertainties in NMR, these values will be slightly different, and the average can be used. Also, in some cases it can be difficult to determine the relative stoichiometries of some of the units, and in cases where the terminals are unknown, Equation 18 can be used alone and, in contrast, if the amount of linear segments are unknown, Equation 17 can be used. Through these equations, the $\overline{M_n}$ can be determined with the constant, relative stoichiometries and molecular weight of the individual units as shown in Equation 19.

$$\overline{M_n} = \sum k * n_x * M_x \tag{19}$$

Considering the BPE2-5 systems, the linear segment A_2 is added in form of ethylene glycol. Here both the horizontal and vertical progressions in Figure 34 have to be considered. Considering the amount of terminal units, this amount will remain unchanged with addition of A_2 segments. Hence, Equations 13, 15 and 17 will remain unchanged for this type of system. However, the amount of linear B_2 segments will increase by one for every A_2 unit added and, as a result, Equation 14 can be expanded to Equation 20, which can then be used to derive a new term for *k* in Equation 21 and 22, which can be used for determining the $\overline{M_n}$ as previously described.

$$N_{B_2} = 2 * N_{A_3} + N_{A_2} + 1 \tag{20}$$

$$k * n_{B_2} = 2 * k * n_{A_3} + k * n_{A_2} + 1 \tag{21}$$

$$k = \frac{1}{n_{B_2} - 2 * n_{A_3} - n_{A_2}} \tag{22}$$

An interesting feature of Equations 13 and 20 is that if the amount of A_3 units (glycerol) approaches zero, the equations will describe a linear system as shown in Equations 23 and 24. These equations, however, do not add novel aspects, since Equations 23 is basically the standard method for determining $\overline{M_n}$ for linear systems from the terminals.

$$N_{A_1} = 2 \tag{23}$$

$$N_{B_2} = N_{A_2} + 1 \tag{24}$$

With these equations, $\overline{M_n}$ could be calculated showing that the BPE systems obtained were of comparable size (Table 14). This was most likely due to the relatively low reaction temperature applied, causing the reaction to stall prior to completion. From Equation 11, DB could also be obtained as shown in Table 14, which showed only minor amounts of branching in BPE4, explaining the crystallinity due to this system resembling LPE1-3. Calculation examples for these types of systems are given in Appendix B.

Table 14: Molecular weights and degrees of branching determined from the derived NMR method.

System	$\overline{M_n}$ g/mol	DB
LPE1	753	N/A
LPE2	918	N/A
LPE3	1333	N/A
BPE1	1319	0.52
BPE2	1109	0.45
BPE3	1185	0.36
BPE4	1321	0.14
BPE5	1220	0.19

This method has been developed especially for the BPE-type systems. It is however easily adaptable to other types of systems (examples for all the following methods are given in Appendix B), for example, cases with other types of branching units, such as the tetrafunctional pentaerythritol. Since each added branching unit will increase the amount of terminals by two and the amount of linear segments by three, this feature simply expands Equations 13 and 20 to Equation 25 and 26.

$$N_{A_1} = 2 * N_{A_4} + 2 \tag{25}$$

$$N_{B_2} = 3 * N_{A_4} + N_{A_2} + 1 \tag{26}$$

In some cases for alkyd systems, even combined mixtures of different branching points can be utilized.[127] Here a general form for equations 13, 20, 23 and 24 can be written as Equation 27 and 28, where A_n is a branching or linear unit with n functionality. Note that these are general equations that apply to all of these types of systems.

$$N_{A_1} = \left(\sum (n-2) * A_n\right) + 2 \tag{27}$$

$$N_{B_2} = \left(\sum (n-1) * A_n\right) + 1 \tag{28}$$

Lastly, another interesting type of hyperbranched system, is the so-called AB_2 system, where the monomer is reacting with itself, yielding dendritic (D), linear (L) and terminal (T) segments, dependent on number of B groups reacted. Since the minimal molecule with only one dendritic segment will have two terminals, and the amount of terminals grow by one with every new dendritic unit, a simple expression for k can be derived in Equations 29-31. However, due to any number of linear segments being possible in sequence, no dependency for n_L can be established, yielding only a single expression for k.

$$N_{\mathrm{T}} = N_D + 1 \tag{29}$$

$$k * n_T = k * n_D + 1 \tag{30}$$

$$k = \frac{1}{n_T - n_D} \tag{31}$$

3.2.2.4 Crosslinking and curing performance of the prepolymer systems.

In order to crosslink the synthesized prepolymers systems, two methods were applied; free radical polymerization and thiol-ene crosslinking with PETMP (similar to Chapter 3.1). Both these methods were initiated thermally with 1 w% of DCP. Ideally, photoinitiated crosslinking would have been preferred, but the high temperatures required to make the systems liquid made this method unfeasible. Samples were cured during a DSC scan, allowing for kinetic parameters to be determined through the Borchardt and Daniels method,[133,134] utilizing the feature that integration across the exothermic curing peak yields the enthalpy of the reaction. This can be exploited through Equations 32-34 where the evolution of enthalpy can be used to determine reaction order and temperature dependent rate constants, and subsequently determine activation energies and pre-exponential factors through an Arrhenius plot.

$$1 - \alpha = \Delta H_T / \Delta H \tag{32}$$

$$\frac{d\alpha}{dt} = \frac{dH}{dt} / \Delta H \tag{33}$$

$$\ln \frac{d\alpha}{dt} = \ln\big(K(T)\big) + n * \ln(1 - \alpha) \tag{34}$$

For Equations 32-34, α is the fractional conversion, ΔH is the total enthalpy for the reaction (obtained from integration of the entire peak), ΔH_T is the remaining enthalpy of the reaction at time, *t*, *n* is the reaction order and *K(T)* is the temperature dependent rate constant. A visual representation of an ideal curing peak is shown in Figure 35. Data points for this type of calculations are obtained from dividing the curve into 20 equal segments, giving dH/dt as their individual integrals. In order to avoid eventual rate changes during the initiation and gelation

phases, a lower limit at 10 % of the peak height and an upper limit at 50 % of the total enthalpy are introduced. The rate constant can be obtained from Equation 34 if the reaction order is known. This is however not the case, and the reaction order is found by multiple regressions of Arrhenius plots with an array of different reaction orders, with the true value being obtained at the maximal coefficient of determination (R^2) for the Arrhenius plot. An example for curing peak, reaction order optimization and Arrhenius plot for the DAFDC monomer with a PETMP crosslinker is shown in Figure 36.

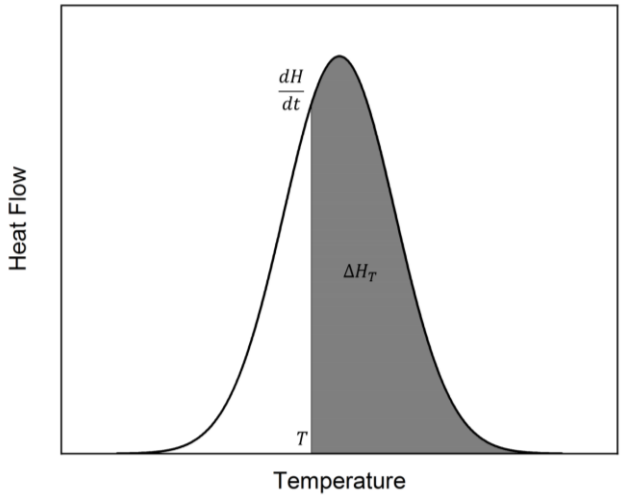

Figure 35: Schematic of an ideal curing peak for determination of kinetic parameters by the Borchardt and Daniels method.

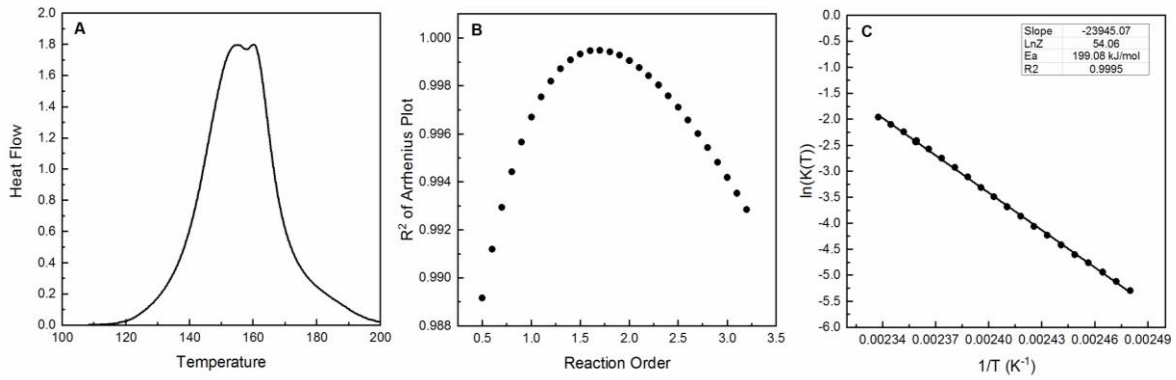

Figure 36: Plots for the Borchardt and Daniels method applied to system BPE1 with a PETMP crosslinker. A. Curing peak, B. Optimization of reaction order, C. Arrhenius plot.

In order to predict conversions at a specific temperature, isothermal conversion plots can be constructed. This was accomplished by deriving a new equation for $\alpha(t)$ from solving the

differential Equation 34, with the initial conditions $\alpha(0) = 0$ which gives Equation 35. Finally, for easy comparison of conversion times, the time required to reach 95 % conversion at 150 °C, $t_{\alpha 95-150^oC}$, is calculated from Equation 35.

$$\alpha(t) = 1 - e^{\frac{\ln\left(\frac{1}{knt-kt+1}\right)}{n-1}} \tag{35}$$

For all synthesized systems and the DAFDC monomer, curative DSC scans were performed with 1 wt% DCP, both with and without a PETMP crosslinker (1:1 allyl:thiol ratio), and the Borchardt and Daniels method was applied. For these calculations, the crystallinity of some of the systems became a challenge. Due to DCP activation above 110 °C and the earliest melting points occurring at 150 °C, the reaction would commence upon melting. This meant that the curing peaks of the DSC for the crystalline system would be a combination with the melting peak, leading to a non-bell curve shape, and thereby making the Borchardt and Daniels method inept. Furthermore, several of these systems were not capable of curing fully, as evidenced by a melting point present on the second heating cycle of the DSC scans. This was mainly the case for the linear systems (where only LPE1 could cure fully when mixed with PETMP), but also for the DAFDC monomer and system BPE4 without PETMP. The curing inability of BPE4 most likely stems from the low DB, giving this system almost linear characteristics.

System BPE4 with a thiol crosslinker and BPE5 without, showed large melting point interference in the curing peak, making determination of kinetic parameters impossible. These systems were, however, able to crosslink fully, as seen by lack of melting point on the second heating cycle. All other systems were subjected to the Borchardt and Daniels method, and the obtained kinetic parameters and glass transition temperatures of the formed networks (determined from the second heating cycle) are stated in Table 15, and predicted isothermal conversion plots are shown in Figure 37.

*Table 15: Kinetic parameters and glass transition temperatures obtained from the Borchardt and Daniels method for all applicable polyester systems (*due to some melting point interference, the reaction order for LPE1 has been set to that of the monomer system).*

System	Allyl:Thiol	Activation Energy kJ/mol	lnZ	n	$t_{\alpha 95-150^oC}$ s	$T_{g,\ network}$ ^oC
Monomer	1:0	N/A	N/A	N/A	N/A	N/A
Monomer	1:1	199.1	54.06	1.68	123.0	-11.1
BPE1	1:0	190.0	48.02	1.25	1775.8	41.1
BPE1	1:1	167.1	42.82	1.38	600.8	51.5
BPE2	1:0	163.3	41.24	1.09	559.6	33.9
BPE2	1:1	143.2	36.38	1.26	342.4	37.9
BPE3	1:0	130.0	32.13	0.91	326.2	25.9
BPE3	1:1	130.2	32.71	1.07	245.4	36.3
BPE4	1:0	N/A	N/A	N/A	N/A	N/A
BPE4	1:1	N/A	N/A	N/A	N/A	43.3
BPE5	1:0	N/A	N/A	N/A	N/A	42.8
BPE5	1:1	122.9	29.97	0.94	392.5	36.6
LPE1*	1:0	N/A	N/A	N/A	N/A	N/A
LPE1	1:1	190.8	49.02	1.68	1822.1	20.1
LPE2	1:0	N/A	N/A	N/A	N/A	N/A
LPE2	1:1	N/A	N/A	N/A	N/A	N/A
LPE3	1:0	N/A	N/A	N/A	N/A	N/A
LPE3	1:1	N/A	N/A	N/A	N/A	N/A

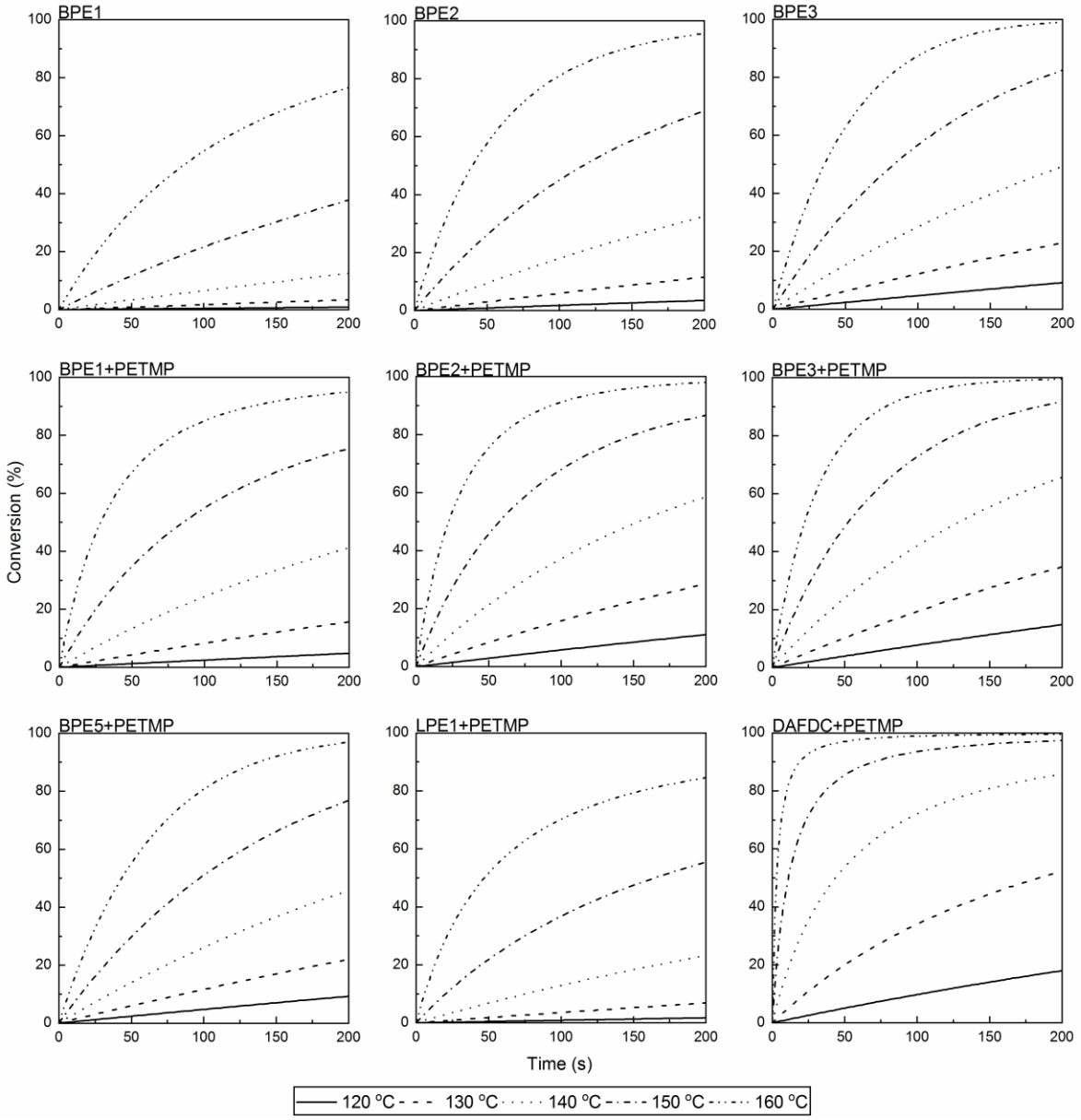

Figure 37: Predicted isothermal conversion plots from the Borchardt and Daniels methods for all applicable polyester systems.

From the data presented in Table 15, an increase in glass transition temperature can be observed compared to those of non-crosslinked polyesters (Table 11), as is expected from the reaction due to increased crosslinking density. Concerning the kinetic parameters, a correlation of decreasing reaction orders, activation energies and pre-exponential factors could be observed with the decrease in amount of glycerol in the feed. This correlation was observed for crosslinking both with and without a PETMP crosslinker. Also, a large decrease in activation energy is observed when applying a PETMP crosslinker, a feature clearly reflected in Figure 37 by the longer conversion times for BPE1-3 without this crosslinker. This

observation stands to reason since the thiol-ene reaction is expected to have a lower activation energy, compared to the free radical polymerization of the allyl esters. Comparing the BPE1-3 systems internally, a decrease in DB yielded more rapid conversion, with BPE2 and BPE3 reaching $t_{\alpha 95-150^oC}$ in less than a third of the time required for BPE1. However, BPE5 shows a slower conversion than BPE3, despite having the lowest activation energy of all systems. This feature is due to the lower pre-exponential factor, which describes the probability of collision of reactive groups.[135] Therefore it stands to reason that a lower DB yields a lower pre-exponential factors, since less branching in the system would cause less accessibility of the allyl groups. Another feature of the pre-exponential factor is observed when comparing crosslinking of the DAFDC monomer with the LPE1 system (both with PETMP). Here similar activation energies are observed. However, the crystallinity and size of LPE1 causes a much lower pre-exponential factor, giving conversion times for LPE1 approximately 15 times larger compared to the monomer system when examining the $t_{\alpha 95-150^oC}$ value.

Interestingly, a general correlation of all four kinetic parameters from the BD method with the degree of branching obtained from the newly developed NMR method (Table 14) could be observed, where generally all kinetic parameters increase with the DB (Figure 38). However, examining the $t_{\alpha 95-150^oC}$ values**,** the fastest curing rates seems to be obtained around the BPE3 systems with a DB of 0.36, most likely due to the fact that further reduction of DB leads to a semi-crystalline system, hindering the reaction (Figure 38-D).

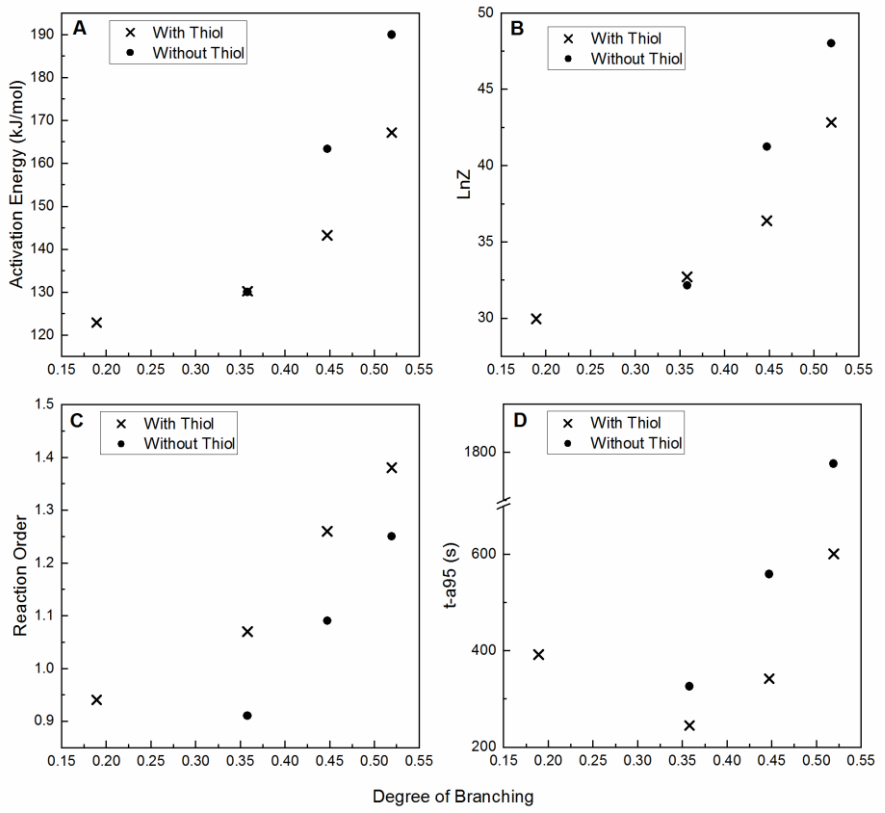

Figure 38: Correlation between the four obtained kinetic parameters from the Borchardt and Daniels method with the degree of branching obtained from NMR.

3.2.3 Concluding Remarks

The study presented in this chapter shows a straight-forward method for synthesis of fully allyl-functionalized hyperbranched and linear polyesters from solely bio-based sources. By means of thorough NMR analysis, relative constituents of the systems along with the mass fractions of each unit in the polyester could be obtained. However, with molecular weights and DB being nearly impossible to determine from SEC, a new method was developed relying exclusively on NMR, by analyzing the intrinsic growth patterns of these types of polyesters. This method proved that systems of similar size with various degrees of branching were obtained. In order to analyze the potential for crosslinking of the synthesized polyesters, thermally initiated DSC curings of the systems were performed with both a direct free-radical polymerization approach and with PETMP as a thiol crosslinker. From this, kinetic parameters could be determined and used to predict isothermal conversion plots through Borchardt and Daniels kinetics. Lastly, cross-examination of NMR and kinetic results proved a correlation between the degree of branching and activation energies, pre-exponential factors, reaction orders and conversion times. As with the thiol-ene systems described in Chapter 3.1, AE and E-factors are optimal for the crosslinking due to no waste being generated in the reaction. For the synthesis of the polyester systems, relatively low E-factors were obtained due to the reaction being run in bulk, and these values can be further improved through possible yield optimization.

3.2.4 Experimental

3.2.4.1 Chemicals

Allyl alcohol (>99.5 %), 2,5-furandicarboxylic acid (97 %), antimony(III)oxide (99 %), ethylene glycerol (>99.8 %), glycerol (99.5 %), pentaerythritol tetrakis(3-mercaptopropionate) (>95 %), dicumyl peroxide (DCP, 98 %), ethyl acetate (99.8 %), methanol (99.8 %), n-heptane (99 %), tetrahydrofuran (>99.9 %) and deuterated trifluoroacetic acid (99.5 atom % D) were all acquired from Sigma-Aldrich and used as received.

3.2.4.2 Analytical Methods

DSC experiments were conducted using a Discovery DSC from TA instruments scanning from -90 °C to 230 °C with a heating rate of 10 K/min. All samples were subjected to two heating cycles, and melting temperatures (T_m) are reported as the peak temperatures of the endothermic melting peaks, while glass transition temperatures were measured at the inflection point.

Nuclear Magnetic Resonance (NMR) spectra were obtained on a 400MHz Bruker Ascend magnet with an Avance II console and equipped with a Prodigy cryoprobe, at 400.13MHz for ^{1}H and 100.61 for ^{13}C. Samples were dissolved in deuterated trifluoroacetic acid and the chemical shift reference set at 11.50 PPM. Data were processed and plotted using Mnova software.

3.2.4.3 General procedure for synthesis of branched and linear polymer systems (System BPE2).

DAFDC (10.1 g, 42.81 mmol), ethylene glycol (0.466 g, 7.51 mmol), glycerol (1.04 g, 11.29 mmol) and antimony trioxide (0.043 g, 0.15 mmol) were mixed as a melt at 50 °C under nitrogen flow for one hour. Nitrogen flow was stopped and the mixture was heated to 150 °C for 20 hours followed by evacuation of formed allyl alcohol under vacuum for 8 hours or until vitrification. Following cooling, the sample was dissolved in THF (50 mL) and precipitated into n-heptane (450 mL), yielding the branched prepolymer system as a white solid (5.54 g, 63 %). Feed composition for all polyester systems are stated in Table 16.

Table 16: Feed compositions for all polyester systems.

	DAFDC		Glycerol		Ethylene Glycol	
System	m *(g)*	n *(mmol)*	m *(g)*	n *(mmol)*	m *(g)*	n *(mmol)*
BPE1[a]	10.1	42.8	1.32	14.3	0	0
BPE2[b]	10.1	42.8	1.04	11.3	0.466	7.5
BPE3[b]	10.7	45.3	0.927	10.1	0.938	15.1
BPE4[c]	10.4	44.0	0.309	3.35	1.87	30.1
BPE5[c]	13.0	55.2	0.226	2.45	2.89	46.6
LPE1[a]	9.25	39.1	0	0	1.22	19.6
LPE2[a]	9.38	39.7	0	0	1.64	26.5
LPE3[d]	8.37	35.4	0	0	2.21	35.6

[a] Purified by dissolution in 50 mL THF and precipitated into 500 mL of methanol

[b] Purified by dissolution in 50 mL THF and precipitated into 500 mL of n-heptane

[c] Purified by dissolution in 100 mL THF and precipitated into 500 mL of methanol

[d] Purified by dissolution in 100 mL THF and precipitated into 700 mL of methanol

3.2.4.4 General procedure for DSC curing

Samples for reactive DSC scans were prepared by mixing the desired prepolymer system with an amount of PETMP resulting in a 1:1 allyl:thiol stoichiometry. To the components were added a stock solution of DCP (10 g/L) in acetone and ground in a mortar until a homogenous sample was obtained. The sample was concentrated and 3-5 mg was transferred to a DSC cup. Samples without a thiol crosslinker were mixed directly with the DCP stock solution in a mortar.

3.3 Cationically Polymerizable Epoxy Thermosets from Furan and Fatty Acid Derivatives

The work described in the following chapter was carried out during an external stay at Kungliga Tekniska Högskolan (KTH) in collaboration with Professor Mats Johansson and Ph.D. student Samer Nameer in the fall of 2017. The results from the DMTA analysis are only briefly described since these were carried out by Samer Nameer after termination of the external stay.

3.3.1 Introduction

With a sustainable synthesis of the DAFDC monomer and thorough testing of its capabilities for crosslinking in free radical and thiol-ene polymerization, the next step we wanted to examine was the possibility of the epoxidized derivative and the possibility of a new type of sustainable epoxy resin. Some work in this field had been carried out earlier by *Deng et al.*[136], where an approach using a multifunctional amine was applied for the synthesis of epoxy resins. Also, epoxy resins from the reduced form of FDCA, furan-2,5-dimethanol, derivatized with glycidyls has been researched.[137,138] Interestingly, this compound has a more suitable electron structure for Diels-Alders reactions mentioned in Chapter 3.1, making it possible to use this reaction constructively for hardening of the final material.[124] Our goal was to synthesize epoxy networks from UV-initiated polymerizations of a multifunctional epoxy to obtain a crosslinked network. However, a system containing only furan-based diepoxide would be expected to crosslink into brittle networks, due to the low amount of flexibility in the final structure. In order to create more flexible networks, we intended to incorporate fatty esters, a type of bio-based monomers derived from plant oils which are receiving a lot of attention due their abundance, low cost and versatility[101]. Also, fatty acid esters exhibit a variety of different functional groups such as alkenes, hydroxyls and epoxides.[139,140] A type of plant oil which has been employed in the production of alkyd paints since the 1920s, is linseed oil (LO),[141,142] which is a triglyceride with a high content of unsaturated C_{18} fatty acids.[139,140] These unsaturations make LO highly interesting from a chemical point of view, since the alkenes can either be used directly in oxidative radical polymerization[143] or they can be employed in epoxy resins following an epoxidation.[144]

By combining the FDCA based epoxy monomer with epoxidized fatty acid esters we aimed at the possibility of engineering polymer systems with desired thermal and mechanical properties through variation of feed compositions (Scheme 16).

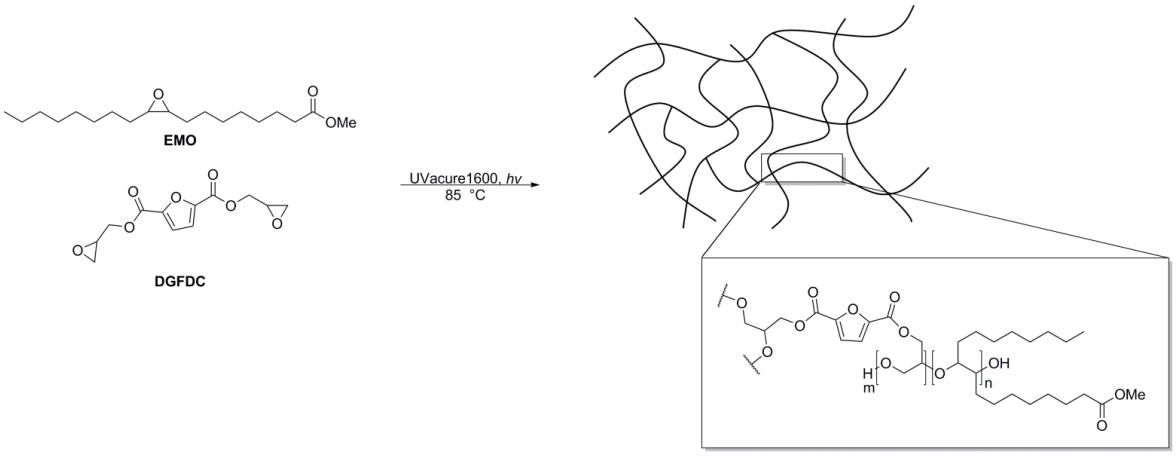

Scheme 16: Schematic representation of synthesis of an epoxy network from EMO and DGFDC.

The work presented in this chapter has been submitted to European Polymer Journal and is currently in review. The manuscript is included in Appendix G.

3.3.2 Results and Discussion

3.3.2.1 Synthesis of Epoxidized Fatty Esters from Linseed Oil (EMX Monomers)

The fatty esters were obtained from linseed oil, which contains the three unsaturated fatty acids oleic acid, linoleic acid and linolenic acid along with the saturated palmitic and stearic acid in abundances of 19.1 %, 15.3 %, 56.6 %, 5.5 % and 3.5 % respectively.[101] By transesterification of epoxidized linseed oil, followed by separation by column chromatography we were able to obtain the three monomers EMO, EMLO and EMLEN (Epoxidized Methyl Ester of Oleic, Linoleic and Linolenic Acid) containing one, two and three epoxide-groups, respectively (Scheme 17). These three monomers will collectively be denoted as EMX.

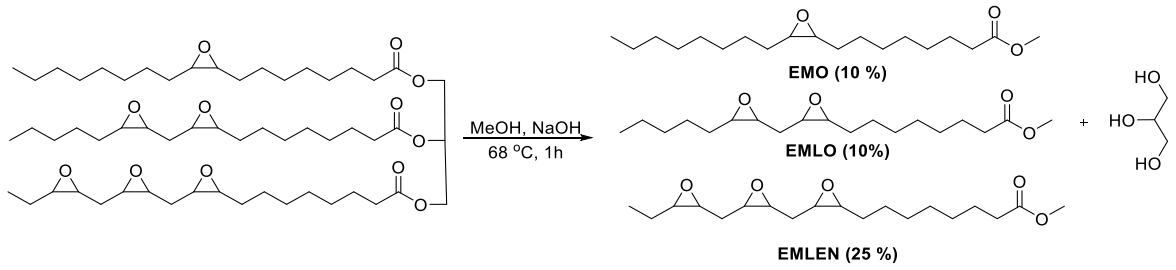

Scheme 17: EMX monomer synthesis by transesterification of epoxidized linseed oil.

3.3.2.2 Epoxidation of DAFDC to Diglycidyl Furan-2,5-dicarboxylate (DGFDC)

As mentioned, the epoxidation of DAFDC had been accomplished earlier.[136] However, this was done using *m*-chloroperoxybenzoic acid (*m*-CPBA), whereas we sought a more renewable approach in line with the rest of the project. Prominent studies shows the possibility of epoxidation by the use of lipase enzymes in presence of hydrogen peroxide and along with an organic carboxylic acid.[145–147] This is achieved by the possibility of the lipase oxidizing the carboxylic acid to a peracid, which then consecutively epoxidizes the alkene as sketched in Scheme 18. In previous studies ε-caprolactone has been applied as a precursor for the carboxylic acid in order to maintain a more neutral pH of the system.[148]

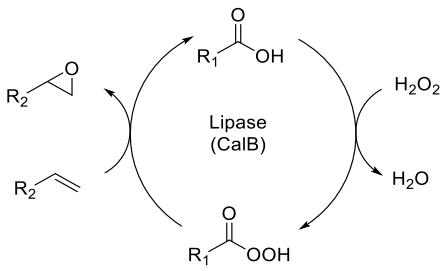

*Scheme **18:** Catalytic cycle for epoxidation with lipase with hydrogen peroxide and a carboxylic acid.*

Unfortunately, attempting this type of epoxidation for DAFDC proved challenging due to polymerization of the ε-caprolactone occurring throughout the reaction. As a replacement, we utilized octanoic acid, which can be extracted from coconut and palm kernel oils[149] and could dissolve the DAFDC. Using this setup, we could monitor the reaction through H-NMR, due to the furan giving distinct signal for the DAFDC and the mono- and di-epoxidized products (Figure 39).

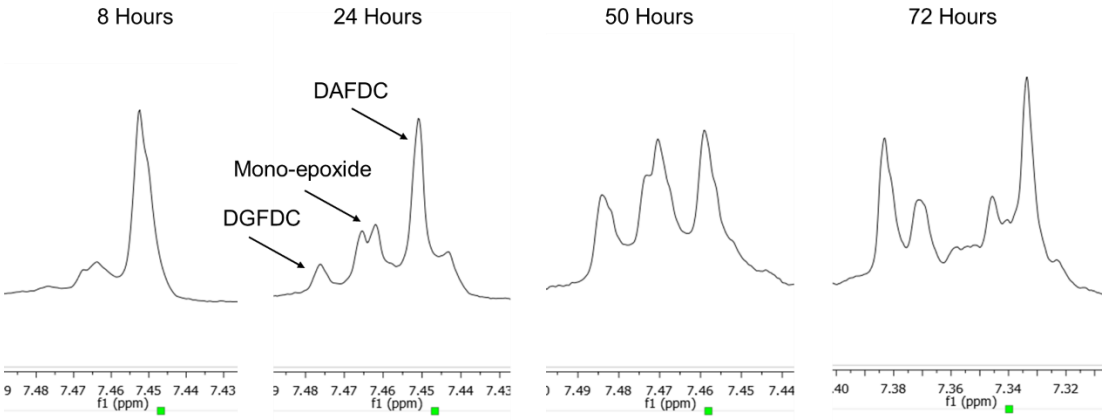

Figure 39: H-NMR monitoring of the lipase-catalyzed epoxidation of DAFDC.

One major obstacle was however encountered during this type of reaction, since it halted at approximately 50 % conversion of the alkenes, yielding a mixture of the reactant and the mono- and di-epoxidized products. The reaction was attempted with 10 w% of resin-mounted CalB at 30 °C, along with two attempts with K_2HPO_4 added to create a buffer system and an attempt with double amount of CalB. All reactions showed a maximum of 45 % conversion after 50 hours (Figure 40). Furthermore, extending the reaction time or increasing the temperature caused the epoxidized products to initiate polymerization, as seen from the spectrum after 72 hours (Figure 39). After 72 hours, the chemical shift was moved significantly up-field, indicating a change in functional groups.

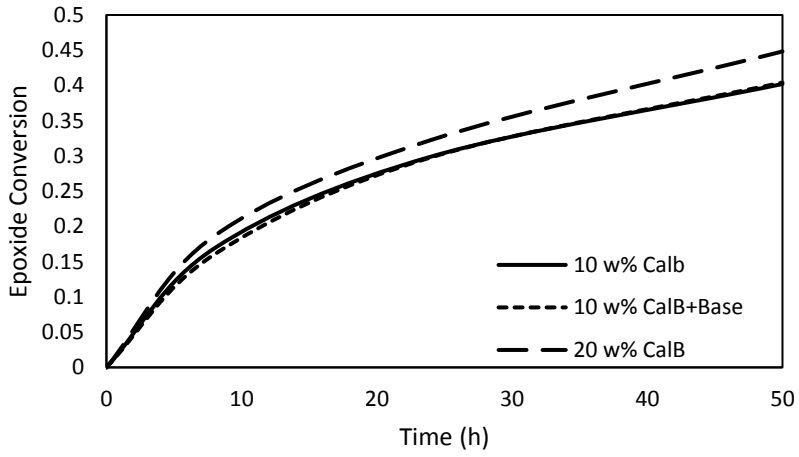

Figure 40: H-NMR monitored conversion of DAFDC. Conversion is calculated from the total amount of epoxides versus allyls present at the given time.

To avoid the polymerization reaction during the epoxidation, we also attempted to synthesize a precursor reagent consisting of only octanoic acid and octanoic peracid by running the reaction without the alkene. The intend was to purify this mixture and use it with DAFDC, however H-NMR showed no significant conversion of the octanoic acid, leading to the conclusion that the lipase was rendered ineffective at these reaction conditions.

Without a feasible solution to this problem, we decided to synthesized the epoxide using the same procedure as *Deng et al.* [136], giving the desired diglycidyl furan-2,5-dicarboxylate (DGFDC) in a 90 % yield (Scheme 19). This reaction further proved the importance of the thorough purification of the diallyl monomer, since the yield was increased with almost 20 % compared to what had previously been reported. Other epoxidations could be tested, however many of the industrially applied processes involve pressure or special catalysts, which would require equipment, chemicals and time not at our disposal.[150] Due to *m*-CPBA being applied,

the AE falls to just 61 %. The E-factor for the process amount to 20.5, however, if recycling of the dichloromethane was performed, this value can be reduced to 2.3.

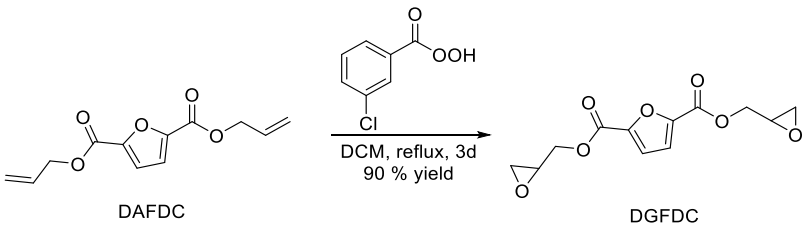

Scheme 19: Applied epoxidation methods for synthesis of DGFDC.

3.3.2.3 UV-initiated Polymerization and Initial Studies of Copolymerization

As mentioned, the aim of the study was to create crosslinked networks with DGFDC and the EMX monomers through UV-initiated polymerization of the epoxides. This is a method based on the ground-breaking work of Crivello and Lam,[151,152] who synthesized diaryliodonium and triarylsulfonium salts, which led to cationic polymerizations of epoxides becoming popular in academia as well as in industry.[153] These types of salts act as a cationic initiator which can be activated by either UV-light or heat which trigger a chain-growth mechanism of the epoxides. Advantages of this type of polymerization include oxygen-insensitivity, speed and low shrinkage of the produced material.[154] Initiation of these salts leads to a strong acid which is capable of protonating the epoxide**,** making the activated epoxide-ring capable of chain-growth propagation (Scheme 20).[155] For the salts, the counter ion employed has to be non-nucleophilic, where PF_6^- or SbF_6^- are widely used. In these studies we apply a diaryliodonium salt with the brand name UVacure1600 (Scheme 20).

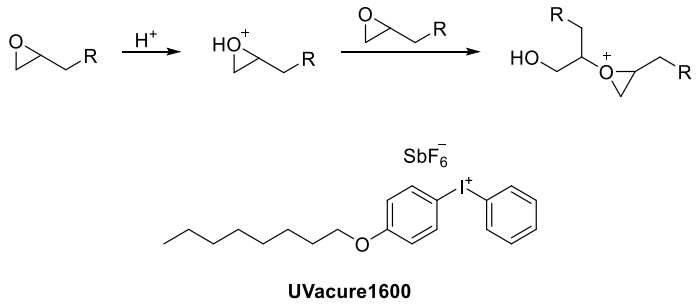

Scheme 20: Mechanism of the cationically initiated propagation and the applied photoinitiator.

In order to confirm a copolymerization of the monomers, reactive DSC studies were performed on the systems, in line with the work described in Chapter 3.2. For this we used the UV-catalyst with the monomers by themselves as well as combined systems with DGFDC and each of the three EMX monomers. Since the UV-initiator is not designed as a thermal initiator, high activation energies for the systems were to be expected. However, it can be assumed that the reaction mechanisms are generally identical to the UV-curing and the relative results are transferable. Firstly, reactions of the pure monomers showed much higher activation energy required for polymerization of DGFDC compared to the EMX monomers – with relative activation energies obtained from Borchardt and Daniels kinetic calculations being 1.00, 1.09 and 2.00 for EMO, EMLO and DGFDC, respectively. Activation energy for EMLEN could not be determined due to the reactive DSC scan yielding two distinct curing peaks due to the trifunctionality of the monomer. The curing peaks for all monomer systems are shown in Figure 41.

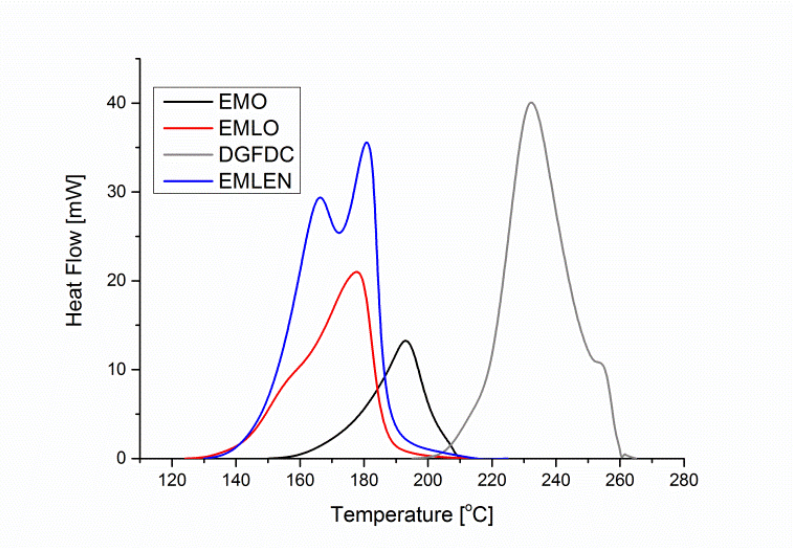

Figure 41: Plots of curing peaks from reactive DSC scans of the four monomer systems.

Following the DSC curings of the monomers, similar experiments were performed using 1:1 epoxy ratio mixed systems from DGFDC and each of the three EMX monomers. Results showed a clear copolymerization of all systems, with all scans yielding only one combined curing peak for all systems, with all curings happening at lower temperatures than required for the polymerization of pure DGFDC (Figure 42). These results led to the conclusion that copolymerization of these types of monomers were a possibility.

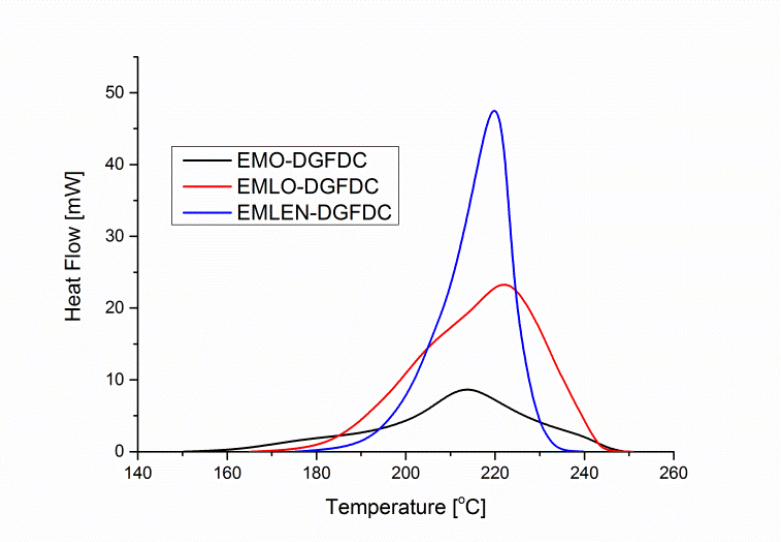

Figure 42: Plots of curing peaks from reactive DSC scans of combined DGFDC-EMX systems.

3.3.2.4 UV-curings of DGFDC-EMX Systems and Kinetics

To fully examine the possibilities of these DGFDC-EMX systems, seven different systems were studied for each EMX monomer, with DGFDC:EMX epoxy ratios of 5:1, 2:1, 3:2, 1:1, 2:3, 1:2 and 1:5, along with curing of the monomer systems by themselves. Initially the kinetic effects of the various stoichiometries were studied using RT-FTIR. Due to the DGFDC monomer having a melting point of ~83 °C and DSC scans of the DGFDC-EMX systems showed combined melting points slightly lower, all UV-curings were carried out 85 °C. Monitoring the reactions were accomplished by close following of the disappearance of epoxy peaks (820 – 900 cm^{-1}) as well as the formation of ether bonds (1050 – 1100 cm^{-1}). However, due to no clearly separated peaks, the absolute conversion could not be determined, and the conversion is calculated as the relative progress towards critical conversion. Kinetic parameters were determined in a similar fashion as seen in Chapter 3.1, with time of completion being estimated at a conversion of 95 % of the maximum value and maximum rate (in %/s) was determined at the maximal slope throughout the reaction. Initiation time was estimated from the tangent at the steepest slope with the initiation time being the intersection of the tangent with the x-axis. However, some of the reaction initiated within the first few scans, making initiation times rough estimates. Results of all curings are presented with conversion plots in Figure 43 and with all kinetic parameters stated in

Table 17.

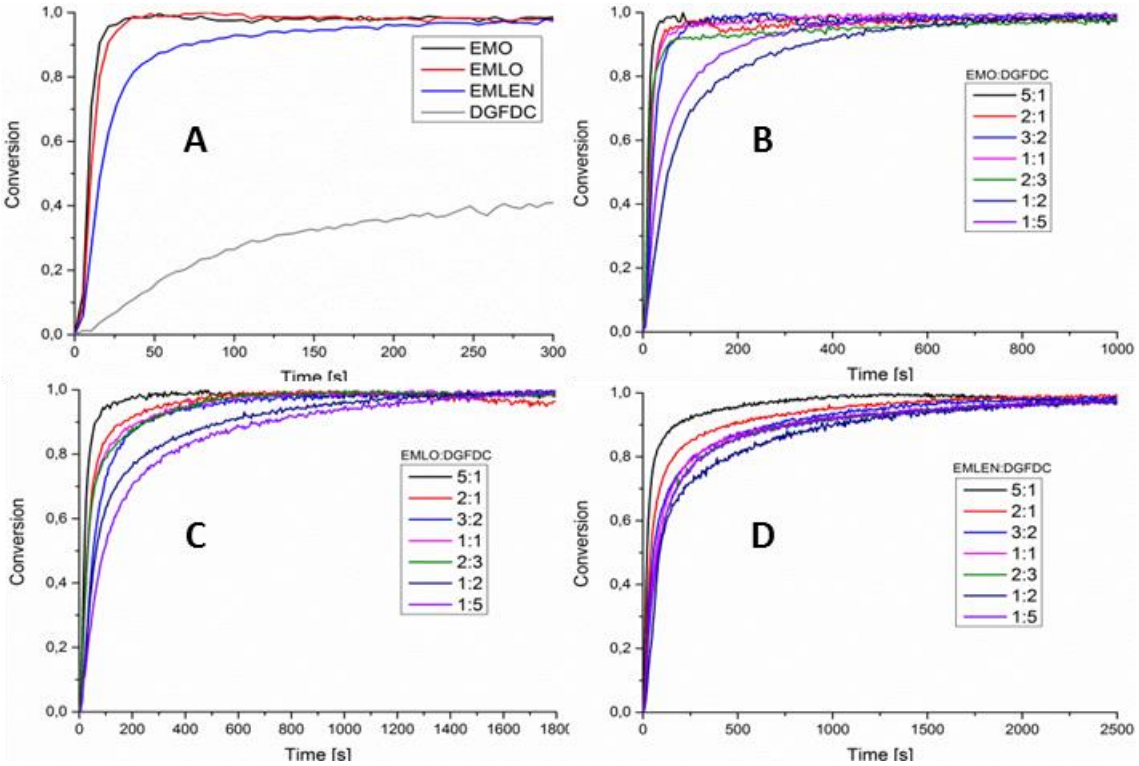

Figure 43: Conversion curves for all examined systems. A: Pure monomer systems. B: DGFDC:EMO systems. C: DGFDC:EMLO systems. D: DGFDC:EMLEN systems.

Table 17: Kinetic parameters for all cured DGFDC-EMX systems.

Entry	EMX	EMX:DGFDC Epoxy ratio	t_{gel} s	t_{ini} s	Max Rate %/s
1	EMO	1:0	20.9	4.1	11.1
2	EMLO	1:0	31.7	4.2	8.3
3	EMLEN	1:0	168.8	3.8	4.0
4	-	0:1	N/A	47.3	0.5
5	EMO	5:1	31.7	4.0	8.3
6	EMO	2:1	57.8	5.9	5.4
7	EMO	3:2	89.7	5.0	3.5
8	EMO	1:1	73.8	3.8	5.7
9	EMO	2:3	332.3	4.2	7.1
10	EMO	1:2	532.8	4.1	1.5
11	EMO	1:5	342.7	5.5	2.4
12	EMLO	5:1	105.6	5.8	4.0
13	EMLO	2:1	295.6	6.0	2.4
14	EMLO	3:2	422.2	12.0	1.4
15	EMLO	1:1	380.1	5.0	2.1
16	EMLO	2:3	417.0	4.9	2.3
17	EMLO	1:2	886.6	10.9	1.2
18	EMLO	1:5	1071.3	7.3	1.1
19	EMLEN	5:1	427.2	4.0	3.3
20	EMLEN	2:1	917.9	5.6	1.9
21	EMLEN	3:2	1197.6	7.2	1.4
22	EMLEN	1:1	1441.8	11.3	1.3
23	EMLEN	2:3	1466.8	7.1	1.3
24	EMLEN	1:2	1545.8	13.2	0.8
25	EMLEN	1:5	1540.6	6.0	1.2

From the data presented in Table 17 a general trend of increased conversion times with increasing functionality of the EMX monomers was observed. A general trend for lower conversion rates with increased amounts of DGFDC can also be observed. However, it was expected that increasing the amounts of DGFDC would cause decreasing reaction rates, but some outliers from this correlation are present. This can be explained, since the correlation would assume free movement of the molecules (e.g. in a solution), but due to widely different molecular structure of the monomers, the overall macromolecular dynamics of the bulk systems change excessively when adjusting the stoichiometric ratios. Therefore, a direct kinetic correlation was not observed.

As mentioned, no clearly separated peak for either the epoxides or ether bonds were present, and the absolute conversion of the epoxides could not be determined. Therefore, the final state of the reaction is set at 100 %, which corresponds to the critical conversion point and not the

epoxy conversion. This means that the point of critical conversion has a strong effect on the conversion rates. The critical conversion could not be determined mathematically (as for step-growth polymerization systems), due to many factors coming into play, such as concentration of epoxides, mobility in the system and the amount of multifunctional epoxy reagents. By examination of the EMO-DGFDC system as an example, the higher amounts of DGFDC was expected to cause a decrease in reaction rates. However, the increase in the amount of DGFDC leads to more multifunctional epoxy compounds, giving a higher degree of crosslinking, and a higher concentration of epoxides (higher functionality and smaller molecule than EMO) which can lead to longer chain growth. Also the shift in monomer stoichiometry causes changes in the dynamics of the bulk system due to the aliphatic chains of EMO yielding a highly hydrophilic system at low DGFDC stoichiometries and vice versa.

3.3.2.5 Thermal and Mechanical Properties of Synthesized DGFDC-EMX Systems

To evaluate the effect of the feed stoichiometry of the reaction on the thermal properties, DSC scans were run on all products from the curings. It became apparent that the systems based on the EMO monomer had glass transitions at much lower temperatures outside the measurable range of our equipment (lower than -50 °C), and we deemed these films to be outside our scope of interest, since characterization of them would require DSC apparatus cooled by liquid nitrogen which we did not have available. On the contrary, glass transition measurements of the EMLO and EMLEN systems showed a clear correlation with the stoichiometry, concluding the ability to control the thermal properties, with glass transition temperatures which could be adjusted in the range of -20 to 80 °C. All glass transition temperatures are stated in Table 18 and a plot showing the correlation between feed stoichiometry and T_g is presented in Figure 44**.** As a reference, samples with stoichiometric feed was run with diglycidyl bisphenol A (DGBPA) since this is a widely used chemical for epoxy resins bearing similar chemical properties to the applied DGFDC. These samples showed comparable glass transitions to the DGFDC systems with the T_g being slightly higher. This most likely stems from the bi-aromatic structure of bisphenol A contrary to the mono-aromatic DGFDC, producing a more rigid system.

Table 18: Glass transition temperatures of synthesized DGFDC-EMX systems.

Entry	EMX	EMX:DGFDC Epoxy ratio	T_g °C
1	EMO	1:0	N/A
2	EMLO	1:0	N/A
3	EMLEN	1:0	-1
4	-	0:1	N/A
5	EMO	5:1	N/A
6	EMO	2:1	N/A
7	EMO	3:2	N/A
8	EMO	1:1	N/A
9	EMO	2:3	N/A
10	EMO	1:2	N/A
11	EMO	1:5	N/A
12	EMLO	5:1	-23
13	EMLO	2:1	-8
14	EMLO	3:2	1
15	EMLO	1:1	20
16	EMLO	2:3	31
17	EMLO	1:2	49
18	EMLO	1:5	65
19	EMLEN	5:1	12
20	EMLEN	2:1	47
21	EMLEN	3:2	44
22	EMLEN	1:1	56
23	EMLEN	2:3	65
24	EMLEN	1:2	71
25	EMLEN	1:5	66
26	EMO	DGBPA 1:1	-23
27	EMLO	DGBPA 1:1	29
28	EMLEN	DGBPA 1:1	71

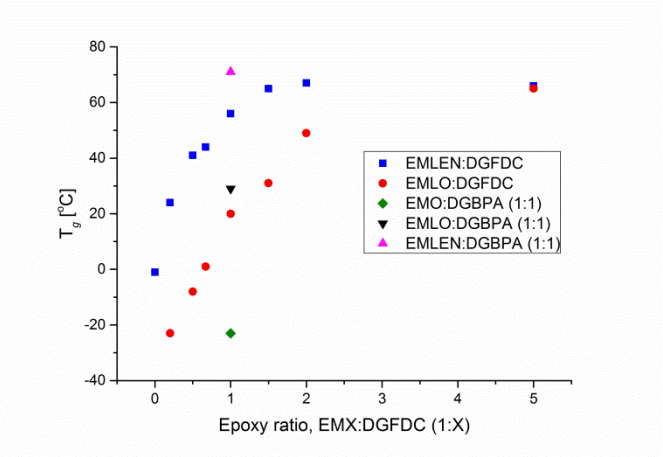

Figure 44: Correlation of glass transition temperatures and stoichiometric feed of DGFDC-EMLO and DGFDC-EMLEN systems.

In order to evaluate mechanical properties of the DGFDC:EMX systems, films for Dynamic Mechanical Thermal Analysis (DMTA) were synthesized. The EMLO-DGFDC system was tested for all applied feed stoichiometries and the EMLEN-DGFDC system with stoichiometric feed was tested for comparison. DMTA experiments presented a correlation with the DSC results regarding the trend of the T_g – with increasing amount of DGFDC an increasing T_g was obtained (Figure 45 B). Examining the storage modulus, *E'*, a similar trend was observed with increased amounts of DGFDC increasing the stiffness of the material as would be expected (Figure 45 A). The analysis of *E'* further proved the co-polymerization of the monomers by showing only two plateaus in the analysis.

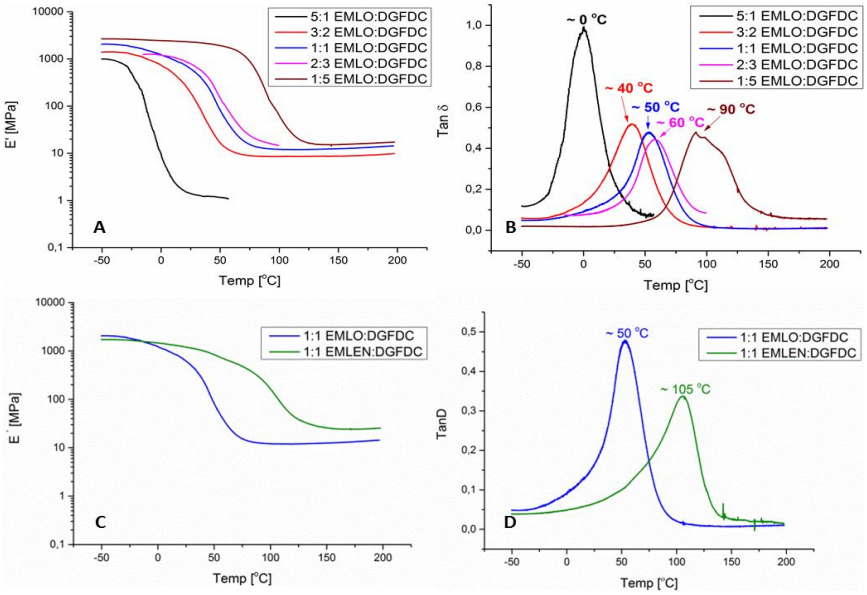

Figure 45: DMTA results for the tested DGFDC-EMX films.

3.3.3 Concluding Remarks

With this study we have shown how the use of the DAFDC monomer can be expanded through epoxidation to DGFDC. This study shows that it is possible to make thermosets by combining the diglycidyl ester of FDCA (DGFDC) with free epoxidized fatty methyl esters (EMX) synthesized from linseed oil. By variations of the feed stoichiometry of these systems it was possible to obtain structure-property control due to the vastly different attributes of the monomers. The aliphatic chains of the EMX monomers provides flexible, hydrophobic structures which synergizes well with the rigidity and stability of the furan-based DGFDC. Furthermore, we have shown how the change in feed stoichiometry affects the reaction rate of UV-initiated cationic polymerization of the epoxized esters, with high amounts of DGFDC lowering the reaction rate drastically. Finally, these bio-based systems showed very comparable thermal properties with analogues synthesized with the commercially available and petrol-based diglycidyl ether of bisphenol A (DGBPA). As for the thiol-ene networks described in Chapter 3.1, the crosslinking themselves produce no waste giving an Atom Economy and E-factor of 100 % and 0 respectively. The synthesis of DGFDC however, has a low atom economy of 61 % due to the *m*-CPBA being used as an epoxidizing agent and the E-factor can be reduced to 2.3 through recycling of dichloromethane.

3.3.4 Experimental

3.3.4.1 Chemicals

2,5-furandicarboxylic acid (FDCA) (97%), allyl alcohol (≥99%), 3-Chloroperbenzoic acid (m-CPBA) (≤77%) and sulphuric acid (H_2SO_4) (95-97%) were purchased from Sigma Aldrich. Epoxidized linseed oil (ELO) was provided by Ackros Chemicals. The photoinitiator UVAcure 1600 was supplied by CYTEC. All materials were used as received, unless otherwise noticed.

3.3.4.2 Analytical methods

Nuclear Magnetic Resonance Spectroscopy (NMR)

In order to obtain ^{1}H-NMR a Bruker spectrometer (400 MHz) was used. The data for ^{1}H-NMR and ^{13}C-NMR were acquired by using 16-32 scans and 512 scans respectively and with 1 second relaxation time. Deuterated chloroform ($CDCl_3$) containing tetramethylsilane (TMS) and DMSO-d6 were used to dissolve the samples. The residual solvent peaks were used as reference ($CDCl_3$: 7.26 ppm (^{1}H-NMR) and 77.16 ppm (^{13}C-NMR) and DMSO-d6: 2.50 ppm (^{1}H-NMR) and 39.52 ppm (^{13}C-NMR). The acquired spectra were analyzed using MNova v9.0.0-12821 (Mestrelab Research S.L. 2013).

Fourier-Transform Infrared Spectroscopy (FTIR) and Real-Time FTIR (RT-FTIR)

FTIR and RT-FTIR were recorded on a Perkin-Elmer Spectrum 100 equipped with a triglycine sulphate (TGS) detector. The instrument was equipped with a single reflection (ATR: attenuated total reflection) accessory unit Golden gate from Graseby Specac LTD (Kent, England). The Golden gate was equipped with a temperature control (Specac, Heated Golden Gate Controller). The FTIR spectra were recorded using 8 scans with a 4.0 cm^{-1} resolution and a range from 600-4000 cm^{-1}. The data was analyzed using Spectrum software v. 10.5.1 from Perkin-Elmer. For RT-FTIR the data were recorded at 1 scan per 5.7 seconds with a resolution of 4.0 cm^{-1}. The software used for RT-FTIR was TimeBase® from Perkin-Elmer

Differential Scanning Calorimetry (DSC)

The thermal analyses were obtained by a Mettler Toledo DSC-1 equipped with Gas Controller GC100. Approx. 5-10 mg of sample was weighed into 100 μL aluminum crucible. The data were collected using heating/cooling cycles from 30 °C to 300 °C for DSC kinetics and -50 to 200 °C for the T_g of the EMX:DGFDC thermosets. The temperature gradient rate was set to 10 °C min^{-1} with 5 min of isotherms at the highest/lowest temperature value for all DSC measurements. The analyses were carried out in inert atmosphere using 10 mL of N_2 gas. The T_g was obtained from the second heating cycle and was reported as the midpoint value of the heat capacity change.

Dynamical Mechanical Thermal Analysis (DMTA)

DMTA was conducted to obtain the physical properties of the synthesized thermosets. A Q800 DMTA TA instrument was used. The instrument was equipped with a clamp for tensile testing. The data were collected using a temperature ramp from -50 °C to 200 °C using a heating rate of 3 °C min^{-1}. The frequency was set to 1 Hz. The T_g of each sample was obtained from the maximum of the tan δ peak.

UV-light source

The UV-light was generated from a Hamamatsu L5662 with a standard medium-pressure 200 W L6722-01 Hg-Xe lamp. The intensity of the UV-light was measured by a Hamamatsu power meter (model C6080-03) calibrated for 365 nm. The intensity was measured to 80-90 mW cm^2.

Automated column purification

The fatty acid methyl esters were separated by Isolera 4 advanced automated flash purification from Biotage equipped with UV detector. A 50 g KP-Sil column packed with silica was used to separate the FAME mixture. The column was packed with approx. 10 wt. % of sample relative to the weight amount of silica in the column.

3.3.4.3 Synthesis of diglycidyl 2,5-furandicarboxylate (DGFDC)

Following modified literature procedure,[156] DAFDCA (4.98 g, 21.08 mmol) and m-CPBA (77 wt. % pure, 11.84 g, 52.83 mmol) was suspended in dichloromethane (40 mL) and heated to 40 °C for 72 hours. The resulting suspension was filtered and rinsed with dichloromethane (30 mL). The organic phase was washed with a 10 % aqueous solution of Na_2SO_4 (50 mL), followed by a 10 % aqueous solution of Na_2CO_3 (50 mL) and lastly demineralized water (50 mL). The organic phase was dried with $MgSO_4$ and concentrated to yield diglycidyl 2,5-furandicarboxylate (DGFDC) (5.11 g, 90.0 %) as a white crystalline solid.

^{1}H-NMR (400 MHz, DMSO-d6) δ 7.49 (s, 2H), 4.68 (dd, J = 12.4, 2.7 Hz, 2H), 4.10 (dd, J = 12.3, 6.6 Hz, 2H), 3.33 (d, J = 4.8 Hz, 2H), 2.84 (t, J = 4.6 Hz, 2H), 2.73 (dd, J = 5.0, 2.6 Hz, 2H).

^{13}C-NMR (101 MHz, DMSO-d6) δ 157.06, 145.91, 119.51, 66.03, 48.80, 43.90.

3.3.4.4 Transesterification of Epoxidized Linseed Oil (ELO)

Following literature procedure[157] the different fatty acid methyl esters EMO, EMLO and EMLEN were retrieved by methanolysis procedure. ELO (20 g) was weighed into a round bottom flask equipped with a magnetic stirrer. To the round bottom flask was NaOH dissolved in methanol (0.02 M, 250 mL) added under stirring. The round bottom flask was then equipped with a condenser and was then heated to 68 °C for 1 hour. The reaction mixture was then cooled to

room temperature and the fatty acids were extracted in n-heptane to remove the glycerol. The n-heptane was rotary evaporated resulting in a fatty acid mixture (15 g, 75 % yield). Automated column chromatography (Isolera 4) was then used to separate the different monomers. Silica was used as a stationary phase and a gradient of n-heptane:ethyl acetate as mobile phase. The pure fractions of each monomer were collected and the solvents were rotary evaporated. To completely dry the monomers from residual solvent the monomers were put in vacuum oven at 50 °C overnight. The pure monomers EMO (2 g, 10 % yield), EMLO (2 g, 10 % yield) and EMLEN (5 g, 25 % yield) were then stored in glass vials at room temperature.

3.3.4.5 General procedure for photo-curing followed by RT-FTIR

The desired amounts of DGFDC and EMX monomers were added to in a small vial and dissolved using a 10 mg mL^{-1} solution of UVAcure 1600 in acetone, resulting in a dry mixture containing 2 wt% UVAcure 1600. For high DGFDC ratios, additional acetone was required for a fully homogenous solution, and the amount of acetone was doubled in these cases. The crystal located on the Golden gate accessory unit was preheated to 85 °C and a background scan was recorded before a 10 µL of the solution (or 20 µL for samples containing additional acetone) was applied to the crystal. The mixture was left at 85 °C for two minutes for all acetone to evaporate. This was followed by irradiation with UV-light and RT-FTIR measurements for 30 minutes for EMO and EMLO systems and 60 min for EMLEN systems and pure DGFDC.

3.3.4.6 General procedure for film curing for DMTA samples

The desired amounts of DGFDC and EMX monomers were weighed in a vial with a magnet and UVAcure 1600 was added amounting to 2 wt% of the total monomer weight. The vial was closed and heated to 85 °C in an oil bath while stirring, yielding a homogenous liquid. The hot solution was added to a preheated silicone mold preheated on a heating plate set at 100 °C. The sample was irradiated with UV-light at this temperature for one hour, resulting in fully cured films usable for DMTA measurements.

4 Conclusion and Future Perspectives

An inevitable exhaustion of fossil resources leads to a necessity of development of green and renewable alternatives to the chemicals used in the current industry. Throughout this thesis, two major chapters have been presented. Here, the first chapter has been focused on the development of reactions for synthesis of bio-based platform chemicals and the second chapter revolved around the utilization of these compounds in polymer chemistry.

Through computational calculations, Chapter 2 has presented studies of two types of reactions, the DODH and the HDO reaction. Both reactions being of interest due to their possible application as oxygen-reducing reactions of biomass, with, for example, the DODH reaction being capable of valorization of glycerol by providing a renewable route to allyl alcohol. This led to discovery of two new mechanisms. In Chapter 2.2 it was revealed that when applying vanadium as a catalyst in the DODH reaction, the electronic structure allowed for triplet states, which subsequently changed the mechanism. Due this triplet state, the extrusion no longer proceeded as a concerted mechanism, but instead cleaved only one of the C-O bonds, allowing for formation of 4-membered oxetane species which could then undergo extrusion. Studies on the molybdenum catalyzed HDO reaction of benzyl alcohol in Chapter 2.4 also showed an unexpected mechanism. Here the molybdenum center of the catalyst was capable of formation of π-benzyl complexes through an intramolecular mechanism. This led to transition states, in which the aromaticity of the benzene ring was interrupted, subsequently explaining the irregular behavior of the previously obtained Hammett studies. This mechanism could be further confirmed from correlation with experimental data. A study of the well-known rhenium catalyzed DODH reaction was also carried out in Chapter 2.3. Though this reaction has been known for more than 20 years, some dispute of the oxidation of rhenium throughout the mechanism remained. The DFT studies of this mechanism revealed favorable energies for a Re(VII)↔Re(V) mechanism. However, due to the studies supporting a Re(V)↔Re(III) mechanism using hydrobenzoin as a substrate, the DFT calculation performed in Chapter 2.3

showed a plausible reductive cleavage mechanism of this substrate which could yield Re(III) moieties.

Chapter 3 has been focused on novel types of thermoset systems, based on the bio-based FDCA in combination with allyl alcohol, to form the new building block DAFDC. The intention for DAFDC was application as a possible rival to the petrol-based DAP monomer. Chapter 3.1 presented a high yield synthesis of the DAFDC compound, along with its application in UV-initiated thiol-ene chemistry, where it could be crosslinked with various multifunctional thiol compounds. This showed that different types of materials could be obtained by changing the chemistry of the thiol and from variation of stoichiometry to form both STE and OSTE materials. Chapter 3.2 expanded the use of the DAFDC, through synthesis of linear and hyperbranched polyester systems with high degrees of allyl functionality. Encountering challenges when attempting to determine molecular weights of these systems led to a novel method, which could estimate the average number molecular weight and degree of branching exclusively from NMR by the examination of the intrinsic growth patterns of the polyesters. With the systems analyzed, crosslinking both with and without a thiol crosslinker was monitored through DSC, allowing for determination of kinetic parameters, which proved excellent correlation to the degrees of branching obtained from the new NMR-based method. The last part of the thesis, Chapter 3.3, was a project carried out at KTH in Stockholm, where the epoxidized form of the monomer, DGFDC, was tested in co-polymer epoxy resins with epoxidized fatty acid esters. The vastly different chemistry of the two types of monomers yielded the ability to control thermal and mechanical properties through adjustments of feed stoichiometry, allowing for possible synthesis of an array of different epoxy resins.

With this thesis, foundation for further development of methods for production of bio-based platform chemicals have been developed along with new methods for the utilization of these chemicals for renewable materials. These materials represents a plausible replacement of their petrol-based analogues, hereby laying parts of the groundwork for a more sustainable and renewable future.

5 References

(1) *BP Statistical Review of World Energy 2017, British Petroleum*.

(2) *World Oil Outlook, Organization of the Petroleum Exporting Countries. 2017 OPEC World Oil Outlook. October 2017. Available from: Http://www.opec.org*.

(3) Smalley, R. E. Future Global Energy Prosperity: The Terawatt Challange. *MRS Bull.* **2005**, *30*, 412–417.

(4) Sheldon, R. A. The E Factor: Fifteen Years on. *Green Chem.* **2007**, *9*, 1273.

(5) Tang, S. L. Y.; Smith, R. L.; Poliakoff, M. Principles of Green Chemistry: PRODUCTIVELY. *Green Chem.* **2005**, *7*, 761–762.

(6) Trost, B. M. The Atom Economy-A Search for Synthetic Efficiency. *Science.* **1991**, *254*, 1471–1477.

(7) Sheldon, R. A. E Factors, Green Chemistry and Catalysis: An Odyssey. *Chem. Commun.* **2008**, No. 29, 3352.

(8) Sheldon, R. A. Fundamentals of Green Chemistry: Efficiency in Reaction Design. *Chem. Soc. Rev.* **2012**, *41*, 1437–1451.

(9) Vassilev, S. V.; Baxter, D.; Andersen, L. K.; Vassileva, C. G.; Morgan, T. J. An Overview of the Organic and Inorganic Phase Composition of Biomass. *Fuel* **2012**, *94*, 1–33.

(10) Corma Canos, A.; Iborra, S.; Velty, A. Chemical Routes for the Transformation of Biomass into Chemicals. *Chem. Rev.* **2007**, *107*, 2411–2502.

(11) Ruppert, A. M.; Weinberg, K.; Palkovits, R. Hydrogenolysis Goes Bio: From Carbohydrates and Sugar Alcohols to Platform Chemicals. *Angew. Chemie - Int. Ed.* **2012**,

51, 2564–2601.

(12) Vennestrøm, P. N. R.; Osmundsen, C. M.; Christensen, C. H.; Taarning, E. Beyond Petrochemicals: The Renewable Chemicals Industry. *Angew. Chemie - Int. Ed.* **2011**, *50*, 10502–10509.

(13) Anastas, P. T.; Kirchhoff, M. M.; Williamson, T. C. Catalysis as a Foundational Pillar of Green Chemistry. *Appl. Catal. A Gen.* **2001**, *221*, 3–13.

(14) James, D. H.; Castor, W. M. *Styrene in Ullman's Encyclopedia of Industrial Chemistry*; 2011.

(15) Dreher, E.-L.; Beutel, K. K.; Myers, J. D.; Lübbe, T.; Krieger, S.; Pottenger, L. H. *Chloroethanes and Chloroethylenes in Ullman's Encyclopedia of Industrial Chemistry*; 2014.

(16) Zimmermann, H. *Propene in Ullman's Encyclopedia of Industrial Chemistry*; 2013.

(17) Zimmermann, H.; Walzl, R. *Ethylene in Ullman's Encyclopedia of Industrial Chemistry*; 2009.

(18) Pässler, P.; Hefner, W.; Buckl, K.; Meinass, H.; Meiswinkel, A.; Wernicke, H.-J.; Ebersberg, G.; Müller, R.; Bässler, J.; Behringer, H.; et al. *Acetylene in Ullman's Encyclopedia of Industrial Chemistry*; 2011.

(19) Morschbacker, A. Bio-Ethanol Based Ethylene. *J. Macromol. Sci. Part C Polym. Rev.* **2009**, *49*, 79–84.

(20) Rasselet, D.; Ruellan, a.; Guinault, a.; Miquelard-Garnier, G.; Sollogoub, C.; Fayolle, B. Oxidative Degradation of Polylactide (PLA) and Its Effects on Physical and Mechanical Properties. *Eur. Polym. J.* **2014**, *50*, 109–116.

(21) Rebsdat, S.; Mayer, D. *Ethylene Glycol in Ullman's Encyclopedia of Industrial Chemistry*; 2000.

(22) Sheehan, R. J. *Terephthalic Acid, Dimethyl Terephthalate, and Isophthalic Acid in Ullman's Encyclopedia of Industrial Chemistry*; 2011.

(23) Ji, N.; Zhang, T.; Zheng, M.; Wang, A.; Wang, H.; Wang, X.; Chen, J. G. Direct Catalytic Conversion of Cellulose into Ethylene Glycol Using Nickel-Promoted Tungsten Carbide Catalysts. *Angew. Chemie* **2008**, *120*, 8638–8641.

(24) Gopalakrishnan, P.; Narayan-Sarathy, S.; Ghosh, T.; Mahajan, K.; Belgacem, M. N.

Synthesis and Characterization of Bio-Based Furanic Polyesters. *J. Polym. Res.* **2014**, *21*, 340–348.

(25) Corey, E. J.; Winter, R. A. E. A New, Stereospecific Olefin Synthesis from 1,2-Diols. *J. Am. Chem. Soc.* **1963**, *85*, 2677–2678.

(26) Cook, G. K.; Andrews, M. A. Toward Nonoxidative Routes to Oxygenated Organics: Stereospecific Deoxydehydration of Diols and Polyols to Alkenes and Allylic Alcohols Catalyzed by the Metal Oxo Complex (C 5 Me 5)ReO 3. *J. Am. Chem. Soc.* **1996**, *118*, 9448–9449.

(27) Ziegler, J. E.; Zdilla, M. J.; Evans, A. J.; Abu-Omar, M. M. H2-Driven Deoxygenation of Epoxides and Diols to Alkenes Catalyzed by Methyltrioxorhenium. *Inorg. Chem.* **2009**, *48*, 9998–10000.

(28) Vkuturi, S.; Chapman, G.; Ahmad, I.; Nicholas, K. M. Rhenium-Catalyzed Deoxydehydration of Glycols by Sulfite. *Inorg. Chem.* **2010**, *49*, 4744–4746.

(29) Arceo, E.; Ellman, J. A.; Bergman, R. G. Rhenium-Catalyzed Didehydroxylation of Vicinal Dials to Alkenes Using a Simple Alcohol as a Reducing Agent. *J. Am. Chem. Soc.* **2010**, *132*, 11408–11409.

(30) Shiramizu, M.; Toste, F. D. Deoxygenation of Biomass-Derived Feedstocks: Oxorhenium-Catalyzed Deoxydehydration of Sugars and Sugar Alcohols. *Angew. Chem. Int. Ed.* **2012**, *51*, 8082–8086.

(31) Raju, S.; Jastrzebski, J. T. B. H.; Lutz, M.; Klein Gebbink, R. J. M. Catalytic Deoxydehydration of Diols to Olefins by Using a Bulky Cyclopentadiene-Based Trioxorhenium Catalyst. *ChemSusChem* **2013**, *6*, 1673–1680.

(32) *U.S. Geological Survey, 2018, Mineral Commodity Summaries 2018: U.S. Geological Survey, 134 P., https://doi.org/10.3133/70194932*.

(33) Chapman, G.; Nicholas, K. M. Vanadium-Catalyzed Deoxydehydration of Glycols. *Chem. Commun. (Camb).* **2013**, *49*, 8199–8201.

(34) Gopaladasu, T. V.; Nicholas, K. M. Carbon Monoxide (CO)- and Hydrogen-Driven, Vanadium-Catalyzed Deoxydehydration of Glycols. *ACS Catal.* **2016**, *6*, 1901–1904.

(35) *U.S. Geological Survey, 2018, Mineral Commodity Summaries 2018: U.S. Geological Survey, 180 P., https://doi.org/10.3133/70194932*.

(36) Dethlefsen, J. R.; Fristrup, P. In Situ Spectroscopic Investigation of the Rhenium-Catalyzed Deoxydehydration of Vicinal Diols. *ChemCatChem* **2015**, *7*, 1184–1196.

(37) Wu, D.; Zhang, Y.; Su, H. Mechanistic Study on Oxorhenium-Catalyzed Deoxydehydration and Allylic Alcohol Isomerization. *Chem. - An Asian J.* **2016**, *11*, 1565–1571.

(38) Liu, S.; Senocak, A.; Smeltz, J. L.; Yang, L.; Wegenhart, B.; Yi, J.; Kenttämaa, H. I.; Ison, E. A.; Abu-Omar, M. M. Mechanism of MTO-Catalyzed Deoxydehydration of Diols to Alkenes Using Sacrificial Alcohols. *Organometallics* **2013**, *32*, 3210–3219.

(39) Dethlefsen, J. R.; Lupp, D.; Teshome, A.; Nielsen, L. B.; Fristrup, P. Molybdenum-Catalyzed Conversion of Diols and Biomass-Derived Polyols to Alkenes Using Isopropyl Alcohol as Reductant and Solvent. *ACS Catal.* **2015**, 3638–3647.

(40) Lupp, D.; Christensen, N. J.; Dethlefsen, J. R.; Fristrup, P. DFT Study of the Molybdenum-Catalyzed Deoxydehydration of Vicinal Diols. *Chem. - A Eur. J.* **2015**, *21*, 3435–3442.

(41) Dethlefsen, J. R.; Lupp, D.; Oh, B. C.; Fristrup, P. Molybdenum-Catalyzed Deoxydehydration of Vicinal Diols. *ChemSusChem* **2014**, *7*, 425–428.

(42) *U.S. Geological Survey, 2018, Mineral Commodity Summaries 2018: U.S. Geological Survey, 110 P., https://doi.org/10.3133/70194932*.

(43) Kohn, W. Electronic Structure of Matter - Wave Functions and Density Functionals. *Nobel Lect. Chem.* **1999**, 213–237.

(44) Koch, W.; Holthausen, Max, C. A Chemist's Guide to Density Functional Theory; Wiley-VCH Verlag GmbH: Weinheim, Germany, 2001; pp 1–89.

(45) Engel, T. Quantum Chemistry & Spectroscopy; Jaworski, A., Ed.; Pearson: Glenview, IL, USA, 2013; pp 1–49, 339–382.

(46) Schrödinger, E. Quantisierung Als Eigenwertproblem. *Ann. Phys.* **1926**, *13*, 437–490.

(47) Atkins, P.; Paula, J. De. Atkins' Physical Chemistry; Oxford University Press: Oxford, New York, 2010; pp 249–287.

(48) Heisenberg, W. Über Den Anschaulichen Inhalt Der Quantentheoretischen Kinematik Und Mechanik. *Zeitschrift für Phys.* **1927**, 172–198.

(49) Born, M.; Oppenheimer, R. Zur Quantentheorie Der Molekeln. *Ann. Phys.* **1927**, *20*, 457–484.

(50) Hartree, D. R. The Wave Mechanics of an Atom with a Non-Coulomb Central Field.Part I. Theory and Methods. *Math. Proc. Cambridge Philos. Soc.* **1928**, *24*, 89–110.

(51) Thomas, L. H. The Calculation of Atomic Fields. *Math. Proc. Cambridge Philos. Soc.* **1926**, 542–548.

(52) Hohenberg, P.; Kohn, W. Inhomogeneous Electron Gas. *Phys. Rev.* **1964**, *136*, B864–B871.

(53) Kohn, W.; Sham, L. J. Self-Consistent Equations Including Exchange and Correlation Effects. *Phys. Rev.* **1965**, *140*.

(54) Becke, A. D. Densityfunctional Thermochemistry . III . The Role of Exact Exchange. *J. Chem. Phys* **1993**, *98*, 5648–5652.

(55) Becke, A. D. A New Mixing of Hartree-Fock and Local Density-Functional Theories. *J. Chem. Phys* **1993**, *98*, 1372–1377.

(56) Ditchfield, R.; Hehre, W. J.; Pople, J. A. Self-Consistent Molecular-Orbital Methods. IX. An Extended Gaussian-Type Basis for Molecular-Orbital Studies of Organic Molecules. *J. Chem. Phys.* **1971**, *54*, 724–728.

(57) Hay, P. J.; Wedt, W. R. Ab Initio Effective Core Potentials for Molecular Calculations. Potentials of K to Au Including the Outermost Core Orbitals. *J. Chem. Phys* **1985**, *82*, 299–310.

(58) Li, X.; Wu, D.; Lu, T.; Yi, G.; Su, H.; Zhang, Y. Highly Efficient Chemical Process to Convert Mucic Acid into Adipic Acid and DFT Studies of the Mechanism of the Rhenium-Catalyzed Deoxydehydration. *Angew. Chem. Int. Ed. Engl.* **2014**, *53*, 4200–4204.

(59) Bochevarov, A. D.; Harder, E.; Hughes, T. F.; Greenwood, J. R.; Braden, D. a.; Philipp, D. M.; Rinaldo, D.; Halls, M. D.; Zhang, J.; Friesner, R. a. Jaguar: A High-Performance Quantum Chemistry Software Program with Strengths in Life and Materials Sciences. *Int. J. Quantum Chem.* **2013**, *113*, 2110–2142.

(60) Schrödinger Release 2015-4: Jaguar, Version 9.0, Schrödinger, LLC, New York, NY, 2015.

(61) Schrödinger Release 2015-4: Maestro, Version 10.4, Schrödinger, LLC, New York, NY, 2015.

(62) Halgren, T. a.; Lipscomb, W. N. The Synchronous-Transit Method for Determining Reaction Pathways and Locating Molecular Transition States. *Chem. Phys. Lett.* **1977**, *49*,

225–232.

(63) Tannor, D. J.; Marten, B.; Murphy, R.; Friesner, R. a.; Sitkoff, D.; Nicholls, A.; Honig, B.; Ringnalda, M.; Goddard, W. a. Accurate First Principles Calculation of Molecular Charge Distributions and Solvation Energies from Ab Initio Quantum Mechanics and Continuum Dielectric Theory. *J. Am. Chem. Soc.* **1994**, *116*, 11875–11882.

(64) Marten, B.; Kim, K.; Cortis, C.; Friesner, R. a; Murphy, R. B.; Ringnalda, M. N.; Sitkoff, D.; Honig, B. New Model for Calculation of Solvation Free Energies : Correction of Self-Consistent Reaction Field Continuum Dielectric Theory for Short-Range Hydrogen-Bonding Effects. *J. Phys. Chem.* **1996**, *100*, 11775–11788.

(65) CYLview, 1.0b; Legault, C. Y., Université de Sherbrooke, 2009 (Http://www.cylview.org).

(66) Petersen, A. R.; Nielsen, L. B.; Dethlefsen, J. R.; Fristrup, P. Vanadium-Catalysed Deoxydehydration of Glycerol Without an External Reductant. *ChemCatChem* **2017**, 769–778.

(67) Yi, J.; Liu, S.; Abu-Omar, M. M. Rhenium-Catalyzed Transfer Hydrogenation and Deoxygenation of Biomass-Derived Polyols to Small and Useful Organics. *ChemSusChem* **2012**, *5*, 1401–1404.

(68) Canale, V.; Tonucci, L.; Bressan, M.; d'Alessandro, N. Deoxydehydration of Glycerol to Allyl Alcohol Catalyzed by Rhenium Derivatives. *Catal. Sci. Technol.* **2014**, *4*, 3697–3704.

(69) Gandini, A. Monomers and Macromonomers from Renewable Resources. In *Biocatalysis in Polymer Chemistry*; Loos, K., Ed.; Wiley-VCH Verlag GmbH & Co. KGaA, 2010; pp 1–33.

(70) Boucher-Jacobs, C.; Nicholas, K. M. Oxo-Rhenium-Catalyzed Deoxydehydration of Polyols with Hydroaromatic Reductants. *Organometallics* **2015**, *34*, 1985–1990.

(71) Boucher-Jacobs, C.; Nicholas, K. M. Catalytic Deoxydehydration of Glycols with Alcohol Reductants. *ChemSusChem* **2013**, *6*, 597–599.

(72) Raju, S.; Jastrzebski, J. T. B. H.; Lutz, M.; Witteman, L.; Dethlefsen, J. R.; Fristrup, P.; Moret, M.-E.; Gebbink, R. J. M. K. Spectroscopic Characterization of a Monomeric, Cyclopentadienyl-Based Rhenium(V) Dioxo Complex. *Inorg. Chem.* **2015**, *54*, 11031–11036.

(73) Wu, D.; Zhang, Y.; Su, H. Mechanism of Oxorhenium-Catalyzed Deoxydehydration and

Allylic Alcohol Isomerization. *Chem. - An Asian J.* **2016**, *11*, 1565–1571.

(74) Stanowski, S.; Nicholas, K. M.; Srivastava, R. S. [Cp*Ru(CO) 2] 2 -Catalyzed Hydrodeoxygenation and Hydrocracking of Diols and Epoxides. *Organometallics* **2012**, *31*, 515–518.

(75) Ota, N.; Tamura, M.; Nakagawa, Y.; Okumura, K.; Tomishige, K. Hydrodeoxygenation of Vicinal OH Groups over Heterogeneous Rhenium Catalyst Promoted by Palladium and Ceria Support. *Angew. Chem. Int. Ed. Engl.* **2015**, *54*, 1897–1900.

(76) Corma, A.; de la Torre, O.; Renz, M.; Villandier, N. Production of High-Quality Diesel from Biomass Waste Products. *Angew. Chem. Int. Ed. Engl.* **2011**, *50*, 2375–2378.

(77) Sutton, A. D.; Waldie, F. D.; Wu, R.; Schlaf, M.; 'Pete'Silks, L. A.; Gordon, J. C. The Hydrodeoxygenation of Bioderived Furans into Alkanes. *Nat. Chem.* **2013**, *5*, 428–432.

(78) Larsen, D. B.; Petersen, A. R.; Dethlefsen, J. R.; Teshome, A.; Fristrup, P. Mechanistic Investigation of Molybdate-Catalysed Transfer Hydrodeoxygenation. *Chem. - A Eur. J.* **2016**, *22*, 16621–16631.

(79) Lupp, D.; Christensen, N. J.; Fristrup, P. Synergy between Experimental and Theoretical Methods in the Exploration of Homogeneous Transition Metal Catalysis. *Dalton Trans.* **2014**, *43*, 11093–11105.

(80) Joshi, V. S.; Kale, V. K.; Sathe, K. M.; Sarkar, a; Tavale, S. S.; Suresh, C. G. Synthesis and Structure of New Molybdenum Pi-Allyl Complexes - Unexpected Hydrolysis of Tris(3,5-Dimethyl-1-Pyrazolyl)Phosphine Oxide. *Organometallics* **1991**, *10*, 2898–2902.

(81) Lin, S.; Lee, G.; Peng, S.-M.; Liu, R.-S. Molybdenum-Pi-Allyl Compounds for Chemoselective Synthesis of Tetrahydrofurans, Cis-1,3-Dienes, Cis-Hexatrienes, and Isoxazole Compounds. *Organometallics* **1993**, *12*, 2591–2599.

(82) Trost, B. M.; Czabaniuk, L. C. Structure and Reactivity of Late Transition Metal H^3-Benzyl Complexes. *Angew. Chem. Int. Ed. Engl.* **2014**, *53*, 2826–2851.

(83) King, R. B.; Fronzaglia, A. Organometallic Chemistry of the Transition Metals. XIII. A π-Benzyl Derivative of Molybdenum with a Temperature-Dependent Proton Nuclear Magnetic Resonance Spectrum. *J. Am. Chem. Soc.* **1966**, *88*, 709–712.

(84) Cotton, F. A.; LaPrade, M. D. Stereochemically Nonrigid Organometallic Molecules. XVI. The Crystal and Molecular Structure of P-Methyl- π Benzyl-π-

Cyclopentadienyldicarbonylmolybdenum. *J. Am. Chem. Soc.* **1968**, *90*, 5418–5422.

(85) Trost, B. M.; Van Vranken, D. L. Asymmetric Transition Metal-Catalyzed Allylic Alkylations. *Chem. Rev.* **1996**, *96*, 395–422.

(86) Clayden, J.; Greeves, N.; Warren, S. Organic Chemistry; Oxford University Press: Oxford, New York, 2012; pp 917–919.

(87) Cohen, R.; Graves, C. R.; Nguyen, S. T.; Martin, J. M. L.; Ratner, M. a. The Mechanism of Aluminum-Catalyzed Meerwein-Schmidt-Ponndorf-Verley Reduction of Carbonyls to Alcohols. *J. Am. Chem. Soc.* **2004**, *126*, 14796–14803.

(88) Kozuch, S. A Refinement of Everyday Thinking: The Energetic Span Model for Kinetic Assessment of Catalytic Cycles. *WIREs Comput Mol Sci* **2012**, *2*, 795–815.

(89) Mielby, J.; Riisager, A.; Fristrup, P.; Kegnæs, S. Mechanistic Investigation of the One-Pot Formation of Amides by Oxidative Coupling of Alcohols with Amines in Methanol. *Catal. Today* **2013**, *203*, 211–216.

(90) Dusselier, M.; Van Wouwe, P.; De Smet, S.; De Clercq, R.; Verbelen, L.; Van Puyvelde, P.; Du Prez, F. E.; Sels, B. F. Toward Functional Polyester Building Blocks from Renewable Glycolaldehyde with Sn Cascade Catalysis. *ACS Catal.* **2013**, *3*, 1786–1800.

(91) Elliot, S. G.; Andersen, C.; Tolborg, S.; Meier, S.; Sádaba, I.; Daugaard, A. E.; Taarning, E. Synthesis of a Novel Polyester Building Block from Pentoses by Tin-Containing Silicates. *RSC Adv.* **2017**, *7*, 985–996.

(92) Garlotta, D. A Literature Review of Poly (Lactic Acid). *J. Polym. Environ.* **2002**, *9*, 63–84.

(93) Trifol, J.; Plackett, D.; Sillard, C.; Szabo, P.; Bras, J.; Daugaard, A. E. Hybrid Poly(lactic Acid)/nanocellulose/nanoclay Composites with Synergistically Enhanced Barrier Properties and Improved Thermomechanical Resistance. *Polym. Int.* **2016**, *65*, 988–995.

(94) Trifol, J.; Plackett, D.; Sillard, C.; Hassager, O.; Daugaard, A. E.; Bras, J.; Szabo, P. A Comparison of Partially Acetylated Nanocellulose, Nanocrystalline Cellulose, and Nanoclay as Fillers for High-Performance Polylactide Nanocomposites. *J. Appl. Polym. Sci.* **2016**, *133*, 43257–43268.

(95) Zhang, H.; Grinstaff, M. W. Recent Advances in Glycerol Polymers: Chemistry and Biomedical Applications. *Macromol. Rapid Commun.* **2014**, *35*, 1906–1924.

(96) Nguyen, H.; Löf, D.; Hvilsted, S.; Daugaard, A. Highly Branched Bio-Based Unsaturated

Polyesters by Enzymatic Polymerization. *Polymers (Basel).* **2016**, *8*, 363–374.

(97) Jones, F. N. *Alkyd Resins in Ullman's Encyclopedia of Industrial Chemistry*; Wiley-VCH Verlag GmbH & Co. KGaA: Weinheim, Germany, 2003.

(98) Wicks, Z. W. *Alkyd Resins in Encyclopedia of Polymer Science*; John Wiley & Sons, Inc.: Weinheim, Germany, 2007.

(99) Holmberg, K. *Alkyd Resins in Coatings Technology Handbook*; Tracton, A. A., Ed.; CRC Press: Boca Raton, FL, USA, 2006.

(100) Rosatella, A. A.; Simeonov, S. P.; Frade, R. F. M.; Afonso, C. A. M. 5-Hydroxymethylfurfural (HMF) as a Building Block Platform: Biological Properties, Synthesis and Synthetic Applications. *Green Chem.* **2011**, *13*, 754.

(101) Belgacem, M. N.; Gandini, A. Monomers, Polymers and Composites from Renewable Resources; Elsevier: Amsterdam, 2008; pp 39–66.

(102) Boisen, A.; Christensen, T. B.; Fu, W.; Gorbanev, Y. Y.; Hansen, T. S.; Jensen, J. S.; Klitgaard, S. K.; Pedersen, S.; Riisager, A.; Ståhlberg, T.; et al. Process Integration for the Conversion of Glucose to 2,5-Furandicarboxylic Acid. *Chem. Eng. Res. Des.* **2009**, *87*, 1318–1327.

(103) Moreau, C.; Belgacem, M. N.; Gandini, A. Recent Catalytic Advances in the Chemistry of Substituted Furans from Carbohydrates and in the Ensuing Polymers. *Top. Catal.* **2004**, *27*, 11–30.

(104) Ståhlberg, T.; Rodriguez-Rodriguez, S.; Fristrup, P.; Riisager, A. Metal-Free Dehydration of Glucose to 5-(Hydroxymethyl)furfural in Ionic Liquids with Boric Acid as a Promoter. *Chem. - A Eur. J.* **2011**, *17*, 1456–1464.

(105) Ait Rass, H.; Essayem, N.; Besson, M. Selective Aerobic Oxidation of 5-HMF into 2,5-Furandicarboxylic Acid with Pt Catalysts Supported on TiO 2 - and ZrO 2 -Based Supports. *ChemSusChem* **2015**, *8*, 1206–1217.

(106) Hansen, T. S.; Sádaba, I.; García-Suárez, E. J.; Riisager, A. Cu Catalyzed Oxidation of 5-Hydroxymethylfurfural to 2,5-Diformylfuran and 2,5-Furandicarboxylic Acid under Benign Reaction Conditions. *Appl. Catal. A Gen.* **2013**, *456*, 44–50.

(107) Eerhart, A. J. J. E.; Faaij, A. P. C.; Patel, M. K. Replacing Fossil Based PET with Biobased PEF; Process Analysis, Energy and GHG Balance. *Energy Environ. Sci.* **2012**, *5*, 6407–6422.

(108) Tomás, R. A. F.; Bordado, J. C. M.; Gomes, J. F. P. P-Xylene Oxidation to Terephthalic Acid : A Literature Review Oriented toward Process Optimization and Development. *Chem. Rev.* **2013**, *113*, 7421–7469.

(109) Krähling, L.; Krey, J.; Jakobson, G.; Grolig, J.; Miksche, L. *Allyl Compounds. In Ullman's Encyclopedia of Industrial Chemistry*; Wiley-VCH, 2012.

(110) Carcinogenesis Bioassay of Diallyl Phthalate in B6C3F1 MICE, U.S. Department of Health and Human Services, 1983.

(111) Hoyle, C. E.; Lee, T. Y.; Roper, T. Thiol-Enes: Chemistry of the Past with Promise for the Future. *J. Polym. Sci. Part A Polym. Chem.* **2004**, *42*, 5301–5338.

(112) Lowe, A. B. Thiol-Ene "click" Reactions and Recent Applications in Polymer and Materials Synthesis. *Polym. Chem.* **2010**, *1*, 17–36.

(113) Posner, T. Beiträge Zur Kenntniss Der Ungesättigten Verbindungen. II. Ueber Die Addition von Mercaptanen an Ungesättigte Kohlenwasserstoffe. *Ber. Dtsch. Chem. Ges.* **1905**, *38*, 646–657.

(114) Morgan, C. R.; Magnotta, F.; Ketley, a. D. Thiol/ene Photocurable Polymers. *J. Polym. Sci. Polym. Chem. Ed.* **1977**, *15*, 627–645.

(115) Fouassier, J.-P.; Rabek, J. F. *Radiation Curing in Polymer Science and Technology*, 1st ed.; Springer Netherlands, 1993.

(116) Carlborg, C. F.; Haraldsson, T.; Öberg, K.; Malkoch, M.; van der Wijngaart, W. Beyond PDMS: Off-Stoichiometry Thiol–ene (OSTE) Based Soft Lithography for Rapid Prototyping of Microfluidic Devices. *Lab Chip* **2011**, 3136–3147.

(117) Hoffmann, C.; Pinelo, M.; Woodley, J. M.; Daugaard, A. E. Development of a Thiol-Ene Based Screening Platform for Enzyme Immobilization Demonstrated Using Horseradish Peroxidase. *Biotechnol. Prog.* **2017**, *33*, 1267–1277.

(118) Lafleur, J. P.; Senkbeil, S.; Novotny, J.; Nys, G.; Bøgelund, N.; Rand, K. D.; Foret, F.; Kutter, J. P. Rapid and Simple Preparation of Thiol-Ene Emulsion-Templated Monoliths and Their Application as Enzymatic Microreactors. *Lab Chip* **2015**, *15*, 2162–2172.

(119) Mazurek, P.; Daugaard, A. E.; Skolimowski, M.; Hvilsted, S.; Skov, A. L. Preparing Mono-Dispersed Liquid Core PDMS Microcapsules from Thiol–ene–epoxy-Tailored Flow-Focusing Microfluidic Devices. *RSC Adv.* **2015**, *5*, 15379–15386.

(120) Durham, O. Z.; Norton, H. R.; Shipp, D. A. Functional Polymer Particles via Thiol–ene and Thiol–yne Suspension “click” Polymerization. *RSC Adv.* **2015**, *5*, 66757–66766.

(121) Lu, H.; Carioscia, J. A.; Stansbury, J. W.; Bowman, C. N. Investigations of Step-Growth Thiol-Ene Polymerizations for Novel Dental Restoratives. *Dent. Mater.* **2005**, *21*, 1129–1136.

(122) Andrisano, R. Ultraviolet Spectra of Some Furandicarboxylic Derivatives. *Gazz. Chim. Ital.* **1951**, *81*, 414–418.

(123) Clayden, J.; Greeves, N.; Warren, S. Organic Chemistry; Oxford University Press: Oxford, New York, 2012; pp 877–896.

(124) Shen, X.; Liu, X.; Wang, J.; Dai, J.; Zhu, J. Synthesis of an Epoxy Monomer from Bio-Based 2,5-Furandimethanol and Its Toughening via Diels-Alder Reaction. *Ind. Eng. Chem. Res.* **2017**, *56*, 8508–8516.

(125) Pacheco, J. J.; Davis, M. E. Synthesis of Terephthalic Acid via Diels-Alder Reactions with Ethylene and Oxidized Variants of 5-Hydroxymethylfurfural. *Proc. Natl. Acad. Sci.* **2014**, *111*, 8363–8367.

(126) Matsumoto, A.; Oiwa, M. Studies of the Polymerization of Diallyl Compounds. XXV. Gel Point in the Polymerization of Diallyl Esters of Aromatic Dicarboxylic Acids. *J. Polym. …* **1970**, *8*, 751–762.

(127) Nguyen, H. D.; Löf, D.; Hvilsted, S.; Daugaard, A. E. Highly Branched Bio-Based Unsaturated Polyesters by Enzymatic Polymerization. *Polymers (Basel).* **2016**, *8*, 1–12.

(128) Odian, G. Principles of Polymerization; John Wiley & Sons, Inc.: Hoboken, New Jersey, 2004; pp 103–112.

(129) Hawker, C. J.; Lee, R.; Frécnet, J. M. J. One-Step Synthesis of Hyperbranched Dendritic Polyesters. *J. Am. Chem. Soc.* **1991**, *113*, 4583–4588.

(130) Hölter, D.; Burgath, A.; Frey, H. Degree of Branching in Hyperbranched Polymers. *Acta Polym.* **1997**, *48*, 30–35.

(131) De Luca, E.; Richards, R. W. Molecular Characterization of a Hyperbranched Polyester. I. Dilute Solution Properties. *J. Polym. Sci. Part B Polym. Phys.* **2003**, *41*, 1339–1351.

(132) Zhu, X.; Chen, L.; Chen, Y.; Yan, D. Using 2D NMR to Determine the Degree of Branching of Complicated Hyperbranched Polymers. *Sci China Ser B-Chem* **2008**, *51*, 1057–1065.

(133) Borchardt, H. J.; Daniels, F. The Application of Differential Thermal Analysis to the Study of Reaction Kinetics. *J. Am. Chem. Soc.* **1957**, *79*, 41–46.

(134) ASTM E2041-13e1 Standard Test Method for Estimating Kinetic Parameters by Differential Scanning Calorimeter Using the Borchardt and Daniels Method, ASTM International, West Conshohocken, PA, 2013, https://doi.org/10.1520/E2041.

(135) Atkins, P.; Paula, J. De. Atkins' Physical Chemistry; Oxford University Press: Oxford, 2010; pp 799–802.

(136) Deng, J.; Liu, X.; Li, C.; Jiang, Y.; Zhu, J. Synthesis and Properties of a Bio-Based Epoxy Resin from 2,5-Furandicarboxylic Acid (FDCA). *RSC Adv.* **2015**, *5*, 15930–15939.

(137) Hu, F.; La Scala, J. J.; Sadler, J. M.; Palmese, G. R. Synthesis and Characterization of Thermosetting Furan-Based Epoxy Systems. *Macromolecules* **2014**, *47*, 3332–3342.

(138) Yang, J. H.; Srikanth, A.; Jang, C.; Abrams, C. F. Relationships between Molecular Structure and Thermomechanical Properties of Bio-Based Thermosetting Polymers. *J. Polym. Sci. Part B Polym. Phys.* **2017**, *55*, 285–292.

(139) Montero De Espinosa, L.; Meier, M. A. R. Plant Oils: The Perfect Renewable Resource for Polymer Science?! *Eur. Polym. J.* **2011**, *47*, 837–852.

(140) Meier, M. A. R.; Metzger, J. O.; Schubert, U. S. Plant Oil Renewable Resources as Green Alternatives in Polymer Science. *Chem. Soc. Rev.* **2007**, *36*, 1788–1802.

(141) Kienle, R. H.; van der Meulen, P. A.; Petke, F. E. The Polyhydric Alcohol-Polybasic Acid Reaction. I. Further Studies of the Glycerol-Phthalic Anhydride. *J. Am. Chem. Soc.* **1929**, *51*, 509–519.

(142) Kienle, R. H.; Ferguson, C. S. Alkyd Resins as Film-Forming Materials. *Ind. Eng. Chem.* **1929**, *21*, 349–352.

(143) Stenberg, C.; Svensson, M.; Johansson, M. A Study of the Drying of Linseed Oils with Different Fatty Acid Patterns Using RTIR-Spectroscopy and Chemiluminescence (CL). *Ind. Crops Prod.* **2005**, *21*, 263–272.

(144) Gall, R. J.; Greenspan, F. P. A Modified Peracid Process for Making Epoxy Compounds from Unsaturated Fatty Acid Esters. *Ind. Eng. Chem.* **1955**, *47*, 147–148.

(145) Aouf, C.; Durand, E.; Lecomte, J.; Figueroa-Espinoza, M.-C.; Dubreucq, E.; Fulcrand, H.; Villeneuve, P. The Use of Lipases as Biocatalysts for the Epoxidation of Fatty Acids and

Phenolic Compounds. *Green Chem.* **2014**, *16*, 1740–1754.

(146) Skouridou, V.; Stamatis, H.; Kolisis, F. N. Lipase-Mediated Epoxidation of α-Pinene. *J. Mol. Catal. B Enzym.* **2003**, *21*, 67–69.

(147) Tang, Q.; Popowicz, G. M.; Wang, X.; Liu, J.; Pavlidis, I. V.; Wang, Y. Lipase-Driven Epoxidation Is A Two-Stage Synergistic Process. *ChemistrySelect* **2016**, *1*, 836–839.

(148) Xu, Y.; Khaw, N. R. B. J.; Li, Z. Efficient Epoxidation of Alkenes with Hydrogen Peroxide, Lactone, and Lipase. *Green Chem.* **2009**, *11*, 2047.

(149) Schumann, K.; Siekmann, K. *Soaps in Ullman's Encyclopedia of Industrial Chemistry*; 2000.

(150) Sienel, G.; Rieth, R.; Rowbottom, K. T. *Epoxides in Ullman's Encyclopedia of Industrial Chemistry*; 2000.

(151) Crivello, J. V.; Lam, J. H. W. Diaryliodonium Salts. A New Class of Photoinitiators for Cationic Polymerization. *Macromolecules* **1977**, *10*, 1307–1315.

(152) Crivello, J. V.; Lam, J. H. W. Photoinitiated Cationic Polymerization with Triarylsulfonium Salts. *J. Polym. Sci.* **1979**, *17*, 977–999.

(153) Michaudel, Q.; Kottisch, V.; Fors, B. P. Cationic Polymerization: From Photoinitiation to Photocontrol. *Angew. Chem. Int. Ed.* **2017**, *56*, 9670–9679.

(154) Decker, C.; Nguyen Thi Viet, T.; Pham Thi, H. Photoinitiated Cationic Polymerization of Epoxides. *Polym. Int.* **2001**, *50*, 986–997.

(155) Crivello, J. V. Cationic Polymerization - Iodonium and Sulfonium Salt Photoinitiators. *Adv. Polym. Sci.* **1984**, *62*, 1–48.

(156) Deng, J.; Liu, X.; Li, C.; Jiang, Y.; Zhu, J. Synthesis and Properties of a Bio-Based Epoxy Resin from 2,5-Furandicarboxylic Acid (FDCA). *RSC Adv.* **2015**, *5*, 15930–15939.

(157) Nameer, S.; Johansson, M. Fully Bio-Based Aliphatic Thermoset Polyesters via Self-Catalyzed Self-Condensation of Multifunctional Epoxy Monomers Directly Extracted from Natural Sources. *J. Coatings Technol. Res.* **2017**, *14*, 757–765.

(158) Jiang, Y. Y.; Jiang, J. L.; Fu, Y. Mechanism of Vanadium-Catalyzed Deoxydehydration of Vicinal Diols: Spin-Crossover-Involved Processes. *Organometallics* **2016**, *35*, 3388–3396.

(159) De Vicente Poutás, L. C.; Castiñeira Reis, M.; Sanz, R.; López, C. S.; Faza, O. N. A Radical

Mechanism for the Vanadium-Catalyzed Deoxydehydration of Glycols. *Inorg. Chem.* **2016**, *55*, 11372–11382.

6 Appendices

Appendix A: Script for data extraction from .mae and .xyz files

Due to the unintuitive nature of the native files of the Maestro program (*.mae), this bash script is made to extract data and print required values and coordinates for compiling supporting information. The script uses the *.mae file for data and requires an *.xyz file for coordinates (same filename as the *.mae file).

```
#!/bin/bash
#print file name
echo "$1" > Supp_$1.txt
sed -i 's/.mae//g' Supp_$1.txt
#find line number were properties start
npropstart=`grep -n ":::" $1 |cut -f1 -d: | head -2 | tail -1`
#Extract Escf (gas)
nGasname=`grep -n "Gas" $1 |cut -f1 -d: | head -1`
nGasdata=`expr $npropstart + $nGasname - 7`
VAR1=`sed -n "$nGasdata"p $1`
echo "Escf (Gas):$VAR1 Hartree" >> Supp_$1.txt
#Extract Escf (Solv)
nSolvname=`grep -n "Solution_Phase_Energy" $1 |cut -f1 -d: | head -1`
nSolvdata=`expr $npropstart + $nSolvname - 7`
VAR2=`sed -n "$nSolvdata"p $1`
echo "Escf (Solv):$VAR2 Hartree" >> Supp_$1.txt
#Extract Gibbs at RT
nGibsRTname=`grep -n "Total_Free_Energy_at_298" $1 |cut -f1 -d: | head -1`
nGibsRTdata=`expr $npropstart + $nGibsRTname - 7`
VAR3=`sed -n "$nGibsRTdata"p $1`
echo "Total Gibbs Free Energy at 298.15 K:$VAR3 Hartree" >> Supp_$1.txt
#Extract Cartesian Coordinates to xyztemp file
echo "Cartesian Coordinates:" >> Supp_$1.txt
echo "$1" > temp1
sed -i 's/.mae/.xyz/g' temp1
xyz=`grep 'xyz' temp1`
rm temp1
sed '1,2d' $xyz >> xyztemp
cat xyztemp | sort > xyztemp2
cat xyztemp2 >> Supp_$1.txt
rename s/.mae// Supp_$1.txt
rm xyztemp
rm xyztemp2
#keywords
#Total_Free_Energy_at_298.15K_(au)
#Solution_Phase_Energy
#Gas_Phase_Energy
```

Appendix B: Calculation examples for molecular weights from NMR

BPE1 type system

Below is given a random molecule similar to system BPE1:

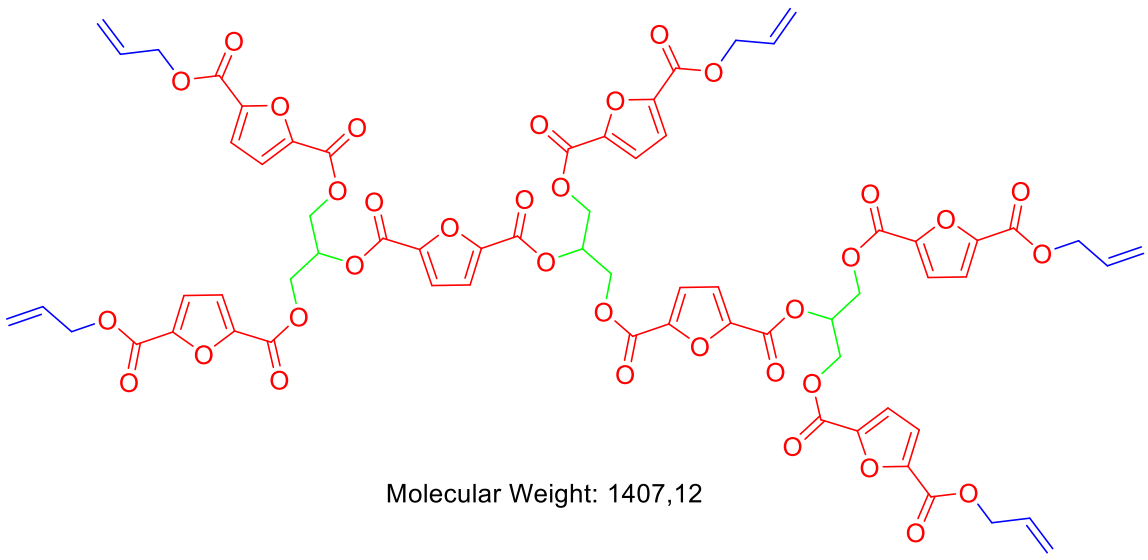

This molecule has an relative Allyl:Furane:Glycerol ratio of 1 : 1.4 : 0.6 and the absolute ratios is sought. Using Equations 17 and 18, two values for k can be obtained:

$$k = \frac{1}{n_{B_2} - 2 * n_{A_3}} = \frac{1}{1.4 - 2 * 0.6} = 5$$

$$k = \frac{2}{n_{A_1} - n_{A_3}} = \frac{2}{1 - 0.6} = 5$$

The values for k are completely identical due to this being an ideal system. Using equation 13 the molecular weight of the molecule can be obtained which is identical to the actual weight shown in the figure.

$$\overline{M_n} = \sum k * n_x * M_x = 5 * 1 * 41.07 + 5 * 1.4 * 154.08 + 5 * 0.6 * 41.07 = 1407.12 \frac{g}{mol}$$

BPE2-5 Type Systems

Below is shown a molecule similar to the one before, with some Ethylene Glycol units added, similar to systems BPE2-5:

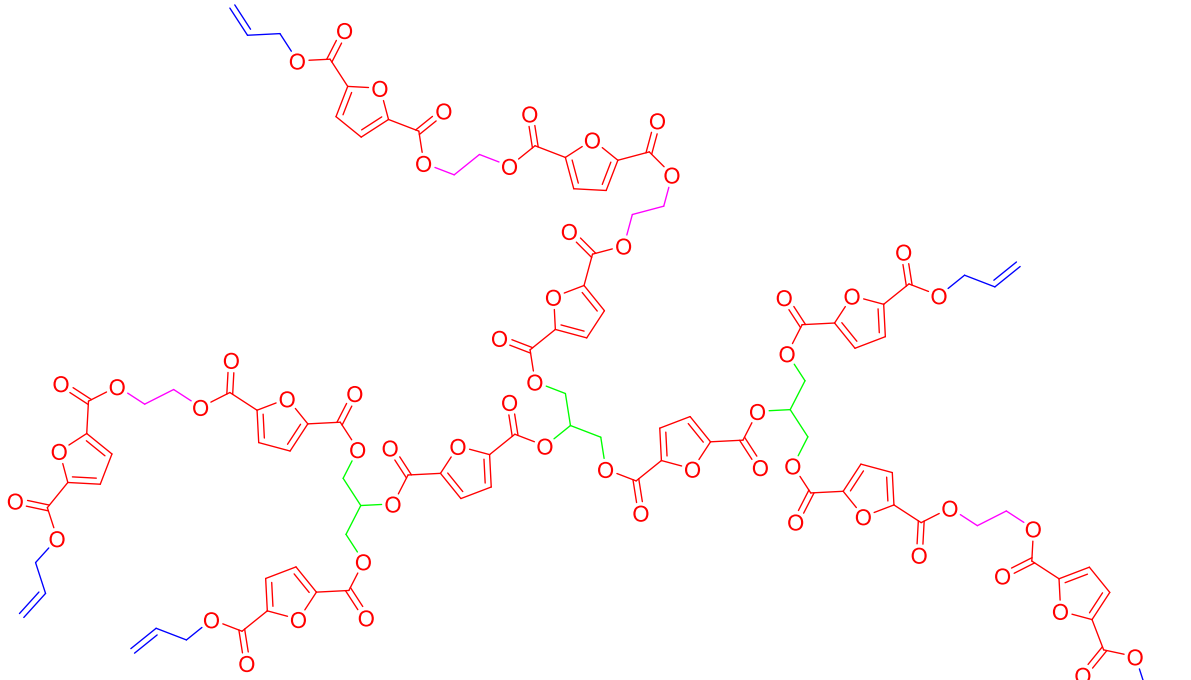

This molecule has an relative Allyl:Furane:Glycerol:Ethylene Glycol ratio of $1 : 2.2 : 0.6 : 0.8$ and again, the absolute ratios is sought. Using Equations 17 and 22, two values for k can be obtained:

$$k = \frac{2}{n_{A_1} - n_{A_3}} = \frac{2}{1 - 0.6} = 5$$

$$k = \frac{1}{n_{B_2} - 2 * n_{A_3} - n_{A_2}} = \frac{1}{2.2 - 2 * 0.6 - 0.8} = 5$$

The values for k are again completely identical due to this being an ideal system. Using equation 13 the molecular weight of the molecule can be obtained which is identical to the actual weight shown in the figure.

$$\overline{M_n} = \sum k * n_x * M_x =$$

$$5 * 1 * 41.07 + 5 * 2.2 * 154.08 + 5 * 0.6 * 41.07 + 5 * 0.8 * 28.05 = 2135.64 \frac{g}{mol}$$

Example with higher functionality dendritic segment

This example is similar to the one for BPE2-5, however using PENTA as a tetrafunctional brancher.

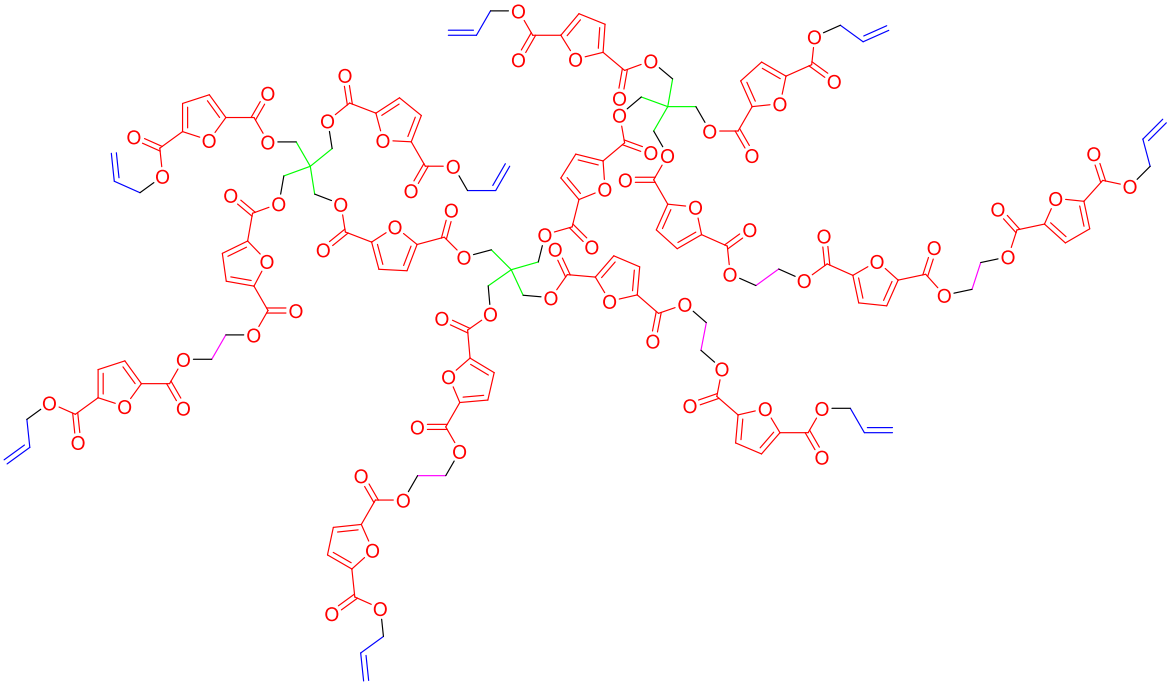

Molecular Weight: 2984,37

This molecule has an relative Allyl:Furane:PENTA:Ethylene Glycol ratio of 1 : 1.875 : 0.375 : 0.625 and again, the absolute ratios is sought. Using Equations 12 and 16 from the article, two values for k can be obtained and Mn can be calculated

$$N_{A_1} = 2 * N_{A_4} + 2$$

$$N_{B_2} = 3 * N_{A_4} + N_{A_2} + 1$$

$$k * n_{A_1} = 2 * k * n_{A_4} + 2$$

$$k * n_{B_2} = 3 * k * n_{A_4} + k * n_{A_2} + 1$$

$$k = \frac{2}{n_{A_1} - 2 * n_{A_4}} = \frac{2}{1 - 2 * 0.375} = 8$$

$$k = \frac{1}{n_{B_2} - 3 * n_{A_4} - n_{A_2}} = \frac{1}{1.875 - 3 * 0.375 - 0.625} = 8$$

$$M_n = 8 * 1 * 41.07\frac{g}{mol} + 8 * 1.875 * 154.08\frac{g}{mol} + 8 * 0.375 * 68.12\frac{g}{mol} + 8 * 0.625 * 28.05\frac{g}{mol} = 2984.37\frac{g}{mol}$$

Example for system with multiple types of dendritic units

This system contains a mix of glycerol and PENTA:

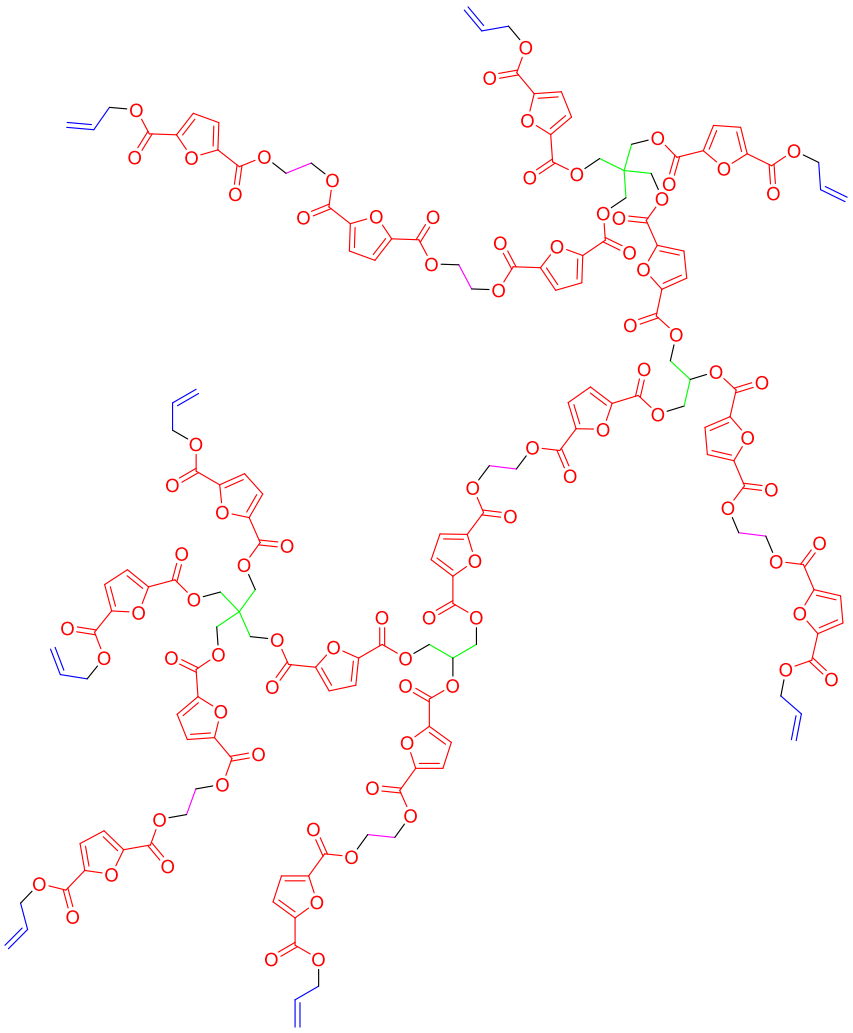

This molecule has an relative Allyl:Furane:PENTA:Glycerol:Ethylene Glycol ratio of 1 : 2.125 : 0.25 : 0.25 : 0.75.

Continues on next page.

Using equation 25-26, *k* values can be derived and Mn calculated:

$$N_{A_1} = \left(\sum (n-2) * N_{A_n}\right) + 2 = (4-2) * N_{A_4} + (3-2) * N_{A_3} + (2-2) * N_{A_2} + 2$$
$$= 2 * N_{A_4} + N_{A_3} + 2$$

$$k * n_{A_1} = 2 * k * n_{A_4} + k * n_{A_3} + 2$$
$$k = \frac{2}{n_{A_1} - 2 * n_{A_4} - n_{A_3}} = \frac{2}{1 - 2 * 0.25 - 0.25} = 8$$

$$N_{B_2} = \left(\sum (n-1) * N_{A_n}\right) + 1 = (4-1) * N_{A_4} + (3-1) * N_{A_3} + (2-1) * N_{A_2} + 1$$
$$= 3 * N_{A_4} + 2 * N_{A_3} + N_{A_2} + 1$$
$$k * n_{B_2} = 3 * k * n_{A_4} + 2 * k * n_{A_3} + k * n_{A_2} + 1$$
$$k = \frac{1}{n_{B_2} - 3 * n_{A_4} - 2 * n_{A_3} - n_{A_2}} = \frac{1}{2.125 - 3 * 0.25 - 2 * 0.25 - 0.75} = 8$$

Type equation here.

$$M_n = 8 * 1 * 41.07\frac{g}{mol} + 8 * 2.125 * 154.08\frac{g}{mol} + 8 * 0.25 * 68.12\frac{g}{mol} + 8 * 0.25$$
$$* 41.07\frac{g}{mol} + 8 * 0.75 * 28.05\frac{g}{mol} = 3334.60\frac{g}{mol}$$

Example for AB_2 system

For this example the condensation of 3,5-dihydroxybenzonic acid is considered:

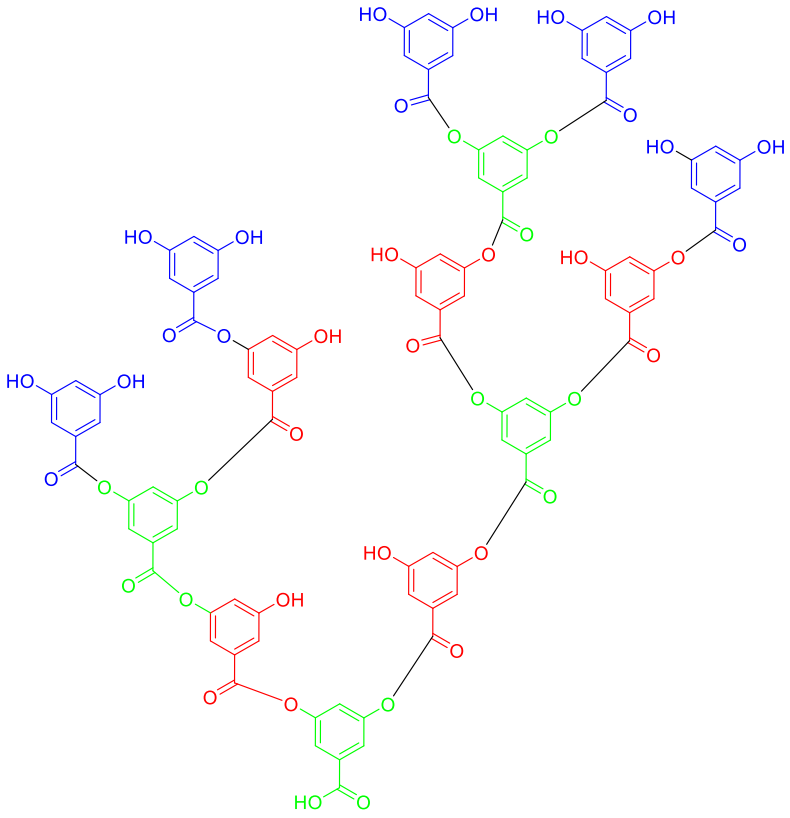

This molecule has an relative Terminal:Linear:Dendritic ratio of 1 : 1 : 0.8. Using Equation 31 k can be determined and molecular weight calculated:

$$k = \frac{1}{n_T - n_D} = \frac{1}{1 - 0.8} = 5$$

$$M_n = 5 * 1 * 153.11 \frac{g}{mol} + 5 * 1 * 136.11 \frac{g}{mol} + 5 * 0.8 * 119.1 \frac{g}{mol} = 1922.5 \frac{g}{mol}$$

Note that the obtained molecular weight is 1 lower than the actual value, this is due to a proton on the starting dendritic unit being unaccounted for.

Appendix C: Manuscript 1

FULL PAPER WILEY-VCH

Vanadium-Catalyzed Deoxydehydration of Vicinal Diols using Isopropyl Alcohol as the Reductant

Lasse B. Nielsen,[a] Daniel Bo Larsen,[a] Johannes R. Dethlefsen[a] and Peter Fristrup*[a]

Abstract: The deoxydehydration (DODH) of diols driven by the oxidation of iPrOH to acetone catalyzed by the cheap and commercially available catalyst ammonium metavanadate, NH4VO3, has been developed. The reaction proceeds at 230 °C in a pressurized autoclave and shows a strong preference for terminal diols: 1,2-Decanediol was converted to 1-decene in 51% yield, whereas 3,4-hexanediol was found to be completely unreactive. The lack of reactivity of internal diols contrasts the analogous rhenium- and molybdenum-catalyzed DODHs, and a theoretical study employing density functional theory (DFT) calculations was therefore warranted. The dramatic difference in reactivity was found to be rooted in the formation of stable but unreactive complexes between the internal diols and the vanadium center, which hindered efficient catalysis. The same reasoning was applicable to ethylene glycol that was found to be unreactive and even capable of inhibiting the reaction of otherwise reactive diols. In addition, a new ester product was identified stemming from oxidation of a primary hydroxyl group in the substrate diol followed by esterification with the isopropyl alcohol solvent.

Introduction

With the political ambitions for substituting large amounts of the fossil fuels used for transportation and energy production with sustainable biomass-based alternatives, it is important to make the production of these as efficient as possible. Since the production of organic platform chemicals (e.g., olefins and aromatics) is closely linked to the production of transportation fuels,[1] the overall economy of biorefineries depends on effective utilization of the whole biomass feedstock. One important stream of biomass that is already being processed is triglycerides, which in methanol undergo trans-esterification to give fatty acid methyl esters (FAME) and glycerol; the valorization of the byproduct glycerol would be a proof of concept of the ability of a biorefinery to utilize the entire biomass stream.[2]
The hydroxyl group is a common motif of carbohydrates, which are a major part of all biomass. One strategy for reducing their oxygen content while preserving functionality is the deoxydehydration (DODH) reaction that transforms a vicinal diol into the corresponding alkene in a single reaction step (Scheme 1). The DODH reaction[3-6] is driven by the oxidation of a sacrificial reductant and has typically been catalyzed by various rhenium-based compounds; although this approach is still being investigated by several groups,[7-9] the recently developed molybdenum[10] and vanadium[11-13] catalyzed DODH reactions could be relevant due to the significantly lower prices of the elements. In addition to a substitution of the scarce element rhenium,[14] the use of the DODH reaction on an industrial scale requires a substitution of the expensive reductant (e.g., PPh_3 or 3-octanol) and the toxic or biomass-immiscible solvents (e.g., benzene, chlorobenzene, or 3-pentanol) normally used. Besides DODH-activity vanadium[15], molybdenum[16] and rhenium[17] also display activity as catalysts for reductive coupling of activated alcohols.

Scheme 1. Generalized Re-, Mo-, or V-Catalyzed DODH of a Vicinal Diol into an Alkene, Driven by the Oxidation of a Scrificial Reductant ("red").

We have recently demonstrated the use of the cheap and commercially available $(NH_4)_6Mo_7O_{24}{\cdot}4H_2O$ as a catalyst for the DODH of vicinal diols in *i*PrOH, which serves as both the solvent and the reductant (Scheme 2).[10] The alkene yield could be as high as 77% and the major byproducts were the carbonyl compounds formed by dehydration of the diol and the alcohols formed by transfer hydrogenation of these carbonyl compounds; the total yield of reduced species could be as high as 92%.

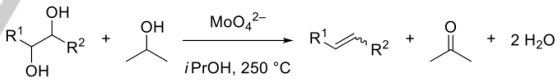

Scheme 2. Molybdate-Catalyzed DODH of a Vicinal Diol into an Alkene, Driven by the Oxidation of iPrOH to Acetone.

In the present work, we demonstrate that a wide variety of commercially available vanadium-based compounds efficiently catalyze the DODH of vicinal diols. At the onset our main objective was to investigate the possibility of using an alcohol as both the solvent and reductant (Scheme 3). In the following sections we deliberate on the range of solvents, reductants, substrates, and ligands that we have tested. During our investigation a specific difference in selectivity for the V-catalyzed DODH was observed, which warranted an in-depth computational study employing DFT calculations.

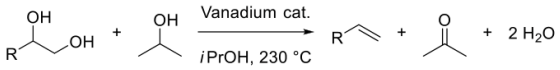

Scheme 3. Vanadium-Catalyzed DODH of a Vicinal 1,2-diol into a Terminal Alkene, Driven by the Oxidation of iPrOH to Acetone.

[a] Title(s), Initial(s), Surname(s) of Author(s) including Corresponding Author(s)
Department
Institution
Address 1
E-mail:
[b] Title(s), Initial(s), Surname(s) of Author(s)
Department
Institution
Address 2

Supporting information for this article is given via a link at the end of the document.((Please delete this text if not appropriate))

Results and Discussion

Initial optimizations

The starting point for this study was the reaction conditions used for Mo-catalyzed DODH.[10] The experiments were performed either in an autoclave or in a Swagelok cylinder, and in a standard experiment with *i*PrOH as the solvent, the maximum pressure would typically be 50–70 bar. A catalyst concentration of 5 mol% with respect to vanadium was employed and the reaction was found to start at 230 °C at which point full conversion of the most reactive substrates was reached within 17 hours (see experimental section for additional details).

The same amounts of products were observed whether the reactions were carried out in the Swagelok cylinders (Reaction Conditions B) or in an autoclave (Reaction Conditions A). The cylinders were firmly sealed and test experiments performed to ensure that they were not leaking out the sample. Treating a mixture of 1-hexene (10 mmol), acetone (10 mmol), and H_2O (20 mmol), in isopropyl alcohol, with the NH_4VO_3 catalyst, according to reaction conditions B, resulted in 94% recovery of the initial 1-hexene which proves that the cylinders are not leaking out the alkene in any considerable amounts. The experiment also showed that the reverse reaction, e.g. dihydroxylation of the alkene, is unlikely to be significant.

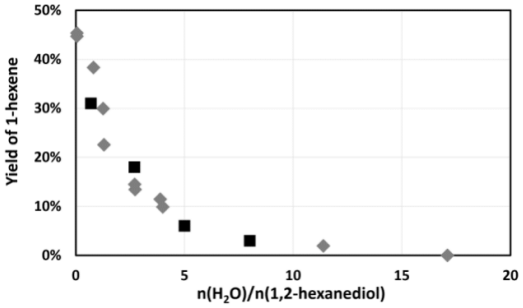

Figure 1. Dependence of the yield of 1-hexene from the DODH of 1,2-hexanediol (Reaction Conditions B) on the amount of added water. *Diamonds*: NH_4VO_3 as catalyst. *Squares*: $(NH_4)_6Mo_7O_{24}\cdot 4H_2O$ as catalyst.

Water is an inherent byproduct from DODH and an investigation of how it affects the reaction was therefore warranted. A series of experiments in which water was added in different amounts from the onset of the reaction, clearly showed that DODH is hampered already at 2 equivalent of water-to-substrate (Figure 1). Interestingly, the sensitivity towards water appears to be very similar for the catalyst based on vanadium (NH_4VO_3), and that based on molybdenum ($(NH_4)_6Mo_7O_{24}\cdot 4H_2O$). An array of known ways to remove water was considered and molecular sieves were found unable to bind water under the high temperature of the reaction conditions. IR spectroscopy was used to assess the ability of molecular sieves to retain water under the reaction conditions. More specifically, the areas at 1645 cm^{-1}, corresponding to the bending mode of water, were compared. A spectrum of *i*PrOH containing 2 wt% water was compared to a spectrum recorded after drying the same sample with 3Å molecular sieves. Subsequently, the dried solvent and the sieves were heated to 230 °C in an autoclave. A sample was extracted and filtered and a new spectrum was recorded at room temperature. This showed that the molecular sieves could not retain water under the reaction conditions.

Chemical reagents known to react with water were also tested as water scavengers. These included 2,2-dimethoxypropane and 1,1-dimethoxycyclohexane in amounts of 0.75 and 2 equivalents relative to the diol, yet both cases resulted in lower yields of alkene at full conversion. Triethyl orthoformate was found to reduce the 1,2-decanediol to 1-decene in a non-catalytic reaction, as already described in literature.[18] Addition of quicklime (CaO) to the experiment resulted in precipitation of a grey powder and no formation of alkene. While these studies did not lead to an improved DODH reaction it is interesting that the dependence of water is so similar for the two different metals, thus leading one to speculate that a suitable method for water separation could be effective for both molybdenum and vanadium-based systems.

Solvent and reductant

The best choices of reductant in terms of price, sustainability, and atom economy are hydrogen and carbon monoxide. However, in our system both hydrogen and carbon monoxide were found to yield practically identical product distributions and yields as the reactions that were carried out using inert N_2 gas (Table 1). Isopropyl alcohol was chosen as a solvent since it is capable of dissolving oxygen rich molecules, while the experiments in hexane should clarify whether the applied gaseous reductants were effective at all. Initially, our assumption was that the reduction of the substrate to alkene, that is observed when the experiment is performed in hexane/N_2 (Table 1, entry 2) is driven by disproportionation of the substrate itself, as was reported for molybdenum.[19] However, when using a vanadium-based catalyst no products from oxidative cleavage were observed. 2-Decanone was the only pronounced by-product appearing in the GC spectrum in this experiment, thus the reaction probably leads to an oxidized intermediate. Later we will show that using different analytical techniques it is indeed possible to observe an oxidation product of the substrate diol, namely the ester formed by oxidation of the primary alcohol moiety into the acid followed by esterification with the solvent, isopropyl alcohol.

Table 1. Test of H_2 and CO as Reductants in the DODH of 1,2-Decanediol Using NH_4VO_3 as Catalyst Under Reaction Conditions A

Entry	Gas	Solvent	Conv.	Yields (%) of[a]			
			(%)	C=C	C=O	2°OH	1°OH
1	H_2	Hexane	Full	32	6	1	1
2	N_2	Hexane	Full	30	9	3	3
3	H_2	*i*PrOH	93	48	2	2	6
4	N_2	*i*PrOH	97	51	2	1	8
5	CO[b]	*i*PrOH	Full	51	2	1	5

[a] Products: 1-decene (C=C), 2-decanone (C=O), 2-decanol (2°OH) and 1-decanol (1°OH). [b] The pressure of CO was 14 bar.

Nicholas and Gopaladasu[12] showed that it is possible to use CO gas for reduction when the DODH is catalyzed by $[Bu_4N](salhyd)VO_2$ (salhyd = salicylaldehyde hydrazide). They were able to convert 1,2-hexanediol into 1-hexene in 97% yield, at 180 °C, when using chlorobenzene as the solvent. It is however, an advantage if the solvent is cheap, green and capable of dissolving the highly oxygenized compounds usually obtained from biomass, if the system is to become industrially feasible. When using NH_4VO_3 in *i*PrOH, neither H_2 nor CO gas can act as reductants and for this reason we decided to investigate the alcohol-driven DODH in which an alcohol is oxidized to form a ketone or an aldehyde. Afterwards, the reductant may be recycled by hydrogenation of the formed carbonyl compound. Results when using a range of different solvents for DODH of 1,2-decanediol is reported in Table 2. Starting from methanol and moving to longer primary alcohols give higher yields of 1-decene (Table 2, entries 1-3). Even better outcomes are obtained when secondary alcohols are used, such as isopropyl alcohol or 3-pentanol (Table 2, entry 4,5).

Table 2. Comparison of Organic Solvents in the NH_4VO_3-Catalyzed DODH of 1,2-Decanediol.

Entry	Solvent	Conv.	Yields (%) of[a]			
		(%)	C=C	C=O	2°OH	1°OH
1	MeOH	35	6	1	1	1
2	EtOH	64	17	4	1	3
3	*n*PrOH	78	27	2	1	3
4	*i*PrOH	97	51	2	1	8
5	3-Pentanol	97	46	2	1	6
6	2,2,2-Trifluoroethanol[b]	67	19	0	0	3
7	Hexafluoroisopropanol[b]	61	13	0	0	4
8	2,4-Dimethyl-3-pentanol[c]	Full	45	10	0	7
9	Cyclohexanol	98	43	2	2	5

[a] Unless otherwise noted, Reaction Conditions A were employed; Products: 1-decene (C=C), 2-decanone (C=O), 2-decanol (2°OH) and 1-decanol (1°OH). *b* [b] Reaction Conditions B; the substrate was 1,2-hexanediol and 1-heptanol was used as an internal reference. [c] Reaction Conditions B; the substrate was 1,2-hexanediol.

The fluorinated alcohols were tested to see if the electron-withdrawing fluorine atoms could facilitate higher alkene yields, but that was not the case (Table 2, entries 7-8). Then 2,4-dimethyl-3-pentanol was tested, as it has already proven successful in rhenium-catalyzed DODH of glycerol[20] and phenylethanediol.[21] An alkene yield of 45% was found (Table 2, entry 9), which is in line with previously reported results on vanadium-catalyzed DODH in benzene with 2,4-dimethyl-3-pentanol as reductant.[11] Benzyl alcohol was also added as a potential reducing agent, but this compound underwent transfer hydrodeoxygenation (HDO) to toluene in about 30 - 40% yield, regardless of whether the solvent was isopropyl alcohol or ethanol and in a similar way to the recently investigated Mo-catalyzed transfer HDO of benzyl alcohol[16] Cyclohexanol was also tested, but only 43% of 1-decene was obtained (Table 2**Error! Reference source not found.**, entry 10). In conclusion, isopropyl alcohol remains the best choice for a system aiming to offer the cheapest possible DODH reactivity and easy recyclability of the reductant.

Catalyst screening

Under these harsh reaction conditions, the vanadium center will presumably exchange most ligands rapidly. Focus was therefore on commercially available vanadium compounds in different oxidation states, rather than development of complex ligand systems. The results show almost identical yields (50%) for all types and oxidation states of the catalysts (Table 3). Even the $(Bu_4N)(dipic)VO_2$ catalyst, that has otherwise proven to be outstanding for DODH carried out in benzene with PPh_3 as the reductant,[11] gave 47% alkene yield when isopropyl alcohol was used (**Error! Reference source not found.**, entry 4).

Table 3. Comparison of Different Vanadium Catalysts for DODH of 1,2-Decanediol.

Entry	Catalyst	Conv.	Yields (%) of[a]			
		(%)	C=C	C=O	2°OH	1°OH
1	NH_4VO_3	97	51	2	1	8
2	Bu_4NVO_3+dipic[b]	90	45	2	1	7
3	$(Bu_4N)(dipic)VO_2$[c]	95	47	2	1	7
4	V_2O_5	93	47	2	1	8
5	VO(isopropoxide)$_3$	92	48	2	1	8
6	VO(acac)$_2$	Full	54	4	2	10
7	V(acac)$_3$	94	50	2	1	7
8	NH_4VO_3+acid[d]	93	50	2	1	7
9	NH_4VO_3+base[e]	87	40	2	1	5
10	$(Bu_4N)_3[V_{10}O_{28}H_3]$+base[f]	91	50	3	0	5
11	$VOSO_4 \cdot xH_2O$	77	2	1	9	7
12	Na_3VO_4	37	1	1	0	1
13	VO(tpp)[g]	84	18	5	0	16
14	$(Bu_4N)_3[V_{10}O_{28}H_3]$[h]	92	23	6	0	19

[a] Unless otherwise noted, Reaction Conditions A were employed. Products: 1-decene (C=C), 2-decanone (C=O), 2-decanol (2°OH) and 1-decanol (1°OH). [b] 1.1 equiv of dipicolinic acid to catalyst. [c] 4.5 mol% catalyst. [d] 1.2 equiv of acetic acid to catalyst. [e] 3 equiv of Bu_4NOH to catalyst. [f] Reaction Conditions B; 3 equiv of Bu_4NOH to catalyst was used and the substrate was 1,2-hexanediol. [g] Reaction Conditions B; 1,2-hexanediol used as substrate; 4 mol% of catalyst was used and the reaction time was 990 min; tpp = 5,10,15,20-Tetraphenylporphyrine. [h] Reaction Conditions B; 1,2-hexanediol used as substrate; the reaction time was 1260 min.

The 5,10,15,20-Tetraphenyl-21H,23H-porphyrine vanadium(IV) oxide, VO(tpp), complex was also tested. The anticipation was that the bulky ligand could give rise to higher yields of alkene or a change in the product distribution, because the ligand would impose a steric hindrance on the metal center. The latter of the two options was indeed found with an increase in the yield of the primary alcohol (16%), accompanied by a decrease in the corresponding yield of alkene (18%;Table 3, entry 13).

A low yield of 23% was observed when using the tetrabutylammonium polymetalate $(Bu_4N)_3[V_{10}O_{28}H_3]$ (Table 3, entry 14). The catalyst only reluctantly gives rise to the DODH-active vanadium-oxo species, but upon addition of tetrabutylammonium hydroxide to the reaction mixture the yield of alkene increases to 50%. This was also found for Mo-catalyzed DODH where the molybdenum complex $(NH_4)_6Mo_7O_{24}{\cdot}4H_2O$ in conjunction with base, increases the yield of 1-hexene from 46% to 77%.[10] We suggest that the base improve break up the polymetalates and thereby increases the solubility and reactivity of the catalyst. The vanadium compounds, $VOSO_4{\cdot}xH_2O$ and Na_3VO_4, resulted in almost no DODH which was ascribed to the low solubility of these complexes.

The highest alkene yield was obtained with $VO(acac)_2$ as catalyst, to give 54% alkene yield and a total of 66% reduced species. This suggests that the catalytic cycle is at least to some extent driven by oxidation of isopropyl alcohol to acetone and not merely by oxidation of the diol itself.

The most pronounced side product is the primary alcohol, followed by a small amount of the ketone. The secondary alcohol is only found in some experiments and always in very small amounts. Upon further inspection of the reaction mixture formed by deoxydehydration of 1,2-hexanediol, we were able to identify and quantify a new product, isopropyl 2-hydroxyhexanoate, which is formed by oxidation of the primary hydroxyl group of the diol, followed by esterification with the isopropyl alcohol solvent. Under standard reaction conditions B (Table 5, entry 1), the ester is expected to be formed in a moderate 11% yield (see supporting information for further details), which may be improved for example by additional fine-tuning of the reaction conditions.

Ligans with diol functionality

In order to test the influence of other possible ligands that might be stable under the reaction conditions, 1.5 equivalents to vanadium of an unreactive additive containing the diol substructure was added (Table 4). The electron-poor tetrafluorocatechol was found to strongly inhibit the DODH, and it is therefore expected to stay coordinated to the vanadium center. Those additives that showed a strong influence on the outcome were further tested with a smaller additive-to-vanadium ratio. The biggest change in product distribution was found for 2,3-dihydroxynaphthalene, which yielded an increased amount of 1-hexanol. Addition of the nitrogen analogues of the tested naphthalene-based additives, had little to no effect on the DODH, thus implying that only oxygen-based ligands are capable of binding to vanadium and affecting the product distribution.

Table 4. Test of Different Additives to NH_4VO_3-Catalyzed DODH of 1,2-Hexanediol.

Entry	Additive	Conv.	Yields (%) of[a]		
		(%)	C=C	C=O	1°OH
1	Ethylene Glycol[b]	97	48	3	6
2	Ethylene Glycol[c]	62	32	2	4
3	Pyrocatechol	64	24	3	15
4	Pyrogallol	9	5	0	3
5	3-Fluorocatechol[d]	31	11	0	8
6	Tetrafluorocatechol	0	5	0	0
7	2,3-Dihydroxynaphthalene	88	15	3	31
8	2,3-Naphthalenediamine	95	50	4	6
9	1,8-Dihydroxynaphthalene	45	19	2	6
10	1,8-Naphthalenediamine	91	47	2	5

[a] Unless otherwise noted, Reaction Conditions B were employed and 1.5 equiv of additive to vanadium were assed. Products: 1-hexene (C=C), 2-hexanone (C=O) and 1-hexanol (1°OH). [b] 1 equiv to vanadium. [c] 8 equiv to vanadium [d] 2 equiv to vanadium.

Substrate scope

The first substrates that we investigated were 1,2-hexanediol and 1,2-decanediol, which both gave roughly 50% alkene yield at full conversion (Table 5, entry 1,2). Then, a dramatic reduction in yield was observed when employing substrates containing only secondary hydroxyl groups. In the case of the cyclic *trans*- and *cis*-1,2-cyclohexanediol, low conversion and almost no DODH products were observed (Table 5, entry 3,4). In the molybdenum-catalyzed DODH, it was possible to convert 29% of *cis*-1,2-cyclohexanediol into the alkene and 14% of the *trans* stereoisomer.[10] These substrates have also been thoroughly investigated with rhenium-catalyzed DODH and there seems to be a general trend for the DODH reaction to prefer the *cis* stereoisomer.[21,22] The preference is in line with the proposed reaction mechanisms for vanadium,[23] molybdenum,[10] and rhenium[24] that go through a diolate complex in which both of the hydroxyl groups are coordinated to the metal center at the same time. This coordination may be obstructed by the different orientations of the hydroxyl groups within the *trans*-stereoisomer, thus explaining why this stereoconfiguration is so unreactive. Vanadium however, showed a low conversion for both *cis* and *trans*-1,2-cyclohexanediol.

Table 5. Comparison of Different Substrates in NH_4VO_3-Catalyzed DODH.

Entry	Substrate	Conversion (%)		Yield (%)of C=C[a]	
		Exp. 1	Exp. 2	Exp. 1	Exp. 2
1	1,2-Hexanediol	90	89	50	49
2	1,2-Decanediol	95	Full	51	50

3	*trans*-1,2-Cyclohexanediol[b]	18	14	5	5
4	*cis*-1,2-Cyclohexanediol[b]	4	3	1	1
5	*cis*-1,2-Cyclohexanediol	23	35	3	5
6	2-Ethyl-1,2-butanediol	Full	Full	9	10
7	*(R,R)*-Hydrobenzoin	Full		16[c]	
8	*meso*-Hydrobenzoin	Full		30[c]	
9	*rac*-1-Phenyl-1,2-propanediol	Full		37[c]	

[a] Reaction Conditions B were employed; some of the experiments were conducted twice to check the reproducibility of the results. [b] Reaction time was 990 min. [c] The *trans* stereoisomer of the product.

The importance of the orientation of the hydroxyl groups was also observed when 1,2-hexanediol underwent DODH in the presence of either *cis*- or *trans*-1,2-cyclohexanediol (Scheme 4). If the *cis* isomer was added to the reaction, the yield of 1-hexene was dramatically lowered, whereas the *trans* version had a much smaller effect on the deoxydehydration. The most likely explanation for this behavior is that *trans*-1,2-cyclohexanediol is unable to form a vanadium diolate complex, while the *cis* isomer can function as a ligand under the reaction conditions and thus impede the DODH.

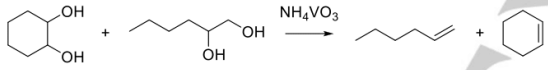

cis-1,2-hexanediol	19%	3%
trans-1,2-hexanediol	43%	4%

Scheme 4. The influence by differently oriented hydroxyl groups.

cis-1,2-Cyclooctanediol was also tested to investigate if a more flexible ring system, compared to the six-membered ring in 1,2-hexanediol, could improve the reaction. Although the conversion was higher than for *cis*-1,2-hexanediol, the alkene yield was still very small (Table 5, entry 5). There was no alkene formation from the rigid *cis*-norbornylene glycol as well, nor from the straight-chain 3,4-hexanediol.

Encouraged to discover how selective the vanadium catalyst is towards substrates with at least one primary hydroxyl group, it was decided to move on to more reactive diols. With 2-ethyl-1,2-butanediol, only 10% of the corresponding alkene was detected due to deoxygenation of the tertiary alcohol group to give 2-ethyl-1-butanol in 50% yield (Table 5, entry 6).

The *meso*- and (*R,R*)-diastereoisomers of hydrobenzoin was also tested (Table 5, Entry 7-8) as the stilbene products will be stabilized by conjugation. In this case, the *trans* isomer of stilbene was almost selectively obtained for both (*R,R*)- and *meso*-hydrobenzoin (16% and 30% respectively). This could be caused by thermal isomerization between *cis*- and *trans* isomers of stilbene or through a selectivity in the reaction pathway. The less reactive 1-phenyl-1,2-propanediol (Table 5, Entry 9) also resulted in a majority of *trans*-β-methylstyrene (37%). However, the DODH of hydrobenzoin and 1-phenyl-1,2-propanediol was found to be driven by oxidative cleavage, rather than oxidation of the solvent.

The substrates tested so far have mostly been model compounds of chemicals derived from biomass. Glycerol is a chemical that is produced in increasing amounts from the production of biodiesel and it is therefore an interesting target molecule for DODH. Our initial experiments on glycerol showed almost no conversion and no formation of allyl alcohol. Small amounts of propylene were detected in the headspace of the cylinders by leading the gas through a solution of Br_2, in CH_2Cl_2, followed by GC detection of the brominated alkene (1,2-dibromopropane). The amounts were not quantified, as the Swagelok cylinders are likely to leak out some of the propylene during the experiment. The same experiment was performed with 1,2-propanediol and ethylene glycol. Interestingly, no 1,2-dibromoethylene was detected in the headspace when using ethylene glycol, whereas much more 1,2-dibromopropane was observed when using the C_3-diol. The ether analog of glycerol, 3-isopropoxy-1,2-propanediol, did react to form the corresponding alkene from DODH, in decent 46% yield at 86% conversion.

Theoretical Calculations

In an attempt to gain a deeper understanding of the mechanism of the vanadium-catalyzed DODH reaction and an understanding of the observed reactivity as a function of substitutions on the diol, a theoretical study of the reaction was carried out using DFT, in line with earlier studies.[10,25] In the calculations, we used the B3LYP-D3 functional and the LACVP** basis set. As in earlier studies on Re and Mo, the vanadium catalysts were treated as the neutral complex VO_2OH in order to simplify the model as well as being a neutral analogue to ammonium metavanadate, the most commercially interesting catalyst used in this study. For the diol, we used 1,2-propanediol as a model compound, the smallest possible diol containing both a primary and secondary alcohol, and a close analogue to 1,2-hexandiol and 1,2-decandiol. All vanadium(V) complexes were considered as singlets (multiplicity of 1), where V(III) complexes were considered in both their singlet and triplet states (multiplicity of 1 and 3, respectively). All transition states and intermediates with a multiplicity of 3 have been marked with an asterisk (*).

We propose the catalytic cycle to consist of the formation of a V(III) diolate followed by an extrusion step which is in line with the analogous extrusion from Re(V)[24,26] and Mo(VI) complexes.[10,25] The formation of the V(III) diolate is expected to follow one of two pathways: either the formation of a vanadium(V) diolate with the diol followed by a reduction with isopropyl alcohol (Pathway A), or a direct reduction of the vanadate catalyst to a free V(III) moiety with subsequent condensation to the target diolate (Pathway B). These pathways and the extrusion step are sketched in Figure 2.

A previous study has shown favorable energies for a pathway similar to B for the vanadium complex with the dipicolinate (dipic) ligand and PPh_3 as reductant,[23]**Error! Bookmark not defined.** a method applied by Nicholas and coworkers.[11] In this project however, the goal is to understand the reactivity of the free vanadate catalyst in reactions where isopropyl alcohol, a much cheaper and easily recyclable alcohol, is used as the reductant. Studies have shown an analogue to Pathway B being favorable for rhenium,[24] whereas another study on a molybdenum analogue demonstrated preference for Pathway A.[10] Both studies proved the reduction to be the rate-determining step.

The reduction step and diolate condensation

The condensation and reduction steps for Pathways A and B were modeled, examining all possible pathways (only intermediates of lowest energies are discussed here – see ESI for all the others). The lowest energy mechanisms to the V(III) diolate **[5]** are shown in Figure 3 (the change in energy from **[A5]** and **[B5]** to **[5]**/**[5]*** is due to loss of micro solvation effect).

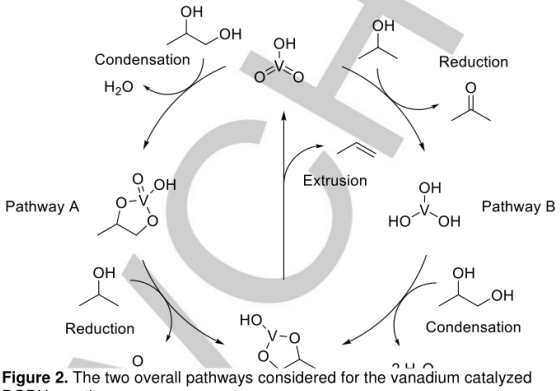

Figure 2. The two overall pathways considered for the vanadium catalyzed DODH reaction.

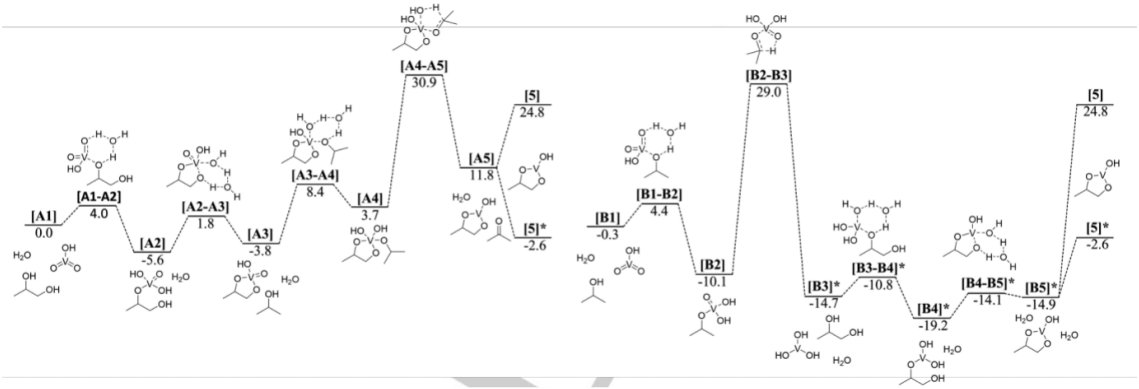

Figure 3. Gibbs free energy diagrams for the lowest energy mechanisms of Pathway A (left) and Pathway B (right).

All vanadium(III) complexes proved to be more stable in the triplet state. Though high stability of the triplet state is observed, we also show the singlet state, **[5]**, due to the importance of its geometry for further calculations. Calculations gave small energy barriers for the condensation steps as expected, with favorable energies for initial condensation to the secondary alcohol of the diol in both pathways (**[A1-A2]** and **[B3-B4]***). Calculations proved the two mechanisms to have very similar energies with a slight selectivity towards Pathway B with **[B2-B3]** being 1.9 kcal/mol lower in energy than **[A4-A5]**. The geometries of the two transition states are depicted in Figure 4.

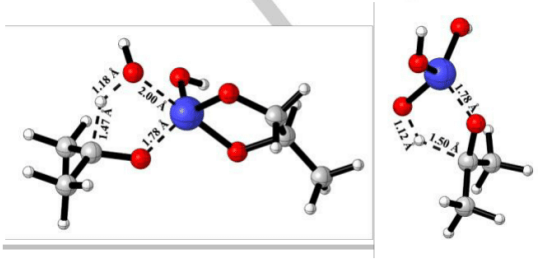

Figure 4. Transition state geometries of [A4-A5] (left) and [B2-B3] (right).

The extrusion step

Following the formation of the V(III) diolate, we suspected the reaction to go through a [2+3] extrusion as previously observed with both molybdenum[3,10,25] and rhenium.[24,26] Calculations however, showed a high energy barrier of 48.6 kcal/mol when compared to the vanadate starting point. Therefore, we examined the possibility of a rearrangement mechanism to a 4-membered oxetane capable of [2+2] extrusion, as seen in Figure 5 with the corresponding energy diagram sketched in Figure 6.

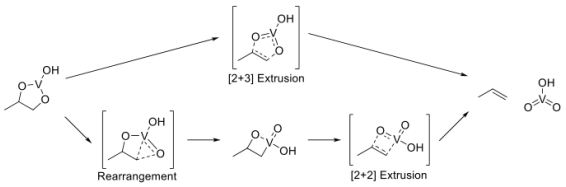

Figure 5. Alternative rearrangement mechanism to the classic [2+3]-extrusion step

The energies of the [2+3] extrusion **[5-1]** and the rearrangement **[5-6]** proved to be very similar with the [2+3] extrusion being 0.5 kcal/mol lower in energy. For the rearrangement **[5-6]** a small energy advantage of 1.5 kcal/mol was observed when cleaving the primary C–O bond compared to the secondary. We also noticed that the oxetane is very stable with a very low energy barrier to the [2+2] extrusion **[6-1]** of 2.2 kcal/mol. The geometries of the transition states **[5-1]** and **[5-6]** are sketched in Figure 7.

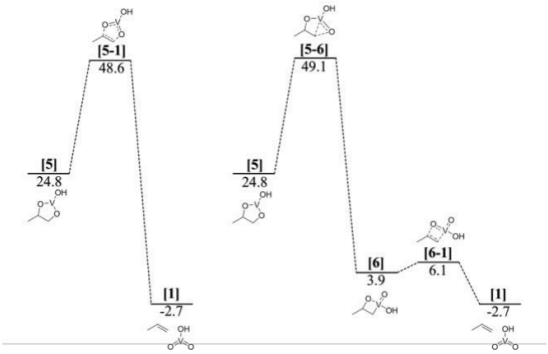

Figure 6. Gibbs free energy barriers for the [2+3] extrusion (left) and the rearrangement followed by a [2+2] extrusion (right).

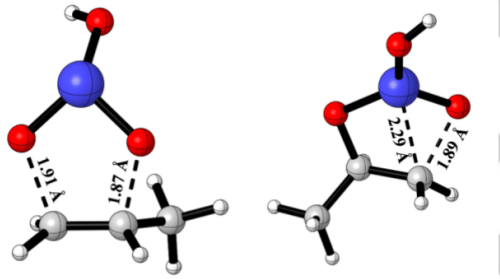

Figure 7. Transition state geometries of **[5-1]** (left) and **[5-6]** (right).

From the reduction mechanism, we noticed that all V(III) complexes had the lowest energy in their triplet state – however, for the transition states **[5-1]** and **[5-6]**, a transition state in the triplet state could not be found. This is because the extrusion takes place in a step-wise manner in the triplet state, which causes the C–O bonds to be broken sequentially.[27,28] The absence of a [2+3] extrusion transition state was identified by the presence of two negative frequencies in the vibrational frequency calculations, for geometries close to other similar transition states (C–O bond distances at 1.8, 1.9 and 2.0 Å). Further calculations showed that the cleavage of one C–O bond lead to the formation of the radical intermediate **[7]*** (Figure 8). This intermediate was more stable in the singlet state due to the possibility for formation of an oxetane (**[6']**), similar to the one seen earlier (a structure non-existent in the triplet state). The breakage of the secondary C–O bond was favored over the primary with a difference of 0.4 kcal/mol. This mechanism has a much lower energy barrier than the classic [2+3] extrusion as shown in Figure 8. The transition state geometries of **[5-7]*** and **[6'-1]** are depicted in Figure 9.

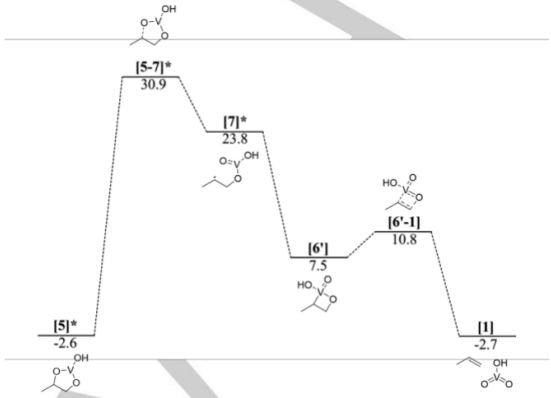

Figure 8. Gibbs free energy diagram for the newly suggested high-spin mechanism for the extrusion step.

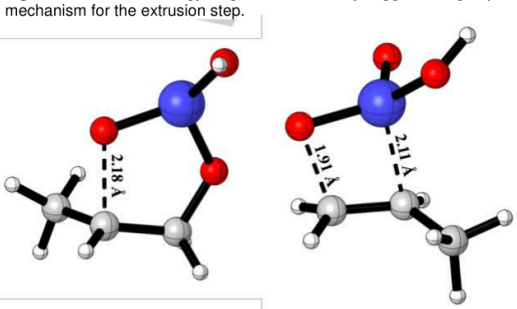

Figure 9. Transition state geometries of **[5-7]*** (left) and **[6'-1]** (right).

From the energy diagrams, we can see that the sequential breakage of the C–O bonds gives a pathway favored by 17.7 kcal/mol compared to the **[5-1]** extrusion, with the energetic advantage mostly arising from the high stability of the triplet state **[5*]** compared to the singlet state **[5]**. This confirmed not only a more favorable pathway for the extrusion step, but also a mechanism different from the ones suggested for the rhenium and molybdenum analogues of this reaction.[24,25]

The rate-determining step

Although a lowest energy mechanism could be established for the vanadium-catalyzed DODH reaction, the overall rate-determining step was hard to pinpoint due to the close energy of the two possible reduction steps and the C–O bond cleavage (29.0, 30.9 and 30.9 kcal/mol, respectively). As mentioned before, we observed a slight advantage when reducing the vanadate moiety before condensation with the diol; this energy difference was however very low. Since the V-catalyzed DODH reaction is carried out at very high temperatures, we wanted to inspect the entropy influence on these reaction steps. This was accomplished by calculating the Gibbs free energies of the three high-energy transition states at various temperatures from 300 K

to 600 K, and observing the changes in Gibbs-Free Energy (Figure 10).

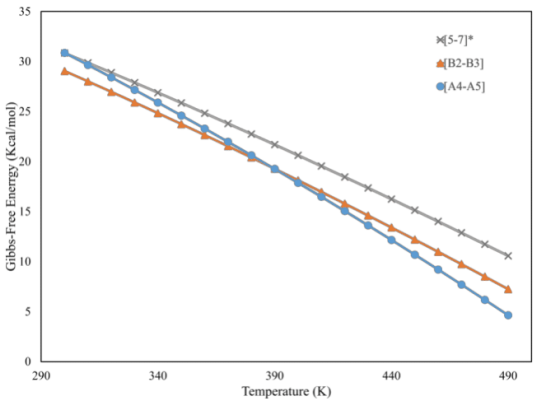

Figure 10. Relative change in the Gibbs free energy for the highest energy transition states at various temperatures.

As seen in Figure 10, the C–O bond cleavage **[5-7]*** will always be the rate determining step for the reaction, especially when it is taken into account that the concentration of the reductant often exceed that of the substrate diol (e.g. when the solvent *i*PrOH is used as reductant). When increasing the temperature, the reaction pathway of the reduction changes from pathway B to pathway A (Figure 2). This change happens around 390 K, which is below our reaction temperature (above 500 K). In conclusion the calculations seem to favor the formation of diolates **[A3]** which reduces to **[5]***, followed by the single bond breakage leading to the oxetane **[6']** that can undergo a [2+2] extrusion yielding the product alkene and restoring the vanadate catalyst.

Explaining the selectivity

As shown by the experiments, the vanadium-catalyzed DODH reaction only operates on terminal diols, with little to no reaction occurring for substrates with an internal diol (i.e., having two vicinal secondary alcohols). First, it was examined whether the unreactive substrates exhibited higher transition state energies. All our calculations however, failed to prove this assumption with all energies for the highest transition states showing little to no difference. As seen from the energies presented in **TABLE**, neither the newly suggested high-spin mechanism, the classic [2+3] extrusion, nor the reduction can explain this selectivity. Only minor differences are observed in the energy barriers for the various transition states relative to the vanadate starting point.

Table 6. Gibbs Free Energy Comparison of Key Transition States with 1,2- and 3,4-Hexanediol as Substrate.

Transition State	1,2-Hexanediol	3,4-Hexanediol
[A4-A5]	11.6	9.8
[5-1]	32.1	30.0
[5-7]*	13.1	12.2
[6'-1]	-11.6	-10.5

Since the explanation for this selectivity could not be found in the mechanism, we decided to examine the differences in binding affinity of the different substrates with vanadium. As seen in Figure 3, only small energy barriers were observed for the binding of diols to vanadium. Meaning, a possible irreversible binding of the diols could lead to a potential "energy sink" which would inhibit the catalyst and increase the energetic span of the reaction. To confirm this possibility, all possible complexes with one or two diols bonded to the vanadium center were optimized (additional diols beyond two per vanadium center proved entropically disfavored, as expected). An overview of these types of complexes is shown in Figure 11.

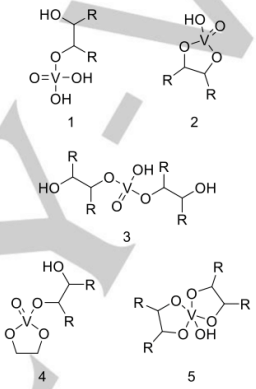

Figure 11. Various examined vanadium–diolate complex types.

All possible complexes were built and optimized (only those of lowest energy are shown here – see ESI for the rest). Figure 12 shows the energies of the complexes for 1,2-hexanediol, 3,4-hexanediol and ethylene glycol, the two latter being unreactive.

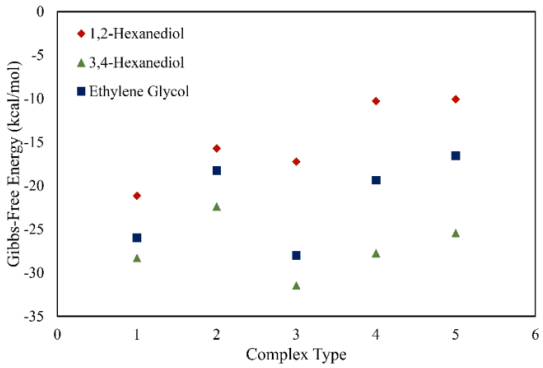

Figure 12. Gibbs free energies of the examined vanadium-diol complexes.

As seen from Figure 12, all 3,4-hexanediol complexes exhibit much lower energies than their 1,2-hexanediol equivalents. Complex type 3 of 3,4-hexanediol is 10.3 kcal/mol lower in energy than the lowest energy complex of 1,2-hexandiol (complex type 1), which leads to an increase of the energetic span of the DODH reaction of 10.3 kcal/mol, when the more substituted diol is used. We attribute this large difference energetic span as being responsible for the markedly different reactivity of vanadium towards diols that have two secondary hydroxyl groups. As exemplified by the sharp difference observed between the model compound 3,4-hexanediol which is unreactive, and 1,2-hexanediol which gives 48% yield of 1-hexene. For comparison, the molybdenum-catalyzed DODH on 3,4-hexanediol and 1,2-hexanediol in *i*PrOH give 69% and 77% of the corresponding alkene, respectively.

A similar energy sink for ethylene glycol was also observed in complex type 3 and that provides an explanation for the observed lack of reactivity as well as an explanation for the inhibitory effect of ethylene glycol. This also explains why this phenomenon is only experienced with the vanadium-catalyzed DODH reactions, compared to the molybdenum and rhenium analogues. For rhenium[29] and molybdenum,[8] complexes 2, 4 and 5 would be favorable intermediates due to the ability to regenerate an active catalyst through oxidative cleavage of one of the coordinated diols whereas for vanadium this type of reactivity is not observed.

Conclusions

The vanadium-catalyzed DODH of polyols driven by the oxidation of *i*PrOH to acetone based on cheap and commercially available ammonium metavanadate, NH_4VO_3 was developed. The reaction is carried out in an autoclave at 230 °C. A dramatic difference in reactivity was observed when comparing terminal diols (1,2-decanediol, 51% yield) and internal diols (e.g. 3,4-hexanediol) where the latter was found to be completely unreactive. In addition to the side-products already known for the Mo-catalyzed DODH we were able to identify isopropyl 2-hydroxyhexanoate as a new and potentially useful product from 1,2-hexanediol. Although the yield of this byproduct was moderate (11%) we suspect that this could be improved for example by additional fine-tuning of reaction conditions.

We have also proven that the two vicinal hydroxyl groups have to be oriented *cis* to each other for the unreactive diolate complexes to be formed, as addition of *cis*-1,2-cyclohexanediol clearly blocks the deoxydehydration of 1,2-hexanediol (19% yield) whereas the *trans*-stereoisomer has little to no effect on the reaction (43% yield of 1-hexene). The target molecule glycerol was found to be remarkably unreactive under our reaction conditions, though the isopropyl ether analogue, 3-isopropoxy-1,2-propanediol, underwent DODH to give the corresponding alkene in a moderate yield (46%).

The original rhenium-catalyzed DODH and the recently developed molybdenum-catalyzed DODH do not differentiate based on diol substitution patterns, which warranted an in-depth theoretical study employing density functional theory (DFT) calculations. The dramatic difference in reactivity was found to be rooted in the creation of complexes between the substrate internal diols and the vanadium center that are too stable and therefore hinder efficient catalysis. The same explanation clarifies why the addition of ethylene glycol inhibits the reaction of otherwise reactive diols. Also, the good correspondence between experiment and theory will prove useful in the development of new and more efficient DODH technologies.

Experimental Section

Reaction Conditions A

Forty millimoles of diol, 2.0 mmol of catalyst (5 mol%, calculated with respect to the amount of vanadium), 500 mg of hexadecane (internal standard), and 100 mL of solvent (isopropyl alcohol) were mixed in a 300 mL PTFE cup and placed in a 400 mL Berghof autoclave with a magnetic stir bar (500 r.p.m.) and computer-controlled heating plate. The autoclave was sealed, pressurized with 15 bar of N_2 or H_2, and heated to 230 °C for 1000 min; the temperature typically stabilized between 225 and 230 °C, while the maximum pressure was 50–70 bar. When the system had cooled to room temperature, the pressure was released, and the reaction mixture was filtered to remove a fine, black precipitate and analyzed by GC (for determination of conversion and yields) and GC-MS (for observation and identification of other products).

Reaction Conditions B.

The experimental setup was identical to that in Reaction Conditions A except for the following changes: The reactions were conducted on half scale in a 150 mL Swagelok cylinder, which for 1020 min was placed in an aluminum block that had been preheated to 250 °C. Neither the temperature nor the pressure could be monitored in this experimental setup.

Computational Methods

DFT calculations were performed in Jaguar[30,31] with the B3LYP functional[32,33] with added D3 corrections.[34] We used the LACVP** basis set, which applies the Hay–Wadt ECP and basis set for vanadium, and the 6-31G** basis set for all other atoms.[35] Transition states were found by either a quadratic synchronous transit (QST) search[36] or the standard transition state search incorporated in the Jaguar suite. Intermediates were found by minimizing the transition states toward both the expected starting material and the expected final product, confirming the correct transition state. All intermediates and transition states were characterized by a full, analytic frequency calculation at 293.15 K that resulted in only positive frequencies for intermediates and exactly one imaginary frequency for transition states. Examination of the Gibbs-Free energy dependence on temperature, single point energy calculation with analytic frequency calculations in gas phase were carried out at temperatures between 300K and 600K with increments of 10 K. All transition states involving a proton transfer were modeled both as a direct transfer and as a transfer mediated through a water molecule. The transition state of the lowest energy is shown and the rest can be found in the supporting information. Approximate Gibbs free energies in the solution phase (G_{solv}) were obtained through addition of total Gibbs free energy and the solvation energy ($E_{SCF,solv} - E_{SCF,gas}$) obtained through a single point energy calculation with the Poisson–Boltzmann solver (PBF) [37,38] using standard parameters for methanol. The computational model

system was kept neutral to avoid complications when comparing charged and neutral species computationally.[39] We do not rule out the possibility of charged molecular species but rather suggest the neutral complexes treated in this work to be suitable computational models of the actual complexes. Visualization and comparison of structures were performed in Maestro.[40] The structural figures in the article were created with CYLview using the POV raytracer for rendering.[41]

Acknowledgements

The research was supported by a Sapere Aude research leader grant (PF) from the Danish Council for Independent Research (Grant no. 11-105487) and the Technical University of Denmark (LBN, Elite PhD scholarship).

Keywords: biomass • deoxydehydration • vanadium • polyols • DFT

[1] H. A. Wittcoff, B. G. Reuben, J. S. Plotkin in *Industrial Organic Chemistry 3rd Edition*, John Wiley & Sons, Inc**, 2013**.
[2] A. Corma, S. Iborra, A. Velty, *Chem. Rev.* **2007**, 107, 2411-2502.
[3] J. R. Dethlefsen, P. Fristrup, *ChemSusChem* **2015**, 8, 767-775.
[4] C. Boucher-Jacobs, K. M. Nicholas in *Selective Catalysis for Renewable Feedstocks and Chemicals*, (Eds.: K. M. Nicholas), Springer International Publishing, **2014**.
[5] S. Raju, M. E. Moret, J. M. Robertus, K. Gebbink, ACS Catal. 2015, 5, 281–300.
[6] A. R. Petersen, P. Fristrup, Chem. Eur. J. 2017, 23, 10235-10243.
[7] C. Boucher-Jacobs, K. M. Nicholas, Organometallics 2015, 34, 1985–1990.
[8] J. R. Dethlefsen, P. Fristrup, ChemCatChem 2015, 7, 1184–1196.
[9] M. Shiramizu, F. D. Toste, Angew. Chem. Int. Ed. 2012, 51, 8082–8086.
[10] J. R. Dethlefsen, D. Lupp, A. Teshome, L. B. Nielsen, P. Fristrup, *ACS Catal.* **2015**, 5, 3638–3647.
[11] G. Chapman, K. M. Nicholas, *Chem. Commun.* **2013**, 49, 8199–8201.
[12] T. V. Gopaladasu, K. M. Nicholas, *ACS Catal.* **2016**, 6, 1901–1904.
[13] A. R. Petersen, L. B. Nielsen, J. R. Dethlefsen, P. Fristrup, *ChemCatChem* **2018**, 10, 769-778.
[14] P. C. K. Vesborg, T. F. Jaramillo, *RSC Adv.* **2012**, 2, 7933−7947.
[15] E. Steffensmeier, K. M. Nicholas, *Chem. Commun.* **2017**, 54, 790-793.
[16] D. B. Larsen, A. R. Petersen, J. R. Dethlefsen, A. Teshome, P. Fristrup, *Chem. Eur. J.* **2016**, 22, 16621-16631.
[17] G. R. Kasner, C. Boucher-Jacobs, J. M. McClain II, K. M. Nicholas, *Chem. Commun.* **2016**, 52, 7257-7260.
[18] C. Boucher-Jacobs, K. M. Nicholas In *Selective Catalysis for Renewable Feedstocks and Chemicals*, (Eds. (K. M. Nicholas), Springer International Publishing **2014** pp. 163.
[19] J. R. Dethlefsen, D. Lupp, B.-C. Oh, P. Fristrup, *ChemSusChem* **2014**, 7, 425–428.
[20] V. Canale, L. Tonucci, M. Bressan, N. d'Alessandro, *Catal. Sci. Technol.* **2014**, 4, 3697–3704.
[21] I. Ahmad, G. Chapman, K. M. Nicholas, *Organometallics* **2011**, 30, 2810–2818.
[22] E. Arceo, J. A. Ellman, R. G. Bergman, *J. Am. Chem. Soc.* **2010**, 132, 11408–11409.
[23] A. Galindo, *Inorg. Chem.* **2016**, 55, 2284–2289.
[24] D. Wu, Y. Zhang, H. Su, *Chem. Asian J.* **2016**, 11, 1565–1571.
[25] D. Lupp, N. J. Christensen, J. R. Dethlefsen, P. Fristrup, *Chem. Eur. J.* 2015, 21, 3435–3442.
[26] X. Li, D. Wu, T. Lu, G. Yi, H. Su, Y. Zhang, *Angew. Chem. Int. Ed.* **2014**, 53, 4200–4204.
[27] Y.-Y. Jiang, J.-L. Jiang, F. Yao, *Organometallics* **2016**, 35, 3388–3396.
[28] L. C. de Vicente Poutás, M. C. Reis, R. Sanz, C. S. López, O. N. Faza, *Inorg. Chem.* **016**, 55, 11372–11382.
[29] S. Liu, A. Senocak, J. L. Smeltz, L. Yang, B. Wegenhart, J. Yi, H. I. Kenttämaa, E. A. Ison, M. M. Abu-Omar, *Organometallics* **2013**, 32, 3210–3219.
[30] Schrödinger Release 2015-2: Jaguar, version 8.8, Schrödinger, LLC, New York, NY, 2015.
[31] A. D. Bochevarov, E. Harder, T. F. Hughes, J. R. Greenwood, D. A. Braden, D. M. Philipp, D. Rinaldo, M. D. Halls, J. Zhang, R. A. Friesner, *Int. J. Quantum Chem.* 2013, 113, 2110–2142.
[32] A. D. Becke, *J. Chem. Phys.* 1993, 98, 5648–5652.
[33] A. D. Becke, *J. Chem. Phys.* **1993**, 98, 1372–1377.
[34] S. Grimme, J. Antony, S. Ehrlich, H. Krieg, *J. Chem. Phys.* **2010**, 132, 154104.
[35] P. J. Hay, W. R. Wadt, *J. Chem. Phys.* **1985**, 82, 299–310.
[36] T. A. Halgren, W. N. Lipscomb, *Chem. Phys. Lett.* **1977**, 49, 225–232.
[37] D. J. Tannor, B. Marten, R. Murphy, R. A. Friesner, D. Sitkoff, A. Nicholls, B. Honig, M. N. Ringnalda, W. A. Goddard III, *J. Am. Chem. Soc.* **1994**, 116, 11875–11882.
[38] B. Marten, K. Kim, C. Cortis, R. A. Friesner, R. B. Murphy, M. N. Ringnalda, D. Sitkoff, B. Honig, *J. Phys. Chem.* **1996**, 100, 11775–11788.
[39] P. Fristrup, M. Ahlquist, D. Tanner, P.-O. Norrby, *J. Phys. Chem. A* **2008**, 112, 12862–12867.
[40] Schrödinger Release 2015-2: Maestro, version 10.2, Schrödinger, LLC, New York, NY, 2015.
[41] CYLview, 1.0b; Legault, C. Y., Université de Sherbrooke, 2009 (http://www.cylview.org).

WILEY-VCH

Appendix D: Manuscript 2

ChemPubSoc Europe

DOI: 10.1002/chem.201603028

CHEMISTRY A European Journal Full Paper

Homogeneous Catalysis

Mechanistic Investigation of Molybdate-Catalysed Transfer Hydrodeoxygenation

Daniel B. Larsen[+], Allan R. Petersen[+], Johannes R. Dethlefsen, Ayele Teshome, and Peter Fristrup*[a]

Abstract: The molybdate-catalysed transfer hydrodeoxygenation (HDO) of benzyl alcohol to toluene driven by oxidation of the solvent isopropyl alcohol to acetone has been investigated by using a combination of experimental and computational methods. A Hammett study that compared the relative rates for the transfer HDO of five *para*-substituted benzylic alcohols was carried out. Density-functional theory (DFT) calculations suggest a transition state with significant loss of aromaticity contributes to the lack of linearity observed in the Hammett study. The transfer HDO could also be carried out in neat $PhCH_2OH$ at 175 °C. Under these conditions, $PhCH_2OH$ underwent disproportionation to yield benzaldehyde, toluene, and significant amounts of bibenzyl. Isotopic-labelling experiments (using $PhCH_2OD$ and $PhCD_2OH$) showed that incorporation of deuterium into the resultant toluene originated from the α position of benzyl alcohol, which is in line with the mechanism suggested by the DFT study.

Introduction

The production of organic platform chemicals from renewable feedstocks requires the development of reactions capable of reducing the oxygen content of biomass. A particularly abundant motif in biomass is the hydroxy group, and an emerging strategy to transform vicinal diols into the corresponding alkenes in a single step is the deoxydehydration (DODH) reaction, which typically involves the use of a rhenium-,[1–6] molybdenum-,[7–10] or vanadium-based[11] catalyst. We have recently shown[10] that the molybdate ion, prepared in situ by the addition of a slight excess of Bu_4NOH to a solution of $[(NH_4)_6Mo_7O_{24}]\cdot 4H_2O$ (AHM), catalyses the DODH reaction of aliphatic diols in *i*PrOH, which serves as both the solvent and reductant (Scheme 1).

In addition, it was discovered that aldehydes and ketones underwent transfer hydrogenation to the corresponding monohydric alcohols. Interestingly, it was also discovered that allylic and benzylic alcohols underwent transfer hydrodeoxygenation (HDO), exemplified by the transfer HDO of benzyl alcohol to toluene in a yield of 93 % (Scheme 2).

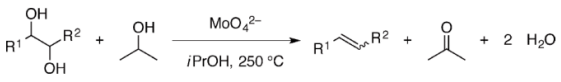

Scheme 1. Molybdate-catalysed DODH reaction of a vicinal diol into an alkene driven by the oxidation of *i*PrOH to acetone.

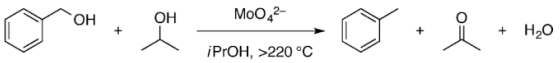

Scheme 2. Molybdate-catalysed transfer HDO of benzyl alcohol into toluene driven by the oxidation of *i*PrOH to acetone.

The traditional hydrogenation and HDO reactions, as well as the other hydrotreatment reactions of hydrodenitrogenation (HDN), hydrodesulfurisation (HDS), and hydrodemetallation (HDM), are employed to remove heteroatoms from fossil resources and saturate double bonds to produce high-quality fuels with good stability.[12,13] For biomass, the removal of oxygen is by far the most important reaction. Consequently, the catalytic upgrading of bio-oil, obtained from the pyrolysis of biomass, by means of the HDO reaction has been extensively reviewed.[14–16] Most research has focused on complete HDO and hydrogenation, in which the products are ultimately alkanes that are suitable biofuels. On the contrary, the production of biomass-derived chemicals requires the removal of oxygen and the preservation of some functionality; therefore, complete HDO with concomitant hydrogenation is not desirable.

The catalysts typically employed in the HDO of biomass are based on noble metals, for example, platinum,[17] ruthenium,[18] palladium,[19] or rhenium,[20] and the products have been alkanes. The hydrogenation of double bonds can, however, be avoided if non-noble metals are used; for example, MoO_3 catalyses the HDO of acetone to propylene,[21] tungsten oxides (in

[a] *D. B. Larsen,[+] Dr. A. R. Petersen,[+] Dr. J. R. Dethlefsen, Dr. A. Teshome, Dr. P. Fristrup*
Department of Chemistry, Technical University of Denmark
Kemitorvet 207, 2800 Kgs. Lyngby (Denmark)
E-mail: pf@kemi.dtu.dk

[+] *These authors contributed equally to this work.*

Supporting information for this article is available on the WWW under http://dx.doi.org/10.1002/chem.201603028.

© 2016 Wiley-VCH Verlag GmbH & Co. KGaA, Weinheim

ChemPubSoc Europe

CHEMISTRY A European Journal Full Paper

combination with Pd) catalyse the transformation of a cyclic vicinal diol into a cyclic monohydric alcohol,[22] and FeS_2 catalyses the HDO (or hydrogenolysis) of dibenzyl ether to toluene.[23] The suppression of the hydrogenation by the addition of a non-noble metal has been illustrated by Abu-Omar and co-workers, who showed that the addition of $ZnCl_2$ in the Pd-catalysed HDO of the carbohydrate-derived platform molecule 5-(hydroxymethyl)furfural[25] prevented the hydrogenation of carbon–carbon double bonds.[25] Herein, we present an alternative "transfer HDO" pathway catalysed by molybdate ions, which was discovered as a minor side reaction during the DODH of vicinal diol. Although the reaction has shown promising results in the conversion of allyl alcohol into propylene and 1,5-hexadiene, it is clear that a more efficient protocol must be developed for the reaction to obtain widespread use. To this end, we have carried out a mechanistic study of the Mo-catalysed transfer HDO that uses the deoxygenation of benzyl alcohol to toluene as a convenient model reaction. The reactivities of other functional groups (i.e., carbonyl compounds, acetals, ethers, amines, and thiols) were also screened.

Computational studies allowed for the proposal of a mechanism, which was corroborated by a combined computational and experimental Hammett study. Furthermore, deuterium-labelling studies were employed to ascertain deuterium incorporation into the products and the change in the product distribution.

Results and Discussion

Disproportionation of neat benzyl alcohol

Akin to our previous study of DODH of 1,2-hexanediol, we hypothesised that $PhCH_2OH$ could disproportionate.[8] Consequently, transfer HDO could be carried out under neat conditions and yield equimolar amounts of toluene and benzaldehyde (Scheme 3a).

$PhCH_2OH$ (1.51 g) and $[(Bu_4N)_2Mo_6O_{19}]$ (21.2 mg, 0.67 mol% of Mo) were heated to 220 °C in a microwave reactor for 3 hours. The three products toluene, bibenzyl, and benzaldehyde and starting-material benzyl alcohol were identified by means of GC and GC-MS (Table 1, entry 1).[26] The sum of the relative molar amounts of toluene and bibenzyl should equal the relative molar amount of benzaldehyde, but due to the presence of other minor by-products ("tribenzyl" and "tetrabenzyl"), this value was somewhat lower. The byproduct bibenzyl presumably forms according to Scheme 3b; even though two molecules of $PhCH_2OH$ end up in bibenzyl, only one molecule of $PhCH_2OH$ needs to be oxidised. The formation of the coupled bibenzyl product has also been observed when employing a rhenium catalyst, which was suggested to be the result of the formation of benzyl radicals that undergo coupling.[26]

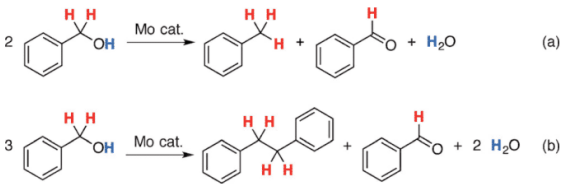

Scheme 3. Molybdenum-catalysed disproportionation of benzyl alcohol to benzaldehyde and a) toluene, or b) bibenzyl.

Deuterium-labelling experiments were carried out to gain further mechanistic insight. Separate experiments with $PhCH_2OD$ and $PhCD_2OH$ indicate where the hydrogen atoms end up in the products. By using $PhCH_2OD$, no deuterium atoms were incorporated in any of the products (Table 1, entry 2; GC-MS in the Supporting Information) and the relative molar amounts of the four components were essentially unchanged. $PhCD_2OH$, on the other hand, resulted in a significantly higher relative amount of bibenzyl relative to toluene (Table 1, entry 3). This outcome may suggest that the stronger C–D bond prevents the formation of toluene. The toluene formed was $PhCD_3$, the benzaldehyde was PhCDO, and the bibenzyl was $PhCD_2CD_2Ph$ (confirmed by GC-MS; see the Supporting Information).

In two competition experiments, equimolar amounts of $PhCH_2OH$ or $PhCD_2OH$ were mixed with *para*-methylbenzyl alcohol. The experiment with $PhCD_2OH$ had significantly more remaining starting material (31 vs. 16% $PhCH_2OH$), thus indicating a kinetic isotope effect (KIE) of greater than 1, which is indicative of C–H/D bond breakage in the rate-determining step (Table 1, entries 4 and 5). Although deuterium incorporation in the products was observed by GC-MS analysis, attempts to distinguish the different isotopologues of toluene and

Table 1. Product distributions obtained in the disproportionation of benzyl alcohol and deuterium-labelled benzyl alcohol at 220 °C.[a]

Reactant	Toluene [%]	Bibenzyl [%]	Benzaldehyde [%]	Benzyl alcohol [%]
$PhCH_2OH$	28	6	39	28
$PhCH_2OD$	31	7	39	24
$PhCD_2OH$	17	16	36	32
$PhCH_2OH$/*p*-$MePhCH_2OH$[b]	35/38	8/10	41/44	16/8
$PhCD_2OH$/*p*-$MePhCH_2OH$[b]	30/40	9/8	30/44	31/9
$PhCH_2OH$[c]	35	5	39	20
$PhCH_2OH$[d]	40	8	44	9

[a] Unless otherwise noted, a total of 1.5 g of reactant and 0.7 mol% of $[(Bu_4N)_2Mo_6O_{19}]$ were heated to 220 °C for 3 h in a microwave oven. [b] For *para*-$MePhCH_2OH$, the four major compounds were xylene, 1,2-di-*para*-tolylethane, *para*-methylbenzaldehyde, and *para*-methylbenzyl alcohol. [c] Heated to 200 °C for 6 h. [d] Heated to 240 °C for 2 h.

© 2016 Wiley-VCH Verlag GmbH & Co. KGaA, Weinheim

ChemPubSoc Europe

CHEMISTRY A European Journal Full Paper

xylene proved inconclusive. Consequently, attention was turned to the bibenzyl species. Only three bibenzyl species were detected, namely, $PhCD_2CD_2Ph$, *p*-$MePhCH_2CD_2Ph$, and *p*-$MePhCH_2CH_2$*p*-MePh (confirmed by GC-MS; see the Supporting Information), thus suggesting that H/D scrambling after the carbon–carbon bond-forming step does not occur.

To study the effect of temperature on the product distribution, the aforementioned disproportionation of neat $PhCH_2OH$ was repeated at intervals of 10 °C between 200 and 240 °C. The reaction was slower at 200 °C, but the product distribution after 6 hours was similar to the distribution obtained at 220 °C after 3 hours (Table 1, compare entries 1 and 6). When the reaction was run at 240 °C for 2 hours, the product distribution was not significantly affected, but the conversion was higher (Table 1, compare entries 1 and 7). This finding indicates that the formation of bibenzyl is not affected by entropy to an extent that could be expected for dimerisation.

Use of *i*PrOH as the solvent

As we previously have reported, *i*PrOH was suitable as the solvent and reductant.[10] The $[MoO_4]^{2-}$-catalysed transfer HDO of $PhCH_2OH$ to toluene at 240–250 °C was conducted in *i*PrOH. To follow the reaction progress, samples were taken out during the course of the reaction. Starting with 100 mmol of $PhCH_2OH$ and 0.358 mol% AHM (2.5 mol% with respect to Mo), the temporal evolution of the concentrations of $PhCH_2OH$, $PhCH_3$, and PhCHO was plotted (Figure 1). The heating plate was turned on at $t=0$, the temperature reached 230 °C after 40 minutes, and the reaction was complete within 3 h (see Figure S2 in the Supporting Information for the heating profile). When starting with 100 mmol of $PhCH_2OH$ in 200 mL of *i*PrOH, some PhCHO was produced and was subsequently reduced as the reaction progresses. For the first few cycles, $PhCH_2OH$ would compete with *i*PrOH for the role as the reductant and some disproportionation took place. A slower reaction with complete conversion of $PhCH_2OH$ within 4 hours resulted by substituting EtOH for *i*PrOH as the solvent and reductant (see Figure S3 in the Supporting Information).

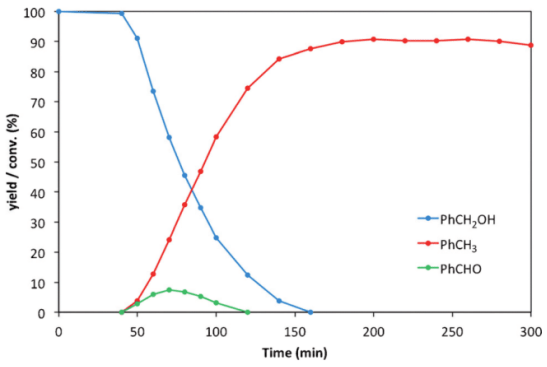

Figure 1. Temporal evolution of the concentrations of benzyl alcohol, toluene, and benzaldehyde.

To assess the nuclearity of the active catalytic species, the monomolybdate $[(Bu_4N)_2MoO_4]$ and polymolybdate $[(Bu_4N)_2Mo_6O_{19}]$ species were tested as catalysts for the HDO of benzyl alcohol. With catalyst loadings of 2.5 and 0.417 mol% for $[(Bu_4N)_2MoO_4]$ and $[(Bu_4N)_2Mo_6O_{19}]$ (2.5 mol% with respect to Mo), respectively, the two catalysts performed near identically (see Figure S4 in the Supporting Information). Interestingly, the two catalysts performed slightly faster than AHM (see Figure S5 in the Supporting Information). Consequently, when $[(Bu_4N)_2MoO_4]$ or $[(Bu_4N)_2Mo_6O_{19}]$ was used, the 100 mmol of benzyl alcohol were consumed within 140 minutes relative to 160 minutes when AHM was employed. This difference is attributed to the slow onset of the reaction between AHM and Bu_4NOH due to the poor solubility of AHM in *i*PrOH.

The near identical reactivities of $[(Bu_4N)_2MoO_4]$ and $[(Bu_4N)_2Mo_6O_{19}]$ suggest that the two catalysts have the same active catalytic species. Polymolybdates are usually obtained from weakly acidic solutions, whereas the Mo^{VI} ion is present as the $[MoO_4]^{2-}$ ion in strongly alkaline solutions. Given that AHM was used with the addition of Bu_4OH, it is proposed that a monomolybdate species similar to $[(Bu_4N)_2MoO_4]$ is the active catalytic species.

By using 100 mmol of benzyl alcohol and varying the amount of AHM, reactions were conducted with catalyst loadings of 0.5, 1.0, 2.5, and 5.0 mol% with respect to Mo (Figure 2). As expected, an increase in the catalyst loading led to a faster consumption of $PhCH_2OH$. A plot of the log of the initial rate of toluene formation v_0 against the log of the concentration of molybdenum gave a partial order with respect to molybdenum of 0.4 (see Figure S6 in the Supporting Information).

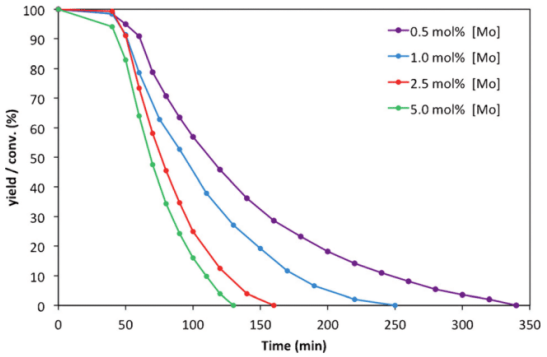

Figure 2. Temporal evolution of the concentration of benzyl alcohol while varying the catalyst loading.

By starting with 8 mmol of benzyl alcohol, the reaction order with respect to molybdenum was also investigated at a low substrate concentration. Reactions were conducted that used AHM loadings of 1.0, 2.5, 5.0, and 7.5 mol% with respect to Mo (see Figure S7 in the Supporting Information). The partial order of molybdenum was determined to be 1.0. When plotting $\ln\{[PhCH_2OH]/[PhCH_2OH]_0\}$ against time for the reac-

© 2016 Wiley-VCH Verlag GmbH & Co. KGaA, Weinheim

ChemPubSoc Europe

CHEMISTRY A European Journal Full Paper

tion with 1.0 mol% Mo, a straight line was obtained that corroborates that the reaction is first order with respect to molybdenum (see Figures S8 and S9 in the Supporting Information). The divergence in the partial order of molybdenum, observed for high and low benzyl alcohol concentrations, is attributed to the aforementioned disproportionation of benzyl alcohol at high concentration.

Dilution experiments were carried out by varying the starting concentrations of $PhCH_2OH$, yet leaving the ratio of $PhCH_2OH$/AHM constant. Hence, the required catalyst turnover number to reach full conversion remained unchanged. Reactions starting with 50, 20, 8, and 4 mmol of $PhCH_2OH$ were followed over time (see Figure S10 in the Supporting Information). The effect of diluting the reaction mixture became apparent when using 8 and 4 mmol of substrate, for which the consumption of $PhCH_2OH$ slowed and the formation of PhCHO was no longer observed.

A deuterium-labelling experiment was conducted to ascertain the role of disproportionation during the reaction. The transfer HDO reaction of 50 mmol of $PhCD(OH)CH_3$ was subjected to the standard reaction conditions in *i*PrOH. Significant disproportionation would result in scrambling of the deuterium atom in the α position, thus leading to the products $PhCHDCH_3$, $PhCH_2CH_3$, and $PhCD_2CH_3$. Nevertheless, the major product was always $PhCHDCH_3$, and minor products α-$[D_1]$-styrene, (1-deutero-1-isopropoxyethyl)benzene, and *meso*- and *rac*-2,3-bideutero-2,3-diphenylbutane were also detected. This outcome excludes the possibility that a significant proportion of the benzylic alcohol undergoes disproportionation to ethylbenzene and acetophenone with concomitant transfer hydrogenation of acetophenone to 1-phenylethanol and subsequent HDO to ethylbenzene. On this basis, we conclude that the main reaction is a transfer HDO that involves *i*PrOH and benzyl alcohol, with disproportionation of benzyl alcohol being of minor importance.

Functional-group reactivity

The versatility of the catalyst was investigated by testing the reactivity toward other functional groups in the benzylic position (Table 2). The secondary alcohol 1-phenylethanol was transformed into ethylbenzene in a yield of 57%, whereas the carbonyl compounds benzaldehyde and acetophenone underwent transfer hydrogenation and subsequent transfer HDO to form toluene and ethylbenzene in yields of 73 and 59%, respectively; furthermore, only trace amounts of styrene were observed from 1-phenylethanol and acetophenone. In the absence of a base, benzaldehyde dimethyl acetal was transformed into toluene in a yield of 61%. Benzoic acid was converted into the ester isopropyl benzoate under the reaction conditions; neither methyl benzoate nor benzyl isopropyl ether displayed any significant reactivity (Table 2, entries 5 and 6). Benzylamine and benzylmercaptan underwent transfer HDN and HDS in low and moderate yields, respectively (Table 2, entries 7 and 8), thus indicating that these reaction conditions might be applicable for the removal of benzylic thiol groups.

Table 2. Reactivity of functional groups in a benzylic position under the conditions optimised for the transfer HDO of benzyl alcohol.[a]

Entry	Substrate	Product	Yield [%]
1	$PhCH_2OH$	$PhCH_3$	93
2[b]	$PhCH_2OH$		60
3	PhCHO		73
4[b,c]	$PhCH(OCH_3)_2$		61
5	$PhCOOCH_3$		≈ 0[d]
6[c]	$PhCH_2OCH(CH_3)_2$		8
7	$PhCH_2NH_2$		13[e]
8	$PhCH_2SH$		57
9	$PhCH(OH)CH_3$	$PhCH_2CH_3$	57
10	$PhCH(O)CH_3$		59

[a] Unless otherwise noted, 100 mmol of substrate was used and the standard reaction conditions were employed with conversions of higher than 90%. [b] No Bu_4NOH was added. [c] An aliquot of 50 mmol of the substrate was added with 50 mmol of *para*-methylbenzyl alcohol. [d] The major product was isopropyl benzoate. [e] The conversion was 84%; the major product was not identified.

Hammett study

To gain further insight into the nature of the rate-determining step of the reaction, a Hammett study was carried out in line with earlier work[27–30] (see the Experimental section for details). The Hammett study was conducted at a concentration low enough to ensure that disproportionation did not affect the result. A series of competition experiments were undertaken in which the relative rates for the transfer HDO of *para*-substituted benzylic alcohols to benzyl alcohol were determined. In a typical experiment, samples were extracted during the HDO of a mixture of 4 mmol of a *para*-substituted benzylic alcohol and 4 mmol of benzyl alcohol, and the reaction progress (i.e., the conversion of the benzylic alcohols) was determined by GC by using hexadecane as an internal standard. The *para*-substituted benzylic alcohols used were *para*-methylbenzyl alcohol, *para*-(methylthio)benzyl alcohol, *para*-chlorobenzyl alcohol, *para*-fluorobenzyl alcohol, and *para*-(trifluoromethyl)benzyl alcohol. *para*-Methoxybenzyl alcohol was excluded from the analysis as *para*-methoxybenzyl isopropyl ether was produced in addition to *para*-methoxytoluene.

In a competition study, the reaction order in each component will be the same for both substrates under the assumption that the substrates follow the same mechanism. Provided that the reaction is first order with respect to the substrate, the relative reactivities of the two benzylic alcohols can be determined by plotting $\ln(X_0/X)$ (where X is the concentration of the *para*-substituted benzylic alcohol and X_0 the initial concentration) against $\ln(H_0/H)$ (where H is the concentration of the benzyl alcohol and H_0 the initial concentration) (Figure 3). The relative reactivity k_{rel} was obtained as the slope of the line (Table 3).

The values of k_{rel} were used to construct the Hammett plot in Figure 4. Albeit none of the Hammett parameters provide a good correlation, σ^+ and the Creary constant $\sigma^{\bullet}_C$ appear to show some correlation. The parameter $\sigma^{\bullet}_C$ is based on the rate of the thermal rearrangement of methylenecyclopropanes to isopropylidenecyclopropanes. This reaction probes the stabiliz-

© 2016 Wiley-VCH Verlag GmbH & Co. KGaA, Weinheim

ChemPubSoc Europe

CHEMISTRY A European Journal Full Paper

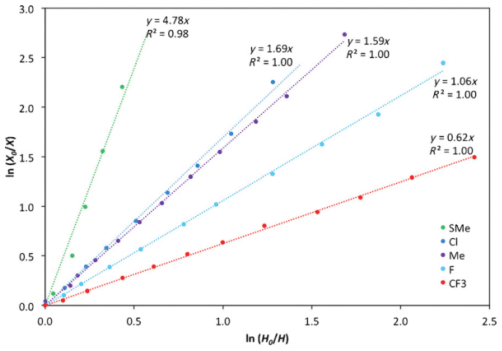

Figure 3. Kinetic data for competitive transfer HDO of benzyl alcohol and *para*-substituted benzylic alcohols.

Table 3. Relative rates and σ parameters for *para*-substituted benzylic alcohols.

Substituent	k_{rel}	σ	σ^+	$\sigma^\cdot_C$
CF_3	0.62	0.54	0.61	0.08
F	1.06	0.06	−0.07	−0.08
CH_3	1.59	−0.17	−0.31	0.11
Cl	1.70	0.23	0.11	0.12
SCH_3	4.78	0.00	−0.60	0.43

ing effect of various substituents on a benzylic radical-like transition state.[31] This intriguing result led us to postulate that the transition state is dissimilar to the archetypical reactions used to determine the various sets of σ values and that DFT calculations could be used to shed more light on this aspect.[32]

Computational studies

In an attempt to gain a deeper understanding of the mechanism of the transfer HDO, a theoretical study of the reaction was carried out by using DFT calculations in line with earlier studies.[28,29,33–35] The interpretation of Hammett studies – and in particular nonlinear Hammett plots – can often be assisted by using computational chemistry.[30] In particular, determination of the rate-determining transition state (TS) can shed light on the intrinsic details of the reaction mechanism.

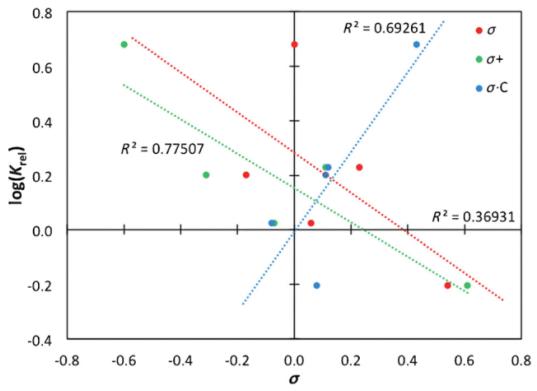

Figure 4. Hammett plot of log(k_{rel}) versus σ, σ^+, and $\sigma^\cdot_C$ values.

The transfer HDO reaction is expected to proceed by initiation through the reduction of Mo^{VI} to Mo^{IV} by using *i*PrOH as the reductant, in line with reported results for the DODH reaction.[9] Herein, we show that the Mo^{IV} moiety can oxidatively form a π-benzyl complex with the benzylic alcohol, which can undergo a reductive transfer hydrogenation, after isomerisation to a σ-benzyl complex, with concomitant reduction of Mo^{VI} to Mo^{IV}, thus closing the catalytic cycle of the reaction (Figure 5).

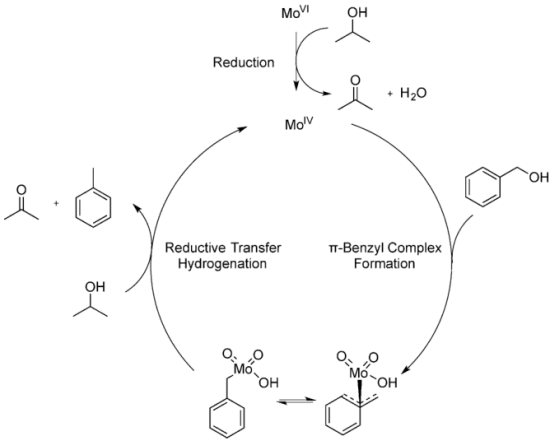

Figure 5. Tentative catalytic cycle for the Mo-catalysed transfer HDO reaction of $PhCH_2OH$ with *i*PrOH as the reductant.

This mechanism is based on the well-known ability of molybdenum to form π-allyl and π-benzyl complexes.[36–39] The first characterised η^3-benzyl/metal complex $[(C_5H_5)(\eta^3\text{-}C_6H_5CH_2)Mo(CO)_2]$ was reported by King and Fronzaglia in 1966.[40] Further evidence of this binding mode was reported by Cotton and LaPrade who reported the X-ray crystal structure of $[(C_5H_5)(\eta^3\text{-}p\text{-}MeC_6H_5CH_2)Mo(CO)_2]$.[41] In addition to the bonding between the Mo centre and the benzylic C1 atom (2.269 Å), bonding between Mo and C2 and Mo and C3 (2.364 and 2.480 Å, respectively) was observed. Moreover, the C–C bond lengths of the four-carbon-atom segment C7-C6-C5-C4 approached that of a *cis*-1,3-butadiene group, thus suggesting some localisation of the π system.[41] A variable-temperature NMR spectroscopic study of the same complex provided evidence of π-σ-π isomerisation of the benzyl ligand that occurs.[42] Loss of aromaticity in the benzene ring is characteristic of η^3-coordination in metal/benzyl complexes.[38]

In the DFT calculations, which used the B3LYP-D3 functional and the LACVP** basis set, the molybdenum catalysts were treated as neutral complexes with oxide and hydroxide ligands. The calculations were carried out at atmospheric pressure at both 293.15 and 523.15 K (the latter is discussed herein and re-

© 2016 Wiley-VCH Verlag GmbH & Co. KGaA, Weinheim

ChemPubSoc Europe

CHEMISTRY A European Journal Full Paper

ported in the Supporting Information; data for the calculations at 293.15 K are also available in the Supporting Information). We are aware of the strong acidity of $[H_2MoO_4]$ and, therefore, complemented our neutral model system with additional calculations involving charged species. A charged model system will suffer from incorrect charge distribution in DFT calculations, although modern solvation models might remedy this artefact to some degree. However, transition states were also modelled in the deprotonated state to assure that the charged species did not cause changes to the mechanistic pathway (see the Supporting Information for further details). Both $[MoO_3]$ and $[MoO_2(OH)_2]$ were considered as the starting moieties for the Mo^{VI} species, and the latter was found to be more stable, which corresponds to the reported results for $[CH_3ReO_2]$ versus $[CH_3ReO(OH)_2]$.[43] This model system is based on the assumption that the heptamolybdate complex AHM will exist mainly as mononuclear molybdenum/oxo complexes at the high temperatures used. This assumption was in agreement with previous work that used the same model system, in which calculations showed higher Gibbs Free energies for the dinuclear complexes.[7] In addition, the experimental results that used the mononuclear $[(Bu_4N)_2MoO_4]$ complex further supports this assumption. We ruled out the existence of molybdenum/hydride intermediates because the molybdenum/hydride complexes proved significantly less stable than the oxo complexes. In previous studies, reduction reactions with molecular hydrogen as the reductant were also proven to be energetically unfavourable.[10]

The initial reduction from Mo^{VI} to Mo^{IV} is expected to go through coordination of *i*PrOH to the Mo^{VI} centre; furthermore, *i*PrOH coordinates as the $iPrO^-$ ion and the proton is transferred to an oxo ligand. This coordination is followed by a reduction reaction, thus yielding a Mo^{IV} species, acetone, and water. The calculated energy profiles of these reactions are shown in Figure 6.

The pathway by complexation of *i*PrOH with $[MoO_3]$ [**1**–**2**] is favoured over complexation with $[MoO_2(OH)_2]$ by 4.5 [**1′**–**2′**] and 14.5 kcal mol^{-1} [**1′**–**2′**] (Figure 6). In addition, this pathway is also favoured at the reduction step because [**2**–**3**] is 14.5 kcal mol^{-1} lower in energy than [**2′**–**3**].

With respect to the π-benzyl complex formation, two possible pathways were considered (Scheme 4). In pathway A, con-

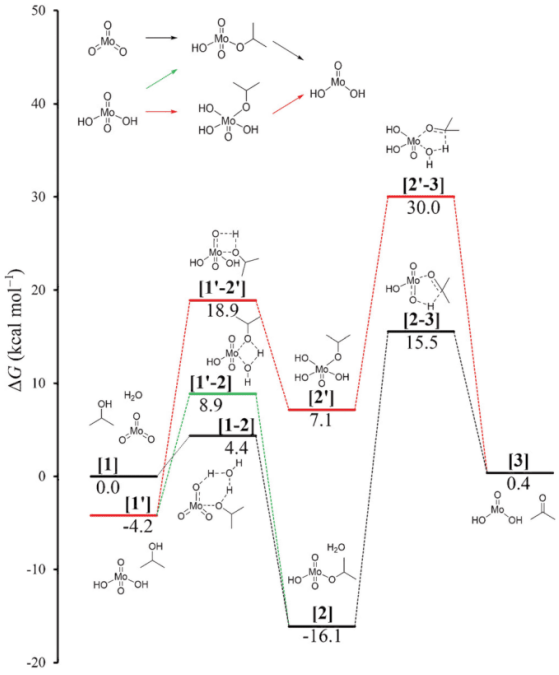

Figure 6. Calculated energy profiles for the reduction of Mo^{VI} to Mo^{IV} with *i*PrOH as the reductant.

densation of the Mo^{IV} moiety [**4**] with $PhCH_2OH$ gives [**5**], which was followed by a [2,3]-sigmatropic rearrangement to yield the π-benzyl complex [**6**]. In pathway B, direct reaction through transition state [**4**–**6**] with the expulsion of water yields the same π-benzyl complex [**6**].

The two energetic profiles for the generation of the Mo/σ-benzyl complex [**7**] show that the energy barrier for the oxidative rearrangement [**5**–**6**] is significantly lower than the [**4**–**6**] transition by 26.2 kcal mol^{-1} (Figure 7). Further calculations showed that complex [**6**] would isomerise toward the σ-benzyl complex [**7**], thus leaving the molybdenum centre bonded to the CH_2 group through a σ bond. This isomerisation is driven by the energetically favourable re-aromatisation of the ben-

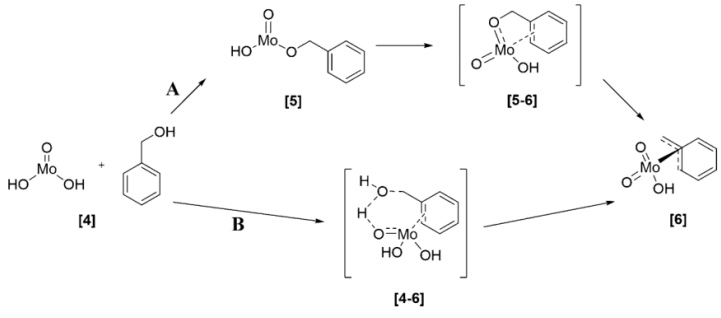

Scheme 4. The two investigated pathways for the formation of the Mo/π-benzyl complex.

© 2016 Wiley-VCH Verlag GmbH & Co. KGaA, Weinheim

ChemPubSoc Europe

CHEMISTRY A European Journal Full Paper

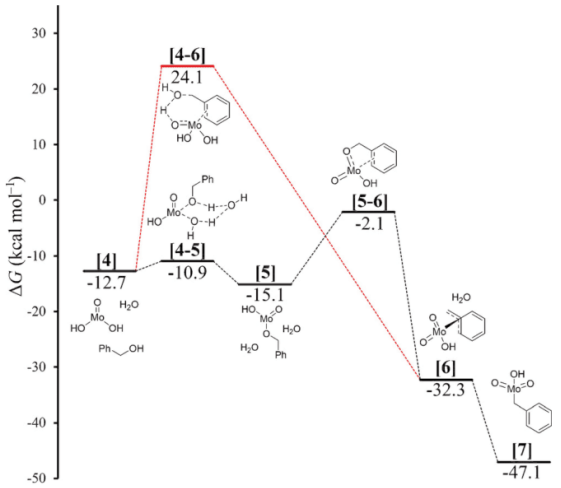

Figure 7. Calculated energy profiles for the oxidative generation of the Mo^{VI}/σ-benzyl complex.

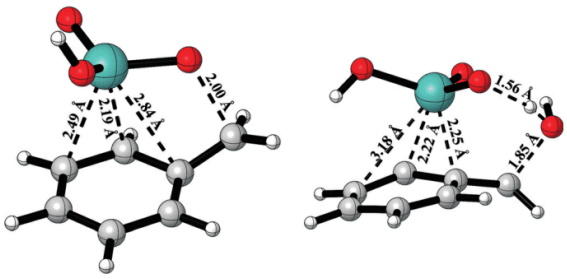

Figure 8. Transition states for the oxidative generation of the Mo/benzyl complex. Left: the favoured TS [**5**–**6**]; right: the disfavoured TS [**4**–**6**].

zene ring. The two transition states for the oxidative generation of the Mo/benzyl complex are shown in Figure 8.

The reduction of oxomolybdenum(VI) to oxomolybdenum(IV) by *i*PrOH can proceed as suggested previously,[10] which upon subsequent coordination of $PhCH_2OH$ results in the formation of intermediate [**5**]. An alternative mechanism is if the coordination of $PhCH_2OH$ to the molybdenum centre took place prior to the oxidation of *i*PrOH, which would require an intermediate with both $PhCH_2OH$ and *i*PrOH bonded to Mo^{VI} species [**I**]. However, for rhenium it has already been shown that benzyl alcohol can also be used as a reductant in this type of reduction reaction, thus yielding benzaldehyde.[44] Calculations were carried out that used a transition state similar to [**2**–**3**] to differentiate between the oxidation of *i*PrOH and $PhCH_2OH$ (Scheme 5).

The energy difference for the two different reduction pathways to [**II**] and [**III**] is only 0.3 kcal mol^{-1} (the oxidation of $PhCH_2OH$ is favoured), which shows that both pathways are possible and that the choice of pathway can be influenced by employing different concentrations (Scheme 5). Furthermore,

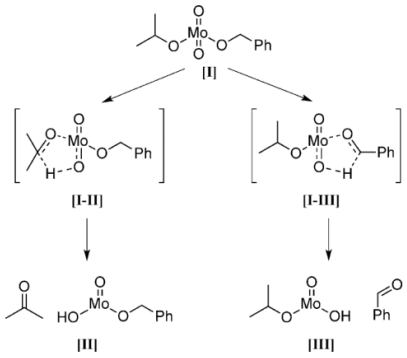

Scheme 5. Two possible oxidation pathways from a Mo^{IV} complex coordinated to benzyl alcohol and *i*PrOH.

this result explains why a small amount of benzaldehyde is observed, even when the transfer HDO of $PhCH_2OH$ is conducted in *i*PrOH. Toward the end of the reaction, the formed PhCHO is presumably reduced to $PhCH_2OH$ followed by the transfer HDO reaction; furthermore, this transfer hydrogenation is assumed to follow a Meerwein–Schmidt–Ponndorf–Verley (MSPV) mechanism with direct hydrogen transfer through a six-membered transition state.[45] No change in the oxidation state of the catalyst is involved in this reaction; therefore, the oxidation state of the molybdenum species can be either +IV or +VI. Consequently, both pathways were calculated and showed similar energy barriers, namely, 37.3 and 37.0 kcal mol^{-1} for Mo^{IV} and Mo^{VI}, respectively, relative to [**2**] and 20.9 and 21.1 kcal mol^{-1}, respectively, relative to [**1**]. These energies correlate well with previously calculated results for the aluminium-catalysed MSPV reductions, which were found to have transition-state energies of roughly 15–20 kcal mol^{-1}.[45] These transition states are shown in Figure 9.

Deuterium-labelling experiments (see below) proved that the hydrogen transfer to toluene takes place reductively; that is, a hydride ion is transferred from the carbon atom in *i*PrOH rather than proton transfer from the oxygen atom. We suggest a complexation of *i*PrOH to the σ-benzyl complex [**7**], which can then undergo hydride transfer from the π complex, thus yielding toluene, acetone, and the Mo^{IV} moiety $[MoO(OH)_2]$. Direct transition from [**7**] to [**9**] was considered, but no feasible transition state could be found. The transition state for this hydride transfer is shown in Figure 11, and these two last steps (i.e., transition states [**7**–**8**] and [**8**–**9**]), with [**4**] as an end point have been added to a full-energy diagram of the catalytic cycle in Figure 10 (constructed from [**4**] because the previous steps serve as initiation). This conversion of benzyl alcohol and isopropanol into toluene, acetone, and water is exergonic by 37.4 kcal mol^{-1}, somewhat lower than the difference between [**4**] and [**9**] due to lower stabilisation from intermolecular bonding in [**9**].

Starting with the deprotonated species $[MoO_2(OH)^-]$, instead of $[MoO(OH)_2]$, the energies of both the transition states and the intermediates of the catalytic cycle in Figure 10 were also determined (see Figure S11 in the Supporting Information). A

© 2016 Wiley-VCH Verlag GmbH & Co. KGaA, Weinheim

ChemPubSoc Europe
CHEMISTRY A European Journal Full Paper

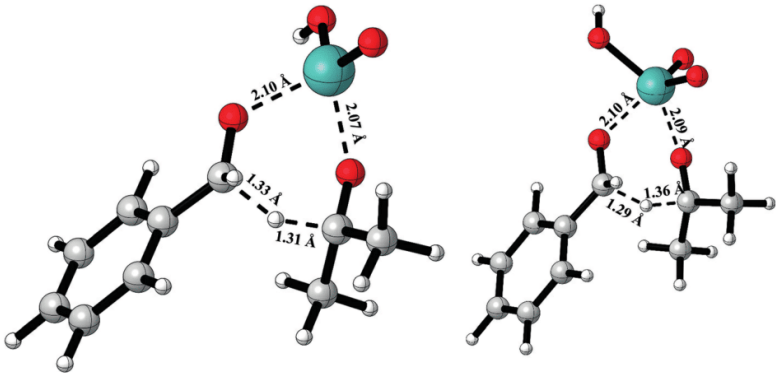

Figure 9. Transition states of the MSPV reduction catalysed by Mo^{IV} (left) and Mo^{VI} (right) species.

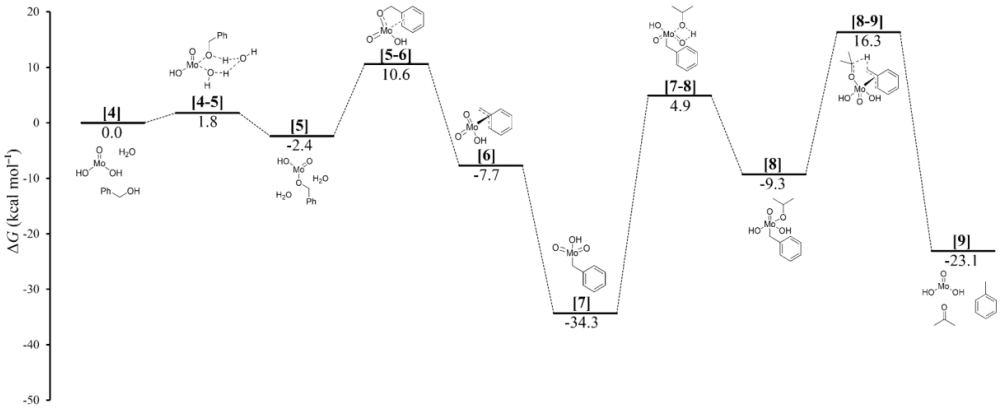

Figure 10. Energy profile for the proposed catalytic cycle for Mo-catalysed transfer HDO of benzyl alcohol with *i*PrOH as the reductant.

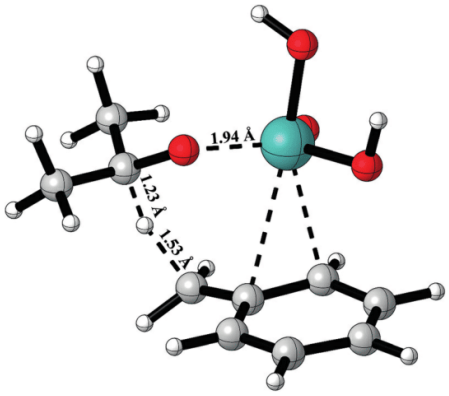

Figure 11. Transition state for the final hydride transfer ([**8**–**9**]).

good agreement between the two sets of calculations that used the charged and neutral catalytic species was observed, although the results differ in the stabilisation of the π complexes ([**6**] in Figure 10 and Figure S11 in the Supporting Information), thus leading to an increase of 3.2 kcal mol^{-1} in the energetic span of the reaction. Due to this increase, the neutral model system was used throughout the following calculations because this system was deemed to be the more probable.

For the final validation of this mechanism, the results from the Hammett study (Figure 4) were reconsidered in light of the proposed mechanism. The lack of linearity with any of the σ values shows that the Hammett study alone cannot be used to elucidate the reaction mechanism. The study can be used for validation of our computational calculations, thus examining the correlation between experiment and theory. Figure 10 shows transition state [**8**–**9**] to be the rate-determining step; therefore, the gap between [**7**] and this transition state constitutes the energetic span for the reaction. However, we note that [**5**–**6**] and [**7**–**8**] are also high in energy, and all these transition states were modelled for the various *para* substituents incorporated in the Hammett study to make certain that the rate-determining step does not switch for any of the *para* substituents. For an evaluation, the turnover frequencies (TOFs) for each mechanistic pathway were calculated by using the

© 2016 Wiley-VCH Verlag GmbH & Co. KGaA, Weinheim

ChemPubSoc Europe

CHEMISTRY A European Journal Full Paper

AUTOF program,[46] and the relative TOF values gave a linear correlation when compared with the experimentally obtained relative reaction rates (Figure 12). The use of relative TOF values presents a method for dealing with reaction pathways with two or more rate-determining steps and also works in cases with only one rate-determining step for which the relative TOF value approaches the k_{rel} value.

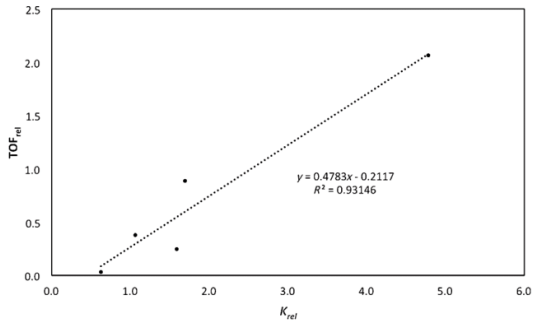

Figure 12. Correlation of the calculated relative TOF values with relative reactivities determined in the competition experiments (Hammett study).

The slope of the linear regression should equal one, but deviations are often observed when correlating theoretical and experimental results of the Hammett studies.[33] However, the overall good correlation between experiment and theory for the proposed mechanism does not explain the nonlinearity observed in the Hammett study. Inspection of TS [**5**–**6**] and [**8**–**9**] demonstrates a significant loss in aromaticity in the benzene ring as a result of the π-benzyl bond (Figure 13). In TS [**5**–**6**], the C–C bonds of the benzene ring involved in the π-benzyl bond are elongated. In contrast, the C–C bond lengths of the benzyl ring in TS [**8**–**9**] alternate between longer and shorter bond values. We propose that the loss of aromaticity that leads to localisation of the π system results in the nonlinearity of the experimental Hammett studies because Hammett theory and correlation to σ values is only suitable for aromatic systems.

Conclusions

The molybdate-catalysed transfer hydrodeoxygenation (HDO) reaction was investigated by using a combination of experimental and theoretical methods. A Hammett study that compared the relative rates for the transfer HDO of five *para*-substituted benzylic alcohols was shown not to correlate with a variety of σ values. We attribute this outcome to the significant loss of aromaticity of the benzyl ring in both TS [**5**–**6**] and [**8**–**9**], as demonstrated by using DFT calculations. The transfer HDO could also be carried out in neat $PhCH_2OH$ at temperatures as low as 175 °C. Under these conditions, $PhCH_2OH$ underwent disproportionation to yield benzaldehyde, toluene, and significant amounts of bibenzyl. Isotopic-labelling experiments (with $PhCH_2OD$ and $PhCD_2OH$) showed incorporation of deuterium atoms into the resultant toluene that originated from the α position of benzyl alcohol, which is in line with the mechanism proposed by the DFT study. The increased mechanistic understanding of the molybdate-catalysed transfer HDO reported herein will be important for further expanding the scope of the reaction to form biomass-derived chemical building blocks.

Experimental Section

Standard reaction conditions

Substrate (441 mg, 100 mmol) $[(NH_4)_6Mo_7O_{24}]\cdot 4H_2O$ (2.5 mol% of Mo), Bu_4NOH in MeOH (7.5 mL, 1 M), hexadecane as an internal standard (1 g), and *i*PrOH (150 mL) were mixed in a 400 mL Berghof autoclave with a magnetic stir bar (500 rpm) and a computer-controlled heating plate. The autoclave was sealed, pressurised with N_2 (15 bar), and heated to 250 °C for 8 h; the temperature typically stabilised between 240 and 250 °C, whereas the maximum pressure was 80–85 bar. The autoclave was sometimes equipped with a setup that allowed liquid sampling during the reaction. In these experiments, the volume of *i*PrOH was increased to 200 mL. The reaction mixture was analysed by means of GC for determination of the conversion and yields and by GC-MS for observation and identification of other products.

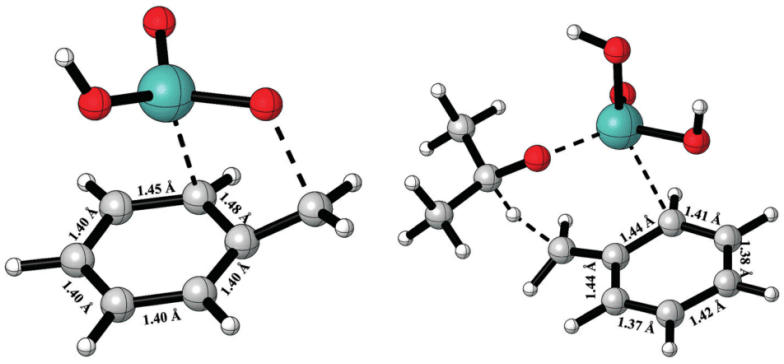

Figure 13. Loss of aromaticity in the benzyl ring (C–C bond lengths are shown). Left: TS [**5**–**6**]; right: TS [**8**–**9**].

© 2016 Wiley-VCH Verlag GmbH & Co. KGaA, Weinheim

ChemPubSoc Europe

CHEMISTRY A European Journal Full Paper

For reactions conducted at lower concentrations (4, 8, 20, and 50 mmol), the ratio of the reactants was kept constant, except for the volume of *i*PrOH. For example, if 20 mmol of benzyl alcohol was used, the quantity of AHM, 1 M Bu_4NOH in MeOH and hexadecane was divided by 5; however, 200 mL of *i*PrOH was still used.

Hammett study

The Hammett study was carried out as five separate competition experiments, in which a mixture of $PhCH_2OH$ (4 mmol), a *para*-substituted benzylic alcohol (4 mmol), $[(NH_4)_6Mo_7O_{24}]\cdot 4H_2O$ (35.4 mg, 2.5 mol% of Mo), Bu_4NOH in MeOH (0.6 mL of 1 M), hexadecane as an internal standard (80 mg), and *i*PrOH (200 mL) were mixed in a 400 mL Berghof autoclave with a magnetic stir bar (500 rpm) and a computer-controlled heating plate. The autoclave was sealed, pressurised with N_2 (15 bar), and heated to 250 °C for 7 h; the temperature typically stabilised between 240 and 250 °C. The autoclave was equipped with a setup that allowed liquid sampling during the reaction and samples were extracted at intervals of 20 min. The reaction mixture was analysed by means of GC for determination of the conversion and yields. By plotting $\ln(X_0/X)$ versus $\ln(H_0/H)$ (H and X are the concentrations of $PhCH_2OH$ and the *para*-substituted benzylic alcohol at time t, respectively, and H_0 and X_0 are the same quantities at time $t=0$) a straight line with an intercept at $y=0$ and a slope equal to the relative rate of $k_{rel}=k_X/k_H$ was obtained.[30] The Hammett plot was constructed by plotting $\log(k_{rel})$ versus different sets of σ values.[31,47–50]

DFT calculations

DFT calculations were performed by using Jaguar[51] with the B3LYP functional[52,53] and added D3 corrections.[54] We used the LACVP** basis set, which applies the Hay–Wadt ECP and basis set for molybdenum, and the 6–31G** basis set for the other atoms.[55] Transition states were found by using either a quadratic synchronous transit (QST) search[56] or the standard transition-state search incorporated in the Jaguar suite. Intermediates were found by minimising the transition states toward both the expected starting material and the expected final product, thus confirming the correct transition state. The intermediates and transition states were characterised by carrying out full analytic frequency calculations at 293.15 and 523.15 K, which resulted in only positive frequencies for intermediates and exactly one imaginary frequency for the transition states. The calculations were performed at atmospheric pressure, and the reported values are given at 523.13 K (see the Supporting Information for the values calculated at 293.15 K). The transition states involving hydrogen transfer were modelled as both a direct transfer and as a transfer mediated through a water molecule. The transition state of the lowest energy is shown and the other transition state can be found in the Supporting Information. Approximate Gibbs free energies in the solution phase G_{solv} were obtained through the addition of the total Gibbs free energy (at 298.15 or 523.15 K) and the solvation energy ($E_{SCF,solv}-E_{SCF,gas}$) obtained through a single-point energy calculation with the Poisson–Boltzmann solver (PBF)[57,58] by using standard parameters for methanol (SCF: Self-Consistent Field). The computational model system was kept neutral to avoid complications when comparing the charged and neutral species computationally.[59] We do not rule out the possibility of charged molecular species, but rather suggest that the neutral complexes treated in this study are suitable computational models of the actual complexes. The main mechanism was also modelled in its deprotonated state (see the Supporting Information for details). The visualisation and comparison of the structures were performed by using Maestro.[60] The structural figures presented herein were created with CYLview using the POV raytracer for rendering.[61]

Acknowledgements

This work was supported by a Sapere Aude research leader grant (P.F.) from the Danish Council for Independent Research, Grant 11-105487, and a grant from the Villum Foundation, Grant 341/300-123012.

Keywords: deoxygenation · density functional calculations · Hammett · homogeneous catalysis · molybdenum

[1] J. R. Dethlefsen, P. Fristrup, *ChemSusChem* **2015**, *8*, 767 – 775.
[2] S. Raju, M.-E. Moret, R. J. M. Klein Gebbink, *ACS Catal.* **2015**, *5*, 281 – 300.
[3] J. R. Dethlefsen, P. Fristrup, *ChemCatChem* **2015**, *7*, 1184 – 1196.
[4] C. Boucher-Jacobs, K. M. Nicholas, *Organometallics* **2015**, *34*, 1985 – 1990.
[5] C. Boucher-Jacobs, K. M. Nicholas, *Top. Curr. Chem.* **2014**, *353*, 163 – 184.
[6] S. Raju, J. T. B. H. Jastrzebski, M. Lutz, L. Witteman, J. R. Dethlefsen, P. Fristrup, M.-E. Moret, R. J. M. Klein Gebbink, *Inorg. Chem.* **2015**, *54*, 11031 – 11036.
[7] L. Hills, R. Moyano, F. Montilla, A. Pastor, A. Galindo, E. Álvarez, F. Marchetti, C. Pettinari, *Eur. J. Inorg. Chem.* **2013**, 3352 – 3361.
[8] J. R. Dethlefsen, D. Lupp, B.-C. Oh, P. Fristrup, *ChemSusChem* **2014**, *7*, 425 – 428.
[9] D. Lupp, N. J. Christensen, J. R. Dethlefsen, P. Fristrup, *Chem. Eur. J.* **2015**, *21*, 3435 – 3442.
[10] J. R. Dethlefsen, D. Lupp, A. Teshome, L. B. Nielsen, P. Fristrup, *ACS Catal.* **2015**, *5*, 3638 – 3647.
[11] G. Chapman, K. M. Nicholas, *Chem. Commun.* **2013**, *49*, 8199 – 8201.
[12] E. Furimsky, *Appl. Catal. A* **2000**, *199*, 147 – 190.
[13] H. A. Wittcoff, B. G. Reuben, J. S. Plotkin, *Industrial Organic Chemicals*, Wiley, Hoboken, 3rd ed., **2013**.
[14] P. M. Mortensen, J.-D. Grunwaldt, P. A. Jensen, K. G. Knudsen, A. D. Jensen, *Appl. Catal. A* **2011**, *407*, 1 – 19.
[15] H. Wang, J. Male, Y. Wang, *ACS Catal.* **2013**, *3*, 1047 – 1070.
[16] Y. Nakagawa, S. Liu, M. Tamura, K. Tomishige, *ChemSusChem* **2015**, *8*, 1114 – 1132.
[17] A. Corma, O. de La Torre, M. Renz, N. Villandier, *Angew. Chem. Int. Ed.* **2011**, *50*, 2375 – 2378; *Angew. Chem.* **2011**, *123*, 2423 – 2426.
[18] S. Stanowski, K. M. Nicholas, R. S. Srivastava, *Organometallics* **2012**, *31*, 515 – 518.
[19] A. D. Sutton, F. D. Waldie, R. Wu, M. Schlaf, L. A. P. Silks, J. C. Gordon, *Nat. Chem.* **2013**, *5*, 428 – 432.
[20] N. Ota, M. Tamura, Y. Nakagawa, K. Okumura, K. Tomishige, *Angew. Chem. Int. Ed.* **2015**, *54*, 1897 – 1900; *Angew. Chem.* **2015**, *127*, 1917 – 1920.
[21] T. Prasomsri, T. Nimmanwudipong, Y. Román-Leshkov, *Energy Environ. Sci.* **2013**, *6*, 1732 – 1738.
[22] Y. Amada, N. Ota, M. Tamura, Y. Nakagawa, K. Tomishige, *ChemSusChem* **2014**, *7*, 2185 – 2192.
[23] N. Ji, X. Wang, C. Weidenthaler, B. Spliethoff, R. Rinaldi, *ChemCatChem* **2015**, *7*, 960 – 966.
[24] R.-J. van Putten, J. C. van der Waal, E. de Jong, C. B. Rasrendra, H. J. Heeres, J. G. de Vries, *Chem. Rev.* **2013**, *113*, 1499 – 1597.
[25] B. L. Wegenhart, L. Yang, S. C. Kwan, R. Harris, H. I. Kenttämaa, M. M. Abu-Omar, *ChemSusChem* **2014**, *7*, 2742 – 2747.
[26] G. R. Kasner, C. Boucher-Jacobs, J. M. McClain, K. M. Nicholas, *Chem. Commun.* **2016**, *52*, 7257 – 7260.
[27] L. Keinicke, P. Fristrup, P.-O. Norrby, R. Madsen, *J. Am. Chem. Soc.* **2005**, *127*, 15756 – 15761.
[28] P. Fristrup, M. Kreis, A. Palmelund, P.-O. Norrby, R. Madsen, *J. Am. Chem. Soc.* **2008**, *130*, 5206 – 5215.
[29] I. S. Makarov, P. Fristrup, R. Madsen, *Chem. Eur. J.* **2012**, *18*, 15683 – 15692.

 © 2016 Wiley-VCH Verlag GmbH & Co. KGaA, Weinheim

ChemPubSoc Europe

CHEMISTRY
A European Journal
Full Paper

[30] D. Lupp, N. J. Christensen, P. Fristrup, *Dalton Trans.* **2014**, *43*, 11093 – 11105.
[31] X. Creary, M. E. Mehrsheikh-Mohammadi, S. McDonald, *J. Org. Chem.* **1987**, *52*, 3254 – 3263.
[32] N. Christensen, P. Fristrup, *Synlett* **2015**, 508 – 513.
[33] J. Mielby, A. Riisager, P. Fristrup, S. Kegnæs, *Catal. Today* **2013**, *203*, 211 – 216.
[34] P. Fristrup, M. Tursky, R. Madsen, *Org. Biomol. Chem.* **2012**, *10*, 2569 – 2577.
[35] C. Engelin, T. Jensen, S. Rodriguez-Rodriguez, P. Fristrup, *ACS Catal.* **2013**, *3*, 294 – 302.
[36] V. S. Joshi, V. K. Kale, K. M. Sathe, A. Sarkar, S. S. Tavale, C. G. Suresh, *Organometallics* **1991**, *10*, 2898 – 2902.
[37] S. H. Lin, G. H. Lee, S. M. Peng, R. S. Liu, *Organometallics* **1993**, *12*, 2591 – 2599.
[38] B. M. Trost, L. C. Czabaniuk, *Angew. Chem. Int. Ed.* **2014**, *53*, 2826 – 2851; *Angew. Chem.* **2014**, *126*, 2868 – 2895.
[39] H. Teruel, N. Romero, I. Henriquez, *Transition Met. Chem.* **1995**, *20*, 426 – 429.
[40] R. B. King, A. Fronzaglia, *J. Am. Chem. Soc.* **1966**, *88*, 709 – 712.
[41] F. A. Cotton, M. D. LaPrade, *J. Am. Chem. Soc.* **1968**, *90*, 5418 – 5422.
[42] F. A. Cotton, T. J. Marks, *J. Am. Chem. Soc.* **1969**, *91*, 1339 – 1346.
[43] X. Li, D. Wu, T. Lu, G. Yi, H. Su, Y. Zhang, *Angew. Chem. Int. Ed.* **2014**, *53*, 4200 – 4204; *Angew. Chem.* **2014**, *126*, 4284 – 4288.
[44] C. Boucher-Jacobs, K. M. Nicholas, *ChemSusChem* **2013**, *6*, 597 – 599.
[45] R. Cohen, C. R. Graves, S. T. Nguyen, J. M. L. Martin, M. A. Ratner, *J. Am. Chem. Soc.* **2004**, *126*, 14796 – 14803.
[46] S. Kozuch, *WIREs Comput. Mol. Sci.* **2012**, *2*, 795 – 815.
[47] C. Hansch, A. Leo, R. W. Taft, *Chem. Rev.* **1991**, *91*, 165 – 195.
[48] C. Hansch, H. Gao, *Chem. Rev.* **1997**, *97*, 2995 – 3060.
[49] L. M. Stock, H. C. Brown, *Adv. Phys. Org. Chem.* **1963**, *1*, 35 – 154.
[50] H. C. Brown, D. P. Kelly, M. Periasamy, *Proc. Natl. Acad. Sci. USA* **1980**, *77*, 6956 – 6960.
[51] Schrödinger Release 2015 – 2012: Jaguar, version 8.8, Schrödinger, LLC, New York, NY, **2015**.
[52] A. D. Becke, *J. Chem. Phys.* **1993**, *98*, 5648 – 5652.
[53] A. D. Becke, *J. Chem. Phys.* **1993**, *98*, 1372 – 1377.
[54] S. Grimme, J. Antony, S. Ehrlich, H. Krieg, *J. Chem. Phys.* **2010**, *132*, 154104 – 154122.
[55] P. J. Hay, W. R. Wadt, *J. Chem. Phys.* **1985**, *82*, 299 – 310.
[56] T. A. Halgren, W. N. Lipscomb, *Chem. Phys. Lett.* **1977**, *49*, 225 – 232.
[57] D. J. Tannor, B. Marten, R. Murphy, R. A. Friesner, D. Sitkoff, A. Nicholls, B. Honig, M. Ringnalda, W. A. Goddard, *J. Am. Chem. Soc.* **1994**, *116*, 11875 – 11882.
[58] B. Marten, K. Kim, C. Cortis, R. A. Friesner, R. B. Murphy, M. N. Ringnalda, D. Sitkoff, B. Honig, *J. Phys. Chem.* **1996**, *100*, 11775 – 11788.
[59] P. Fristrup, M. Ahlquist, D. Tanner, P.-O. Norrby, *J. Phys. Chem. A* **2008**, *112*, 12862 – 12867.
[60] Schrödinger Release 2015 – 2012: Maestro, version 10.2, Schrödinger, LLC, New York, NY, **2015**.
[61] CYLview, 1.0b, C. Y. Legault, Université de Sherbrooke, **2009**, http://www.cylview.org.

Received: June 25, 2016
Published online on October 10, 2016

 © 2016 Wiley-VCH Verlag GmbH & Co. KGaA, Weinheim

Appendix E: Manuscript 3

European Polymer Journal 102 (2018) 1–8

Contents lists available at ScienceDirect

European Polymer Journal

journal homepage: www.elsevier.com/locate/europolj

Investigation of curing rates of bio-based thiol-ene films from diallyl 2,5-furandicaboxylate

Daniel Bo Larsen[a,b], Rene Sønderbæk-Jørgensen[a], Jens Ø. Duus[b], Anders E. Daugaard[a,*]

[a] Danish Polymer Centre (DPC), Department of Chemical and Biochemical Engineering, Technical University of Denmark, Søltofts Plads Building 227, 2800 Kgs. Lyngby, Denmark
[b] Department of Chemistry, Technical University of Denmark, Kemitorvet, Bygning 207, 2800 Kgs. Lyngby, Denmark

A B S T R A C T

The bio-based monomer, 2,5-furandicarboxylic acid, has been adapted to classic thiol-ene chemistry by derivatization of the acid with allyl alcohol. This new monomer has allowed for the synthesis of new thermoset systems, capable of forming green, sustainable materials through UV-crosslinking. In this study, the synthesis of the new monomer along with thorough kinetic studies of the new thermoset systems are presented. In order to determine kinetic values for the systems, all reactions have been followed by real-time FT-IR. Initially, a study of three different photoinitiators is performed on a classic TEMPIC-TATATO system, in order to determine the superior initiator for the new systems. The new monomer is crosslinked with five different thiol compounds in both stoichiometric and off-stoichiometric ratios, yielding an array of bio-based thermosets. The properties of these systems are determined through DSC, TGA and tensile testing, allowing determination of the systems with superior properties. In general, most systems proved to cure fully, with the exception of issues encountered from thiols with long ethoxylated chains.

1. Introduction

As the world progresses and oil reserves dwindle, the search for substitute resources intensifies [1] driven by increasing necessity. With an array of secondary products from bio-mass [2], this opens up for new solutions replacing traditional materials. For the polymer industry, the search has led to bio-mass derivatives capable of replacing their petro-based counterparts, either by drop-in bio-based monomers directly replacing materials such as ethylene, propylene and methacrylic acid [3], or brand new types of monomers such as methyl vinyl glycolate (MVG) [4] or *trans*-2,5-dihydroxy-3-pentenoic acid methyl ester (DPM) [5], leading to novel types of bio-based plastics. A monomer receiving interest is glycerol, which is obtained from hydrolysis of triglycerides found in plant and animal biomass [6] and can be used for block copolymers [7], or as branch points in polyesters [8]. The bio-based derivative polylactic acid (PLA) has found use as an alternative to the petro-based polymers used in the packaging industry given its bio-degradability [9] as well as in nanocomposites with improved gas permeability [10,11]. 5-Hydroxymethylfurfural (HMF) has previously been identified as green monomer of interest due to its multiple applications as bio-based platform molecule [12]. It is obtained by dehydration without the use of metals from simple sugars and polysaccharides [13], and is seeing applications for bulk chemicals and bio-fuels, for example through oxidation to 2,5-furandicarboxylic acid (FDCA), a monomer proven suitable for synthesis of polyesters (Scheme 1). FDCA has previously been obtained through oxidation of HMF by ruthenium hydroxide [14], but has recently been produced through Cu catalyzed oxidation in good yields [15]. FDCA is a bio-based monomer, which has been receiving a great deal of interest, mainly due to its great resemblance to terephthalic acid (TPA), which, when polymerized with ethylene glycol, is used for the production of polyethylene terephthalate (PET) in the production of synthetic fibers and plastic bottles. The petro-based nature of TPA has led to a search for a suitable analogue and a probable solution has been the material polyethylene furanoate (PEF), a polyester of FDCA and ethylene glycol, which in many ways resemble PET and which is currently in use for this very purpose [1]. The potential of using PEF as replacement for PET plastics paves the way for a new market that is expected to reduce the price of FDCA over the coming years.

Many other bio-based building blocks have been developed over the last years. An example of this is allyl alcohol, which can be produced from catalytic conversion of glycerol through catalytic deoxydehydration reaction with transition metals such as rhenium [16,17].

In this paper, we report the derivatization of FDCA to the diallyl

* Corresponding author.
E-mail address: adt@kt.dtu.dk (A.E. Daugaard).

https://doi.org/10.1016/j.eurpolymj.2018.03.005
Received 10 November 2017; Received in revised form 8 February 2018; Accepted 3 March 2018
Available online 05 March 2018
0014-3057/ © 2018 Elsevier Ltd. All rights reserved.

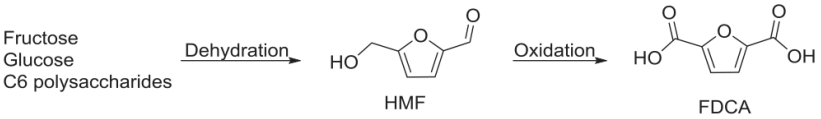

Scheme 1. Synthetic route for the production of HMF and FDCA.

ester, diallyl furan-2,5-dicarboxylate (DAFDC) with allyl alcohol, in order to provide a new polymer building block. This potential building block will be employed in thiol-ene chemistry with bio-based or partly bio-based thiol compounds, which through photo polymerization could yield a new thermoset material. Thiol-ene networks [18,19] have previously been shown to have highly desirable mechanical behavior, due to narrow glass transition temperatures [20] and the uniformity and conversion of the crosslinking. Such behavior includes lower stress in films and higher adhesion to surfaces [21]. Building a cross-linked system through thiol-enes also gives the opportunity for off-stoichiometric systems [22] producing a functionalizable surface, which have been exploited for enzyme immobilization [23,24] and particles [25,26].

We aim to produce several new types of thermoset systems, utilizing the new DAFDC building block in connection with different multifunctional thiol compound shown in Scheme 2. Most of the chosen thiol compounds contain some degree of bio-based components, increasing the overall green content of the targeted systems. This will expand the application of the bio-based FDCA to the classically known thiol-ene chemistry, yielding the opportunity for novel bio-based thermosets.

2. Experimental

2.1. Chemicals

The chemicals used were all purchased with the exception of DAFDC, which was produced in laboratories at DTU Department of Chemistry. Acetone (HPLC grade, 99.8%), 1,3,5-triallyl-1,3,5-triazine-2,4,6-(1H,3H,5H)-trione (98%), trimethylolpropan tri(3-mercaptopropionate) and pentaerythriol tetrakis(3-mercaptopropionate) (> 95%) were acquired from Sigma Aldrich® and used as received. Tris[2-(3-mercaptopropionyloxy)ethyl]isocyanurate, ethoxilated-trimethylolpropan tri(3-mercaptopropionate) (THIOCURE® ETTMP 700), ethoxilated-trimethylolpropan tri(3-mercaptopropionate) (THIOCURE® ETTMP 1300) and polycaprolactone tetra(3-mercaptopropionate) (THIOCURE® PCL4MP 1350) were obtained from Bruno Bock Thiocure® and used as received. The photo initiators Ommirad 1000 and Omnirad 4265 came from IGM Resins® while Lucirin is a product of BASF, all used as received. The three commercially available photo initiators used are Lucirin (P1) a yellow initiator consisting only of ethyl(2,4,6-trimethylbenzoyl)-phenyl phosphinate, Ommirad 1000 (P2) a clear initiator consisting of 80% Omnirad 73 (2-hydroxy-2-methyl-1-phenylpropanone) and 20% Omnirad 481 (1-hydroxycyclohexyl-phenyl ketone) and Omnirad 4265 (P3) a slightly yellow initiator consisting of 50% Lucirin and 50% Omnirad 481.

2.2. Method and characterization

Identification of thiol-ene compounds and determination of reaction kinetics were performed on Nicolet iS50 FT-IR equipped with an iS50 ATR crystal from Thermo Scientific. The software used for the analysis was Omnic 9.7.46 firmware version 1.14 along with the macro software Macro Basic version 10.0.

The thiol-ene mixture was kept in darkness until the polymerization was initiated by a UV-LAMP (365 nm, 11 W, 230 V) as the only light source. A series of spectra were recorded with scans taken every four seconds until the reaction speed decreased and the ratio of scans was reduced to 24 s intervals and later 1 min. The reaction was irradiated

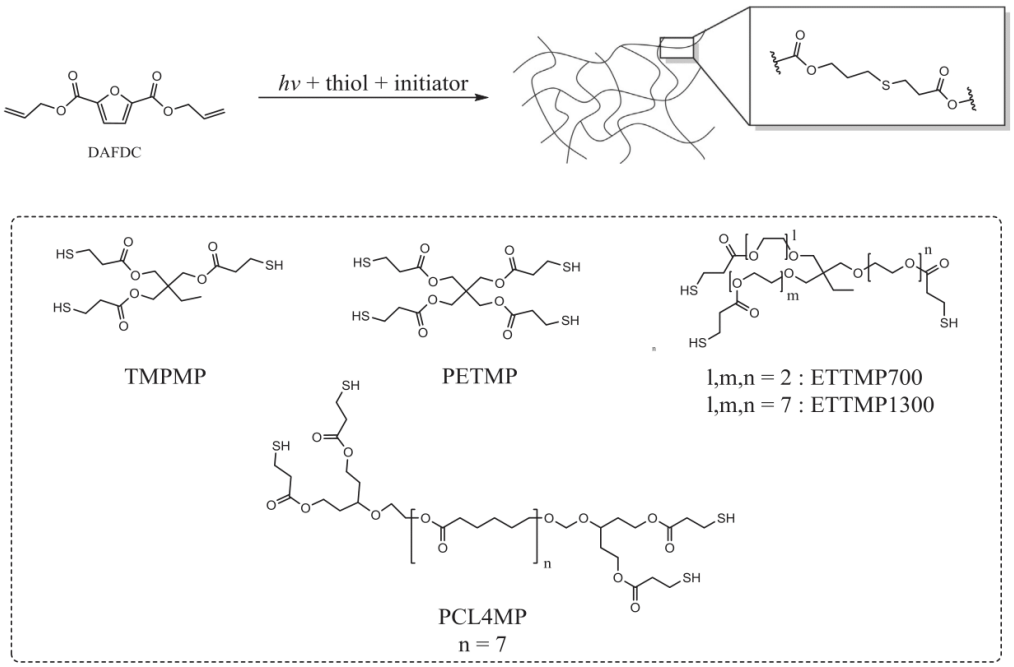

Scheme 2. Reaction scheme for the targeted thermoset systems and the various examined multifunctional thiols.

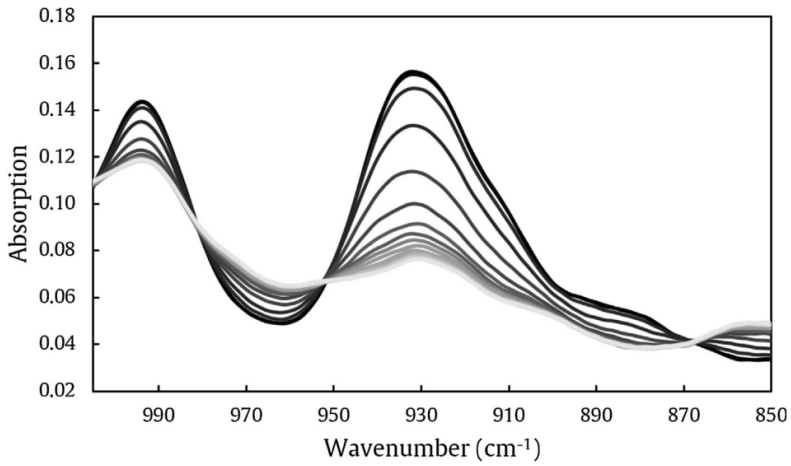

Fig. 1. Real-time FTIR absroption spectra of the thiol-ene TEMPIC-TATATO system with the absorption ~930 cm^{-1} corresponding to the allylic C-H out-of-plane bend of DAFDC.

until no further reaction was detected (no decrease in the functional groups of interest). The allylic conversion was monitored through the allylic C—H out-of-plane bend at 930–940 cm^{-1}, as seen from Fig. 1, and calculated using Eq. (1) where $A(0)$ is the initial absorption and $A(t)$ is the adsorption at the time t. Reactions were monitored until no observable integral changes were present.

$$x(t) = \frac{A(0)-A(t)}{A(0)} * 100\% \quad (1)$$

The maximum reaction rates were determined at the point with highest conversion rate (%/s) and the inhibition phase as the intercept of the tangent to this point with the t-axis. The maximum conversion was determined as the overall highest conversion observed. For estimation of total reaction time, the reaction was defined as complete when the reaction rate was less than 0.05%/s.

Glass transition temperatures (T_g) and melting temperatures (T_m) were recorded using a TA instruments Discovery DSC. The thermal analysis was performed with a heating/cooling cycle of 10 °C /min ranging from −90 °C to 210 °C. T_g was measured at the inflection point and T_m at the peak temperature. The thermogravimetric analysis (TGA) data supplied was obtained using TA instruments Discovery TGA. The measurement was performed from room temperature to 700 °C.

Nuclear Magnetic Resonance (NMR) spectra were obtained on a 400 MHz Bruker Ascend magnet with an Avance II console and equipped with a Prodigy cryoprobe, at 400.13 MHz for ^{1}H and 100.61 for ^{13}C. Samples were dissolved in DMSO and the chemical shift reference set at 2.54 PPM. Data were processed and plotted using Mnova software.

Tensile tests were performed on a TA Electroforce equipped with a 45 N load cell. Tests were carried out on dog-bones, molded with a cut-out steel plate on a glass surface with the length, width and thickness of the dog-bone being 25.0 mm, 5.0 mm and 0.5 mm respectively. The dog-bones were pulled at a rate of 0.1 mm/s for a total of 12 mm (the maximum of the instrument) or until rupture occurred. Young's moduli of the samples were determined from the slope of the initial 0.3 mm of the test, and ultimate strength and maximum strain were determined from the rupture point. All systems were tested with quintuplicate measurements.

2.3. Synthesis of diallyl furan-2,5-dicarboxylate

2,5-furandicarboxylic acid (80 g, 0.513 mol) was suspended in allyl alcohol (1000 mL) and concentrated sulfuric acid (2 mL) was added. The suspension was heated to reflux for 72 h, yielding a clear yellow solution. Following cooling to room temperature, the reaction mixture was concentrated to near dryness, yielding a black residue, which was dissolved in diethyl ether (1000 mL), and washed twice with a saturated sodium bicarbonate solution (2 × 1000 mL). The organic phase was concentrated yielding a yellow solid, which upon distillation (b.p. 140 °C at 15 mbar. Corrected b.p. 276 °C) yielded the desired diallyl furan-2,5-dicarboxylate (92.2 g, 76%).

^{1}H NMR (400 MHz, DMSO-d_6) δ 7.47 (d, J = 2.3 Hz, 1H), 6.02 (ddt, J = 17.4, 10.7, 5.5 Hz, 1H), 5.45–5.25 (m, 2H), 4.82 (dt, J = 5.6, 1.4 Hz, 2H).
^{13}C NMR (101 MHz, DMSO-d_6) δ 157.0, 146.0, 132.0, 119.3, 118.7, 65.6.
FTIR (cm^{-1}): 470, 505, 562, 602, 622, 769, 815, 862, 924, 955.41, 982, 995, 1010, 1035, 1098, 1158, 1231, 1272, 1293, 1377, 1386, 1417, 1454, 1507, 1572, 1653, 1717, 3013, 3110.

2.4. General procedure: Synthesis of thiol-ene TEMPIC/TATATO thin film

The general procedure applies to all the experiments performed for this paper exemplified with this synthesis (see supporting information for all thiol-ene procedures). The thiol component Tris[2-(3-mercaptopropionyloxy)ethyl]isocyanurate (TEMPIC) (1.393 g, 2.65 mmol) was added to the allylic component 1,3,5-triallyl-1,3,5-triazine-2,4,6-(1H,3H,5H)-trione (TATATO) (0.672 g, 2.69 mmol) and the initiator Lucirin (5.04 mg, 0.016 mmol). The mixture was dissolved in acetone (1 mL) and stirred on a vortex mixer at 2500 rpm for approximately one minute or until fully dissolved. While being kept in darkness two drops of the solution were added to the ATR crystal with a pipette yielding a film of approximately 1 mm in thickness. Ambient light was blocked so that only the light from the UV-lamp initiated the reaction.

2.5. General procedure: Synthesis of films for tensile testing

Diallyl furan-2,5-dicarboxylate (2.20 g, 9.29 mmol), Pentaerythritol tetrakis(3-mercaptopropionate) (2.40 g, 4.66 mmol) and OMNIRAD 4265 (109 mg) were weighed in a cup and mixed on a speed mixer for 10 min at 3500 RPM or until homogenous. The mixture was poured into a cut-out steel plate with dog-bone-shapes mounted on a glass plate and any excess was removed with an industrial razorblade. The plate was placed in an UV-chamber (365 nm) for 10 min yielding the cured dog-bones for tensile testing.

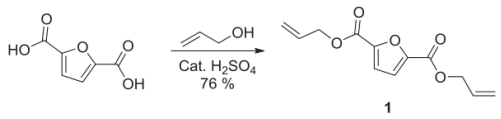

Scheme 3. Synthesis of the DAFDC monomer.

3. Results and discussion

3.1. Monomer synthesis

We synthesized DAFDC through acidic esterification with allyl alcohol and a catalytic amount of sulfuric acid (Scheme 3).

This monomer has been synthesized in similar fashion previously [27], and was originally reported as a yellow oil. Initially we observed the same appearance, with both IR and NMR experiments showing apparent sufficient purity for further experiments. However, it was proven that small amounts of impurities were present in the yellow oil, as evidenced by the fact that high temperature experiments lead to degradation to a black residue. This could be circumvented by subjecting the compound to a basic wash followed by a distillation, yielding the monomer as a white crystalline solid. This pure material could be used in high temperature reactions without the formation of black residue. Since direct distillation of the yellow oil without basic wash yielded the same black residue, it was concluded that the impurities stem from minor traces of acid. NMR spectroscopy of the black residue revealed relative increase in the amount of aromatic protons (Fig. 2), leading to the theory that the degradation of the compound could derive from a possible inverse electron demand Diels-Alder reaction between the allyl groups and the furan ring. This creates an oxygen-bridged six membered ring system, which, through dehydration, yields aromatic benzene rings (Scheme 4).

3.2. Photoinitiators and kinetics

In order to evaluate the strengths and drawbacks of different photoinitiator systems we tested three commercially available photoinitiators, Lucrin (P1), Ommirad 1000 (P2) and Omnirad 4265 (P3), in the classically known thiol-ene reaction of TEMPIC and TATATO, by using 0.25 wt%, 0.05 wt% and 0.025 wt% of the initiators, respectively. The conversion was calculated using Eq. (1) and the results are presented in Fig. 3 with accommodating data in Table 1.

A general trend observed is that the amount of initiator is limiting for the reaction rate. Most reactions exhibited short inhibition phases, with the exception of P2, which shows longer inhibition times present in less than 0.25 wt%. In addition, the rate of reactions initiated by P2 are much lower compared to P1 and P3. The reactions of TEMPIC and TATATO show that the choice of initiator can limit the maximum conversion. All initiators show the highest conversion rates with a 0.05 wt% loading. For P1 and P2 it is observed that using only 0.025 wt % initiator limits the maximum conversion by 5–10%, whereas the conversion rates when utilizing P3 remain predominantly constant. P3 has thereby shown to have superior kinetic properties under the given conditions in the acetone diluted thiol-ene composition. Meanwhile the conversion percentage does not seem to be affected by the three initiators themselves, which has led to P3 being the chosen initiator for further testing. A factor contributing to the higher performance of the P1 and P3 systems compared to P2, is most likely the choice of the UV source with a 365 nm wavelength, since P1 and P3 have absorption wavelengths at 370 and 379 nm respectively, whereas the highest absorption wavelength of P2 is 340 nm.

3.3. Synthesis of bio-thiol-ene thin films

From the initial studies of the photoinitiators, P3 was deemed the most efficient. With this, the targeted bio-thiol-ene cross-linked networks were polymerized using equimolar amount of functional groups i.e. allyl and thiol groups and 2.5 wt% P3 initiator for all five thiol monomers shown in Scheme 2. The amount of initiator has been increased due to the slower propagation rate of of DAFDC compared to TATATO in the thiol-ene system, and the ten-fold increase of initiator was required in order to obtain reaction rates equivalent to those observed for the TEMPIC/TATATO system. The conversions were calculated as before using Eq. (1) with the resulting curves presented in Fig. 4 (conversion curves for off-stoichiometric systems are presented in Supporting Information, Figs. S2 and S3).

The five different thiol monomers represents a variety of different functionalities and are the standard for a thiol-ene system. To examine how the system reacted to off-stoichiometric ratios, each of the systems was polymerized using both a 1.3 stoichiometric surplus of allyl and thiol groups. Using Carothers equation and the statistical method the theoretical gel-point has been calculated for tri- and tetra functional thiol compounds with a di-functional allyl compound before experiments started. Calculated critical conversions are given in Table S1 and S2 (see Supporting Information). The thiol-ene reactions using DAFDC as the allylic monomer all yielded cross-linked products each with different properties. Most of the thiol-ene systems reached high levels of conversion and yielded solid samples with varying mechanical properties. ETTMP1300 based systems did not fully cure, but yielded coherent flexible films with sticky surfaces, which were observed to be unstable over time (both ETTMP700 and ETTMP1300). The systems reverted to a viscous liquid state after storage for several months, with IR spectra showing a large broad peak at $\sim 3400\,cm^{-1}$ consistent with formation of hydroxyl groups, indicating hydrolysis of the PEG chains (Supporting Information, Fig. S4).

Conversion rates were measured with FT-IR as for the TEMPIC-TATATO system, and all kinetic data are shown in Table 2.

The conversion speeds of the thiol-ene reactions (Table 2) were greatly affected by the choice of thiol monomer. High reaction rates are observed when employing the PCL4MP1350 thiol in surplus. While the ETTMP monomers exhibit generally lower reaction rates and inferior conversions, especially ETTMP1300. This phenomena is attributed to the aforementioned instability of the systems, which was observable within the timeframe of the experiments for ETTMP1300 (Supporting Information, Fig. S1). This also show that the higher molecular weight ETTMP monomers are slower reacting and more unstable compared to

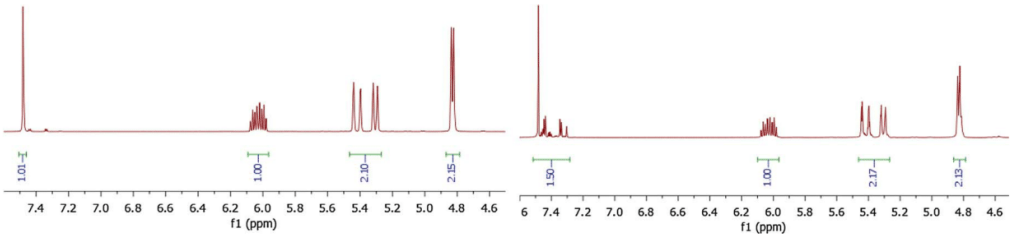

Fig. 2. H NMR spectra of the DAFDC monomer (left) and the obtained black residue from heating (right) showing increased integral for the aromatic region at δ ≈ 7.4 ppm.

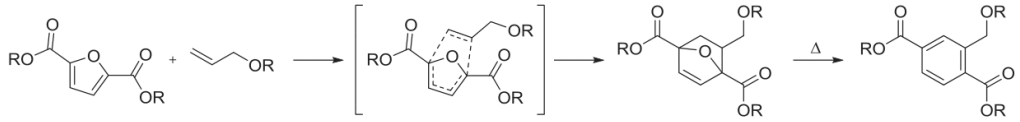

Scheme 4. Proposed mechanism for Diels-Alders reaction and following dehydration of the furane ring and the allyl group at high temperatures.

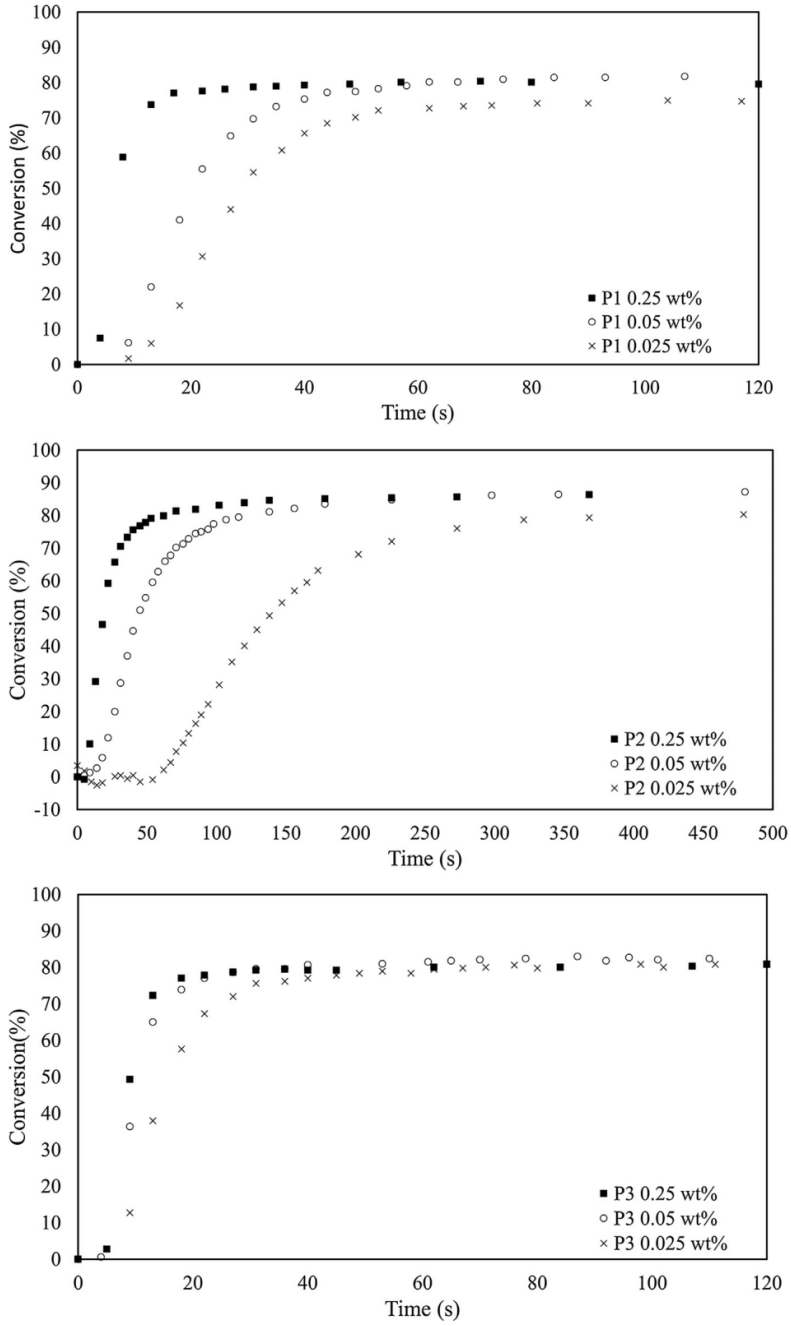

Fig. 3. Allylic conversion of the TEMPIC-TATATO system with the three different examined photoinitiators.

Table 1
Kinetic data for the TEMPIC-TATATO system with the different photoinitiators.

Sample	Max. rate (%/s)	Rel. rate	Inh. phase (s)	Max. conv. (%)	Conv. time (s)
P1 0.25 wt%	12.85	1	3.4	82.04	48
P1 0.05 wt%	3.95	0.31	7.4	85.79	107
P1 0.025 wt%	3.48	0.27	13.2	76.99	117
P2 0.25 wt%	4.79	0.37	6.9	87.66	85
P2 0.05 wt%	2.19	0.17	17.9	88.56	226
P2 0.025 wt%	0.83	0.06	65.8	78.22	368
P3 0.25 wt%	11.63	0.91	4.8	82.83	40
P3 0.05 wt%	7.17	0.56	3.9	84.38	136
P3 0.025 wt%	6.30	0.49	7.0	82.55	151

their lower molecular weight counterparts. ETTMP1300 has long ethoxylated chains, which likely prevents complete curing, supported by the conversions between 30 and 45% and lower conversions obtained with increased amounts of the thiol component.

The thiol-enes are fully capable of reacting off-stoichiometrically while maintaining approximately the same conversion, around 90%. Naturally, due to conversion being measured from the IR signal of allyl groups, systems with an excess of allyl functionality exhibit lower conversions. Though with conversions above 77% (the natural stoichiometric limitation), it is suspected that some allyl-allyl propagation is occurring besides the expected thiol-allyl crosslinks. The even distribution in maximum conversion can be contributed to restrictions of the network preventing further reaction once it has reached the gel-point. Comparing the DAFDC systems and a conventional system like TEMPIC-TATATO, a higher conversion of the functional groups are attained with the exception of ETTMP1300.

All systems were subjected to DSC and TGA analysis, with their thermal properties being presented in Table 3. The data obtained by DSC shows a large variation of the thiol-ene systems with T_g varying from −61.4 °C to 9.3 °C. In general, T_g is heavily influenced by molecular weight and the rotational freedom of the compound, which can then be used as an indicator for the ability of the system to create networks. This is exemplified by PETMP systems having the highest T_g (9.3 °C) of the five systems, resulting from its small size and high functionality. An absence of melting points was observed during the second heating cycle of the DSC scans. We expect this phenomenon to occur from slow crystallization of the polymers, hindering re-crystallization of the systems. The TGA results (Table 3) generally show a small initial weight loss around 100 °C corresponding to between 4 and 15%, which is attributed to residual solvent trapped during the curing reaction. The primary degradation starts around 270–300 °C and

Table 2
Kinetic data for the synthesized thermoset systems.

Thiol	[SH]:[C=C]	Max. rate (%/s)	Rel. rate	Inh. phase (s)	Max. conv. (%)	Conv. time (s)
TMPMP	1.0:1.0	2.0	1.00	32.0	92.9	225
TMPMP	1.3:1.0	1.8	0.89	13.4	92.6	296
TMPMP	1.0:1.3	1.2	0.61	22.3	84.8	178
PETMP	1.0:1.0	1.5	0.75	27.8	91.6	278
PETMP	1.3:1.0	2.4	1.20	12.8	91.5	207
PETMP	1.0:1.3	2.7	1.38	6.0	84.5	202
ETTMP700	1.0:1.0	1.6	0.82	42.3	89.2	513
ETTMP700	1.3:1.0	3.1	1.54	8.8	88.6	202
ETTMP700	1.0:1.3	1.1	0.54	20.5	77.0	298
ETTMP1300	1.0:1.0	1.4	0.69	28.3	39.4	369
ETTMP1300	1.3:1.0	0.9	0.47	11.6	32.5	249
ETTMP1300	1.0:1.3	0.9	0.45	78.0	45.2	250
PCL4MP1350	1.0:1.0	1.1	0.57	24.3	92.5	321
PCL4MP1350	1.3:1.0	4.7	2.39	9.6	94.8	71
PCL4MP1350	1.0:1.3	1.7	0.86	27.5	83.8	298

ends at approximately at 400–500 °C, losing approximately 90% of the total mass. It is clear that the content of DAFDC increases the thermal stability as well as the residual mass after degradation, where e.g. the PETMP systems (that are high in DAFDC) show the highest residue with 23% and the highest end temperature (T_{end}) of degradation. The overall order of performance of the thiol monomers based on the end of degradation are rated as PETMP > TMPMP > PCL4MP1350 > ETTMP700 > ETTMP1300 (Table 3). This order also reflects the instability of the ETTMP based systems. Regarding the onset of degradation, the performance of the systems change. Here the ETTMP1300 and PCL4MP1350 systems perform well, with degradations starting in the 285–300 °C interval, followed by PETMP, ETTMP700 and TMPMP respectively decreasing in stability. A general trend that is observed, is the stoichiometric systems tend to initiate degradation later than the off-stoichiometric systems, indicating an excess of functional groups contributing to the degradation process.

To evaluate the mechanical properties of the examined bio-films, tensile tests were performed on a selection of the films. In order to observe both the effect of the various thiols and stoichiometric change in the reaction feed, all stoichiometric systems with the five different thiols were tested along with a test series of the PETMP system with the variances on stoichiometry. All results are summarized in Table 4 (plots of the tensile tests are presented in Supporting Information). The tests showed that off-stoichiometric ratios caused softer and more flexible materials, as anticipated due to a less densely crosslinked network.

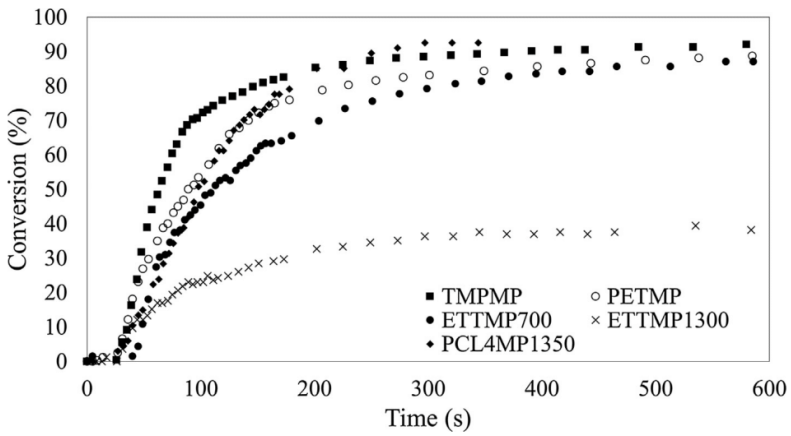

Fig. 4. Allylic conversion of 1:1 SH/C = C stoichiometric systems with DAFDC, the different thiols and 2.5 wt% P3.

Table 3
Thermal properties of the synthesized thermoset systems.

Thiol	[SH]:[C=C]	*Tg* (°C)[a]	*Tm* (°C)[a]	T_{start} degradation (°C)	T_{end} degradation (°C)	Mass loss (%)
TMPMP	1.0:1.0	−8.5	–	267.8	521.5	89.9
TMPMP	1.3:1.0	−54.8	135.0	268.4	521.4	83.0
TMPMP	1.0:1.3	−24.5	137	271.6	521.4	87.3
PETMP	1.0:1.0	9.3	135	280.7	539.7	77.5
PETMP	1.3:1.0	9.19	124	278.3	547.0	73.4
PETMP	1.0:1.3	0.0	135	277.3	543.1	76.3
ETTMP700	1.0:1.0	−55.5	148	280.2	485.3	88.9
ETTMP700	1.3:1.0	−35.0	–	267.6	489.3	94.4
ETTMP700	1.0:1.3	−55.5	148	279.7	483.6	88.3
ETTMP1300	1.0:1.0	−57.0	162	301.4	464.3	93.0
ETTMP1300	1.3:1.0	−53.4	–	283.9	457.4	93.3
ETTMP1300	1.0:1.3	−49.5	162	281.0	466.4	91.0
PCL4MP1350	1.0:1.0	−36.0	190	299.3	508.0	90.8
PCL4MP1350	1.3:1.0	−61.4	160.0	286.4	518.8	91.6
PCL4MP1350	1.0:1.3	−55.0	150	291.6	511.1	88.7

[a] Determined from first DSC heating cycle.

Table 4
Mechanical properties obtained from tensile testing.

Thiol	[SH]:[C=C]	Young's Modulus (MPa)	Tensile strength (MPa)	Maximum strain
PETMP	1.0:1.0	6.1 ± 0.4	1.1 ± 0.3	0.23 ± 0.06
PETMP	1.3:1.0	5.4 ± 0.7	1.2 ± 0.1	0.30 ± 0.04
PETMP	1.0:1.3	3.1 ± 0.3	0.75 ± 0.09	0.35 ± 0.01
TMPMP	1.0:1.0	3.0 ± 0.3	0.83 ± 0.09	0.38 ± 0.04
ETTMP700	1.0:1.0	1.69 ± 0.03	0.44 ± 0.09	0.35 ± 0.07
ETTMP1300	1.0:1.0	0.67 ± 0.03	N/A	N/A
PCL4MP1350	1.0:1.0	4.8 ± 0.5	0.5 ± 0.1	0.12 ± 0.04

However, excess of thiols led only to a minor reduction in modulus, while an increase in tensile strength was observed. Contrary to this, an increase in allyl functionality led to a reduction of modulus by approximately 50% along with a lowering of tensile strength. This difference was attributed to the difference in functionality between the thiols and DAFDC, which effectively gives a better integrity in the network at higher amounts of the multifunctional thiols compared to excess of the bifunctional DAFDC.

The various thiols also resulted in great differences in mechanical behavior of the systems. PETMP, TMPMP based systems resulted in stiffer and stronger materials, while PCL4MP was stiff but of intermediate tensile strength and ETTMP700 and 1300 systems were much softer and exhibited almost elastomeric properties.

In order to claim the thiol-ene systems as bio-based the thiol compounds have been scrutinized by retrosynthetic analysis. The core of TMPMP, ETTMP700 and ETTMP1300 is 2-ethyl-2-(hydroxymethyl) propane-1,3-diol, 2,2-bis(hydroxymethyl)propane-1,3-diol for PETMP, which can be synthesized from propan-1-ol, *n*-butanol and formic acid that are all available from renewable resources [28,29]. The spacers used in ETTMP monomers are ethylene oxide which can be produced by oxidation of bio-ethylene [30]. 3-Mercaptopropionate, the thiol constituent in all the thiol compounds, can be synthesized by hydrogen sulfide and but-3-enioc acid, which can be found as derivatives of biomass [31,32]. This makes thiol-ene systems based on TMPMP, PETMP and ETTMPs at least theoretically available as 100% bio-based systems. On the other hand, PCL4MP1350s main constituency is poly(caprolactone), which is still only a derivative of crude oil, resulting in a thiol-ene network such as T-PCL1 being 42 wt% bio-based.

4. Conclusion

In this study, we have presented a green synthetic route to the monomer DAFDC with high purity, using a simple procedure allowing effective upscaling. We have shown the necessity of thorough purification by distillation of this monomer in order to avoid unwanted side-reaction at higher temperatures. With the aim of using DAFDC in UV-initiated thiol-ene crosslinking reaction, we have studied the reaction rates of three different photo initiators in a model TEMPIC/TATATO system with the objective of determining the most suitable initiator. The results revealed Omnirad 4265 to be superior to both Lucirin and Omnirad 1000 under the tested conditions. Omnirad 4265 was then employed in the screening of DAFDC with five fully or partly bio-based thiol compounds, TMPMP, PETMP, ETTMP700, ETTMP1300 and PCL4MP. All five thiol compounds were shown to be fully capable of forming crosslinked networks in a thiol-ene reaction, and be able to maintain fast curing rates with the photo initiator. Generally, high conversions were observed for the curing and the reactions yielded materials with desirable thermal qualities, their glass transition temperatures ranging between −61.4 °C and up to 9.3 °C. Only ETTMP1300 systems showed conversion percentages too low for fully cross-linked networks and also displayed susceptibility to hydrolysis of the ethoxylated chains during storage. Mechanical properties of the systems were directly correlated to the type of thiol and stoichiometry of the mixture, where PETMP and TMPMP resulted in stiffer materials and highest tensile strength, PCL4MP resulted in an intermediate strength and ETTMP700 and ETTMP1300 systems were softer and weaker systems. With this study, we step towards the incorporation of the bio-based FDCA into known sulfide chemistry, giving the opportunity of numerous new sustainable thermoset systems. In future work, we aim at investigating the potential of such systems in composites or elastomers by use of reinforcing agents.

Acknowledgements

We would like to thank Peter Fristrup for initializing the project collaboration and Liyun Yu for help with thermal analysis as well as Bruno Bock and IGM Resins for supplying chemicals.

Appendix A. Supplementary material

Supplementary data associated with this article can be found, in the online version, at https://doi.org/10.1016/j.eurpolymj.2018.03.005.

References

[1] A. Gandini, Monomers and macromonomers from renewable resources, in: K. Loos (Ed.) (Ed.), Biocatal. Polym. Chem. Wiley-VCH Verlag GmbH & Co. KGaA, 2010, pp. 1–33.
[2] S.N. Naik, V.V. Goud, P.K. Rout, A.K. Dalai, Production of first and second generation biofuels: a comprehensive review, Renew. Sustain. Energy Rev. 14 (2010) 578–597.
[3] L. Axelsson, M. Franzén, M. Ostwald, G. Berndes, G. Lakshmi, N.H. Ravindranath,

Perspective: Jatropha cultivation in southern India: assessing farmers' experiences, Biofuels, Bioprod. Biorefining. 6 (2012) 246–256.
[4] M. Dusselier, P. Van Wouwe, S. De Smet, R. De Clercq, L. Verbelen, P. Van Puyvelde, F.E. Du Prez, B.F. Sels, Toward functional polyester building blocks from renewable glycolaldehyde with sn cascade catalysis, ACS Catal. 3 (2013) 1786–1800.
[5] S.G. Elliot, C. Andersen, S. Tolborg, S. Meier, I. Sádaba, A.E. Daugaard, E. Taarning, Synthesis of a novel polyester building block from pentoses by tin-containing silicates, RSC Adv. 7 (2017) 985–996.
[6] H. Zhang, M.W. Grinstaff, Recent advances in glycerol polymers: chemistry and biomedical applications, Macromol. Rapid Commun. 35 (2014) 1906–1924.
[7] G.Z. Papageorgiou, V. Tsanaktsis, D.N. Bikiaris, Synthesis of poly(ethylene furandicarboxylate) polyester using monomers derived from renewable resources: thermal behavior comparison with PET and PEN, PCCP 16 (2014) 7946–7958.
[8] H. Nguyen, D. Löf, S. Hvilsted, A. Daugaard, Highly branched bio-based unsaturated polyesters by enzymatic polymerization, Polymers (Basel). 8 (2016) 363–374.
[9] H. Tsuji, Poly (Lactic Acid), Bio-Based Plast. Mater. Appl. John Wiley & Sons Ltd, Chichester, UK, 2014, pp. 171–239.
[10] J. Trifol, D. Plackett, C. Sillard, P. Szabo, J. Bras, A.E. Daugaard, Hybrid poly(lactic acid)/nanocellulose/nanoclay composites with synergistically enhanced barrier properties and improved thermomechanical resistance, Polym. Int. 65 (2016) 988–995.
[11] J. Trifol, D. Plackett, C. Sillard, O. Hassager, A.E. Daugaard, J. Bras, P. Szabo, A comparison of partially acetylated nanocellulose, nanocrystalline cellulose, and nanoclay as fillers for high-performance polylactide nanocomposites, J. Appl. Polym. Sci. 133 (2016) 43257–43268.
[12] A.A. Rosatella, S.P. Simeonov, R.F.M. Frade, C.A.M. Afonso, 5-Hydroxymethylfurfural (HMF) as a building block platform: Biological properties, synthesis and synthetic applications, Green Chem. 13 (2011) 754–793.
[13] T. Ståhlberg, S. Rodriguez-Rodriguez, P. Fristrup, A. Riisager, Metal-free dehydration of glucose to 5-(hydroxymethyl)furfural in ionic liquids with boric acid as a promoter, Chem. - A Eur. J. 17 (2011) 1456–1464.
[14] Y.Y. Gorbanev, S. Kegnæs, A. Riisager, Selective aerobic oxidation of 5-hydroxymethylfurfural in water over solid ruthenium hydroxide catalysts with magnesium-based supports, Catal. Lett. 141 (2011) 1752–1760.
[15] T.S. Hansen, I. Sádaba, E.J. García-Suárez, A. Riisager, Cu catalyzed oxidation of 5-hydroxymethylfurfural to 2,5-diformylfuran and 2,5-furandicarboxylic acid under benign reaction conditions, Appl. Catal. A Gen. 456 (2013) 44–50.
[16] C. Boucher-Jacobs, K.M. Nicholas, Catalytic deoxydehydration of glycols with alcohol reductants, ChemSusChem. 6 (2013) 597–599.
[17] C. Boucher-Jacobs, K.M. Nicholas, Oxo-rhenium-catalyzed deoxydehydration of polyols with hydroaromatic reductants, Organometallics 34 (2015) 1985–1990.
[18] C.E. Hoyle, C.N. Bowman, Thiol-ene click chemistry, Angew. Chem. Int. Ed. Engl. 49 (2010) 1540–1573.
[19] A.B. Lowe, Thiol-ene "click" reactions and recent applications in polymer and materials synthesis, Polym. Chem. 1 (2010) 17.
[20] J.-P. Fouassier, J.F. Rabek, Radiation Curing in Polymer Science and Technology, first ed., Springer, Netherlands, 1993.
[21] C.E. Hoyle, T.Y. Lee, T. Roper, Thiol-enes: chemistry of the past with promise for the future, J. Polym. Sci. Part A Polym. Chem. 42 (2004) 5301–5338.
[22] C.F. Carlborg, T. Haraldsson, K. Öberg, M. Malkoch, W. van der Wijngaart, Beyond PDMS: off-stoichiometry thiol–ene (OSTE) based soft lithography for rapid prototyping of microfluidic devices, Lab Chip 3136–3147 (2011).
[23] C. Hoffmann, M. Pinelo, J.M. Woodley, A.E. Daugaard, Development of a thiol-ene based screening platform for enzyme immobilization demonstrated using horseradish peroxidase, Biotechnol. Prog. 33 (2017) 1267–1277.
[24] J.P. Lafleur, S. Senkbeil, J. Novotny, G. Nys, N. Bøgelund, K.D. Rand, F. Foret, J.P. Kutter, Rapid and simple preparation of thiol-ene emulsion-templated monoliths and their application as enzymatic microreactors, Lab Chip 15 (2015) 2162–2172.
[25] P. Mazurek, A.E. Daugaard, M. Skolimowski, S. Hvilsted, A.L. Skov, RSC Advances Preparing mono-dispersed liquid core PDMS microcapsules from thiol – ene – epoxy-tailored, RSC Adv. 5 (2015) 15379–15386.
[26] O.Z. Durham, H.R. Norton, D.A. Shipp, Functional polymer particles via thiol–ene and thiol–yne suspension "click" polymerization, RSC Adv. 5 (2015) 66757–66766.
[27] R. Andrisano, Ultraviolet spectra of some furandicarboxylic derivatives, Gazz. Chim. Ital. 81 (1951) 414–418.
[28] B. Ndaba, I. Chiyanzu, S. Marx, N-Butanol derived from biochemical and chemical routes: a review, Biotechnol. Reports. 8 (2015) 1–9.
[29] R. Wölfel, N. Taccardi, A. Bösmann, P. Wasserscheid, Selective catalytic conversion of biobased carbohydrates to formic acid using molecular oxygen, Green Chem. 13 (2011) 2759–2763.
[30] A. Morschbacker, Bio-ethanol based ethylene, Polym. Rev. 49 (2009) 79–84.
[31] J.J. Su, Y.C. Chang, Y.J. Chen, K.C. Chang, S.Y. Lee, Hydrogen sulfide removal from livestock biogas by a farm-scale bio-filter desulfurization system, Water Sci. Technol. 67 (2013) 1288–1293.
[32] O. Novotný, K. Cejpek, J. Velíšek, Formation of carboxylic acids during degradation of monosaccharides, Czech J. Food Sci. 26 (2008) 117–131.

Appendix F: Manuscript 4

Submitted to Macromolecules

This document is confidential and is proprietary to the American Chemical Society and its authors. Do not copy or disclose without written permission. If you have received this item in error, notify the sender and delete all copies.

Synthesis of Functionalized Hyperbranched FDCA Polyesters and Characterization of Molecular Weight and Branching by NMR

Journal:	*Macromolecules*
Manuscript ID	ma-2018-00848u
Manuscript Type:	Article
Date Submitted by the Author:	21-Apr-2018
Complete List of Authors:	Larsen, Daniel; Danmarks Tekniske Universitet, Department of Chemistry Rønsbro, Kristoffer; Danmarks Tekniske Universitet, Danish Polymer Center Duus, Jens; Technical University of Denmark, Chemistry Daugaard, Anders; Technical University of Denmark, Chemical Engineering

SCHOLARONE™
Manuscripts

ACS Paragon Plus Environment

Synthesis of Functionalized Hyperbranched FDCA Polyesters and Characterization of Molecular Weight and Branching by NMR

*Daniel B. Larsen,[†,‡] Kristoffer Rønsbro,[†] Jens Ø. Duus,[‡] and Anders E. Daugaard[†] **

[†]Danish Polymer Centre (DPC), Department of Chemical and Biochemical Engineering, Technical University of Denmark, Søltofts Plads Building 229, 2800 Kgs. Lyngby, Denmark.

[‡]Department of Chemistry, Technical University of Denmark, Kemitorvet, Bygning 207, 2800 Kgs. Lyngby, Denmark.

ABSTRACT

The inevitable exhaustion of fossil resources leads to the necessity for development and utilization of bio-based platform chemicals for production of renewable materials. This study presents a synthetic method for obtaining fully allyl-functionalized linear and hyperbranched polyesters from bio-based 2,5-furandicarboxylic acid (FDCA). By variation of the feed composition, both linear and differently branched polyesters were prepared. Due to their limited solubility, molecular weights of FDCA polyesters cannot be determined by size exclusion chromatography in classical solvents. A novel NMR method based only on the concentration of linear, dendritic and terminal units was therefore developed to allow determination of molecular

weights and degree of branching of hyperbranched polymers. With this method, it was shown that branched polyesters in the range of 750-1350 g/mol and degrees of branching in the range of 0.14 and 0.52 had been obtained. A kinetic study of the crosslinking reaction of the prepared polyesters using free radical and thiol-ene polymerizations was conducted to illustrate the potential uses in thermosets. Kinetic parameters were determined using the Borchardt and Daniels method, which showed lowering of activation energies, pre-exponential factors and reaction orders with decreasing amounts of glycerol in the feed mixture. Finally, cross-examination of the obtained NMR and kinetic data showed an overall correlation between degree of branching and kinetic parameters, underlining the importance of designing degree of branching in hyperbranched polyesters for future applications in thermoset materials.

TEXT

Introduction

The necessity for development of bio-based alternatives to petrol-based plastics[1], has led to numerous new monomers, which are showing promise as replacement for some of the oil-based monomers currently applied in the plastic industry[2]. These new bio-based compounds leads the way for new types of plastics, where they can either be used as direct replacements of widely used compounds such as bio-based polyethylene or as novel types of monomers such as methyl vinyl glucolate (MVG) [3] and *trans*-2,5-dihydroxy-3-pentenoic acid methyl ester (DPM)[4], leading to novel types of plastics.

A platform chemical which has received large interest over the last years is 5-hydroxymethylfurfural (HMF), which can be produced from carbohydrate sources such as glucose[5] and fructose[6]. Especially the oxidized form of HMF, 2,5-furandicarboxylic acid (FDCA), is finding applications in polymer science and showing similarities with currently

applied petrol-based chemicals such as terephthalic acid[7–9], traditionally produced from xylene[10]. FDCA is as mentioned obtained from oxidation of HMF by sustainable approaches using catalytic methods with ruthenium[11] or copper[12].

Another important bio-feedstock is glycerol, a byproduct from bio-diesel production. Large amounts are readily available[13] and efficient usage of this chemical is therefore highly sought. Though glycerol can be directly incorporated into polymer chemistry as a suitable branching point, e.g. in alkyds,[14–17] it also provides a platform for a vast amount of different chemical building blocks[18]. One of these building blocks is allyl alcohol, which can be obtained from deoxydehydration of glycerol, possible with an array of different catalysts such as rhenium[19,20] and molybdenum[21].

We have recently shown how derivatized FDCA can be used in thiol-ene crosslinking chemistry[22]. In order to maximize the content of green monomers in the systems, the intention here is to synthesize linear and branched prepolymer systems with high allyl functionality. To achieve this goal, we use the allyl derivatized FDCA, diallyl 2,5-furandicarboxylate (DAFDC),[22] in excess for polyesterifications with ethylene glycol and glycerol units for branching (Scheme 1).

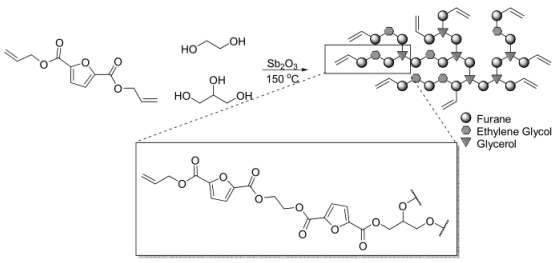

Scheme 1. Schematic representation of targeted hyperbrachned polyester systems.

By varying the stoichiometry of these types of polyesterifications (always with DAFDC in excess) targeting systems with various degrees of branching and full allyl termination, making these systems suitable for crosslinking, either with themselves or with multifunctional thiol crosslinkers. The allylated monomer bears resemblance to diallyl phthalate, a petrol-based monomer, which is used in thermoset systems due to its high heat and solvent resistance.[23] Besides the petrol-based nature of diallyl phthalate, several concerns are raised for its use due to suspected toxicity and carcinogenicity.[24] It is therefore of interest to identify alternative bio-based compounds with a similar reactivity that can be used as replacements of diallyl phthalate.

We here examine both a direct free radical crosslinking of the allyl groups as well as crosslinking with the tetrafunctional thiol, pentaerythritol tetrakis(3-mercaptopropionate) (PETMP). Thiol-ene networks[25,26] have shown desirable properties, stemming from their uniformity and conversion in crosslinking as well as their narrow glass transition temperatures[27]. This generally leads to lower stress in films and higher adhesion to surfaces[28], which would all be desireable properties for a replacement of diallyl phthalate.

Materials and Methods

Chemicals

Allyl alcohol (>99.5 %), 2,5-furandicarboxylic acid (97 %), antimony(III)oxide (99 %), ethylene glycerol (>99.8 %), glycerol (99.5 %), pentaerythriol tetrakis(3-mercaptopropionate) (>95 %), dicumyl peroxide (DCP, 98 %), ethyl acetate (99.8 %), methanol (99.8 %), n-heptane (99 %), tetrahydrofuran (>99.9 %) and deuterated trifluoroacetic acid (99.5 atom % D) were all acquired from Sigma-Aldrich and used as received.

Analytical Methods

Differential Scanning Calorimetry (DSC) experiments were conducted using a Discovery DSC from TA instruments scanning from -90 ^{o}C to 230 ^{o}C with a heating rate of 10 K/min. All samples were subjected to two heating cycles, and melting temperatures (T_m) are reported as the peak temperatures of the endothermic melting peaks, while glass transition temperatures (T_g's) were measured at the inflection point.

Nuclear Magnetic Resonance (NMR) spectra were obtained on a 400MHz Bruker Ascend magnet with an Avance II console and equipped with a Prodigy cryoprobe, at 400.13MHz for ^{1}H and 100.61 for ^{13}C. Samples were dissolved in deuterated trifluoroacetic acid and the chemical shift reference set at 11.50 PPM. Data were processed and plotted using Mnova software.

Borchardt and Daniels kinetic calculations

Kinetic calculations were performed using the Borchardt and Daniels method[29,30], in which the reaction rates, constants and orders are determined from the enthalpy obtained by integration of the reaction peak from a single DSC scan. The Borchardt and Daniels method utilizes Equation 1-3 in order to construct an Arrhenius plot. For these equations, α is the fractional conversion, ΔH is the total enthalpy for the reaction, ΔH_T is the remaining enthalpy of the reaction at time, t, n is the reaction order and $K(T)$ is the temperature dependent rate constant. The data points for these calculations are obtained by dividing the integral of the DSC reaction peak into 20 evenly spaced areas from the temperature at 10 % of the peak height until 50 % of the reaction has occurred (at $\Delta H_T = 0.5$), this limit being introduced to avoid calculation at the reduced reaction rate at high conversions.

$$1 - \alpha = \Delta H_T / \Delta H \qquad (1)$$

$$\frac{d\alpha}{dt} = \frac{dH}{dt}/\Delta H \qquad (2)$$

$$\ln\frac{d\alpha}{dt} = \ln\big(K(T)\big) + n * \ln(1-\alpha) \qquad (3)$$

Equations 1-3 can be used for the determination of the conversion rate, dα/dt, as well as the fractional conversion at time *t*. With these two values, a linear plot can be constructed from Equation 3 if the reaction order is known. However, in this case the order of the reaction is unknown. This was solved by plotting Equation 3 for a series of reaction orders and evaluating the coefficient of determination, R^2, and identifying the reaction order matching the highest R^2 value. The corresponding reaction order leading to the correct Arrhenius Plot can then be used for further determination of the activation energies and pre-exponential factors. With this method, the reaction order was refined to two significant digits. In order to predict isothermal conversion plots, the conversion function, $\alpha(t)$, was determined. This was accomplished by solving the differential Equation 3 with the standard condition $\alpha(0) = 0$, yielding Equation 4 which could be used for construction of the isothermal conversion plots.

$$\alpha(t) = 1 - e^{\frac{\ln\left(\frac{1}{knt-kt+1}\right)}{n-1}} \qquad (4)$$

For accessible comparison of all systems, the time required to reach 95 % conversion, $t_{\alpha 95-150^oC}$, was calculated for all systems.

Synthesis of diallyl furan-2,5-dicarboxylate (DAFDC)

Furan-2,5-dicarboxylic acid (100.0 g, 0.64 mol) was suspended in allyl alcohol (1000 mL) and concentrated sulfuric acid (4 mL) was added. The suspension was heated to reflux for 48 hours at

approximately 115 °C, yielding a clear yellow solution. Excess allyl alcohol (approximately 950 mL) was removed by distillation and the remaining residue was dissolved in ethyl acetate (1000 mL). The organic solution was washed twice with saturated $NaHCO_3$ solution (2x1000mL), followed by concentration of the organic phase by rotary evaporation. The obtained black residue was distilled at reduced pressure (b. p. 112 °C at 4 mbar, corrected b. p. 274 °C) yielding the desired diallyl furan-2,5-dicarboxylate as a white crystalline solid upon cooling (139.1 g, 0.59 mol, 92 %).

General procedure for synthesis of branched and linear polymer systems (System BPE2).

Diallyl furan-2,5-dicarboxylate (10.1 g, 42.81 mmol), ethylene glycol (0.466 g, 7.51 mmol), glycerol (1.04 g, 11.29 mmol) and antimony trioxide (0.043 g, 0.15 mmol) were mixed as a melt at 50 °C under nitrogen flow for one hour. Nitrogen flow was stopped and the mixture was heated to 150 °C for 20 hours followed by evacuation of formed allyl alcohol under vacuum for 8 hours or until vitrification. Following cooling, the sample was dissolved in THF (50 mL) and precipitated into n-heptane (450 mL), yielding the branched prepolymer system as a white solid (5.54 g, 63 %). A comprehensive list of all syntheses and applied solvents can be located in the Supporting Information.

General procedure for DSC curing

Samples for reactive DSC scans were prepared by mixing the desired prepolymer system with an amount of PETMP resulting in a 1:1 allyl:thiol stoichiometry. To the components were added a stock solution of DCP (10 g/L) in acetone and ground in a mortar until a homogenous sample

was obtained. The sample was concentrated and 3-5 mg was transferred to a DSC cup. Samples without a thiol crosslinker were mixed directly with the DCP stock solution in a mortar.

Results and Discussion

Synthesis of prepolymeric systems

The DAFDC monomer was synthesized according to previous work.[22] The linear and branched systems were synthesized using the DAFDC monomer, ethylene glycol and glycerol for branching with an adapted procedure using catalytic antimony(III)oxide,[8] making all systems fully bio-based. Eight systems (three linear and five branched systems) were synthesized with various feed stoichiometries and excess of DAFDC. The compositions of systems are listed in Table 1. For all branched systems, a percentage of ethylene glycol was replaced by glycerol such that the highest degree of branching without the possibility of critical crosslinking was obtained. These amounts were calculated using both Carother's and Statistical methods[31], using the lowest obtained value as a threshold. DSC analysis for all prepolymers were performed for measurement of glass transition temperatures (T_g) and melting points (T_m) and are stated along with yields and obtained molecular weights in Table 1. Melting points were only observed for the linear systems and BPE4 due to these being semi-crystalline.

Table 1. Overview of synthesized hyperbranched polyester systems.

Entry	Type of Polymer	Functionality of feed	Glycerol Content	T_m	T_g	M_n[c]	DB	Yield
		COOAll:OH	% of EG	°C	°C	g/mol		%
LPE1	Linear	2:1	0	151.6	-22.1	753	N/A	41
LPE2	Linear	1.5:1	0	173.4	-19.8	918	N/A	48
LPE3	Linear	1:1	0	186.1	15.6	1333	N/A	78
BPE1	Branched	2:1	100	[d]	8.7	1319	0.52	56
BPE2	Branched	1.75:1	60	[d]	15.1	1109	0.45	63
BPE3	Branched	1.5:1	40	[d]	9.5	1185	0.36	63
BPE4	Branched	1.25:1	10	180.8	22.2	1321	0.14	94
BPE5[a]	Branched	1.1:1	5	[d]	28.6	1220	0.19	59

[a] Vitrification of reaction before completion.

[b] Did not cure fully

[c] Determined from NMR

[d] Amorphous

NMR analysis proved full allyl termination of all the systems, except for LPE3 (with stoichiometric feed functionality), leading to straight-forward assignment of the linear polymers and determination of their molecular weights as shown in Table 1. System LPE3 showed presence of peaks corresponding to hydroxyl-chain ends of the ethylene glycol, corresponding to 23 % of all chains being terminated with ethylene glycol units. NMR spectra of the branched systems proved slightly more challenging due to proton overlap of the glycerol units with those of the ethylene glycols and allyls. HSQC experiments of the branched systems showed only a single correlation of the carbon of the secondary position of glycerol, corresponding to an ether, proving that all glycerol units were fully branched (Supporting Information, Figure S1). Figure 1

shows a schematic H-NMR analysis with the functional groups identified through a combination of HSQC and COSY. From integrals of these H-NMR spectra the amount of branching points and allyl end groups could be determined using the secluded peak of the two terminal hydrogen atoms of the allyls (Peak C) to identify the integrals of the overlapping peaks, which led to the relative amounts of allyl-, furane-, glycerol-, and ethylene glycol-units (these values along with an overview of the NMR analyses are stated in Table S1 in the Supporting Information), with the abundances of these units presented as relative concentration of units in the polymer system in mmol/g and weight percentages presented in Table 2. Correct assignment of the H-NMR peaks was confirmed by all relative integrals following the stoichiometric balance of functional groups. The results obtained from the NMR analysis proved the expected trend of decreased allyl concentrations with decreasing amounts of glycerol in the feed. BPE5 differs from this trend due to vitrification at the reaction temperature (150 ^{o}C), while the other branched systems remained liquid throughout the polymerization, causing the reaction of BPE5 to halt before reaching as high conversion as the other systems. NMR results however still confirmed that a fully allyl functionalized system had been obtained.

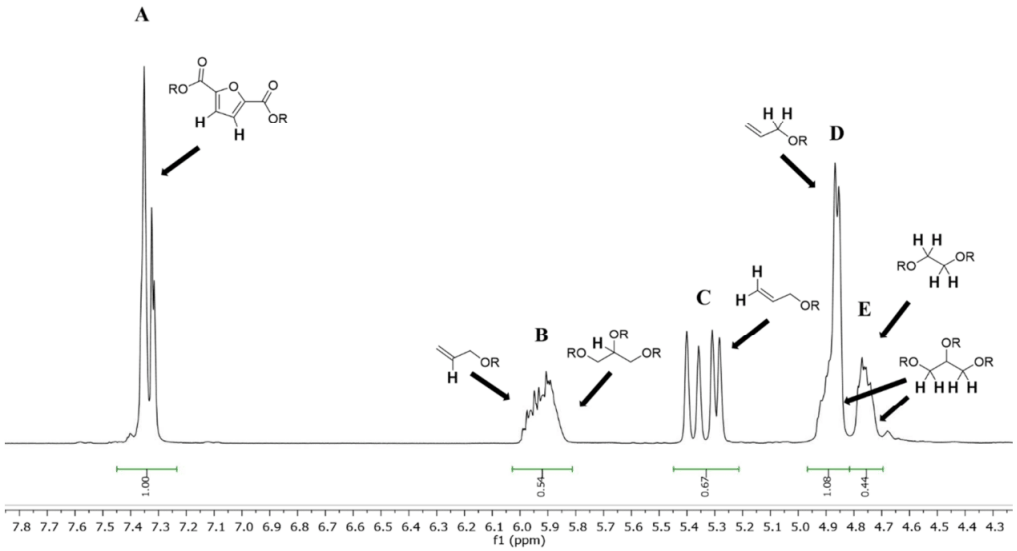

Figure 1. Schematic analysis of peak overlap for the hyperbranched polyester systems (BPE1 as example).

Table 2. Concentrations of the different units of the synthesized hyperbranched polyester systems.

	Abundances							
	mmol/g				*w%*[a]			
	Allyls	Furanes	Glycerol	Ethylene Glycol	Allyls	Furanes	Glycerol	Ethylene Glycol
L1	2.66	5.11	0	3.71	10.82	78.79	0	10.4
L2	2.18	5.18	0	3.96	9.04	79.84	0	11.12
L3[b]	1.16	5.26	0	4.84	4.75	81.08	0	14.16
B1	3.38	5.04	2.07	0	13.87	77.65	8.49	0
B2	3.27	5.02	1.56	0.95	13.52	77.41	6.4	2.68
B3	2.71	5.11	1.17	1.84	11.33	78.69	4.82	5.16
B4	1.48	5.28	0.11	4.22	6.39	81.33	0.43	11.84
B5	1.78	5.24	0.31	3.7	7.54	80.8	1.29	10.37

[a] For weight percentages, the oxygen atoms of the esters have been included with the furane-units.

[b] L3 showed two additional peaks corresponding to 1.54 mmol/g ethylene glycol termination, 7 % of all ethylene glycol units or 23 % of all chain ends.

Determination of molecular weight of prepolymeric systems

With the intention of determining the molecular weights of the branched systems, we initially attempted size exclusion chromatography. However, the poor solubility of the systems and their high affinity for the column prohibited this analysis. With the relative stoichiometries of each type of unit known from NMR, it was possible to derive a mathematical set of formulas for a given type of system which could be used to determine M_n. These types of calculations relate to the method used for determining degree of branching (DB) with either Equation 5[32] or Equation

6[33] from the amounts of the various units in the polymer system (D: Dendritic segments, L: Linear segments, T: Terminal segments). For this, the molecular weight is normally known along with the relative stoichiometries of the various units – allowing for easy determination of the average number of units in the molecule. The relative stoichiometries are usually obtained from NMR, where it is possible to distinguish between the linear, dendritic and terminal segments. In many cases, this can be determined by H-NMR, but in cases with severe overlap, quantitative C-NMR[34] or 2D[35] methods can be applied.

$$DB = \frac{D+T}{D+L+T} \quad (5)$$

$$DB = \frac{2D}{2D+L} \quad (6)$$

In order to construct equations for M_n which depend solely on the relative stoichiometric ratios of units in the polymer system, an analysis of the growth patterns of the specific type of system is needed. For this, the relative ratios for the hyper branched system are noted as n_x and the actual number of a type of unit in the average molecule is denoted as N_x. In order to distinguish between different types of linear segments, units will be named with an AB_x nomenclature, such as for example glycerol is an A_3 dendritic segment (if fully branched), the FDCA unit is a B_2 linear segment, ethylene glycol is an A_2 linear segment and the allyl groups are an A_1 terminal unit. (A: alcohol, B: carboxylic acid). Considering systems such as BPE1-5 a systematic growth pattern can be observed when increasing the amount of branching and linear segments as shown in Figure 2 with the amounts of each type of unit stated below each example.

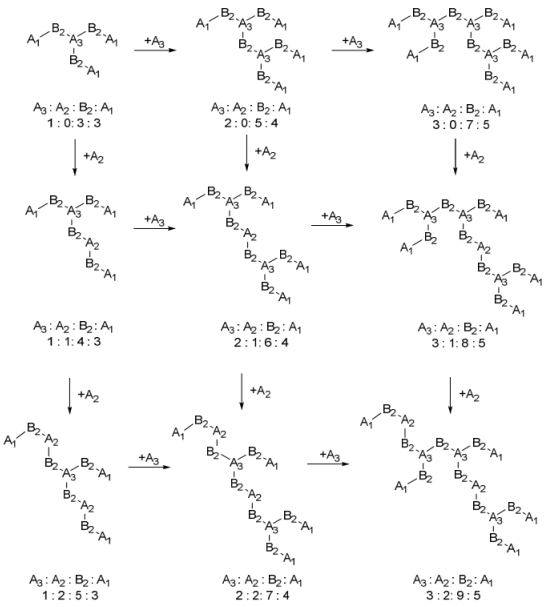

Figure 2. Growth pattern for BPE systems when increasing the amount of dendritic units (horizontal progression) and linear units (vertical progression).

Examining the horizontal progression of the first line of Figure 2, a representation of the BPE1 system where no ethylene glycol (A_2) is present can be seen. This allows two equations to be constructed for this type of system (Equation 7 and 8), describing the amount of B_2 (furanes) and A_1 (allyls) from the amount of A_3 (glycerol). Note that in the case of N_{A_3} approaching 0, N_{A_1} approaches 2 and N_{B_2} approaches 1, which corresponds to the monomer.

$$N_{A_1} = N_{A_3} + 2 \qquad (7)$$

$$N_{B_2} = 2 * N_{A_3} + 1 \qquad (8)$$

Since only the relative and not absolute stoichiometries are known for the system, a constant value, k, has to be determined which follows $k * n_x = N_x$, which yields equations 9 and 10, which can be arranged to yield two expressions for k in Equation 11 and 12.

$$k * n_{A_1} = k * n_{A_3} + 2 \quad (9)$$

$$k * n_{B_2} = 2 * k * n_{A_3} + 1 \quad (10)$$

$$k = \frac{2}{n_{A_1} - n_{A_3}} \quad (11)$$

$$k = \frac{1}{n_{B_2} - 2 * n_{A_3}} \quad (12)$$

These two expressions allow for different determination of k dependent on what factors are known for a given system. In cases like the BPE systems where all relative stoichiometries are known, both expressions can be calculated and the average value, k_{av}, can be used to determine the number average molecular weight (M_n), using the respective molar mass of each unit, M_x, as shown in Equation 13.

$$\overline{M_n} = \sum k * n_x * M_x \quad (13)$$

In the case of systems BPE2-5, an ethylene glycol linear segment (A_2) is added, extending the equations as shown in Equations 14-16. The amount of terminal units remain unchanged and still follow Equation 7. Secondly, every added A_2 segment will necessarily lead to one additional B_2 unit, extending Equation 8 to Equation 14. These can in turn lead to a new term for k in Equations 15-16 allowing determination of M_n from Equation 13. Note that for $N_{A_2} = 0$ the Equation 15 transforms to the original Equation 10.

$$N_{B_2} = 2 * N_{A_3} + 1 + N_{A_2} \quad (14)$$

$$k * n_{B_2} = 2 * k * n_{A_3} + k * n_{A_2} + 1 \quad (15)$$

$$k = \frac{1}{n_{B_2} - 2 * n_{A_3} - n_{A_2}} \quad (16)$$

Using this approach, the average molecular weights of the BPE systems were determined as shown in Table 1. The systems are of similar molecular weight, most likely due to the low temperature applied, causing the reaction to stall before completion. This however, is not a drawback for this study since the intention was to synthesize highly functional low molar mass branched systems suitable for further crosslinking. Degree of branching (DB) could also be calculated as stated in Table 1, where a very low DB was observed for BPE4, which explains the crystallinity since this system is almost analogue to the linear systems. Examples of this calculation method are presented in Supporting Information.

Though this method is especially developed for the BPE-type systems, it is easily adaptable to other types of systems (examples for all the following methods are given in the Supporting Information), for example, cases with other types of branching units, such as the tetrafunctional pentaerythritol. Since each added branching unit will increase the amount of terminals by two and the amount of linear segments by three, this feature simply expands Equations 7 and 14 to Equation 17 and 18. Also, a generalized formulation of these equations can be made which can be applied for any system with any mixture of linear and branching molecules, A_n, shown in Equations 19 and 20.

$$N_{A_1} = 2 * N_{A_4} + 2 \quad (17)$$

$$N_{B_2} = 3 * N_{A_4} + N_{A_2} + 1 \quad (18)$$

$$N_{A_1} = (\sum(n-2) * A_n) + 2 \quad (19)$$

$$N_{B_2} = (\sum(n-1) * A_n) + 1 \quad (20)$$

Finally, other interesting types of hyperbranched systems, are the so-called AB_2 systems, where the monomer is reacting with itself, yielding dendritic (D), linear (L) and terminal (T) segments, dependent on number of B groups reacted. Since the minimal molecule with only one

dendritic segment will have two terminals, and the amount of terminals grow by one with every new dendritic unit, a simple expression for *k* can be derived in Equations 21-23. However, due to any number of linear segments being possible in sequence, no dependency for n_L can be established, yielding only a single expression for *k*.

$$N_{\mathrm{T}} = N_D + 1 \qquad (21)$$

$$k * n_T = k * n_D + 1 \qquad (22)$$

$$k = \frac{1}{n_T - n_D} \qquad (23)$$

Crosslinking of prepolymer systems

With the allyl content of the systems known, the prepolymer systems were crosslinked with and without PETMP using dicumyl peroxide as a thermal initiator. Photocrosslinking was not possible due to the high crystallinity and melting points of the prepolymer systems making this type of crosslinking unfeasible, and a thermal approach was used instead. In order to study the curing process, the crosslinking reactions were performed in DSC cups, allowing for close monitoring of the reaction process.

The curing process was evaluated using Borchardt and Daniels kinetics, allowing determination of reaction constant, reaction order and prediction of isothermal conversion plots from the enthalpy of the reaction, obtained from a single DSC scan. Curing experiments without a thiol crosslinker proved the ineffectiveness of the allyl groups as substrate for free radical polymerization. This was observed by DSC scans showing some curing reaction along with a prominent melting point on the second heating cycle, indicating a not fully crosslinked system. A fully crosslinked system could however be obtained by increasing the amount of initiator to 5 wt%, an amount deemed too high for the purpose of this study. General problems were observed when crosslinking both the linear and branched systems without a thiol crosslinker, while BPE1-

3 were able to cure fully also in the absence of thiol crosslinker. When adding the tetrafunctional thiol in a 1:1 thiol:allyl ratio, crosslinking of most of the systems could be observed, with the exception of the linear systems LPE2 and LPE3 that showed melting points on the second heating cycle of the DSC scan. Figure 3 shows this for a system consisting of the monomer, PETMP and 1 wt% of DCP, with normalized DSC curing peak, reaction order refinement and Arrhenius plot, respectively. The Borchardt and Daniels method were applied to the systems, yielding the kinetic parameters systems, where it was possible to extract the kinetic data. BPE4 has been excluded due to interference between the melting transition and the curing peak, along with the systems that did not fully cure. All kinetic data are collected in Table 3 and all excluded plots relating to the calculations are presented in Supporting Information.

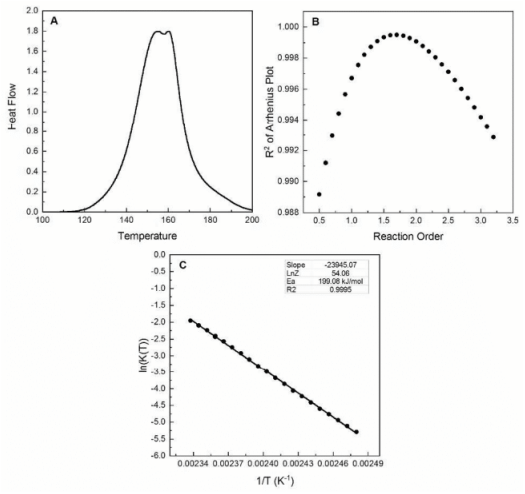

Figure 3. Plots for the Borchardt and Daniels kinetics for the monomer with a PETMP crosslinker. A: Normalized curing peak. B: Refinement of reaction order. C: Arrhenius plots with the obtained reaction order.

From the data presented in Table 3 a clear correlation of decreasing activation energies and reaction orders could be observed, both for systems with and without a thiol crosslinker, with an increased branching. Secondly, a large decrease in activation energies and an increase in reaction order was further observed when adding the thiol crosslinker. This was expected, due to the generally more favorable thiol-ene reaction compared to the free radical polymerization of allyl esters. Furthermore, T_g determined from second heating cycle of the crosslinking showed a clear increase from the hyperbranched system, which was expected due to network formation. Using the data in Table 3 isothermal conversion plots for temperatures in the range of 120 ^oC to 160 ^oC could be constructed through Equation 4 for all systems as shown in Figure 4.

Table 3. Kinetic parameters for curing of the hyperbranched systems.

System	Allyl:Thiol	Activation Energy kJ/mol	lnZ	n	$t_{\alpha 95-150^{o}C}$ s	$T_{g,\ network}$ ^{o}C
Monomer	1:0	N/A	N/A	N/A	N/A	N/A
Monomer	1:1	199.1	54.06	1.68	123.0	-11.1
BPE1	1:0	190.0	48.02	1.25	1775.8	41.1
BPE1	1:1	167.1	42.82	1.38	600.8	51.5
BPE2	1:0	163.3	41.24	1.09	559.6	33.9
BPE2	1:1	143.2	36.38	1.26	342.4	37.9
BPE3	1:0	130.0	32.13	0.91	326.2	25.9
BPE3	1:1	130.2	32.71	1.07	245.4	36.3
BPE4	1:0	N/A	N/A	N/A	N/A	N/A
BPE4	1:1	N/A	N/A	N/A	N/A	43.3
BPE5	1:0	N/A	N/A	N/A	N/A	42.8
BPE5	1:1	122.9	29.97	0.94	392.5	36.6
LPE1[a]	1:0	N/A	N/A	N/A	N/A	N/A
LPE1	1:1	190.8	49.02	1.68	1822.1	20.1
LPE2	1:0	N/A	N/A	N/A	N/A	N/A
LPE2	1:1	N/A	N/A	N/A	N/A	N/A
LPE3	1:0	N/A	N/A	N/A	N/A	N/A
LPE3	1:1	N/A	N/A	N/A	N/A	N/A

[a] Due to some melting point interference, a decent reaction order could not be obtained for system LPE1 and the reaction order has been set to that of the monomer.

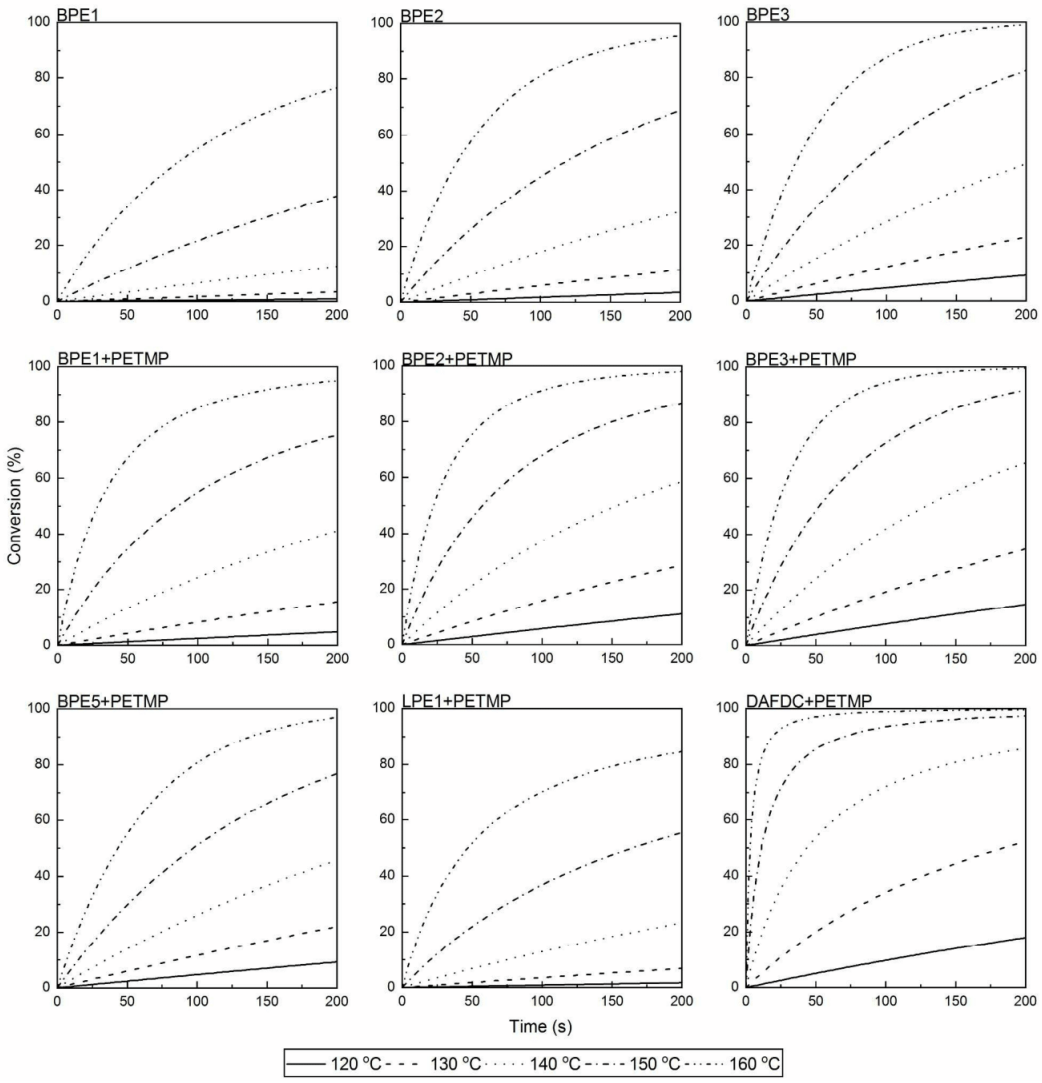

Figure 4. Predicted isothermal plots for curings of the hyperbranched polyester systems.

A general trend is an increased conversion rate when decreasing the amount of branching points in the hyperbranched system. Figure 4 show that curing of systems BPE1-3 without a thiol crosslinker showed major increases in conversion rates, with BPE2 and BPE3 reaching 95 % conversion in less than a third of the time required for system BPE1. This increased conversion

rate can most likely be attributed to the lower amounts of allyl esters undergoing polymerization before reaching a fully crosslinked systems, while still maintaining relative accessibility of the ester groups.

For systems employing the thiol crosslinker, the same trend is observed for systems BPE1-3. However, system BPE5 exhibits slower conversion rates than BPE3 (Figure 4), despite showing the lowest activation energy of all the system. Again, this behavior stems from the accessibility of the allyl esters, a phenomenon clearly visible from the decrease in the pre-exponential factor, *LnZ*, which corresponds to the frequency of collision of the reactive groups.[36] With decreasing degree of branching, it stands to reason that the probability of collisions will be lowered, thereby decreasing the reaction rate even at low activation energies. Also, with BPE5 having a very low DB, it is almost analogue to the linear systems which show the slowest conversion. Lastly, this effect is very prominent when comparing crosslinking of the monomer system with LPE1 with thiol crosslinkers (Figure 4). These two reaction show comparable activation energies, but with the conversion of the monomer system progressing approximately 15 times faster than LPE1 (estimated from $t_{\alpha 95-150\,^oC}$) due to the higher mobility of the monomeric system leading to more collisions and thereby the highest pre-exponential factor of all the systems.

Interestingly, the obtained kinetics parameters show correlation with the degree of branching stated in Table 1. In general, all three parameters increase with the degree of branching (Figure 5). However, as seen from the $t_{\alpha 95-150^oC}$ values in Table 3**,** fastest curing rates seems to be obtained around the BPE3 systems with a DB of 0.36, most likely due to lower DBs lead to a semi-crystalline system, which hinders the reaction (Figure 5-D).

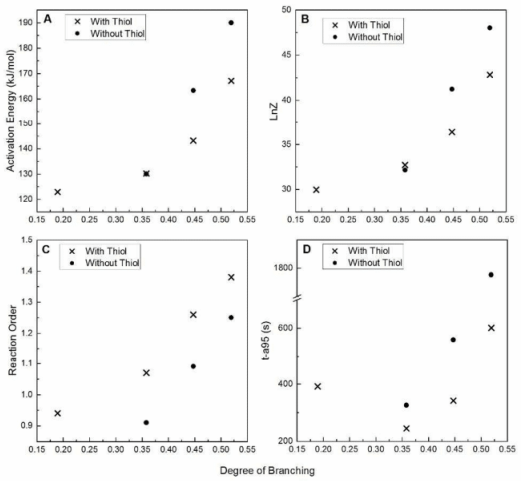

Figure 5. Correlation between the degree of branching obtained from NMR and the kinetic parameters calculated from the Borchardt and Daniels method.

Conclusion

We have shown a straight-forward and sustainable method of synthesizing fully allyl-functionalized hyperbranched and linear polyesters from solely bio-based sources. Through NMR spectroscopy it was possible to conduct a complete analysis of the synthesized systems, and to obtain the relative constituents of the systems along with the mass fractions. The incapability to determine molecular weight by SEC led to the development of a new method for determining molecular weights for hyperbranched polyesters from NMR. Results showed that systems of similar molecular weight with various degrees of branching were obtained. DSC analysis of the thermally initiated curing of the systems through both a direct free-radical polymerization approach and with thiol crosslinkers allowed determination of kinetic parameters and prediction of isothermal conversion plots through Borchardt and Daniels kinetics. Cross-examination of NMR and kinetic results proved a correlation between degree of branching and

activation energies, pre-exponential factors, reaction orders and conversion times. With this study we have produced a new type of renewable thermoset material, with controllable curing chemistry through feed stoichiometries and crosslinking methods. This type of novel material is an interesting candidate for replacement of thermosets derived from petrol-based sources such as polydiallyl phthalate, which in turn can lead to a generally more renewable polymer industry.

ASSOCIATED CONTENT

Supporting Information includes NMR spectra and analysis, feed compositions of hyperbranched polyester systems, DSC experiments and and plots relating to the Borchardt and Daniels kinetics.

AUTHOR INFORMATION

Corresponding Author

*E-mail: adt@kt.dtu.dk

ACKNOWLEDGMENT

We would like to thank The Technical University of Denmark (DTU) for financial support and Senior Researcher Liyun Yu for assistance with DSC analysis.

REFERENCES

(1) Gandini, A. Monomers and Macromonomers from Renewable Resources. In *Biocatalysis in Polymer Chemistry*; Loos, K., Ed.; Wiley-VCH Verlag GmbH & Co. KGaA, 2010; pp 1–33.

(2) Naik, S. N.; Goud, V. V.; Rout, P. K.; Dalai, A. K. Production of First and Second

Generation Biofuels: A Comprehensive Review. *Renew. Sustain. Energy Rev.* **2010**, *14* (2), 578–597.

(3) Dusselier, M.; Van Wouwe, P.; De Smet, S.; De Clercq, R.; Verbelen, L.; Van Puyvelde, P.; Du Prez, F. E.; Sels, B. F. Toward Functional Polyester Building Blocks from Renewable Glycolaldehyde with Sn Cascade Catalysis. *ACS Catal.* **2013**, *3* (8), 1786–1800.

(4) Elliot, S. G.; Andersen, C.; Tolborg, S.; Meier, S.; Sádaba, I.; Daugaard, A. E.; Taarning, E. Synthesis of a Novel Polyester Building Block from Pentoses by Tin-Containing Silicates. *RSC Adv.* **2017**, *7* (2), 985–996.

(5) Ståhlberg, T.; Rodriguez-Rodriguez, S.; Fristrup, P.; Riisager, A. Metal-Free Dehydration of Glucose to 5-(Hydroxymethyl)furfural in Ionic Liquids with Boric Acid as a Promoter. *Chem. - A Eur. J.* **2011**, *17* (5), 1456–1464.

(6) Rosatella, A. A.; Simeonov, S. P.; Frade, R. F. M.; Afonso, C. a. M. 5-Hydroxymethylfurfural (HMF) as a Building Block Platform: Biological Properties, Synthesis and Synthetic Applications. *Green Chem.* **2011**, *13* (4), 754–793.

(7) Eerhart, A. J. J. E.; Faaij, A. P. C.; Patel, M. K. Replacing Fossil Based PET with Biobased PEF; Process Analysis, Energy and GHG Balance. *Energy Environ. Sci.* **2012**, *5* (4), 6407–6422.

(8) Gopalakrishnan, P.; Narayan-Sarathy, S.; Ghosh, T.; Mahajan, K.; Belgacem, M. N. Synthesis and Characterization of Bio-Based Furanic Polyesters. *J. Polym. Res.* **2014**, *21*, 340–348.

(9) Papageorgiou, G. Z.; Tsanaktsis, V.; Bikiaris, D. N. Synthesis of Poly(ethylene Furandicarboxylate) Polyester Using Monomers Derived from Renewable Resources: Thermal Behavior Comparison with PET and PEN. *Phys. Chem. Chem. Phys.* **2014**, *16* (17), 7946–7958.

(10) Tomás, R. A. F.; Bordado, J. C. M.; Gomes, J. F. P. P-Xylene Oxidation to Terephthalic Acid : A Literature Review Oriented toward Process Optimization and Development. *Chem. Rev.* **2013**, *113*, 7421–7469.

(11) Gorbanev, Y. Y.; Kegnæs, S.; Riisager, A. Selective Aerobic Oxidation of 5-Hydroxymethylfurfural in Water over Solid Ruthenium Hydroxide Catalysts with Magnesium-Based Supports. *Catal. Lett.* **2011**, *141* (12), 1752–1760.

(12) Hansen, T. S.; Sádaba, I.; García-Suárez, E. J.; Riisager, A. Cu Catalyzed Oxidation of 5-Hydroxymethylfurfural to 2,5-Diformylfuran and 2,5-Furandicarboxylic Acid under Benign Reaction Conditions. *Appl. Catal. A Gen.* **2013**, *456*, 44–50.

(13) Ma, F.; Hanna, M. A. Biodiesel Production: A Review. *Bioresour. Technol.* **1999**, *70* (1), 1–15.

(14) Nguyen, H.; Löf, D.; Hvilsted, S.; Daugaard, A. Highly Branched Bio-Based Unsaturated Polyesters by Enzymatic Polymerization. *Polymers (Basel).* **2016**, *8* (10), 363–374.

(15) Jones, F. N. *Alkyd Resins in Ullman's Encyclopedia of Industrial Chemistry*; Wiley-VCH Verlag GmbH & Co. KGaA: Weinheim, Germany, 2003.

(16) Wicks, Z. W. *Alkyd Resins in Encyclopedia of Polymer Science*; John Wiley & Sons, Inc.: Weinheim, Germany, 2007.

(17) Holmberg, K. *Alkyd Resins in Coatings Technology Handbook*; Tracton, A. A., Ed.; CRC Press: Boca Raton, FL, USA, 2006.

(18) Zhang, H.; Grinstaff, M. W. Recent Advances in Glycerol Polymers: Chemistry and Biomedical Applications. *Macromol. Rapid Commun.* **2014**, *35* (22), 1906–1924.

(19) Shiramizu, M.; Toste, F. D. Deoxygenation of Biomass-Derived Feedstocks: Oxorhenium-Catalyzed Deoxydehydration of Sugars and Sugar Alcohols. *Angew. Chem. Int. Ed.* **2012**, *51* (32), 8082–8086.

(20) Boucher-Jacobs, C.; Nicholas, K. M. Oxo-Rhenium-Catalyzed Deoxydehydration of Polyols with Hydroaromatic Reductants. *Organometallics* **2015**, *34* (10), 1985–1990.

(21) Dethlefsen, J. R.; Lupp, D.; Oh, B. C.; Fristrup, P. Molybdenum-Catalyzed Deoxydehydration of Vicinal Diols. *ChemSusChem* **2014**, *7* (2), 425–428.

(22) Larsen, D. B.; Sønderbæk-Jørgensen, R.; Duus, J.; Daugaard, A. E. Investigation of Curing Rates of Bio-Based Thiol-Ene Films from Diallyl 2,5- Furandicaboxylate. *Eur. Polym. J.* **2018**, *102* (March), 1–8.

(23) Krähling, L.; Krey, J.; Jakobson, G.; Grolig, J.; Miksche, L. *Allyl Compounds. In Ullman's Encyclopedia of Industrial Chemistry*; Wiley-VCH, 2012.

(24) Carcinogenesis Bioassay of Diallyl Phthalate in B6C3F1 MICE, U.S. Department of Health and Human Services, 1983.

(25) Hoyle, C. E.; Bowman, C. N. Thiol-Ene Click Chemistry. *Angew. Chem. Int. Ed.* **2010**, *49* (9), 1540–1573.

(26) Lowe, A. B. Thiol-Ene "click" Reactions and Recent Applications in Polymer and Materials Synthesis. *Polym. Chem.* **2010**, *1*, 17–36.

(27) Fouassier, J.-P.; Rabek, J. F. *Radiation Curing in Polymer Science and Technology*, 1st ed.; Springer Netherlands, 1993.

(28) Hoyle, C. E.; Lee, T. Y.; Roper, T. Thiol-Enes: Chemistry of the Past with Promise for the Future. *J. Polym. Sci. Part A Polym. Chem.* **2004**, *42* (21), 5301–5338.

(29) Borchardt, H. J.; Daniels, F. The Application of Differential Thermal Analysis to the Study of Reaction Kinetics. *J. Am. Chem. Soc.* **1957**, *79* (1), 41–46.

(30) ASTM E2041-13e1 Standard Test Method for Estimating Kinetic Parameters by Differential Scanning Calorimeter Using the Borchardt and Daniels Method, ASTM International, West Conshohocken, PA, 2013, https://doi.org/10.1520/E2041.

(31) Odian, G. Principles of Polymerization; John Wiley & Sons, Inc.: Hoboken, New Jersey, 2004; pp 103–112.

(32) Hawker, C. J.; Lee, R.; Frécnet, J. M. J. One-Step Synthesis of Hyperbranched Dendritic Polyesters. *J. Am. Chem. Soc.* **1991**, *113* (12), 4583–4588.

(33) Hölter, D.; Burgath, A.; Frey, H. Degree of Branching in Hyperbranched Polymers. *Acta Polym.* **1997**, *48*, 30–35.

(34) De Luca, E.; Richards, R. W. Molecular Characterization of a Hyperbranched Polyester. I. Dilute Solution Properties. *J. Polym. Sci. Part B Polym. Phys.* **2003**, *41*, 1339–1351.

(35) Zhu, X.; Chen, L.; Chen, Y.; Yan, D. Using 2D NMR to Determine the Degree of

Branching of Complicated Hyperbranched Polymers. *Sci China Ser B-Chem* **2008**, *51* (11), 1057–1065.

(36) Atkins, P.; Paula, J. De. Atkins' Physical Chemistry; Oxford University Press: Oxford, 2010; pp 799–802.

Appendix G: Manuscript 5

ACS Sustainable Chemistry & Engineering

This document is confidential and is proprietary to the American Chemical Society and its authors. Do not copy or disclose without written permission. If you have received this item in error, notify the sender and delete all copies.

Bio-based cationically polymerizable epoxy thermosets from furan and fatty acid derivatives

Journal:	*ACS Sustainable Chemistry & Engineering*
Manuscript ID	sc-2018-01817u
Manuscript Type:	Article
Date Submitted by the Author:	23-Apr-2018
Complete List of Authors:	Nameer, Samer; KTH Royal Institute of Technology, Fibre and Polymer Technology, Division of Coating Technology Larsen, Daniel; Danmarks Tekniske Universitet, Department of Chemistry Duus, Jens; Technical University of Denmark, Chemistry Daugaard, Anders; Technical University of Denmark, Chemical Engineering Johansson, Mats; KTH Royal Institute of Technology, Fibre and Polymer Technology, Division of Coating Technology

SCHOLARONE™
Manuscripts

ACS Paragon Plus Environment

Bio-based cationically polymerizable epoxy thermosets from furan and fatty acid derivatives

Samer Nameer[†1], Daniel B. Larsen[†2,3], Jens Ø. Duus[3], Anders E. Daugaard[2], Mats Johansson*[1]

[1]*KTH Royal Institute of Technology, Department of Fibre and Polymer Technology, Division of Coating Technology, SE-100 44 Stockholm, Sweden.*

[2]*Danish Polymer Centre (DPC), Department of Chemical and Biochemical Engineering, Technical University of Denmark, Søltofts Plads Building 227, 2800 Kgs. Lyngby, Denmark.*

[3]*Department of Chemistry, Technical University of Denmark, Kemitorvet, Bygning 207, 2800 Kgs. Lyngby, Denmark.*

† These authors contributed equally to the work.

**Correspondence to: Mats Johansson (E-mail: matskg@kth.se)*

Keywords:

Renewable; epoxy; FDCA; UV; thermoset

1 Abstract

In the pursuit of environmentally friendly building blocks in polymer chemistry the utilization of bio-based monomers is highly desired. In the present study has the bio-based monomer 2,5-furandicarboxylic acid (FDCA) been extended into epoxy thermosets. The study presents the synthesis of diallyl furan-2,5-dicarboxylate (DAFDC) followed by an epoxidation of the allyls to form diglycidyl furan-2,5-dicarboxylate (DGFDC). DGFDC was then co-polymerized in both stoichiometric and off-stoichiometric ratios with epoxidized fatty acid methyl esters to form a range of thermosets. The cross-linking reaction was either thermally or UV-induced cationic polymerization utilizing onium salt initiators where the reactivity was studied by DSC and real-time FTIR. Furthermore, the structure-property relationships of the final thermosets were determined by DMTA revealing a possibility to tune the properties over a wide range. In addition thermosets were made from diglycidyl Bisphenol-A (DGBPA) with epoxidized fatty acid methyl esters made for comparative purposes.

2 Introduction

The inevitable exhaustion of fossil resources leads to a necessity for development of bio-based alternatives to previously petrol-based industries. An example of this is the plastics industry, where the most widely used commodity plastics have been oil-based.[1] In addition, the discussion of depleting fossil oil reserves together with environmentally hazardous emissions of gases has caused the need for development of an array of new environmentally benign routes towards bio-based monomers and polymers. With a vast amount of different bio-feedstocks becoming available from bio-refineries,[2] the development of new methods for the utilization of these are highly desired.

An interesting source of bio-based raw materials is fatty acids due to their abundance, low cost and versatility.[3] Fatty acids are available both from annual crops, e.g. vegetable oils, or conifers, e.g. tall oil fatty acid, in a wide variety with the common feature that they contain an acyl group and a long hydrocarbon chain. Furthermore, many fatty acids have additional functionalities such as alkenes, hydroxyls, or epoxides.[4,5] One example of plant oil utilized for material applications is linseed oil (LO) used for alkyd paints already developed in the 1920s.[6,7] LO is a triglyceride composed of glycerol and fatty acids with a high average number of unsaturations in C_{18} fatty acids.[4,5] From a chemist point of view LO is highly interesting due to its intrinsic functionalities. The unsaturations can either be used directly in an oxidative radical polymerization e.g. autoxidation[8] or be oxidized by a peracid to form an epoxide.[9] Epoxidized vegetable oils are already established in several applications such as printing inks, e.g. epoxidized soy bean oil. These resins are however limited to applications without high demands on the mechanical performance.[5] Several routes to overcome this issue have been tested and amongst the most successful is the combination of epoxidized fatty acids with sucrose as a rigid component in fatty acid sucrose esters.[10,11] In addition, epoxy-functional fatty acids are also found directly as synthesized in natural systems e.g. vernolic acid in *Vernonia species*[12] and *Euphorbia lagascae*[13] or *cis*-9,10-epoxy-18-hydroxyoctadecanoic acid in birch bark[14] (*betula pendula*), leaf cutin[15] (c*amelina*) and in tea leaves[16] (*camellia sinensis*).

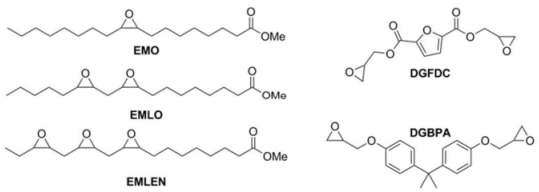

Figure 1: Chemical structures of the monomers used

Another type of monomer which has received great attention through the latest years is the bio-based 2,5-furandicarboxylic acid (FDCA), which can be produced from sugars with hydroxyl methylfurfural (HMF) as an intermediate.[3,17,18] The reason for the attention is due to that FDCA share similar properties with the petrol-based terephthalic acid,[19] produced from xylene, which finds broad application in polymer science.[20] Terephthalic acid constitutes the major building block of poly ethylene terephthalate (PET), the plastic used for the production of plastic bottles, food containers as well as fibers in cloth fiber applications. In addition, FDCA is one of the twelve building block chemicals that is considered to be a platform for synthesis of high-value bio-based chemicals or materials.[2] FDCA has not only been considered as a building block for thermoplastics such as PET but also as a building block in various other polyesters used for thermosets.[18] Moreover, FDCA has been be functionalized with allyl groups using allyl alcohol[21] or allyl bromide[22] which has in turn would paved the way for FDCA to be used in thiol-ene thermosets. The production of FDCA has also recently been scaled up and is now available in larger quantities on the market by companies e.g. BASF, Avantium and Corbion.

One specific type of functionality that has obtained increased attention in the development of new bio-based polymer systems is the epoxide group.[5] The epoxy functional group has a suitable reactivity due to its ring-strain it is a versatile functionality for a wide range of chemical transformations. The epoxide opening can be catalyzed under both basic and acidic conditions hence, providing a unique platform for different types of reactions.[23] Epoxide chemistry is also well established in numerous applications ranging from surface (protective) coatings, electronics, inks, adhesive, to composites just to mention a few. Commonly used epoxy resins in thermosetting applications are the diglycidyl ether of bisphenol A (DGBPA) and the cycloaliphatic epoxy resin 3,4-epoxycyclohexylmethyl-3',4'-epoxycyclohexanecarboxylate (ECC).[24,25] They have both been studied in thermal or radiation induced curing reactions. The main advantage of using them are predominantly due to their inherent ring structures which provide thermal stability i.e. high glass transition temperature (Tg) to the final thermoset. However, they are derived from fossil fuels hence, considered environmentally less benign.[26]

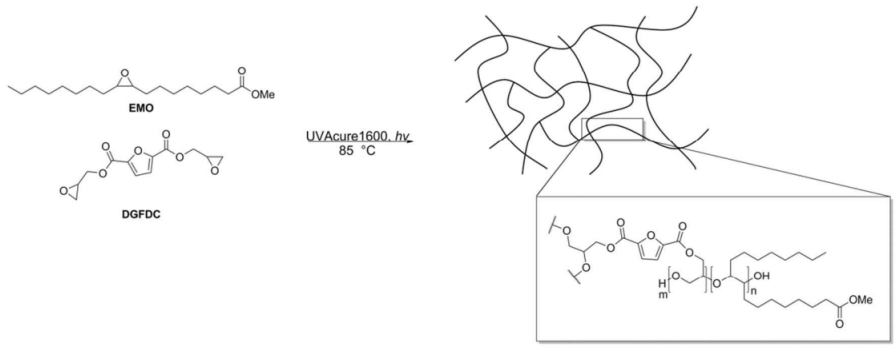

Scheme 1: Schematic illustration of the reaction between EMO and DGFDC forming a cross-linked thermoset.

Since the ground breaking work by Crivello and Lam[27,28] in the synthesis of diaryliodonium and triarylsulfonium salts, cationic polymerization of epoxides has gained popularity in both academia and industry.[29] Today cationic polymerization is a commonly used synthetic route for polymer thermosets through cyclic ether monomers. The reaction follows a chain-growth mechanism and can be triggered by e.g. UV light or temperature. In addition, cationic polymerization is considered oxygen insensitive, fast, and has an inherent low shrinkage of the final material.[30] Triggered photochemically or thermally, the initiator (a diaryliodonium or triarylsulfonium salt) dissociates to form a strong acid that protonates the epoxy-ring which then leads to an event of chain-growth propagation via the activated epoxy-ring.[31] A key feature is that the counter ion needs to be non-nucleophilic, which is the case for the most commonly used counter ions e.g. PF_6^- and SbF_6^-. Most utilized epoxides in commercial systems are either glycidyl ethers, cycloaliphatic, or 1,2-disubstituted aliphatic epoxides.

In this paper we expand the scope of FDCA-based monomers by using the diglycidyl ester of FDCA, diglycidyl furan-2,5-dicarboxylate (DGFDC) as a rigid monomer structure in combination with the aforementioned epoxidized fatty esters, from here on denoted EMX (Figure 1), in order to produce new types of bio-based epoxy resins. The study also reveals details on the intrinsic reactivities of the involved epoxides both by themselves and in co-polymerization reactions revealing intrinsically different reactivity of glycidyl esters compared to more conventional epoxides. It is demonstrated that both the final thermoset properties as well as the curing performance can be adapted by a proper choice of monomer mixtures.

3 Experimental

3.1 Materials

2,5-furandicarboxylic acid (FDCA) (97%), allyl alcohol (≥99%), 3-Chloroperbenzoic acid (m-CPBA) (≤77%), acetone (HPLC grade, 99.8 %), and sulphuric acid (H_2SO_4) (95-97%) were purchased from Sigma Aldrich. Epoxidized linseed oil (ELO) was provided by Ackros Chemicals. The photoinitiator UVAcure 1600 was supplied by CYTEC. All materials were used as received, unless otherwise noticed

3.2 Analytical methods

3.2.1 Nuclear Magnetic Resonance Spectroscopy (NMR)

In order to obtain ^{1}H-NMR a Bruker spectrometer (400 MHz) was used. The data for ^{1}H-NMR and ^{13}C-NMR were acquired by using 16-32 scans and 512 scans respectively and with 1 second relaxation time. Deuterated chloroform ($CDCl_3$) containing tetramethylsilane (TMS) and DMSO-d6 were used to dissolve the samples. The residual solvent peaks were used as reference ($CDCl_3$: 7.26 ppm (^{1}H-NMR) and 77.16 ppm (^{13}C-NMR) and DMSO-d6: 2.50 ppm (^{1}H-NMR) and 39.52 ppm (^{13}C-NMR). The acquired spectra were analysed using MestReNova v9.0.0-12821 (Mestrelab Research S.L. 2013).

3.2.2 Fourier-Transform Infrared Spectroscopy (FTIR) and Real-Time FTIR (RT-FTIR)

FTIR and RT-FTIR were recorded on a Perkin-Elmer Spectrum 100 equipped with a triglycine sulphate (TGS) detector. The instrument was equipped with a single reflection (ATR: attenuated total reflection) accessory unit Golden gate from Graseby Specac LTD (Kent, England). The Golden gate was equipped with a temperature control (Specac, Heated Golden Gate Controller). The FTIR spectra were recorded using 8 scans with a 4.0 cm^{-1} resolution and a range from 600-4000 cm^{-1}. The data was analysed using Spectrum software v. 10.5.1 from Perkin-Elmer. For RT-FTIR the data were recorded at 1 scan per 5.7 seconds with a resolution of 4.0 cm^{-1}. The software used for RT-FTIR was TimeBase® from Perkin-Elmer. The results from the RT-FTIR experiments were evaluated from conversion towards end of the reaction i.e. when changes in the spectra occurred, why the traces can be seen as comparative rates between the different reactions. Absolute values of epoxy conversion could not be obtained due overlapping peaks. The conversion was calculated as the relative change between the initial and final states of the curing reaction i.e. setting the initial state to 0 and the final state to 1. For comparative purposes the point in time for 95 % conversion and maximum rate (in %/s) was determined at the maximal slope throughout the

reaction. Initiation time was estimated from the tangent at the steepest slope, with the initiation time being determined as the intersection of the tangent with the x-axis

3.2.3 Differential Scanning Calorimetry (DSC)

The thermal analyses were obtained by a Mettler Toledo DSC-1 equipped with Gas Controller GC100. Approx. 5-10 mg of sample was weighed into 100 µL aluminum crucible. The data were collected using heating/cooling cycles from 30 °C to 300 °C for DSC kinetics and -50 to 200 °C for the Tg of the EMX:DGFDC thermosets. The temperature gradient rate was set to 10 °C min^{-1} with 5 min of isotherms at the highest/lowest temperature value for all DSC measurements. The analyses were carried out in inert atmosphere using 10 mL of N_2 gas. The Tg was obtained from the second heating cycle and was reported as the midpoint value of the heat capacity change. Determination of kinetic parameters from DSC scans were achieved using Borchardt and Daniels kinetics[32,33] in which the reaction rates, constants and orders are determined from the enthalpy obtained by integration of the reaction peak from a single DSC run. The Borchardt and Daniels method utilizes equation (1)-(3) in order to construct an Arrhenius plot. For these equation α is the fractional conversion, ΔH is the total enthalpy for the reaction, ΔH_T is the enthalpy of the reaction left to proceed at time, t, n is the reaction order and K(T) is the temperature dependent rate constant. The data points for these calculations are obtained by dividing the integral of the DSC exothermal reaction peak into 20 evenly spaced areas from the temperature at 10 % of the peak height until 50 % of the reaction has occurred (at $\Delta H_T = 0.5$). This limitation was introduced in order to circumvent the decrease in reaction rate from the increase in cross-linking density.

$$1 - \alpha = \Delta H_T / \Delta H \quad (1)$$

$$\frac{d\alpha}{dt} = \frac{dH}{dt} / \Delta H \quad (2)$$

$$\ln \frac{d\alpha}{dt} = \ln\big(K(T)\big) + n * \ln(1 - \alpha) \quad (3)$$

3.2.4 Dynamical Mechanical Thermal Analysis (DMTA)

DMTA was conducted to obtain the physical properties of the synthesized thermosets. A Q800 DMTA (TA instruments was used. The instrument was equipped with a clamp for tensile testing. The data were collected using a temperature ramp from -50 °C to 200 °C using a heating rate of 3 °C min^{-1}. The frequency was set to 1 Hz. The Tg of each sample was obtained from the maximum of the tan δ peak.

3.2.5 UV-light source

The UV-light was generated from a Hamamatsu L5662 with a standard medium-pressure 200 W L6722-01 Hg-Xe lamp. The intensity of the UV-light was measured by a Hamamatsu power meter (model C6080-03) calibrated for 365 nm. The intensity was measured to 80-90 mW cm^{-2}.

3.2.6 Automated column purification

The fatty acid methyl esters were separated by Isolera 4 advanced automated flash purification from Biotage equipped with UV detector. A 50 g KP-Sil column packed with silica was used to separate the FAME mixture. The column was packed with approx. 10 wt. % of sample relative to the weight amount of silica in the column

3.3 Synthesis procedures

3.3.1 Synthesis of diallyl furan-2,5-dicarboxylate (DAFDC)

Following literature procedure,[21] FDCA (50.0 g, 0.32 mol) was added allyl alcohol (500 mL) and concentrated H_2SO_4 (1 mL). The suspension was heated to 115 °C (mildly refluxing) for 72 hours. The obtained solution was cooled to room temperature and the reaction mixture was concentrated until almost fully dry, yielding a black residue, which was diluted with diethyl ether (500 mL), and washed twice with a saturated sodium bicarbonate solution (1000 mL in total). The organic phase was concentrated yielding a yellow solid, which upon distillation (b.p. 140 °C at 15 mbar. Corrected b.p. 276 °C) yielded diallyl furan-2,5-dicarboxylate (56.2 g, 74.2 %). **^{1}H NMR** (400 MHz, DMSO-d6) δ: 7.47 (d, J = 2.3 Hz, 1H), 6.02 (ddt, J = 17.4, 10.7, 5.5 Hz, 1H), 5.45 – 5.25 (m, 2H), 4.82 (dt, J = 5.6, 1.4 Hz, 2H). **^{13}C NMR** (101 MHz, DMSO-d6) δ: 157.0, 146.0, 132.0, 119.3, 118.7, 65.6.

3.3.2 Synthesis of diglycidyl furan-2,5dicarboxylate (DGFDC)

Following modified literature procedure,[22] DAFDC (4.98 g, 21.08 mmol) and m-CPBA (77 wt. % pure, 11.84 g, 52.83 mmol) was suspended in dichloromethane (40 mL) and heated to 40 °C for 72 hours. The resulting suspension was filtered and rinsed with dichloromethane (30 mL). The organic phase was washed with a 10 % aqueous solution of Na_2SO_4 (50 mL), followed by a 10 % aqueous solution of Na_2CO_3 (50 mL) and lastly demineralized water (50 mL). The organic phase was dried with $MgSO_4$ and concentrated to yield diglycidyl furan-2,5-dicarboxylate (DGFDC) (5.11 g, 90.0 %) as a white crystalline solid. **^{1}H-NMR** (400 MHz, DMSO-d6) δ 7.49 (s, 2H), 4.68 (dd, J = 12.4, 2.7 Hz, 2H), 4.10 (dd, J = 12.3, 6.6 Hz, 2H), 3.33 (d, J = 4.8 Hz, 2H), 2.84 (t, J = 4.6 Hz, 2H), 2.73 (dd, J = 5.0, 2.6 Hz, 2H). **^{13}C-NMR** (101 MHz, DMSO-d6) δ 157.06, 145.91, 119.51, 66.03, 48.80, 43.90.

3.3.3 Transesterification of Epoxidized Linseed Oil (ELO)

Following literature procedure[34] the different fatty acid methyl esters EMO, EMLO and EMLEN were retrieved by methanolysis procedure. ELO (20 g) was weighed into a round bottom flask equipped with a magnetic stirrer. To the round bottom flask was NaOH dissolved in methanol (0.02 M, 250 mL) added under stirring. The round bottom flask was then equipped with a condenser and was then heated to 68 °C for 1 hour. The reaction mixture was then cooled to room temperature and the fatty acids were extracted in n-heptane to remove the glycerol. The n-heptane was rotary evaporated resulting in a fatty acid mixture (15 g, 75 %). Automated column chromatography (Isolera 4) was then used to separate the different monomers. Silica was used as a stationary phase and a gradient of n-heptane:ethyl acetate as mobile phase. The pure fractions of each monomer were collected and the solvents were rotary evaporated. To completely dry the monomers from residual solvent the monomers were put in vacuum oven at 50 °C overnight. The pure monomers EMO (2 g, 10 %), EMLO (2 g, 10 %) and EMLEN (5 g, 25 %) were then stored in glass vials at room. temperature. ^{1}H-NMR and ^{13}C-NMR (Figure S5-10) and FTIR (Figure S12) of the monomers can be found in supporting information.

3.3.4 General procedure for photo-curing followed by RT-FTIR

The desired amounts of DGFDC and EMX monomers (see Table 1 for monomer ratios) were added to in a small vial and dissolved using a 10 mg mL^{-1} solution of UVAcure 1600 in acetone, resulting in a dry mixture containing 2 wt. % UVAcure 1600. For high DGFDC ratios, additional acetone was required for a fully homogenous solution, and the amount of acetone was doubled in these cases. The crystal located on the Golden gate accessory unit was preheated to 85 °C and a background scan was recorded before a 10 µL of the solution (or 20 µL for samples containing additional acetone) was applied to the crystal. The mixture was left at 85 °C for two minutes for all acetone to evaporate. This was followed by irradiation with UV-light and RT-FTIR measurements for 30 minutes for EMO and EMLO systems and 60 min for EMLEN systems and pure DGFDC.

3.3.5 General procedure for curing of films for DMTA

The desired amounts of DGFDC and EMX monomers were weighed in a vial with a magnet and UVAcure 1600 was added amounting to 2 wt. % of the total monomer weight. The vial was closed and heated to 85 °C in an oil bath while stirring, yielding a homogenous liquid. The hot solution was added to a preheated silicone mould preheated on a heating plate set at 100 °C. The sample was irradiated with UV-light at this temperature for one hour, resulting in fully cured films usable for DMTA measurements.

4 Results and Discussions

4.1 Synthesis of monomers

The DGFDC monomer was synthesized using a green esterification of FDCA and allyl alcohol using a catalytic amount of sulfuric acid, forming diallyl furan-2,5-dicarboxylate as shown in previous works,[21] followed by epoxidation with m-CPBA in high yield as illustrated in Scheme 2. The synthesis procedure was confirmed both by NMR (Figure S1-4) and FTIR (Figure S11). The obtained DGFDC was white crystalline solid with a melting point of 83 °C confirmed by DSC (Figure S22).

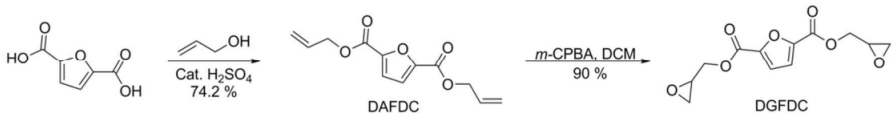

Scheme 2: Synthesis of DAFDC and DGFDC monomers

4.2 Curing performance

In order to evaluate the activation energies of the utilized monomers reactive DSC runs of all systems were carried out using the intended UV-initiator as a thermal initiator. Because this type of activation requires higher amount of energy compared to UV-initiation the absolute activation energies obtained are unrepresentative of the UV-initiated system. However, assuming thermal activation follows the same polymerization mechanism the relative activation energies would be comparable to those of the UV-initiated system. For this setup the pure monomers were run in a DSC scan with 2 wt. % of UVAcure 1600, yielding an exothermal curing peak (Figure 2A), which upon integration gives the enthalpy of the curing reaction. Using Borchardt and Daniels kinetics it is hereby possible to obtain activation energies for the monomers. This type of kinetic calculation could not be applied to the tri-functional epoxide EMLEN due to multiple curing peaks as a result of the different reactivity of the epoxides. However, activation energies were obtained for DGFDC, EMO and EMLO, showing much lower activation energies for the fatty-acid based epoxides. The relative activation energies being 1.00, 1.09 and 2.00 for EMO, EMLO and DGFDC respectively. Details on these calculations, including Arrhenius plots and reaction order refinements are available in the supporting information (Figure S13-25).

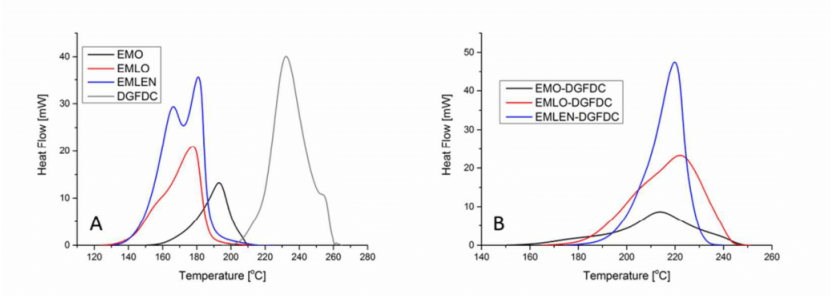

Figure 2: Reactive DSC thermograms of A: pure monomers EMO, EMLO, EMLEN and DGFDC; and B: mixtures of 1:1 epoxy molar ratio of EMO:DGFDC, EMLO:DGFDC and EMLEN:DGFDC. In both A and B the reactions were thermally initiated by using UVAcure 1600.

Furthermore, reactive DSC runs of the reactive mixtures were used to investigate the co-polymerization of DGFDC and EMX monomers. The monomers were mixed using a 1:1 epoxy molar ratio and 2 wt. % UVAcure 1600 was added as initiator. The DSC thermograms showed a combined curing peak much below the curing temperature of pure DGFDC. Even though the curing reactions were occurring simultaneously the observed peaks did not show as a bell-shaped curve making the Borchardt and Daniels kinetics method inadequate for determining kinetic parameters for the combined reaction. The curing peaks for the three mixed EMX-DGFDC systems are shown in Figure 2B. Though kinetic parameters for these reactions could not be estimated with Borchardt and Daniels kinetics the combined peaks did however show that co-polymerization of the DGFDC and EMX monomers takes place with the reaction occurring at lower temperatures compared to pure DGFDC.

In order to cure mixtures of EMX-DGFDC using UV-light some heating had to be applied. Though all EMX monomers are liquids, a DSC analysis of pure DGFDC revealed a melting point of 83 °C, which was gradually lowered in mixtures with EMX monomers. Therefore all curing reactions were carried out at 85 °C in order to keep the feed liquid. To evaluate the effect of the stoichiometry of the feed mixture curing reactions were carried out with DGFDC and each of the three EMX monomers in various epoxy molar ratios, namely EMX:DGFDC ratios of 5:1, 2:1, 3:2, 1:1, 2:3, 1:2 and 1:5 (Table 1). All systems were cured using 2 wt. % of the UVAcure 1600 initiator.

Entry	EMX	EMX:DGFDC Epoxy molar ratio	T_g [a] °C	t_{end} s	t_{ini} s	Max Rate %/s
1	EMO	1:0	N/A	20.9	4.1	11.1
2	EMLO	1:0	N/A	31.7	4.2	8.3
3	EMLEN	1:0	-1	168.8	3.8	4.0
4	-	0:1	N/A	N/A	47.3	0.5
5	EMO	5:1	N/A	31.7	4.0	8.3
6	EMO	2:1	N/A	57.8	5.9	5.4
7	EMO	3:2	N/A	89.7	5.0	3.5
8	EMO	1:1	N/A	73.8	3.8	5.7
9	EMO	2:3	N/A	332.3	4.2	7.1
10	EMO	1:2	N/A	532.8	4.1	1.5
11	EMO	1:5	N/A	342.7	5.5	2.4
12	EMLO	5:1	-23	105.6	5.8	4.0
13	EMLO	2:1	-8	295.6	6.0	2.4
14	EMLO	3:2	1	422.2	12.0	1.4
15	EMLO	1:1	20	380.1	5.0	2.1
16	EMLO	2:3	31	417.0	4.9	2.3
17	EMLO	1:2	49	886.6	10.9	1.2
18	EMLO	1:5	65	1071.3	7.3	1.1
19	EMLEN	5:1	24	427.2	4.0	3.3
20	EMLEN	2:1	41	917.9	5.6	1.9
21	EMLEN	3:2	44	1197.6	7.2	1.4
22	EMLEN	1:1	56	1441.8	11.3	1.3
23	EMLEN	2:3	65	1466.8	7.1	1.3
24	EMLEN	1:2	67	1545.8	13.2	0.8
25	EMLEN	1:5	66	1540.6	6.0	1.2
26	EMO	1:1 DGBPA	-23	N/A	N/A	N/A
27	EMLO	1:1 DGBPA	29	N/A	N/A	N/A
28	EMLEN	1:1 DGBPA	71	N/A	N/A	N/A

[a] Determined by second heat cycle from DSC

Table 1: The different monomer mixtures studied and their respective Tg obtained from DSC. The table also shows results from the RT-FTIR measurements

The products of the UV-curing reactions were all analyzed using DSC, giving their respective Tg presented in Table 1. It was observed that all systems containing EMO yielded products with Tg below -50 °C and was undetectable by the applied instrument. Due to these low Tg's, EMO-DGFDC systems were deemed redundant due to their poor mechanical properties. DSC analyses of the EMLO-DGFDC and EMLEN-DGFDC systems however showed varied Tg's in ranges of -25 °C to 70 °C, with increases corresponding to the increase in the amount of DGFDC (Figure 3).

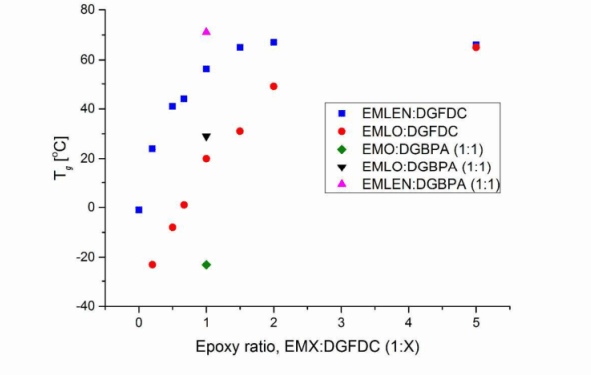

Figure 3: Tg's of the different thermoset systems EMLO-DGFDC and EMLEN-DGFDC determined by DSC. The Tg increases with increasing amount of DGFDC in both thermoset systems. DGBPA thermosets with EMX (1:1) equivalents yielding slightly higher Tg's

Curing of systems containing only pure monomers were also carried out for the 4 applied reagents. Here only a glass transition of cross-linked EMLEN could be observed (following the trend in Tg's of the mixed systems). However, the Tg of cross-linked EMO and EMLO could not be observed most likely due to these temperature being below -50 °C and therefore below the detection limit of the applied instrument. Cured DGFDC on the other hand yielded an irregular DSC curve, which hinted that the system could not cross-link properly. RT-FTIR experiments confirmed that the reaction of pure DGFDC was too slow to finish within the time window of the reaction. In order to evaluate the usability of DGFDC as a replacement for petrol-based monomers, a comparison to the widely used diglycidyl ether of bisphenol A (DGBPA) was made. This was done by curing 1:1 epoxy molar ratio systems with the three EMX monomers (Table 1 Entry 26-28). These results showed comparable results with DGBPA systems yielding Tg's of 9 °C and 15 °C higher than their DGFDC analogues for EMLO and EMLEN systems respectively. This increased temperature most likely stems from DGBPA containing two aromatic rings compared to the furan in DGFDC thus providing more rigidity to the system.

All UV-curing reactions were followed using RT-FTIR (except the ones with DGBPA), allowing close following of the disappearance of epoxy peaks (820 – 900 cm^{-1}) as well as the formation of ether bonds (1050 – 1100 cm^{-1}). The conversions of the various systems are presented in Figure 4.

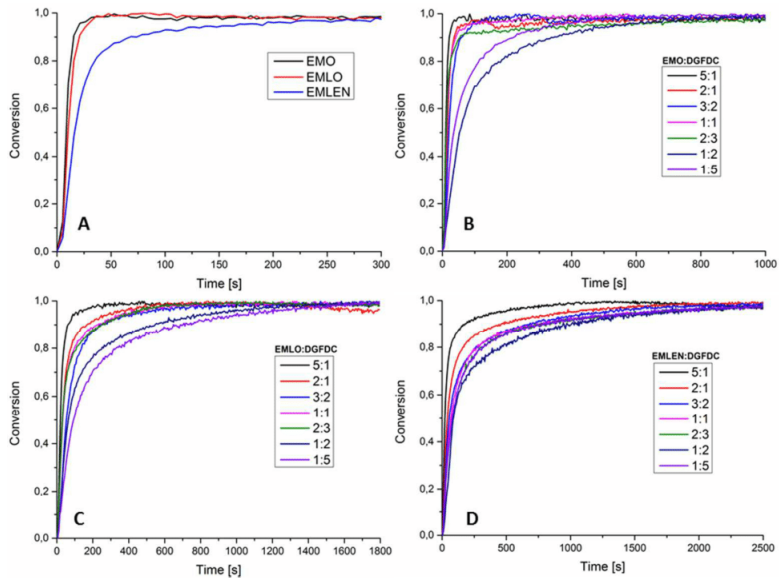

Figure 4: RT-FTIR measurements A: pure monomers; B: EMO-DGFDC; C: EMLO-DGFDC and D: EMLEN-DGFDC. In all cases following the formation of ether bonds at 1050 – 1100 cm^{-1}

From the RT-FTIR results some pseudo-kinetic parameters could be determined. The main obstacle using this measurement was the lack of clearly isolated peaks for either the epoxides or the ethers. Therefore all results are relative between initial and final states of the curing system meaning 100 % conversion correlates to point in time when the reaction stalls and no change in the traces from the ether region were observed. From these results it was possible to determine initial rates in %/s, initiation time as well as the time elapsed until no change occurred. All these values are summed in Table 1. For all EMX-DGFDC systems maximal rate and initiation time occurred within the first few scans (0-15 seconds), making the obtained values highly unprecise with the current resolution. This however still proves the efficiency of the applied polymerization method on this system with almost no initiation phase affecting the curing reaction. The measurements of maximal reaction rates showed the general trend of highest rates present at lower concentration of DGFDC as expected. Experiments with feeds containing only pure EMX monomers were also carried out in general showing that both EMO and EMLO were faster than EMLEN. However, DGFDC in its pure form had much slower reaction rates than the EMX monomers. The RT-FTIR traces for pure DGFDC showed that the ether region never levelled of most likely due to vitrification effect hence, the data was not comparable to data from pure EMX monomers. The respective order of the pure

monomer reaction rates being EMO>EMLO>EMLEN>>DGFDC, corroborating the trends observed by DSC (Figure 2A).

From the data presented in Table 1 no clear correlation of kinetic parameters to stoichiometry of feed could be observed except for the general trend of higher conversion times in EMLO and EMLEN systems when increasing the amount of DGFDC. It was expected that increased amounts of DGFDC would cause a direct correlation to decreasing reaction rate, assuming the free movement of the molecules (e.g. in a solution). However, the different molecular structures of the monomers the overall macromolecular dynamics of the bulk systems changes significantly when adjusting the stoichiometric ratios. Therefore, direct kinetic correlations were not observed.

4.3 Structure-Property relationship of the final thermosets

In order to understand the influence of the thermo-mechanical behavior of the cured EMX-DGFDC systems, films for DMTA were made. Figure 5 shows the DMTA results.

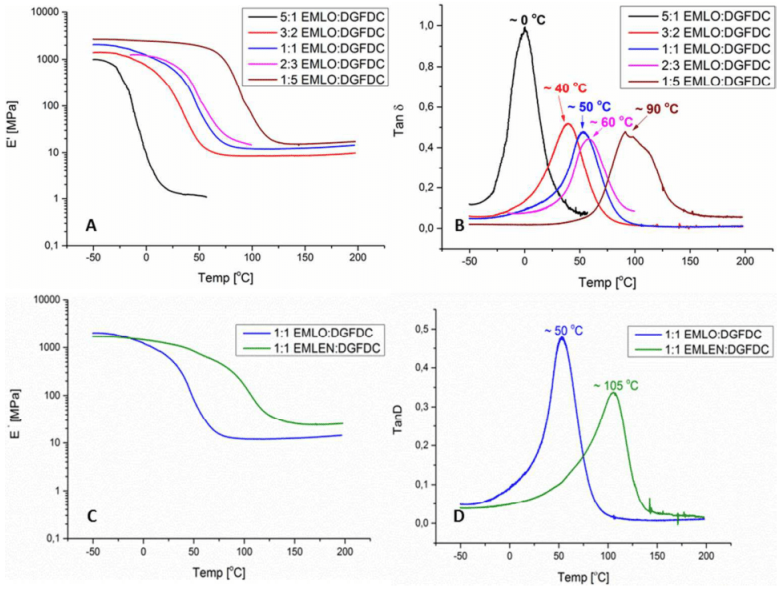

Figure 5: DMTA measurements on photo-cured thermosets A-B shows the EMLO-DGFDC system and C-D shows comparison between EMLO and EMLEN thermosets.

The results strengthen the hypothesis that the reaction between EMX-DGFDC leads to a cross-linked network. This can be observed in Figure 5A and C which shows that the rubbery plateau showed no flow behavior in any case. In addition the results indicate that both an increase in

DGFDC and a higher epoxy functional fatty acid results in a greater cross-linking density. The glassy region however, showed small differences in the value of storage modulus (E') ranging from 1.0 – 2.7 GPa (-50°C). The highest value was obtained from the sample with most DGFDC (1:5 EMLO:DGFDC) which is comparable to common commercial plastics such as PET analyzed by DMTA.[35]

The Tg can also be detected by DMTA however, this transition usually shows higher values than Tg measured by DSC due to frequency effects.[36] The Tg results from DMTA showed similar trend to the DSC results. This was the expected results due to the increased amount of rigidity stemming from the furan rings of DGFDC. Furthermore, only one Tg was observed in all EMLO-DGFDC monomer ratios indicating that the reaction between EMLO and DGFDC is not phase separated.

The different fatty acids had a clear impact on the Tg. Both DMTA (Figure 5C-D) and DSC (Figure 3) results showed that EMLEN-DGFDC system exhibited higher Tg's compared to the corresponding EMLO system. This may be attributed to the amount of linear aliphatic chain-ends in the cross-linked network. The chain-end of EMLO is based on 5 carbon atoms while the EMLEN only have 2 carbon atoms. Longer chain-ends gave rise to higher degree of movement in the network which in turn resulted in a lower Tg observed (1:1 EMLO:DGFDC) and vice versa. It was also observed that increasing epoxides on the fatty acid provide a broader Tg i.e. a less homogeneous thermoset.

5 Conclusions

In the pursuit of utilizing bio-feedstocks as building blocks in polymers the application area of FDCA-based monomers has been extended into epoxy thermosets. In this study we aimed to address the influence of stoichiometry ratios on structure-property relationship. The study shows that it was possible to make thermosets by combining the diglycidyl ester of FDCA (DGFDC) with free epoxidized fatty methyl esters (EMX) retrieved from epoxidized linseed oil. The combination of the bio-based monomers showed that it was possible to have structure-property control due to the vastly different attributes of the monomers. EMX monomers provided flexible, hydrophobic structures and the furans of the DGFDC provided rigidity and mechanical stability. Moreover, it was also shown that UV-curing of the pure DGFDC showed very slow reaction speed. However, the reaction speed was significantly increased when DGFDC was mixed with any of the fatty acids. The thermo-mechanical properties was also assessed which showed that the bio-based DGFDC had promising results in comparison to the commercially available and petrol-based diglycidyl ether of

bisphenol A (DGBPA) regarding Tg properties. In addition, the storage modulus was in the range of 1.0 – 2.7 GPa which is comparable to common plastics such as PET.

6 Corresponding Author

Correspondence to: Mats Johansson (E-mail: matskg@kth.se)

KTH Royal Institute of Technology, Department of Fibre and Polymer Technology, Division of Coating Technology, SE-100 44 Stockholm, Sweden.

7 Author Contributions

All authors have written the manuscript and given approval of the final version of the manuscript.

8 Acknowledgements

The authors would like to acknowledge the Swedish research council, FORMAS (Grant number 211-2013-70) and Technical University of Denmark, Augustinus Fonden and Otto Mønsteds Fond for financial support.

9 References

(1) Andrady, A. L. *Plastics and the Environment*; John Wiley & Sons, 2003.

(2) Werpy, T.; Petersen, G. Top Value Added Chemicals from Biomass Volume I — Results of Screening for Potential Candidates from Sugars and Synthesis Gas Top Value Added Chemicals From Biomass Volume I : Results of Screening for Potential Candidates. *U.S. Dep. Energy* **2004**, *1*.

(3) Belgacem, M. N.; Gandini, A. *Monomers, Polymers and Composites from Renewable Resources*; Elsevier: Oxford, 2008.

(4) Montero De Espinosa, L.; Meier, M. A. R. Plant Oils: The Perfect Renewable Resource for Polymer Science?! *Eur. Polym. J.* **2011**, *47* (5), 837–852.

(5) Meier, M. A. R.; Metzger, J. O.; Schubert, U. S. Plant Oil Renewable Resources as Green Alternatives in Polymer Science. *Chem. Soc. Rev.* **2007**, *36* (11), 1788.

(6) Kienle, R. H.; Hovey, A. G. The Polyhydric Alcohol-Polybasic Acid Reaction. I. Glycerol-Phthalic Anhydride. *J. Am. Chem. Soc.* **1929**, *51* (2), 509–519.

(7) Kienle, R. H.; Ferguson, C. S. Alkyd Resins as Film-Forming Materials. *Ind. Eng. Chem.* **1929**, *21* (4), 349–352.

(8) Stenberg, C.; Svensson, M.; Johansson, M. A Study of the Drying of Linseed Oils with Different Fatty Acid Patterns Using RTIR-Spectroscopy and Chemiluminescence (CL). *Ind. Crops Prod.* **2005**, *21* (2), 263–272.

(9) Gall, R. J.; Greenspan, F. P. A Modified Peracid Process for Making Epoxy Compounds

from Unsaturated Fatty Acid Esters. *Ind. Eng. Chem.* **1955**, *47* (1), 147–148.

(10) Pan, X.; Sengupta, P.; Webster, D. C. High Biobased Content Epoxy-Anhydride Thermosets from Epoxidized Sucrose Esters of Fatty Acids. *Biomacromolecules* **2011**, *12* (6), 2416–2428.

(11) Pan, X.; Webster, D. C. New Biobased High Functionality Polyols and Their Use in Polyurethane Coatings. *ChemSusChem* **2012**, *5* (2), 419–429.

(12) Gunstone, F. D. Fatty Acids. Part II. The Nature of the Oxygenetad Acid Present in Vernonia Anthelminitca (Willd.) Seed Oil. *J. Chem. Soc.* **1954**, 1611–1616.

(13) Muuse, B. G.; Petrus Cuperus, F.; Derksen, J. T. P. Composition and Physical Properties of Oils from New Oilseed Crops. *Ind. Crops Prod.* **1992**, *1* (1), 57–65.

(14) Krasutsky, P. A. Birch Bark Research and Development. *Nat. Prod. Rep.* **2006**, *23* (6), 919.

(15) Tomasi, P.; Wang, H.; Lohrey, G. T.; Park, S.; Dyer, J. M.; Jenks, M. A.; Abdel-Haleem, H. Characterization of Leaf Cuticular Waxes and Cutin Monomers of Camelina Sativa and Closely-Related Camelina Species. *Ind. Crops Prod.* **2017**, *98*, 130–138.

(16) Tsubaki, S.; Sakumoto, S.; Uemura, N.; Azuma, J. I. Compositional Analysis of Leaf Cuticular Membranes Isolated from Tea Plants (Camellia Sinensis L.). *Food Chem.* **2013**, *138* (1), 286–290.

(17) Boisen, A.; Christensen, T. B.; Fu, W.; Gorbanev, Y. Y.; Hansen, T. S.; Jensen, J. S.; Klitgaard, S. K.; Pedersen, S.; Riisager, A.; Ståhlberg, T.; et al. Process Integration for the Conversion of Glucose to 2,5-Furandicarboxylic Acid. *Chem. Eng. Res. Des.* **2009**, *87* (9), 1318–1327.

(18) Moreau, C.; Belgacem, M. N.; Gandini, A. Recent Catalytic Advances in the Chemistry of Substituted Furans from Carbohydrates and in the Ensuing Polymers. *Top. Catal.* **2004**, *27* (1–4), 11–30.

(19) Eerhart, A. J. J. E.; Faaij, A. P. C.; Patel, M. K. Replacing Fossil Based PET with Biobased PEF; Process Analysis, Energy and GHG Balance. *Energy Environ. Sci.* **2012**, *5* (4), 6407–6422.

(20) Tomás, R. A. F.; Bordado, J. C. M.; Gomes, J. F. P. P-Xylene Oxidation to Terephthalic Acid : A Literature Review Oriented toward Process Optimization and Development. *Chem. Rev.* **2013**, *113*, 7421–7469.

(21) Larsen, D. B.; Sønderbæk-Jørgensen, R.; Duus, J.; Daugaard, A. E. Investigation of Curing Rates of Bio-Based Thiol-Ene Films from Diallyl 2,5- Furandicaboxylate. *Eur. Polym. J.* **2018**, *102* (November 2017), 1–8.

(22) Deng, J.; Liu, X.; Li, C.; Jiang, Y.; Zhu, J. Synthesis and Properties of a Bio-Based Epoxy Resin from 2,5-Furandicarboxylic Acid (FDCA). *RSC Adv.* **2015**, *5* (21), 15930–15939.

(23) Burrows, A.; Holman, J.; Parsons, A.; Pilling, G.; Price, G. *Chemistry3: Introducing Inorganic, Organic and Physical Chemistry*, 1st ed.; Oxford University Press: New York, 2009.

(24) Sangermano, M.; Vitale, A.; Dietliker, K. Photolatent Amines Producing a Strong Base as

Photocatalyst for the in-Situ Preparation of Organic–inorganic Hybrid Coatings. *Polymer (Guildf).* **2014**, *55* (7), 1628–1635.

(25) Carioscia, J. A.; Stansbury, J. W.; Bowman, C. N. Evaluation and Control of Thiol-Ene/thiol-Epoxy Hybrid Networks. *Polymer (Guildf).* **2007**, *48* (6), 1526–1532.

(26) Ashcroft, W. R.; Cantwell, W. J.; Chen, X. M.; Ellis, B.; Johari, G. P.; Jones, F. R.; Kausch, H. H.; Shaw, S. J. *Chemistry and Technology of Epoxy Resins*; 1993.

(27) Crivello, J. V.; Lam, J. H. W. Diaryliodonium Salts. A New Class of Photoinitiators for Cationic Polymerization. *Macromolecules* **1977**, *10* (6), 1307–1315.

(28) Crivello, J. V.; Lam, J. H. W. Photoinitiated Cationic Polymerization with Triarylsulfonium Salts. *J. Polym. Sci. Part A Polym. Chem.* **1996**, *34* (16), 3231–3253.

(29) Michaudel, Q.; Kottisch, V.; Fors, B. P. Cationic Polymerization: From Photoinitiation to Photocontrol. *Angew. Chemie - Int. Ed.* **2017**, *56* (33), 9670–9679.

(30) Decker, C.; Nguyen Thi Viet, T.; Pham Thi, H. Photoinitiated Cationic Polymerization of Epoxides. *Polym. Int.* **2001**, *50* (9), 986–997.

(31) Crivello, J. V. Cationic Polymerization - Iodonium and Sulfonium Salt Photoinitiators. *Adv. Polym. Sci.* **1984**, *62*, 1–48.

(32) Borchardt, H. J.; Daniels, F. The Application of Differential Thermal Analysis to the Study of Reaction Kinetics. *J. Am. Chem. Soc.* **1957**, *79* (1), 41–46.

(33) Designation: E2041-13. Estimating Kinetic Parameters by Differential Scanning Calorimeter Using the Borchardt and Daniels Method 1. *Astm* **2015**, *14*, 1–7.

(34) Nameer, S.; Johansson, M. Fully Bio-Based Aliphatic Thermoset Polyesters via Self-Catalyzed Self-Condensation of Multifunctional Epoxy Monomers Directly Extracted from Natural Sources. *J. Coatings Technol. Res.* **2017**, *14* (4), 757–765.

(35) Mouzakis, D. E.; Papke, N.; Wu, J. S.; Karger-Kocsis, J. Fracture Toughness Assessment of Poly(ethylene Terephthalate) Blends with Glycidyl Methacrylate Modified Polyolefin Elastomer Using Essential Work of Fracture Method. *J. Appl. Polym. Sci.* **2001**, *79* (5), 842–852.

(36) Nielsen, L. E. *Mechanical Properties of Polymers and Composites*; CRC press: New York, 1994.

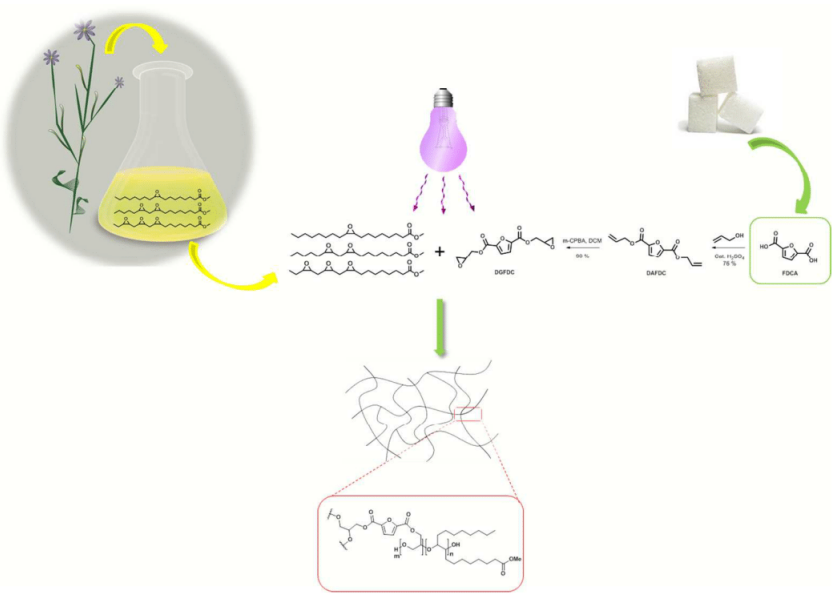

Radiation curing of building blocks from renewable resources

244x172mm (150 x 150 DPI)